Design and characterisation of a photonic sensor platform for the detection of biofilm formation

by

Salem Elmaghrum

A thesis presented to Dublin City University

for the Degree of Doctor of Philosophy

Research supervisor:

Dr. Brian Corcoran

School of Mechanical & Manufacturing Engineering

Dublin City University

January 2015

Preface

Declaration

I hereby certify that the material, which I now submit for assessment on the programme of study leading to the award of Doctor of Philosophy, is entirely my own work and has not been taken from the work of others save and to the extent that such work has been cited and acknowledged within the text of my work.

Signed: .

ID No: **53135121**

Date: **14 / 08 / 2014**

Acknowledgments

Abstract

This thesis focuses on the development and characterisation of a waveguide-based photonic sensing platform for the detection of biofilm. This integrated photonic platform is based upon the high sensitivity of an optical field distribution formed in optical waveguides and the resulting changes in the refractive index and absorption of this environment.

The sensor platform and materials formulations were established from simulation studies conducted with the Olympios software. These simulations demonstrated the importance of correctly specifying the material refractive index to achieve single-mode waveguides. They also highlighted the necessity to deposit a high refractive index layer (HRIL) on top of the optical waveguides in order to increase the intensity of the evanescent field responsible for the sensing performance of the platform.

Platform fabrication exploited a low-cost process using photocurable organic-inorganic hybrid sol–gel materials, which were microstructured by UV-photolithography to form channel optical waveguides. A tantalum-based material was synthesized using the sol–gel process with refractive index as high as 1.87. This material was developed, optically characterised and applied as an evanescent field enhancement layer, deposited at the surface of the waveguide to increase the sensitivity of the sensing platform. The sensor characterisation was performed by monitoring the output intensity of the optical waveguide while contaminated water was monitored in both quasi-static and dynamic flow-rates on the platform. It is shown that the sensing performance of this biosensor platform relies on the applied flow-rate. In quasi-static flow rate, the biofilm formation was detected after 10 min of reactions, demonstrating the early stage biofilm formation in quasi-static flow-rate. The progressive increase of the flow-rate showed an increase of the detection time. Furthermore, the sensing performances of this photonic platform were found to be strongly dependent on the thickness of the HRIL, confirming the simulations studies.

This work proved the concept of employing a waveguide-based photonic platform for the early detection of biofilm formation, including the induction phase, and as such, I believe this system has immense potential for future applications as a label-free and real-time biosensor platform for bioenvironmental applications.

Table of Contents

List of Figures

List of Tables

Nomenclature

HRI	High Refractive Index
HRIL	High Refractive Index Layer
EF	Evanescent Field
BL	Buffer Layer
GL	Guiding Layer
PL	Protective Layer
n	Refractive Index
Δn	Refractive Index Difference
MATPMS	3(trimethoxy- silyl)propylmethacrylate
MAAH	Methacrylic Acid
TAO	Tantalum Ethoxide
ZPO	Zirconium(iv) n-propoxide
Pi	Photoinitiator
IPA	Isopropanol
SPR	Surface Plasmon Resonance
MZI	Mach-Zehnder Interferometer
RIE	Reactive Ion Etching
PLCs	Planar Lightwave Circuits
CVD	Chemical Vapor Deposition
FTTH	Fiber-To-The-Home
OEO	Optical-Electrical-Optical
DO	Dissolved Oxygen
LB	Langmuir-Blodgett
QCL	Quantum-Cascade Laser
PIE	Potassium-Ion-Exchange
COWG	Composite Optical Waneguide
L.O.D	Limit of Detection
BTB	Bromothymol Blue
MZI	Mach-Zehnder Interferometer
RIfS	Reflectometric Interference Spectometry

FTIR	Fourier Transform Infrared
NDIR	Nondispersive Infrared
TIR	Total Internal Reflection
TE	Transverse Electron
TM	Transverse Magnetic
TEM	Transverse Electron Magnetic
HOIM	Hybrid Organic-Inorganic Materials
RIC	Refractive Index Contrast
SERS	Surface-Enhanced Raman Spectroscopy
IR	InfraRed

Chapter 1

Introduction and Objectives

Over the past decade the biosensor market has grown exponentially to respond to a constant demand/ increase in novel multifunctional biodetection methodologies and devices for medical and environmental applications. In particular, with the growing awareness of health diseases associated with ecological and bioenvironmental pollution, the development of innovative biosensing solutions has sought to address this need with varying results being achieved.

Amongst the most popular bioenvironmental concerns microbial adhesion to surfaces and the subsequent biofilm formation has been a critical problem for many industrial sectors including food, environmental, clinical and pharmaceutical. The attachment and growth of microorganism on wet surfaces is a natural behavior involving several complex physico-chemical processes, the most well-defined of which are surface preconditioning, cell deposition and adsorption as well as replication and growth, as thoroughly described in a recent review. They can mature to highly complex cell agglomerates formed by bacteria and multi-cellular eukaryotic organism to reach thicknesses of up to 300 microns within less than a month. In natural ecosystems, they can enable or prevent the formation of micro- and macro-organisms. In clinical environment and in the pharmaceutical industry the formation of biofilm is a crucial factor provoking chronic diseases and microbial infections in higher purity water systems. Biofilm detection is an area of interest for ecological/environmental and health studies as well as for biomass control. Over the past decade a large variety of sensing platforms have been developed including those exploiting microscopy, electrochemical, and optical techniques. Of the optical techniques, the vast majority are based on optical transduction techniques with luminescence based biosensors gaining increased popularity. Amongst these techniques, the electrochemical and optical biosensors are probably the most popular. Though many of these techniques provide excellent sensitivity and selectivity, owing to their technical limitation or complexity, the majority of methods are only applicable in the laboratory rather than in field studies or other harsh environments.

The central objective of this thesis was to develop a methodology to enable the development of an innovative biosensing platform utilizing optical transduction techniques for the detection of the EARLY STAGE FORMATION of biofilm formation.

A promising technology for the development of these components is the use of photocurable hybrid sol-gel materials to fabricate planar lightwave circuits employing standard photolithography processes such as those used in the semi-conductor industry. The sol-gel process allows the production of advanced multifunctional materials, from which it is possible to fabricate compact, low-cost and mass-producible devices which can match and exceed performances of many of the established materials routinely used for PLC fabrication. Synergizing these materials with microstructuration techniques along with innovative platform designs, which will associate sensitivity and specificity to biomolecules and microorganisms, the development of an innovative biosensing platform can be achieved.

Therefore, to do this, the sub-objectives of this thesis will concentrate on:

1. Establishing the current state-of-the-art in both sensing methodologies and designs
2. Identifying the physical principles that will enable the optimization of the sensitivity of optical platforms
3. Designing a label free optical biosensing platform capable of simultaneously verifying the required optical conditions to achieve high sensitivity and to fulfil the microfabrication requirements imposed by standard photolithography techniques
4. Developing materials that can simultaneously respect the defined optical conditions and be compatible with the standard photolithography processes while exhibition a high specificity to biofilm components.

Key to the success of this thesis will be the ability to put all the pieces together, including optical platform design, optimization of microfabrication techniques, integration of optical systems and detection methodologies as well as the development of suitable materials fulfilling both the optical and microfabrication requirements in order to achieve sensing performances exceeding those currently proposed in the state-of-the-art.

Chapter 2

Literature review

2.1 Biofilm

2.1.1 Definition

Biofilm refers to a layer of living and dead micro-organisms, surrounded by the mucus secretion, that are attached to an inert or living surface. Simple examples of biofilm include plaque found on teeth, the gel-like film found on the inside of a flower vase, or the slime found on river stones. The presence of biofilm threatens the quality of Water for Injection WFI or Purified Water [1].

2.1.2 Historical Bases of Biofilm

First direct observation of microbial biofilm can be accredited to Antoni van Leeuwenhoek. His discovery consisted of inspecting with a microscope the 'animalcule' that he found on the surface of his teeth [2, 3]. With the development of microscopic technologies in last century, many researchers were able to study biofilm in depth.

Heukelekian and Heller[4[4] reported bacterial growth and an increase in the activity of marine microorganisms when a surface favoured their attachment This phenomena is also called the "bottle effect". Zobell had reported similar outcomes. He observed the increased number of bacteria on surface of seawater [5]. These early observations were not able to examine in detail biofilms due to the lack of technology. A detailed examination of biofilms had to wait until the late nineteen sixties with the development of the electron microscope. Jones et al. [6] were one of the first researcher groups that used scanning and transmission electron microscopy to inspect biofilms on trickling filters in a wastewater treatment plant. They revealed the composition of these biofilms and confirmed that they are composed of a variety of organisms. By coupling a specific polysaccharide- stain called Ruthenium red with osmium tetroxide fixative, they showed also that the matrix material surrounding and enclosing cells in these biofilms was polysaccharide

The development of microscopic technologies has promoted the rise in biofilm related research. By the early nineteen seventies, it had been shown that microbial slimes in industrial water systems were not only very tenacious but also highly resistant to disinfectants such as chlorine [7].

In 1978, Costerton et al. studied dental plaque and sessile communities in mountain streams. From their observations, they presented a theory of biofilms that elucidated the mechanisms behind the adhesion of microorganisms to living and nonliving materials and the benefits that can be extracted from their presence [8].

2.1.3 Biofilm Development

Biofilm development occurs in the following steps:

2.1.4 Surface Conditioning

As soon as water contacts a solid surface, an organic layer deposits on the liquid/solid boundary. These organics form a 'conditioning layer' that neutralizes the surface charge, which may repel approaching bacteria. The absorbed organic molecules may also often serve as a nutrient source for bacteria [1].

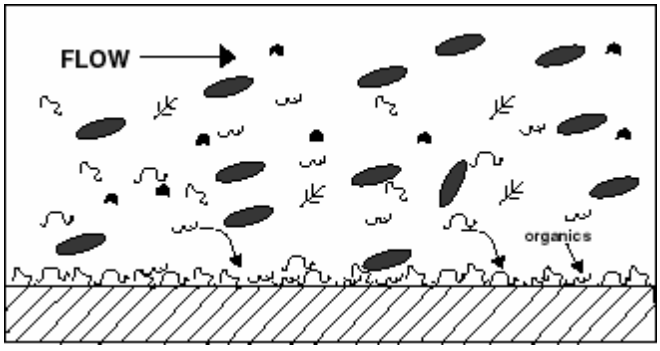

Figure 2-1: Adsorption of organic molecules on a clean surface forms a conditioning film [1].

2.1.5 Adhesion of 'Pioneer' Bacteria

In a pipe of flowing water, some of planktonic (free floating) bacteria approach the pipe wall and become entrained within the boundary layer. The boundary layer refers to the laminar quiescent zone adjacent to the pipe wall where the flow velocity falls to zero. Some of these cells will collide and adsorb to the surface for some time, and will then become unadsorbed, frequently referred to as reversible adsorption. Some

of the reversibly adsorbed cells may then permanently adhere to the surface, and are then referred to as irreversibly adsorbed cells (Figure 2-2) [1].

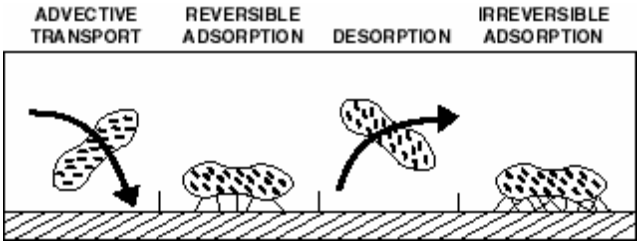

Figure 2-2: Transport of bacteria cells to the conditioned surface, adsorption, desorption, and irreversible adsorption.

2.1.6 Glycocalyx or Slime' Formation

Biofilm bacteria excrete a sticky substance, which hold the biofilm together and cement it to a surface. The biofilm also acts as an ion-exchange system that traps trace nutrients from the water. As nutrients accumulate, the pioneer cells reproduce. As shown in Figure 2-3, this process continues, which greatly increases the volume of the ion exchange surface and a thriving colony of bacteria is soon established.

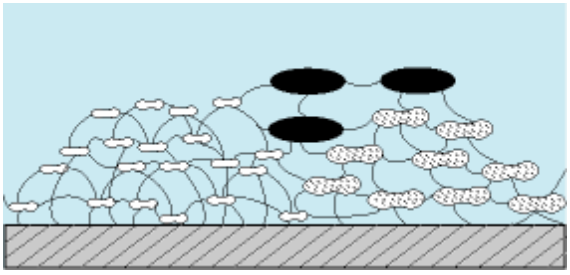

Figure 2-3: Biofilm is made up microbes and "spiders web" of extracellular polymers.

2.1.7 Problems Related to Biofilm

Microbial adhesion to surfaces and the subsequent biofilm formation has been a critical problem for many industrial sectors, including food, environmental, clinical and pharmaceutical. The attachment and growth of microorganism on wet surfaces is a natural behavior involving several complex physico-chemical processes, the most well-defined of which are surface preconditioning, cell deposition and adsorption as well as replication and growth, as thoroughly described in a recent review [9]. They can mature to highly complex cell agglomerates formed by bacteria and multi-

cellular eukaryotic organism to reach thicknesses of up to 300 microns within less than a month [10] . In natural ecosystems, they can enable or prevent the formation of micro- and macro-organisms [11]. In clinical environments and in the pharmaceutical industry the formation of biofilm is a crucial factor provoking chronic diseases and microbial infections in high purity water systems [12]. Biofilm detection is an area of interest for ecological/environmental [13] and health [14, 15] studies as well as for biomass control [16, 17]. A biofilm is a bacterial colony protected by its self-generated polymer matrix. Any contact between solid and liquid results in growth of the biofilm, and can change the surface properties such as the reduction of thermal conductivity. For example, a biofilm can reduce 20% of the ship speed or reduce thin pipe flow rate by 50% [18]. Biofilms can also decrease the efficiency of the heat exchangers by forming a layer between the two mediums increases the resistance of heat transfer [19] . A sensor that can monitor the early stage biofilm growth could help to avoid such problems.

2.2 Biosensors

2.2.1 Introduction

One might consider the ears, eyes and fingers to be physical sensors as they detect physical sensations of sound, light and heat respectively. What one detect with the nose – smells – are in fact small quantities of chemicals. The nose is extremely sensitive and selective instrument which is very difficult to emulate artificially. It can distinguish between many different chemical substances qualitatively and can give a general idea of "quantity" down to very low detection limits. The chemicals to be detected pass through the olfactory membrane to the olfactory bulbs, which contain biological receptors that sense the substrate. The response is an electrical signal which is transmitted to the brain via olfactory nerves. The brain then transduces this response into the sensation we know as smell. The tongue operates in a similar way [20].

Figure 2-4 shows a schematic diagram of the nasal olfactory system, illustrating the comparison with a generalized sensor. The nostrils collect the smell sample, which is sensed by the olfactory membrane, i.e. the sensing element. Afterwards, the responses of the olfactory receptors are converted by the olfactory nerve cell, which is equivalent to the transducer, into electrical signals which pass along the nerve

fiber to the brain acting as a microprocessor; turning the signal into a sensation which we call smell.

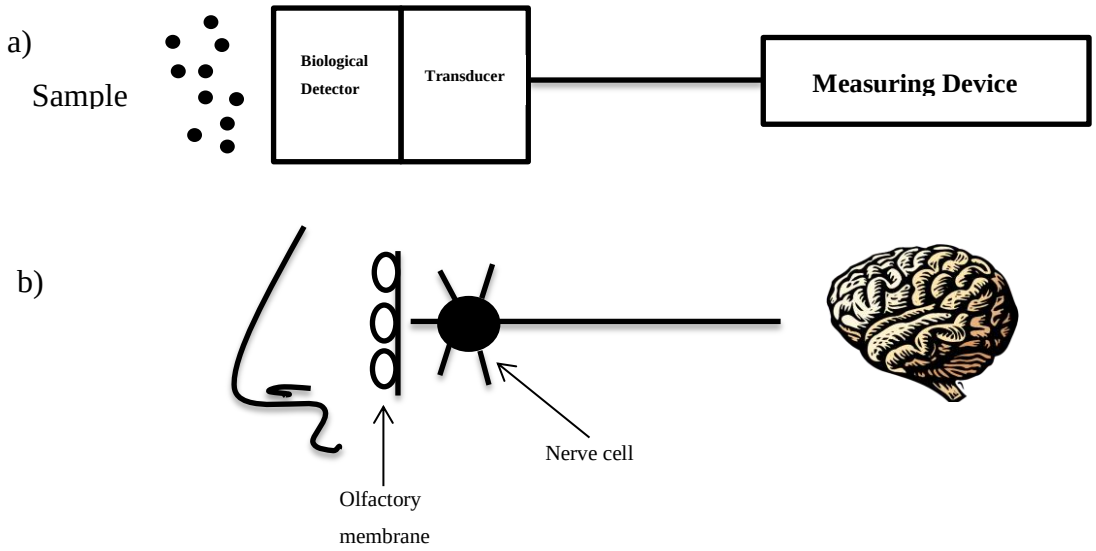

Figure 2-4: a) Schematic of a sensor, showing the component parts, i.e. analyte, recognition element, transducer, actuator and measuring device. b) Analogy with the nose as asensor (actually a biosensor) in which olfactory membrane is the biological recognition element, the nerve cell is the transducer, the nerve fibre is the actuator and the brain is the measuring element [20].

There are sometimes different meanings for the terms sensors, transducers, biosensors and actuators. So it is worth defined them as following:

- A sensor is a device that detects or measures a physical property and records, indicates or otherwise responds to it.
- A transducer is a device that converts an observed change (physical or chemical) into a measurable signal. In chemical sensors, the latter is usually an electric signal whose magnitude is proportional to the concentration of a specific chemical or a set of chemicals.
- An actuator (put in action) is the part of the device which produces the display.

The generalised principles of a biosensor are outlined in Figure 2-5.

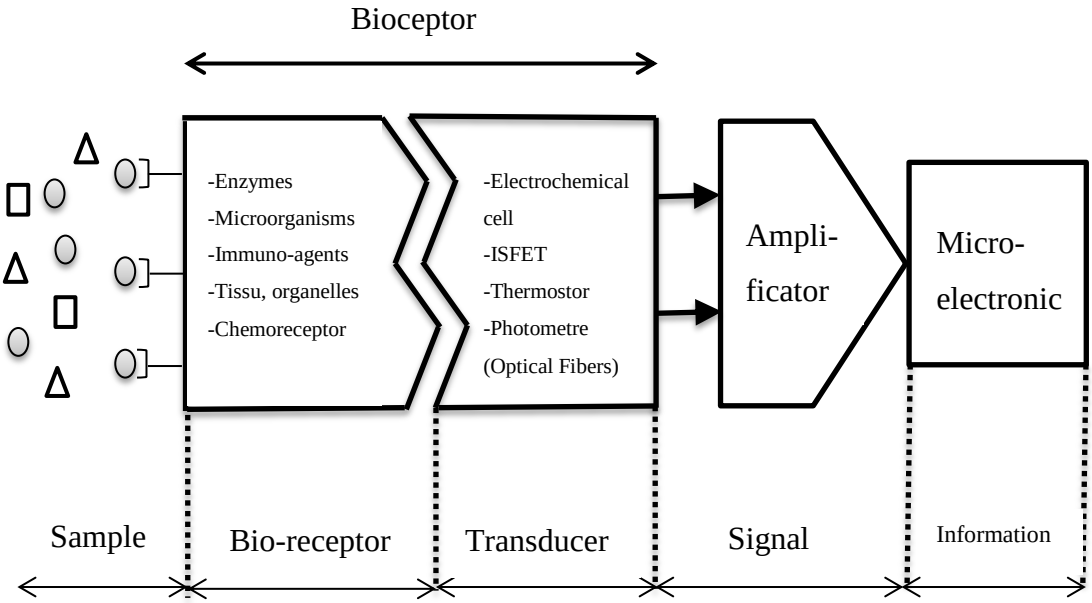

Figure 2-5: General principles for a biosensor. The specific chemical target (analyte) is recognized by the biological element, creating stimulus to the detecting transducer from which a reproducible signal is measured.

2.2.2 Electrochemical Sensors

Electrochemical sensors can be subdivided into various types, as follows.

(a) Potentiometric. These involve the measurement of the e.m.f. (potential) of a cell at zero current. The e.m.f. is proportional to the logarithm of the concentration of the substance being determined.

(b) Voltammetric. An increasing (or decreasing) potential is applied to the cell until oxidation (or reduction) of the substance to be analysed occurs. There is a sharp rise (or decrease) in the cell current to give a peak current. The height of this peak current is directly proportional to the concentration of the electro active material.

If the appropriate oxidation (or reduction) potential is known, one may step the potential directly to that value and observe the current. This mode is known as amperometric.

(c) Conductimetric. Solutions containing ions conduct electricity. The magnitude of this conductance may change due to a chemical or a biochemical reaction. The relationship between conductance and concentration depends on the nature of the reaction.

2.2.3 Thermal Sensors

The first law of thermodynamics tells us that any process in which the internal energy of the system changes is accompanied by absorption or by evolution of heat. Thermal sensors utilize kinetic selectivity; therefore, some form of catalysis is always involved. The important point to realize is that thermal sensors are in situ microcalorimeters, which means that batch calorimetry could provide important information for thermal chemical sensors. There are two properties of heat that are quite unique from any other physical parameter. First, heat is totally nonspecific. Second, it cannot be contained; that is, it spontaneously flows from the warmer (T1) part of the system to the colder (T2). From the sensing point of view, this defines the optimal design of a thermal sensor. The general strategy is to place the chemically selective layer on top of a thermal probe and measure the heat evolved in the specific chemical reaction; taking place in that layer, either as the change in temperature of the sensing element, or as the heat flux through the sensing element [21].

2.2.4 Optical Sensors

Direct Spectroscopic

Many direct sensors such as, gas sensors, measure the intrinsic optical absorption usually in the Infrared (IR), using several techniques including Fourier Transform InfraRed (FTIR) spectroscopy or correlation spectroscopy. A variety of optical configurations can be utilized, from free-space sensors to fibre-based configurations to optical waveguide sensors. A brief discussion on UV absorption and development in IR sensing is offered below, as well as recent developments in Surface-Enhanced Raman Spectroscopy (SERS) based sensing.

Absorption-Based sensors:

IR Absorption:

This technique has been widely used for detection of gases, such as, CO_2, CO, NO_2, NH_3 and CH_4. IR spectroscopy in its simplest form confines a sample of the gas in an optical absorption cell at specific IR wavelengths and measuring the absorption.

These wavelengths are characteristic of the vibrational mode of the molecules. The system usually consists of an IR source, a detector which is sensitive at the wavelength of interest and optical filters to choose specific absorption wavelength that the detector is sensitive too. In many molecules of interest, the fundamental vibrational transitions occur in the near or mid-IR, spanning wavelengths from 1 to >10 μm.

Conventional IR sensing used IR sources. Recent developments in laser diode technology and the recent availability of Quantum-Cascade Laser (QCL) sources, have led to advancement of deeply sensitive and selective systems. This included Fourier Transform InfraRed (FTIR) which is a very impressive interpretive tool. Also Nondispersive InfraRed (NDIR) sensors are extensively used for gas analysis, and many commercial gas analyzers are based on this principle [22-25].

FTIR-Based analysers

FTIR-based sensing can be considered as an alternative to NDIR-based sensors for many applications. The recent advanced FTIR sensors are compact and have precise quantification of many analytes compared to the complex unit offered in the past.

An FTIR spectrometer usually consists of a Michelson interferometer, that can generate an interferogram from the IR emission of the sample and then perform a Fourier transform to obtain the spectrum. The FTIR technique has capability to measure multiple analytes together, which differentiates it from NDIR sensors. Reyes et al. has measured the emission of a hybrid car including CO, NO, SO_2 and NH_3 under different driving conditions using FTIR. FTIR imaging has been used for high-throughput analysis of processes such as epoxy curing [26]

NDIR sensors

NDIR sensors have been used in ocean sensing to monitor CO_2 concentrations in order to audit the effects of increased atmospheric CO_2 on the global carbon cycle.

Kalten et al. [24] demonstrated this method to measure the extracted CO_2, and the system continually compares the signal to a certified reference material, which

constitutes the baseline signal. This system was found to be three times faster than the colorimetric method. Bandstra et al. [25] tried to produce the speed of measurement desired to enable high speed continuous analysis, used a gas permeable hydrophobic membrane contractor, which continuously strips the CO_2 out from the flowing stream of the seawater. NDIR analyser have been used to quantify the CO_2 concentration continuously, with the use of a lead selenide detector and broadband blackbody source

Laser Diode Sensing Systems

Werle [27] and Allen [28] composed a comprehensive review of diode laser-based gas sensor systems for applications such as automated control of industrial processes, environmental monitoring, and combustion process monitoring. Near and mid-IR spectral regions laser with wavelength from 1>2 μm has been used for gas analysis for conventional diode laser from 2 to >4 μm for recently developed QCL lasers.

Wavelength modulation has been used in the design of Fiber-coupled multiwavelength diode laser sensor systems to monitor gas emission in industrial processed [29]. In order to achieve parts per billion detection levels of atmospheric gases such as methane, tuneable diode laser absorbtion spectroscopy TDLAS systems have been used on IV-VI semiconductors. Quantum-Cascade Laser QCL lasers are semiconductor laser based on transitions in a multi quantum well hetrostructures. QCLs at near room temperature at wavelengths in the MIR starting at 3 μm to produce milliwatts of radiation and have the ability of tailoring the emission wavelength within a broad range of frequencies [30, 31]. The most widely used technique that have been developed with QCLs are based on InGaAs-InAlAs and GaAs-AlGaAs hetrostructure [32]. They are commonly fabricated as single mode lasers and usually in distributed feedback DFB configuration. QC-DFB lasers for gas sensing produce highly monochromatic radiation that is suitable for high resolution spectroscopy [33]. Sharpe et al. [34] was first to examine gas sensing using a CW QC-DFB laser by presenting the absorption data for NO and NH_3 at low

temperature. Schaden et al. were the first to use QCL-base for detection of CO_2 in aqueous solution [35].

A QCL has also been used by Kosterev [36] as a gas sensor for determining the trace gases such as CH_4 and N_2O in air detected down to ppb levels. Also QC-DFB laser systems were used to measure ppl levels of NO in vehicle emissions [37]. High-precision measurement of N_2O and CH_4 were reported by Nelson et al. [38]

Direct Fluorescence sensing

Biomedical sensors typically apply direct fluorescence as the main sensing method. For example, autofluorescence spectroscopy is a useful tool for the non-invasive detection of precancerous development of the epithelium. This is where most human cancers originate and develop basically from two intrinsic fluorophores; nicotinamide adenine dinucleotide (NADH) and flavin adenine dinucleotide (FAD). These were used in the monitoring of cell activity. Time-resolved confocal fluorescence spectroscopy systems were used to study cell metabolism and as a result, were able to deduce the difference between cancerous and normal cells by analysing the dual-exponential decay of NADH. [39]

Furthermore, as fluorescence is dependent on chemical composition, it can be used in the characterisation of different oils such as, crude petroleum oils. These can be analysed through synchronizing fluorescence, wherein both the excitation and emission monochromators are scanned simultaneously, and their lifetime measurements carried out [40, 41]. This also implies that synchronous fluorescence has also been used to discriminately quantify between virgin olive oil and sunflower oil [42]. The classification of a range of edible oils has been combined with artificial neural networks spectroscopy [43].

Confocal microscope and multiple excitation wavelengths have been used in the study of different layers of the epithelium through depth-resolved fluorescence spectroscopy [44]. Through excitation between 355 and 405 nm, the fluorescence from different sub layers were able to be isolated. From this analysis, the presence of precancerous cells were able to be justified through determining the ratio of NADH and FAD and the associated patterns in the auto-fluorescence following changes in the cervical tissues [45, 46]. Fluorescence can be used to study protein folding and

unfolding and hence it is very sensitive to the environment. As a result of the conformational changes of protein, wherein the peak emission wavelength, is shifted from 308 to 350 nm [47][48].

Raman and SERS Sensing

The occurrence of Raman effects results when a photon interacts with the vibrational energy levels of a molecule and scatter [49]. This therefore requires laser excitation which relies on good optical filtering in the separation of the scattered photon from the intense incident beam due to the Raman spectroscopy normality. This is comparable with the IR-based absorption spectroscopy as it probes the vibrational energy levels of molecules and as a result can be used as a highly selective technique which will distinguish between similar molecules [49]. On a highly preferential scale, Raman spectroscopy is advantageous to the IR absorption in that there is no interference from the vibrational spectrum of water sensing liquid. This therefore makes it a better choice as a technique for life science applications, including biomedical diagnostics such as the study of living cells.

On the other hand, Raman scattering cross-sections are very small, many orders of magnitude smaller than fluorescence cross-sections. It is still useful as a technique in gaseous and liquid analytes sensing but the down side are the low scattering sections. These can be overcome to a large extent using the SERS technique. Owen et al. [50] analyzed imaging through Raman by using diffraction-limited spot-size lasers to map chemical distribution in a cell. Uzunbajakava et al. [51] used lasers with high lateral resolution to map the DNA and RNA distribution in GeLa cells. Shafer-Peltier and Puppels [52, 53] used Raman spectra to distinguish between different cancer cells. Optical fibre probes were also used to image breast tissue [54] and the difference in tissue showcased were acknowledged and identified from differences in the Raman spectra. Accuracies to the level of 88.6% and 71.4% for sulphur mustard and ricin as toxins were identified respectively in cells through using Raman spectroscopy [55].

In the consideration of Surface-Enhanced Raman Spectroscopy (SERS), its use in obtaining quantitative in-vivo glucose measurements has been reported [56]. Suitable SERS surface were acheived through the use of a silver-coated self-assembled monolayer (SAM) of polystyrene nanospheres. As developments in material

fabrication continues, SERS is being increasingly used in diverse fields such as biomedicine and environmental analysis. A near-field scanning optical microscopy and SERS combined has been used in detecting dye-labelled DNA with 100 nm resolution [57] and SERS have also been used in detecting specific dyes such as Anthraquinone [58] and alizarin dyes [59]. Based on these references, the advantage of SERS over conventional Raman has been showcased. Due to the strong fluorescence of the dye being used this completely masked the Raman signal. The fluorescence was quenched due to the presence of a metal substrate, enabling detection of the enhanced Raman signals in the SERS measurement.

From an analytical point of view, there have been two principal conditions for SERS to be used. The presence of a suitable SERS-active nanostructured metal surface and the requirement that the sample under investigation be immobilized on or in close proximity to the surface. Routine application of the technique has been successful. However a poor understanding of the theoretical background and SERS substrate materials reproducibility has held back progress.

Regent-Mediated Sensors

Reagent-mediated sensing in principle is considered an optical oxygen sensing, whereby the luminescence intensity or decay time of an oxygen-sensitive luminescent complex, for example, a ruthenium polypyridyl or a porphyrin complex, is quenched in the presence of oxygen. This in theory allows oxygen partial pressure to be measured as a function of the intensity or luminescence decay time of the complex. From current use, reagent based optical sensing has been based mainly on solid-phase immobilization matrices. Here the reagent dye can be adsorbed, covalently or ionically attached, or simply encapsulated in a solid matrix that is permeable to the analyte. If the immobilization matrix has the capability of being coated on a substrate in liquid form, a wide range of sensor configurations are then enabled including, planar waveguide and array-based sensors. Using a reagent as mediated sensor is necessary when an analyte does not exhibit a convenient spectroscopic optical response. Sensing can then be achieved through monitoring the optical response of an intermediate species or reagent wherein the presence of the analyte has its response modulated in some way [60].

Reagents

Reagents for Colorimetric Sensing

Colorimetric CO_2 sensing is normally achieved by measuring the pH change of an indicator in response to carbonic acid generated by the acidic CO_2 gas. As with many others of the same reagent that are uses for pH sensing for adsorption-based CO_2 sensing; bromothymol blue in an ionic liquid matrix has been used for both gas-phase and dissolved CO_2 sensing [61]. Cresol red has been used in an optical fiber configuration in order to measure in vivo gastric CO_2 [62]. Thymol blue immobilized in a sol-gel matrix has also been used for gaseous CO_2 sensing [63]. Selective colorimetric optical probes based on pyrylium dyes have been developed not too long ago in the detection of aliphatic amines [64] while novel, highly selective probes for formaldehyde detection developed by Suzuki et al., [65] shows similar ideas and a formaldehyde sensor, based on the reagent 4-amino dydrazine-5-mercapto-1,2,4-triazole, was also reported recently [66].

Fluoride ion complexes with an aluminium octaethylporphyrin ionophore dye with fluoride-selective sensor based has been shown and reported by [67], while Teshima et al. [68] showcased the detection of a coloured product which is formed when acetone reacts with alkaline salicylaldehyde - a breath sensor for acetone measurement.

Indirect colorimetric pH sensing uses organic pH indicators. These measure the absorbance which is modified by the pH of the environment. Lobnik [69] highlighted that the pKa of these indicators shows the centre of the measurable pH range such as, cresol red, bromophenol blue, and bromocresol purple which shows response to acidic pH ($pH < 7$), while cresol red, naphtholbenzene, and phenolphthalein shows the response to basic pH ($pH > 7$). In a similar view, Lin et al. [70] asserts such narrow pH response range of most of the above dyes has been addressed and are considered relative, a case whereby several indicators with different pKa values have been combined in one sensor in order to produce a linear pH response over a wide range. Makedonski et al. [71] synthesized new reactive azo dyes for use in pH sensing; a situation wherein sensor stability is increased through dyes being covalently bound to a polymer matrix.

Reagents for Luminescence Sensing

Many cations and anions as well as other analytes such as pH, CO_2, ammonia and O2 can be measured using luminescent probes and change in luminescence of a pH indicator allows the measurement of pH, CO_2, and ammonia. The principle of luminescence is regarded as absorption-based sensors. This is intrinsically more sensitive than absorption as a sensing technique, and for many applications, it therefore offers higher sensitivity than absorption based luminescence sensors. The literature is dominated by two pH-dependent luminescent probes; fluorescein and 8-hydroxypyrene-1, 3, 6-trisulfonic acid (HPTS).

Self-referencing techniques otherwise known as ratiometric sensing a situation wherein either an analyte-insensitive excitation or a luminescence band of the dye is alighned with the analyte-dependent band. Using methacryloyl-modified HPTS resulted in the achievement of Excitation ratiometric sensing which facilitates covalent bonding to a polymer matrix with a sensing range of pH 6-9 [72]. Through Ratiometric pH sensing has also demonstrated mercurochrome, another fluorescein-related dye, in a sol-gel matrix [73] and newly synthesized boron-dipyrromethene derivative has been used in a single-excitation dual-emission ratiometric scheme in the measurement of pH in human gastric juices [170]. This is considered a newly synthesized boron dipyrromethene derivative. Based on further investigation as analysed by Le, Thao P and áPrasanna de Silva [74, 75], Naphthalimides have also been seen as luminescent probes, in the same way as pH sensor using covalently immobilized piperazinyl-1,8-napthalimide has been published recently [76]. Metal complexes with luminescent transition also have larger Stokes shifts and longer lifetimes than, for example, fluorescein or HPTS. This allows flexibility to a greater extent in terms of excitation/detection optoelectronics as well as enabling lifetime-based sensing schemes. pH sensing has been demonstrated recently using a range of ruthenium and rhenium complexes based on the pH-sensitive ligand 5-carboxyl-1,10-phenanthroline [77].

Optical fiber imaging sensors using Fluorescein have also been used recently on drop-on-demand inkjet printing [78]. Hence fluorescein-related dyes have been used so as to have covalent immobilization facilitated in the elimination of dye leaching through the sensor matrix. For example, pH sensing has been realized using a fluoresceinamine isomer II complex which was bounded covalently to a sol-gel matrix [79].

Optical oxygen sensing has also been explored through luminophores. These use mainly organometallic complexes of ruthenium, in particular ruthenium polypyridyl complexes, and also metalloporphyrin complexes. Ruthenium polypyridyl complexes are characterised by high quantum efficiency and convenient absorption and emission maxima located in the visible spectrum with a large Stokes shift and long lifetime (~1 μs). As these complexes are quenched efficiently in oxygen this gives rise to a decrease in luminescence intensity as well as its lifetime. The complex Ru(dpp)3 above in terms of the context of pH sensing shows one of the longest unquenched lifetimes (~5 μs) and this has been widely reported for oxygen-sensing applications, both in polymer and sol-gel matrices [80-82] Porphyrin complexes are thought to have a longer lifetimes (~100 μs), and are generally considered to have inferior photo stability properties as against the ruthenium complexes. The most common and widely used complexes for oxygen-sensing applications are platinum and palladium octaethylporphyrin (PtOEP and PdOEP) [83, 84]. Other recognisable complexes are platinum and palladiumtetrakis (pentafluorophenyl) porphyrin (PtTFPP and PdTFPP) as analysed by O'Riordan [85]. However, fluorinated porphyrins have been shown to be highly stable against photo-oxidation and photoreduction [86].

In a similar way, Aminofluorescein has also been recognised for use in optical ammonia sensing. This is where an enhancement has been achieved compared to fluorescein-based sensing as a result of the reaction of the ammonia with the amine group on the fluorescent dye [77]. While being exposed to ammonia this lead to increase in the deprotonated band of the pH indicator thereby giving rise to energy transfer wherein the luminescence and lifetime of the Ru-(dpp)3 complex reduce.

Glenn, Bedoya and McGaughey [87-89] on the other hand highlighted Ruthenium complexes as having been used for luminescence-based relative humidity sensing as a result of the quenching of a phenazine ligand by protons. There are many literature reports based on the use of luminescent probes to measure anionic and cationic species as well as organic chemicals previously dealt with, to further ascertain the above.

Immobilization Matrices

Immobilization matrices in the form of sol-gel and polymer materials will be discussed here and as with most reagent-based optical sensors, the reagent is immobilized in a solid matrix usually in the form of a monolith or a thin film. Since the immobilization matrix frequently influences the sensor response, the matrix therefore serves to encapsulate the reagent in such a way that it is accessible to the analyte while being impervious to leaching effects.

Sol-Gel Matrices

Sol-gel process provides a relatively benign support matrix for analyte-sensitive reagents and dyes immobilization .It involves the hydrolysis and polycondensation of the appropriate metal alkoxide solution to produce a porous glass matrix. In this matrix, the reagent is encapsulated in a nanometer-scale cage-like structure through which the analyte molecules can diffuse. The process versatility facilitates the tailoring of the material physicochemical properties so as to optimize sensor performance. A typical example is when the sol-gel process parameters such as sol pH, precursor type and concentration, water content, and curing temperature could be adjusted to produce materials of desired porosity and polarity [90]. McDonagh [82] showcased this tailoring to demonstrates oxygen-sensitive films being doped with the Ru(dpp)3 complex and fabricated through using different ratios of tetraethoxyorthosilane (TEOS) and methyltriethoxysilane (MTEOS) precursors. Further to this, Tao et al. [91] demonstrated the effect of the alkyl (R) chain length on the oxygen sensitivity being measured of the Monoalkoxysilanes of the form (CnH2n+1)-Si-(OR)3, where n ranges from 1 to 12, have been investigated and exhibit a linear oxygen response which increases up to C8 and then begins to decrease. The decrease in response at longer alkyl chain lengths was correlated with a decrease in oxygen diffusion coefficient in the matrix for these films. Very high oxygen sensitivities have been achieved using fluorinated sol-gel precursors. For example, oxygen sensitivities have been achieved using precursors such as 3,3,3-trifluoropropyl-trimethoxysilane (TFP-TMOS), which are ~10 times higher than that achieved for MTEOS based sensors [92, 93]. These materials exhibited very high stability, with stabilities of up to 2 years being achieved for some formulations. Also

highlighted was the high sensitivity attributable to the highly hydrophobic and nonpolar nature of the fluoro films.

Highly stable and sensitive oxygen was obtained in response, and the films then became sterilizable from the conducted analysis [94]. As an alternative to physical entrapment, the analyte sensitive dye can also be covalently bound to the sol-gel matrix. This increased stability and eliminate dye-leaching effects in aqueous environments. Considering the structure of sol-gel, the standard materials have a non-ordered, amorphous structure where diffusion of analytes could be limited by the random micro porosity of the structure and Mesostructured porous films.

On the other hand, having a large open porosity, this could offer enhanced diffusion and accessibility for analytes. Meso-porous sol-gel sensor films have been realized via an evaporation-induced self-assembly (EISA) approach [95, 96]. These films are highly structured in terms of meso-porosity and have excellent optical quality and the films are surfactant cetyltrimethylammonium bromide (CTAB) based.

The sensor exhibited no leaching and was used for dissolved oxygen measurement. Sol-gel matrices have also been used for other analytes such as in pH and CO_2 sensing. Previous studies show that pH sensing has a hydrophilic matrix which allows ingress of protons, whereas in CO_2 sensing a more complex matrix is required which retains the water required for conversion of the gas to carbonic acid in the films but has sufficient hydrophobicity to be pH insensitive. It is indicated that the stability, homogeneity, and sensitivity of the matrix was superior to a nonmesoporous matrix where the dye was just physically entrapped. A novel sol-gel-based sensor application has also been reported whereby an optical fibre core is fabricated from reagent-doped porous sol-gel. Hence, the core acts as an active fibre core optical sensor (AFCOS). Through the fabrication and optical properties of the fibre being investigated, a humidity sensor was constructed as proof of principle [97].

Sensor Platforms

In relation to the operating principle, optical sensors may be categorised under the heading of direct sensors where the analyte is directly detected via some intrinsic optical properties. These including absorption and luminescence. Reagent-mediated sensors which depend upon the change in the optical response of an intermediate

agent, usually an analyte-sensitive dye molecule, are used to monitor analyte concentration. This technique is useful where the analyte has no convenient optical property, which is the case of many analytes

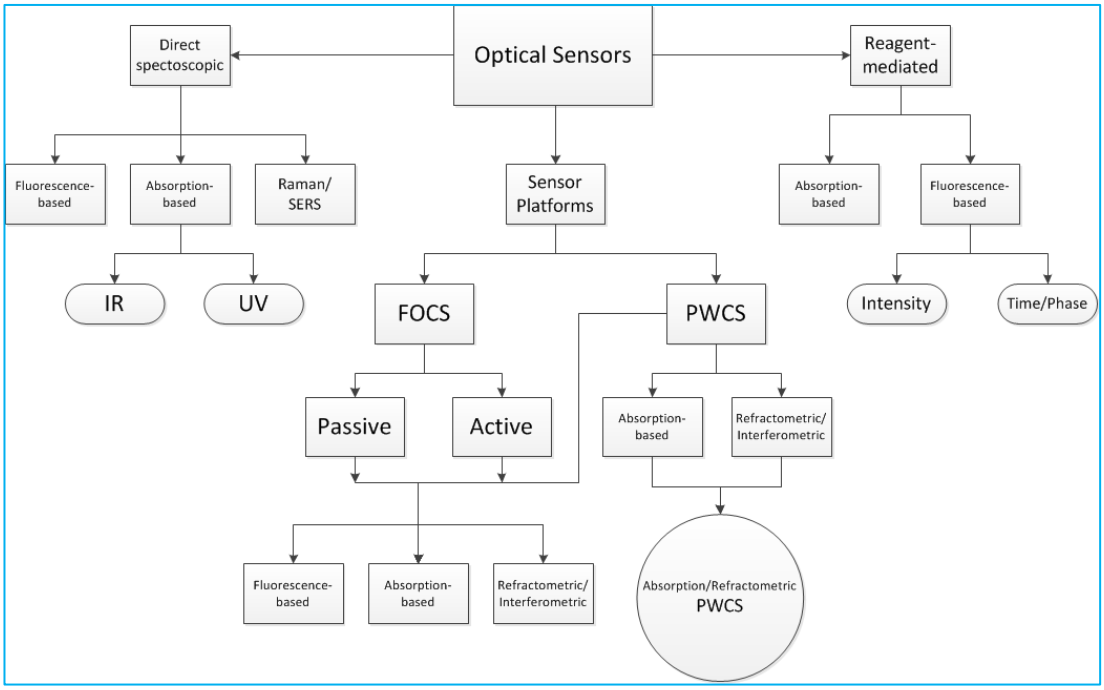

Figure 2-6: The structure of the operating principle of optical sensors

Figure 2-6 shows the structure of the operating principle of optical sensors. The sensing platforms are grouped according to the underlying waveguide properties.

Fiber Optic Chemical Sensors

The Fiber Optic Chemical Sensors (FOCS) can be divided into two configuration and sensing schemes, passive and active sensor, depending upon to their sensing strategies. The fiber role is considered to be passive if the sensor response is not linked in any way to an intrinsic change in the optical properties of the fiber. If the optical properties of the fiber are in some way modulated by the presence of the analyte, it is considered as an active sensor [98] .

Passive FOCS

The fiber-coupled spectrometer is the most prevalent example of passive FOCS. The sensing strategy of a passive FOCS is to take the form of a separate sensor element that is interrogated in some other fashion by the fiber optic assembly. Many

configurations are commonly used to achieve this. In colorimetric or absorption-based FOCS is common to use the reflection-based configurations instead of delivering the light to the analyte-sensitive component through the central fiber in the bundle fiber and the reflected light is collected by the outer fiber around the central fiber. In this case the bundle fiber delivers the light to this material and collects the reflected light. Also reflection-based configurations were used with development of amine-vapour based sensors. Bifurcated fiber bundle were used for the detection sulfer dioxide reflection–based configuration is not limited to the detection of analytes by only colorimetric means. They can be applied to the detection of fluorescence, which is used to detect dissolved oxygen [99]. This configuration is extensively used for the detection of a different analytes including oxygen, iodine, dinitrophenol, PH, and chloride [100-103].

In recent years, transmission-based configurations could be considered as commonly employed configurations in the development of FOCS. (For example a subnanometer spectroscopic gas sensor, using IR for detecting acetylene). Also the development of dual-wavelength measurement can be used for refractive index and turbidity compensation in liquid flow systems, red and blue, red is used as a reference.

Active FOCS

Active FOCS are categorized into three headings according to the transduction mechanism applied; 1) Fluorescence based, 2) Absorption based (colorimetric and spectroscopic) and 3) Referactometric.

Fluorescence-Based Active FOCS

It is important to add fluorescent indicator molecules to the fiber platform to impart analyte-sensitive fluorescence to the fiber in some manners, in order to transform a standard optical fiber into a fluorescence-based optical chemical sensor. This can be performed by replacing the cladding of the fiber over a portion of its length with a solid matrix that contains the fluorescent compound. Ahmed et al. [104] described a system based on two, “positive” fibers attached to either end of a “negative” fiber. This system was declad for a portion of its length and coated with a solution of rehodamine 6G in glycerol. This system consisted of a single fiber.

The detection of inner- intracellular dissolved oxygen DO that uses “pulled tip” fibers has been described by Park et al. [105] These are multimode fibers, and the

Tip coated with a liquid PVC matrix incorporating two luminescent dyes, one for sensing the oxygen and the other is a reference.

Preejith et al. [106] declad the fiber over the length of 5cm and the tip was coated with a sol-gel in which the fluorescent complex NanoOrange was encapsulated to detection the human serum albumin by the evanescent wave excitation of fluorescence.

Absorption based (colorimetric and spectroscopic)

Absorption-based optical sensors means either colorimetric or spectroscopic, Spectroscopic absorption-based depends upon the detection of the analyte by probing its intrinsic molecular absorption. Colorimetric absorption-based relies on the detection of an analyte-induced colour change in the sensor material. Some examples and development of sensors for ammonia, pH and ethanol, can also be found in literature.

A doped-dye can be used for the fiber cladding of the sensor in some cases to increase the evanescent field in order to increase the interaction with the analyte-sensitive reagent thereby enhancing the device sensitivity. A U-bend configuration was used for spectroscopic monitoring of ethanol [107-109]. James and Tatam described the development of a Langmuir-Blodgett (LB) film-based sensor for pH. This platform can monitor pH-induced changes in the absorption of the LB film at 725 nm [109].

Referactometric

In the past decade, a number of refractometric FOCSs have been developed that involves addition of refractive index-sensitive optical structures to the optical fiber. Fiber Bragg gratings FBG's one of the refractometric FOCS has been developed. FBG's are written into germanosilicate fiber using a suitable laser source.

Sang et al. [110] developed the twin FBG-based mode used by the second grating in order to provide temperature compensation for the sensor. This platform detects different concentrations of sugar and propylene glycol solutions. In the same manner of FBG's structure, the long period fiber gratings LPFG are fabricated for detection of sodium chloride, ethylene, ethylene glycol [111] and antibodies [112]. Pisco et al. reported a distal tip-based sensor for dissolved ammonia. The platform consisted of a

thin film of a thin dioxide (SuO_2) deposited into the distal tip of a fiber using electrostatic spray pyrolysis (ESP) which is an example of a Fabry-Perot interferometric (FPI) FOCS. Liu et al. employed a zeolite thin-film-based FPI sensor for detection of organic solvents in water [113]. Where the optic configuration employed was similar to the ammonia sensor as SnO_2 replaced by ziolite. Another example was developed by Benounis et al. [114] for detection of Methane. This sensor exploited a cryptphane-doped section of fiber cladding coupled with evanescent wave interrogation. The cryptphane absorbing the Methane causes a change in the cladding refractive index. Jung et al. [115] developed a refractive index sensor based on threesegment optical fiber platform that contains a coreless silica fiber (CSF) sandwiched between two multimode fibers.

Planar waveguide-based sensor platforms

Planar waveguide chemical sensors PWCS are relatively recent compared with FCOS. According to the principal transduction mechanism employed, the PWCS are categorized to three principals, fluorescence, absorption, and refractometry.

The PWCS comprised a planar substrate (glass, plastic, or silicon) that forms the basis of the sensor chip. In some cases the substrate acts as the waveguide. While in the others an additional waveguide layer is deposited. In many cases, the light that propagates within the waveguide facilitates the operation of its evanescent field with the sensing environment above the waveguide. This is not always the case, where some sensors employ field-based techniques.

Fluorescence-Based PWCS

Various authors and researchers have dealt with the issues being developed through PWCS detection of fluorescence [82, 116-122]. Through these developments, the systems have employed evanescent wave excitation of fluorescence as technique which in other word is turned as total internal reflection fluorescence.

Chronis and Lee viewed this development of a total internal reflection-based biochip platform which excites the fluorescence from within a microfluidic network using a reflection singly. Contradicting this view are that described by Rowe-Taitt et al.

[121] and Duveneck et al. [122] which are in multiple reflection of wave guiding base with evanescent wave excitation systems. These are considered well suited in the development of array-type of optical sensor chips. This evanescent field of the guided light are known to extends into the sensing environment and have a distant of 1000-200 nm from the waveguide surface induced through the fluorescence in susception of molecules within.

Absorption-Based PWCS

As evanescent-wave absorption is one of the most prevalent examples of absorption based PWCS platforms, its configuration is similar to evanescent-wave excitation-based fluorescence sensors. As the absorption coefficient of the sensing environment results in the sensing functionality, this therefore causes more or less absorption of the evanescent field intensity which is reflected as a change in the detected output intensity of the sensor.

The detection of the analytes such as gaseous ammonia, pH, iodine and water vapour have been employed in PWCS utilization of thin-film based sensing layers. These are therefore doped with colorimetric, analyte-sensitive indicators and are deposited onto the upper surface of the waveguide, and any analyte-induced colour that changes are probed by the evanescent field of a suitable light source (i.e., one that is spectrally matched to the indicator used) [123-127].

Most recently, several platforms developed proves that a shift away from what might be seen as conventional evanescent wave absorption-based platforms. These therefore incorporate design features considered to improve the interaction of the interrogating light with the sensing environment. This improves platform sensitivity. Puyol et al. [128] developed an integrated waveguide absorbance optode (IWAO) incorporates a PVC-based sensor membrane that is located between two antiresonant reflecting optical waveguides (ARROWs) as shown in Figure 2-7.

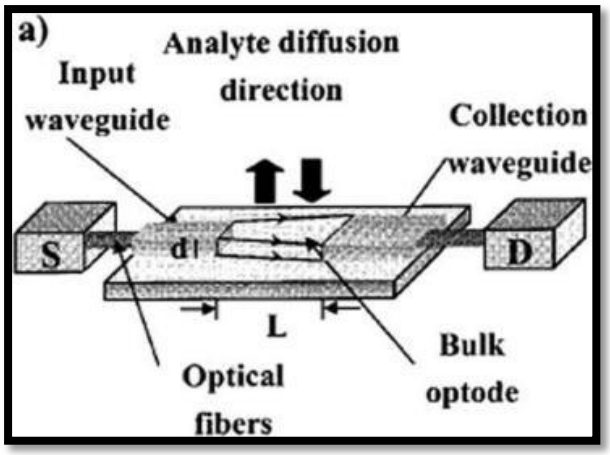

Figure 2-7: Integrated waveguide absorbance optode (IWAO) configuration developed by Puyol et al.[128]

The optical path increases in length in the sensing layer. Therefore, this provides enhancement in sensitivity, and assests the device in the detection of potassium chloride solutions of varying strength through its application, hence the sensor membrane therefore serves as a waveguide, and transports the interrogating radiation from the input ARROW to the output waveguide. As part of further analysis, Hisamoto et al [129] reported development of ion-selective optodes that employ a similar strategy in that the sensing layer acting as a waveguide [130].

Refractometric PWCS

Apart from PWCS designed for the measurement refractive index whose changes represent an extensively developed types of planar waveguide platforms, it also exploit techniques such as interferometry, surface plasmon resonance, and light-coupling strategies to transduce refractive index changes as part of the literature and previously published by Lambeck and Gauglitz [131, 132]. Sensor based on surface plasmon resonance (SPR) are considered the most widely known of refractometric optical sensor platforms and another form is the MZI (Mach-Zehnder Interferometer) as shown in the Figure 2-8.

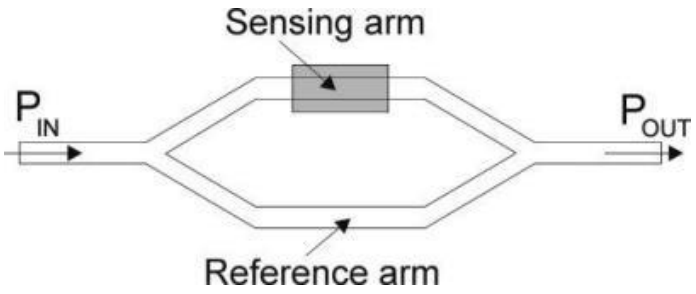

Figure 2-8: Schematic of a Mach-Zehnder interferometer.

This consists of a single-input waveguide whose transported optical power is equally split between two parallel waveguide branches using a Y-splitter and a second Y-splitter recombines the optical signals from both branches into a single-output waveguide which at the end, the output power is measured through using a suitable photodetector. Also, through the recombination of the two optical signals; sensor and interference, the measured output power changes, depending on the phase shift between them. This is a result of the changes in the refractive index of the sensing layer/environment which in essence influences the effective refractive index, Neff, in the sensing channel. These have recently been reviewed by Lambeck [133]; in a comprehensive paper reviewing the treatment of MZI interferometric platforms. Based on these principles, Lambeck highlighted discussion of a range of strategies which are intended to enhance the sensitivity and general sensor performance. He further discusses optimizing parameters such as operating wavelength, interaction length as well as waveguide composition.

Other PWCS which considered interferometry are the Young interferometer [134-136], Michelson interferometer [137] as well the difference interferometer otherwise known as polarimeter [138, 139]. Also important are the Young-type interferometer commercialized by Farfield Sensors [www.farfield-scientific.com] and the Zeeman interferometer, [140]. This is a variant of the difference interferometer with refractive index resolving capability of order changes of 10-8. Further to this, is the development of a multimode interference (MMI) coupler with tunable sensitivity described by Kribich et al [141] and this is used in detecting changes in relative humidity and therefore consist of a platform with single-mode input and output waveguides which are centrally coupled.

2.3 Optical Waveguiding

2.3.1 Introduction

In the 1840s, Daniel Colladon and Jacques Babinet were first demonstrated optical waveguiding in Paris [142]. This phenomenon was experimented by an Irish physicist named John Tyndall in 1870. He exposed a light on a container filled with water, with a hole at the bottom, in a darkened room. The light shone the curved path of water as shown in Figure 2-9. The difference between the refractive index of the water and the refractive index of the air provides the capability of guiding the light around bends of the water stream [143]. This demonstration exploited the internal reflection of the light at the boundary of core and cladding. The core (water) is the high refractive index medium and the cladding (air) is the lower one (As illustrated by the ray diagram in Figure 2-10).

Alexander Graham Bell in 1880 demonstrated the photophone, an optical telephone modulating the intensity of reflected sunlight with voice signals [144].

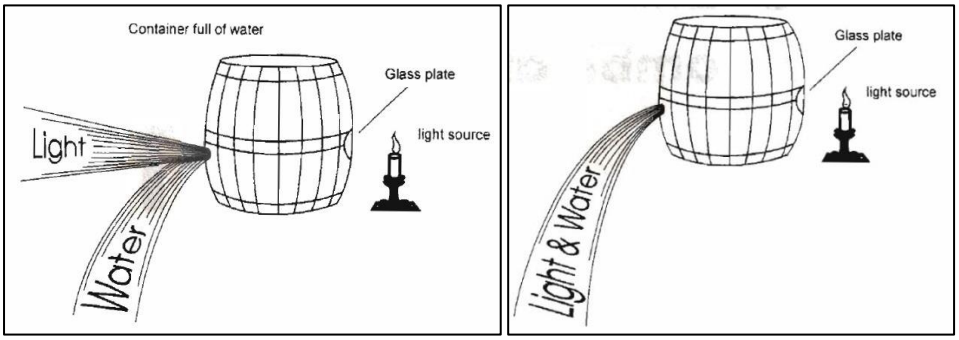

Figure 2-9: (a) What was expected to happen to the light. (b) What actually happened to the light [143].

In the mid-1950's, the first serious application of optical fibers appeared when the first fiberscope was invented by Kapany [145]. The fiberscope was used in remote imaging applications for weld inspection in harsh environments such as aircraft fuel tanks and in the first endoscopic examinations.

The first time the ability of the light to carry information was seriously considered was in the early 1960s, when the semiconductor was invented [146].

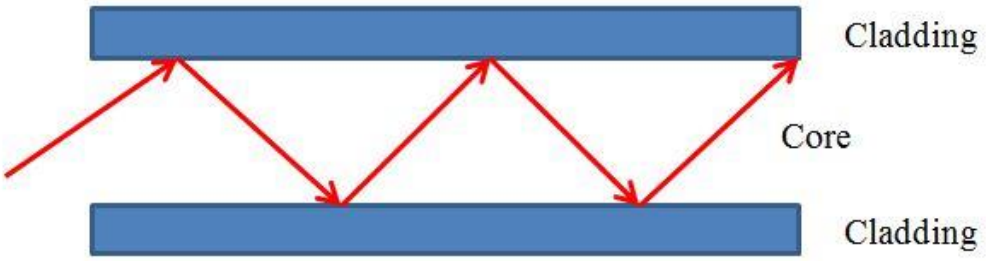

Figure 2-10: Light guiding in an optical fiber by total internal reflection.

While light sources and receivers are important to the task of light communication, far more critical to the successful fabrication of a practical light guide system was the parameter of attenuation in the transmission medium. Dispersion is another important parameter, but this was not as critically important as attenuation, and loomed in significance only after attenuation improvement made fiber light-guide systems of nontrivial lengths possible [147]. Figure 2-11 shows the history of attenuation improvement in glass, beginning with the Egyptian types which were relatively poor, through the Venetian and Bohemian improvements, to modern window glass

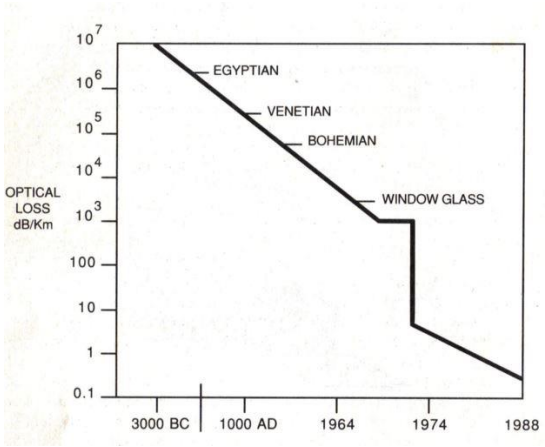

Figure 2-11: History of Attenuation [147]

A number of materials have received attention as potential guiding media, including liquids, gases, plastics and glasses [147]. In 1970 the United States was the first to produce good high-silica fiber. The 1970's can be regarded as the beginning of the optical communications age [148].

2.3.2 Planar Lightwave Circuits

During the late 1970's, optical fiber networks were implemented with new components waveguides in electronic circuits made of thin dielectric layers on a silicon substrate. Optical communications industry followed semiconductor electronics in miniaturizing and compacting components. This widespread technology, called "integrated optics", "planar waveguide circuits" or "planar lightwave circuits" (PLCs), has components of optical networking which function such as, splitting, switching, wavelength filtering, signal attenuation/amplification and dispersion compensation [145]. PLC technology is currently a multi-billion dollar industry, utilizing the same microfabrication techniques and materials as the semiconductor electronics industry.

During the late 1970's, optical fiber networks were implemented with new components waveguides in electronic circuits made of thin dielectric layers on a silicon substrate. The optical communications industry followed the semiconductor electronics in miniaturizing and compacting components.

Asymmetric Slab Waveguide

The asymmetric slab waveguide is the most general waveguide format, which is used in this section to explain the physical principles that underlie waveguiding. To understand the physics of waveguiding, two approaches are commonly adopted: ray optics and wave optics. The ray optic approach is outlined briefly, serving to introduce the core concepts of waveguiding before adopting wave optics for a more rigorous examination of the subject.

Ray Optic Approach

As a first step, the standard slab waveguide structure is described in Figure 2-12, where the waveguide core (refractive index ng) is surrounded on top and below by two layers (the substrate and the superstrate/cover layer) both having a lower refractive index than the core (ns and nc respectively). The higher refractive index of the core is a critical requirement of optical waveguides, so that light can propagate along the waveguide with minimal loss by total internal reflection (TIR) off the upper and lower waveguide boundaries. Total internal reflection refers to the total

reflection of a light ray travelling from a high to a lower refractive index medium. The conditions for total internal reflection are dictated by Snell's law of refraction, where the angle of incidence of the light ray (θi) must exceed the critical angle (θc). In the case of an asymmetric slab waveguide the critical angles for each interface are defined as follows,

$\theta_c^l = \sin\left(\frac{n_l}{n_g}\right)$ Waveguide – cover interface

$\theta_c^s = \sin\left(\frac{n_s}{n_g}\right)$ Waveguide – substrate interface

Where $n_g > n_s > n_l$ for the purposes of this explanation.

Brief examination of the Fresnel reflection coefficient, which is equal to the ratio of the reflected to incident electric field amplitudes, is revealing in this case. The Fresnel reflection coefficient for transverse electric (TE) waves [149], r_{TE} is,

$$r_{TE} = \frac{E_{0r}}{E_{0i}} = \frac{cos(\theta_i) - \sqrt{sin^2(\theta_c) - sin^2(\theta_i)}}{cos(\theta_i) + \sqrt{sin^2(\theta_c) - sin^2(\theta_i)}} \quad (2\text{-}1)$$

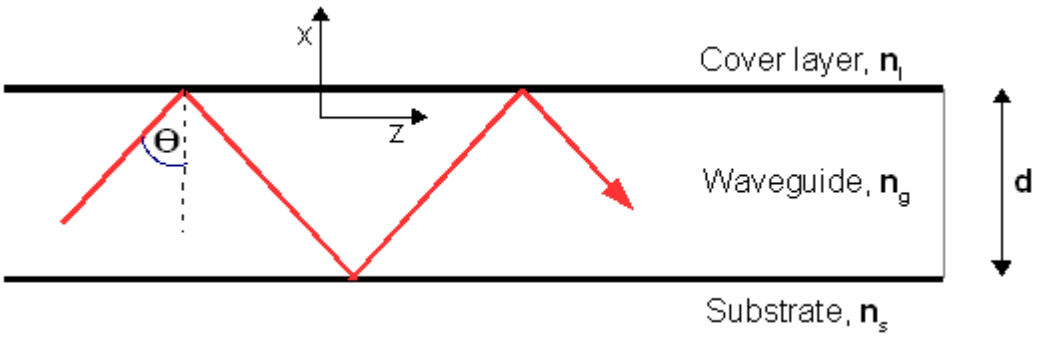

Figure 2-12: An asymmetric slab waveguide with guided mode: $\theta_c^s < \theta < 90^\circ$

In the case of TIR, it is evident that r_{TE} is a complex quantity since $sin^2(\theta_c) - sin^2(\theta_i) < 1$. The physical consequence of this is that the modulus of the complex reflection coefficient is always equal to 1 for all $\pi/2 > \theta_i > \theta_c$ (i.e. $|r_{TE}| = \sqrt{rr*} = 1$, meaning that in this range of angles all incident light is reflected).

As outlined above, the angle of incidence of the ray determines whether or not TIR can occur. Depending upon this angle, three different waveguide propagation behaviours can result. These are:

- $\theta_c^l < \theta_i < 90^\circ$: This range corresponds to total internal reflection of light from both the lower and the upper waveguide boundary, which results in propagation of a guided wave with low loss, as depicted in Figure 2-12.
- $\theta_c^s < \theta_i < \theta_c^l$: In this range the light is confined by TIR at the waveguidecover interface. However, at the waveguide-substrate interface it is free to escape and so this is called a cover radiation mode.

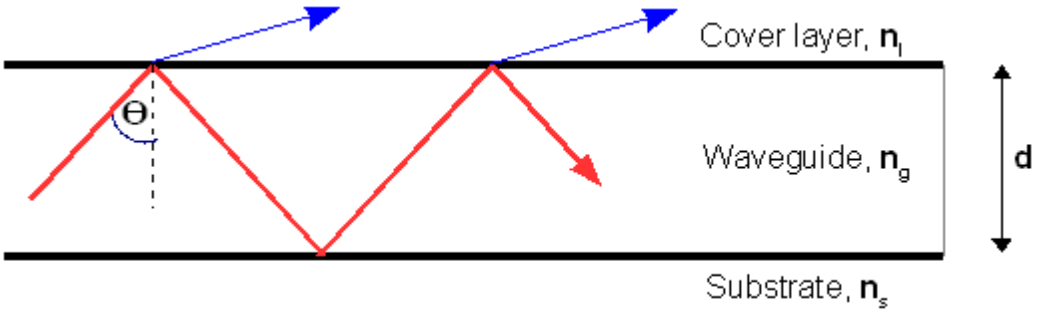

Figure 2-13 : Cover radiation mode. $\theta_c^l < \theta < \theta_c^l$

- $\theta_i < \theta_c^s$: This situation results in light escaping at both the substrate and the cover interfaces, resulting in a substrate-cover radiation mode (Figure 2-13 and Figure 2-14).

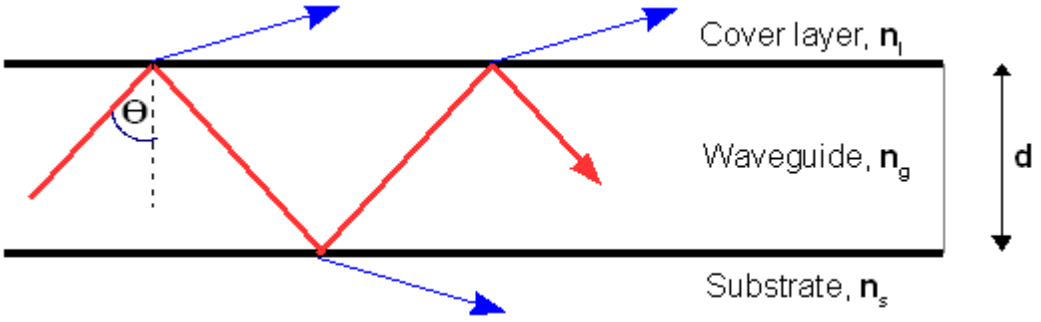

Figure 2-14 : Substrate-cover radiation mode. $\theta < \theta_c^s$

Wave Optic Approach

The ray optic approach allows a simple introduction to light propagation within a waveguide. However, the wave optic treatment of the subject permits a more rigorous determination of the propagation conditions of a particular waveguide structure, and the purpose of this Section is to derive the waveguide propagation condition.

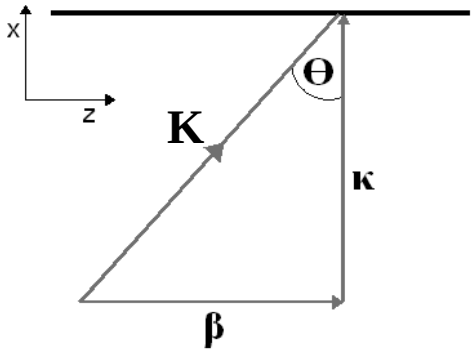

Figure 2-15 : Wavevector diagram showing the propagation constant (k), and the lon-gitudinal and transverse propagation constants ((β) and k, respectively)

The first step toward this goal is to introduce the effective refractive index. This is a characteristic of a waveguide derived from the propagation constant, k ($k = k_0 n_g$), where $k_0 = 2\pi/\lambda_0$, with λ_0 being the free space light wavelength. Drawing from the ray optic approach, the propagation constant can be considered as a vector pointing in the direction of the ray, as illustrated in Figure 2-15. The longitudinal and transverse wavevectors shown in Figure 2-15 (β and κ respectively) are fundamental waveguiding parameters, and are defined as,

$$\beta = k_0 n_g sin\theta \tag{2-2}$$

And

$$k = k_0 n_g sin\theta = \sqrt{k^2 - \beta^2} \tag{2-3}$$

Having introduced the propagation wavevectors, another fundamental waveguiding parameter is the effective refractive index, which is defined as,

$$n_{eff} = n_g sin\theta \tag{2-4}$$

Using this definition of the n_{eff} , it is clear that this quantity provides a link between the ray optic approach to waveguide mode analysis (defined by the incident angle θ) and the wave optics approach characterised by n_{eff}.

Derivation of the propagation conditions for a lossless dielectric medium begins with the Maxwell Equations, which are,

$$\nabla \times \tilde{E} = -\mu_0 \frac{\partial \tilde{H}}{\partial t} \tag{2-5}$$

And

$$\nabla \times \tilde{H} = -\epsilon_0 n^2 \frac{\partial \tilde{E}}{\partial t} \tag{2-6}$$

Where ϵ_0 and μ_0 are the dielectric permitivity and magnetic permeability of free space respectively and n is the refractive index of the dielectric medium.

Analysis of a slab waveguide of infinite extent in the y-direction greatly simplifies the steps necessary to derive the mode propagation condition. The analysis for a transverse electric (TE) mode is given here, where the electric field is perpendicular to both the propagation direction z, and the plane of incidence (x-z plane). Therefore only three electric/magnetic vectorial field components exist: Ey, Hx and Hz.

In order to simplify the Maxwell equations to arrive at a wave equation for the slab structure, the approach taken by Marcuse is shown here [150]. Assuming that the z dependence of the mode fields is given by the function exp(-jβz), and that the fields are strictly time harmonic, the electric and magnetic fields in the slab can be expressed as,

$$\tilde{E} = E_x(x) exp\big(j(\omega t - \beta_z)\big) \tag{2-7}$$

$$\tilde{H} = H(x) exp\big(j(\omega t - \beta_z)\big) \tag{2-8}$$

Substituting these equations into equations (2-5) and (2-6) , and exploiting the fact that ∂/∂y = 0, for a slab waveguide, results in the following identities,

$$-j\beta H_x - (\partial H_x/\partial x) = j\epsilon_0 n^2 E_y \tag{2-9}$$

$$j\beta E_y = -j\omega\mu_0 H_x \tag{2-10}$$

$$\partial E_y/\partial x = -j\omega\mu_0 H_z \tag{2-11}$$

Using these relations, it is possible to obtain the H components in terms of the Ey component,

$$H_x = -(\beta/\omega\,\mu_0)E_y \tag{2-12}$$

And

$$H_z = -(\beta/\omega\,\mu_0)\,\partial E_y/\partial x \tag{2-13}$$

Substitution of equations (2-12) and (2-13) into equation (2-9) yields the simplified one-dimensional wave equation for the Ey component (for TE mode),

$$\left(\frac{\partial^2 E_y}{\partial x}\right) + (k^2 + \beta^2)E_y = 0 \tag{2-14}$$

The general solution of equation (2-14) is,

$$E_y(x) = E_0 exp\left(\pm ix\sqrt{k^2 - \beta^2}\right) = E_0 exp(\pm ikx) \tag{2-15}$$

where κ is defined in equation (2-3) . In the waveguide core k0ng > β, and so equation (2-15) is unaltered and remains complex and oscillatory in this region.

In the substrate and cover, k0ns < k0nc < β, and so the complex factor in equation (2-15) is eliminated as follows,

$$E_y(x) = E_0 exp\left(-x\sqrt{\beta^2 - k_{s,c}^2}\right) = E_0 exp\left(-\alpha_{s,c}x\right) \tag{2-16}$$

where αs,c is an attenuation constant of the structure in the substrate or cover layers respectively $\left(\alpha_{s,c} = \sqrt{\beta^2 - k_{s,c}^2}\right)$. Unlike in equation (2-15), the exponential here is real and decaying (as denoted by the minus sign) in the x-direction; this is the evanescent wave of the waveguide.

Therefore, the TE mode distributions (Ey(x)) can be summarised as follows;

$$E_y(x,z) = \begin{Bmatrix} E_j exp[-\alpha_j x] \\ E_g cos(kx + \psi) \\ E_s exp[+\alpha_s x] \end{Bmatrix} exp(-j\beta z) \qquad \begin{matrix} \text{Cover} \\ \text{Waveguide} \\ \text{Substrate} \end{matrix} \tag{2-17}$$

Where, φ is a phase term, representing the asymmetry of the structure. By exploiting the requirement of continuity of tangential E and H at both interfaces, i.e. at x = ±d/2, and applying the boundary conditions at these interfaces [151], it is possible to write

$$\frac{kd}{2} + \psi = \frac{1}{2}\emptyset_i^{TE} \pm n\pi \tag{2-18}$$

$$\frac{kd}{2} - \psi = \frac{1}{2}\emptyset_s^{TE} \pm m\pi \tag{2-19}$$

where φTE l and φTE s are the Fresnel phase shifts that light under goes upon TIR at an interface, and may be derived from the phase of equation (2-1), resulting in

$$\emptyset_i^{TE} = \tan^{-1}\left(\frac{\mu_g \alpha_i}{\mu_i k}\right) \tag{2-20}$$

$$\emptyset_s^{TE} = \tan^{-1}\left(\frac{\mu_g \alpha_s}{\mu_s k}\right) \tag{2-21}$$

Adding equations (2-18) and (2-19) has the effect of eliminating ψ to produce the following relation,

$$2kd - \emptyset_i^{TE} - \emptyset_s^{TE} = 2p\pi \qquad p = 0,1,\ldots \tag{2-22}$$

Equation (2-22) is a generalised guiding condition for TE modes within an asymmetric slab waveguide.

Dispersion relation for the asymmetric slab waveguide

In order to obtain a plot of ω vs β for each waveguide mode, the guidance condition derived in equation (2-22) must be solved numerically for β at a number of frequencies. First, β, $\emptyset_i^{TE}$, $\emptyset_s^{TE}$, ωl and ωs are substituted into the guidance condition to obtain,

$$d\sqrt{\omega^2\mu_g\epsilon_g - k_z^2} = p\pi + \tan^{-1}\left(\frac{\mu_g\sqrt{k_z^2 - \omega^2\mu_l\epsilon_l}}{\mu_l\sqrt{\omega^2\mu_g\epsilon_g - k_z^2}}\right) + tan^{-1}\left(\frac{\mu_g\sqrt{k_z^2 - \omega^2\mu_s\epsilon_s}}{\mu_s\sqrt{\omega^2\mu_g\epsilon_g - k_z^2}}\right) \tag{2-23}$$

Knowing that β = ω√μϱeff and making the reasonable assumption that all regions are magnetically equivalent (μg = μs = μc = μ0) results in a further simplification, which yields

$$d\omega\sqrt{\mu}\sqrt{\epsilon_g - \epsilon_{eff}} = p\pi + \tan^{-1}\left(\sqrt{\frac{\epsilon_{eff} - \epsilon_l}{\epsilon_g - \epsilon_{eff}}}\right) + \tan^{-1}\sqrt{\frac{\epsilon_{eff} - \epsilon_s}{\epsilon_g - \epsilon_{eff}}} \tag{2-24}$$

This equation can now be rewritten in terms of the normalised parameters as,

$$V\sqrt{1-b} = p\pi + \tan^{-1}\left(\sqrt{\frac{b - a^{TE}}{1-b}}\right) + \tan^{-1}\sqrt{\frac{b}{1-b}} \tag{2-25}$$

where b is the normalised waveguide index, a^{TE} is a measure of the asymmetry of the waveguide and V is a normalised frequency parameter that is a measure of the number of modes a waveguide can support (also called the V number) [151]. These parameters are defined as follows:

$$b = \frac{\epsilon_{eff} - \epsilon_s}{\epsilon_g - \epsilon_s} \tag{2-26}$$

$$a^{TE} = \frac{\epsilon_s - \epsilon_l}{\epsilon_g - \epsilon_s} \tag{2-27}$$

$$V = k_0 d \sqrt{(\epsilon_g - \epsilon_s)/\epsilon_0} \tag{2-28}$$

Equation (2-25) fully describes the guidance condition for TE modes within a planar asymmetric slab waveguide and yields the dispersion plot shown in Figure 2-16. Such a plot enables the rapid determination of the properties of any guided mode. Examination of Figure 2-16 shows that for all of the modes displayed, there is a critical value of the normalised frequency (V), below which the guided mode is not supported by the waveguide structure in question (characterised by its normalised effective index).

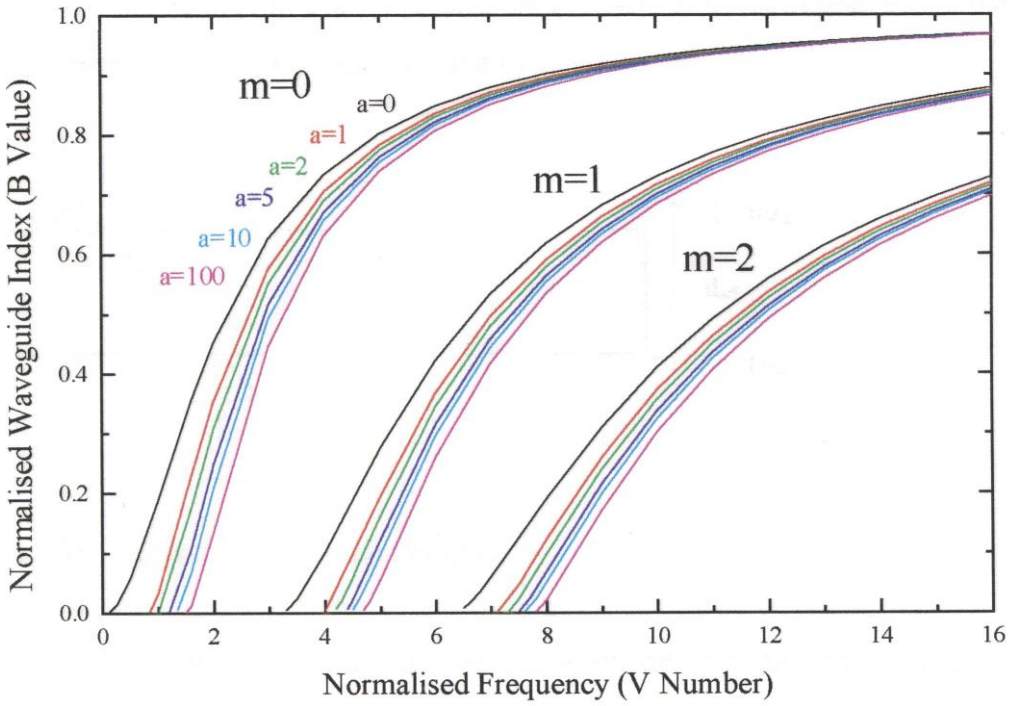

Figure 2-16 : Dispersion curve for TE modes in a slab waveguide

This value of V is normally referred to as the cutoff frequency (Vm) of the guided mode and can be calculated as follows,

$$V_m = V_0 + m\pi \tag{2-29}$$

Where, $V_0 = \tan^{-1}\sqrt{a}$ is the cut-off value of the fundamental mode and m is the mode number. Cut-off occurs when the effective refractive index of the mode is less than or equal to the refractive index of the cover or substrate.

Evanescent Wave

A consequence of total internal reflection is that all of the light incident on the interface is reflected back from the interface. However, if we assume there is no transmitted wave it becomes impossible to satisfy the boundary conditions which stipulate that the tangential components of E and H are continuous across the interface. In order to resolve this problem, it is instructive to examine the Fresnel reflection coefficient equation (2-1) once more where θi > θc. As stated in Section 2.3.2.3, when θi > θc, TIR occurs (as $|r^{TE}| = 1$). The phase of the complex

Fresnel reflection coefficient is the phase shift that light experiences upon total internal reflection.

In the case of TIR, the boundary conditions still require continuity of the electric and magnetic field vectors at the waveguide interfaces. Therefore, according to this requirement there is a transmitted wave which at first appears to contradict TIR. A more thorough examination of the behaviour of light during TIR shows that all of the above requirements can be met within the constraints of the boundary conditions, as follows.

With time dependence exp(−ωt) implicit, the form of the transmitted wave will be:

$$E_t = E_{0t} exp(-k.r) \tag{2-30}$$

Where, $k_t = k_{tx}x + k_{tz}z, k_{tx} = k_t \cos(\theta_t)$ and $k_{tz} = k_t \sin(\theta_t)$. Application of Snell's law in this case states that

$$sin(\theta_t) = \frac{n_i}{n_t} sin(\theta_i) \tag{2-31}$$

Use of the geometric identity $cos(\theta_t) = \sqrt{(1 - \text{six}^2(\theta_t))}$ in conjunction with equation (2-31) results in,

$$cos(\theta_t) = \sqrt{\left(1 - \left(\frac{n_i}{n_t}\right)^2 sin^2(\theta_i)\right)} = \sqrt{\left(1 - \frac{sin^2(\theta_i)}{sin^2(\theta_c)}\right)} \tag{2-32}$$

However, since $\theta_i > \theta_c$ then $\frac{sin^2(\theta_i)}{sin^2(\theta_c)} > 1$. Application of this condition to equation (2-32) results in an imaginary function as follows;

$$cos(\theta_t) = i\sqrt{\left(\frac{sin^2(\theta_i)}{sin^2(\theta_c)} - 1\right)} \tag{2-33}$$

Using equation (2-33) the coefficient α can be defined as,

$$\alpha = -ik_t cos(\theta_t) = -k_t \sqrt{\left(\frac{sin^2(\theta_i)}{sin^2(\theta_c)} - 1\right)} \quad (2\text{-}34)$$

Returning to and expanding equation (2-30) gives,

$$E_t = E_{0t} exp[-k_t cos(\theta_t)\, x - k_t\, sin(\theta_t)\, z] \quad (2\text{-}35)$$

The α coefficient defined in equation (2-34) can be substituted here to give,

$$E_t = E_{0t} exp(-i\alpha x - k_t\, sin(\theta_t)\, z) \quad (2\text{-}36)$$

which can be expressed as,

$$E_t = E_{0t} exp(-i\alpha x) exp\left(-\sqrt{(k_t^2 - \alpha^2)z}\right) \quad (2\text{-}37)$$

since, $k_t sin(\theta_t) = \sqrt{(k_t^2 - \alpha^2)}$. According to equation (2-37), the transmitted wave is propagates parallel to the surface and is attenuated exponentially in the x direction. Energy flows along the z direction but not in the x direction, thus satisfying the condition that energy is not transmitted across the boundary. The distance by which the transmitted wave travels into the sub/superstrate medium is called the penetration depth dp of the evanescent wave, and is defined such that

$$d_p = \frac{1}{\alpha} \quad (2\text{-}38)$$

This is the distance beyond the interface where the E-field will have decayed to 1/e of its original value at the interface, and in this context α (the transverse propagation constant in the cover/substrate) is known as the evanescent decay constant. The derivation for transverse electric (TE) polarisation has been shown here, which can be altered slightly to produce a different evanescent decay constant for the transverse magnetic (TM) polarisation.

Multi-mode Interference Coupler Theory

A multi-mode interference coupler (MMIC) is composed of a multi-mode waveguide, to which at least one single-mode input and output waveguide is attached for delivering and collecting light, as shown in Figure 2-17. MMICs have developed rapidly in recent years since their introduction by Ulrich and Ankele [152-154]. They are widely used in many PLCs, such as power splitters [155], ring lasers [156], optical switches [157, 158], and wavelength division multiplexers/demultiplexers [159, 160].

When the input light enters the MMIC section, high-order modes of the multimode waveguide section are excited. Through the interference between the excited modes, images of the input light can be formed, which are known as self-images.

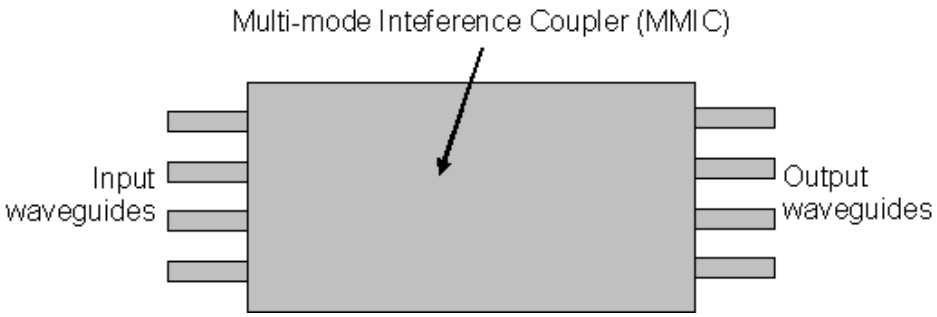

Figure 2-17 : General structure of an MMIC

The MMIC operates by producing single and multiple self-images of its input light distribution at various points along its length, as shown by the simulation image in Figure 2-18. The theoretical treatment of self-image formation in an MMIC is taken from Ref. [161]. The relation between the transverse wavenumber κ and the longitudinal propagation constant β of the νth order mode can be described, as before, by the dispersion equation:

$$k^2 n_g^2 = k_v^2 + \beta_v^2 \tag{2-39}$$

For strong guiding waveguides,

$$k_{xv}^2 = (v - 1)\,\pi / W_e \tag{2-40}$$

Where W_e is the effective width of the multi-mode section. By substituting equation (2-40) into (2-39) and using the paraxial approximation, the propagation constant β_v can be expressed as:

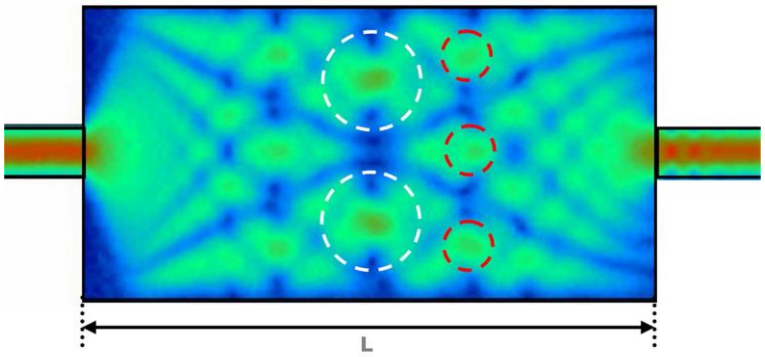

Figure 2-18 : Simulation image (using BPM software) of the electric field distribution with multiple self-images in an MMIC

$$\beta_v \approx n_{co}k_0 - \frac{(v+1)^2\pi\lambda}{4W_e^2 n_{co}} \tag{2-41}$$

where n_{co} and n_{cl} is the refractive index of the MMIC core and cladding respectively. The beat length between the fundamental and the first mode can be defined as:

$$L_\pi = \frac{\pi}{\beta_0 - \beta_1} = \frac{4n_{co}W_e^2}{3\lambda} \tag{2-42}$$

and equation (2-41) can be rewritten as:

$$\beta_v \approx \beta_0 - \frac{v(v+2)\pi}{3L_\pi} \tag{2-43}$$

By assuming that the MMIC has at least a few guided modes and that the radiative modes of the MMIC section are not excited, the input field Ψ (x,0) can be expanded in terms of all the guided modes in the multi-mode region:

$$\Psi(x,0) = \sum_v c_v\psi_v(x) \tag{2-44}$$

where $\psi_v(x)$ is the vth order mode distribution and c_v is the vth order mode excitation coefficient, given by:

$$c_v = \frac{\int \Psi(x,0)\psi_v(x)dx}{\sqrt{\psi_v^2(x)dx}} \tag{2-45}$$

The field ψ(x,z) propagating along z direction can be expressed as a superposition of all the guided modes, that is

$$\psi(x,z) = \sum_v c_v\psi_v(x)exp[j(\omega t - \beta_v)] \tag{2-46}$$

Finally, by substituting equation (2-43) into (2-46) the equation specifying the field within the MMIC section is arrived at:

$$\psi(x,z) = \sum_v c_v\psi_v(x)exp\left[j\frac{v(v+2)\pi}{3L_\pi}z\right] \tag{2-47}$$

From equation (2-47), one can easily find that the field at z = L is determined by the mode excitation coefficient c_v and the phase term: $exp\left[j\frac{v(v+2)\pi}{3L_\pi}z\right]$. Under certain conditions, the field at z = L will be a reproduction of the input field. By using the symmetry and anti-symmetry of the even and odd modes with respect to the plane at x =W/2, equation 2.49 shows that $\psi(x, z = L)$ will be a self-image of $\psi(x, z = 0)$ if the phase term satisfies the following condition,

$$xp\left[j\frac{v(v+2)\pi}{3L_\pi}z\right] = 1 \ \ or \ \ (-1)^v \tag{2-48}$$

in which case it can be seen that equations (2-47) and (2-44) are equivalent, i.e., the field at z = L is a reproduction of the field at z = 0. However, depending upon the excitation position, some of the modes will not be excited. This results in some special cases which can be analysed as follows:

General Interference

General interference means that there is no specific restriction on the excitation position. It is found that there are N-folded images of the input field at a distance L from z = 0:

$$L = \frac{3ML_\pi}{N} \tag{2-49}$$

where M indicates the imaging periodicity along z (known as the self-image rank). At this length, N-fold images are positioned at xi with phase φi given by the following:

$$x_i = p(2i - N)\frac{W_e}{N} \tag{2-50}$$

$$\emptyset_i = p(N - i)\frac{\pi}{N} \tag{2-51}$$

Paired Interference

The modes ν=2, 5, 8,... present a odd symmetry at x=±We/6. By launching an even symmetric field at these positions, the excitation coefficients c_v will be zero for ν=2, 5, 8,..., since the overlap integrals of equation (2-45) between even symmetric input field and the odd symmetric modes will vanish. For the other excited modes with $c_v \neq 0$:

$$mod_3\,[v(v+2)] = 0 \quad for\ v \neq 2{,}5{,}8, \ldots \tag{2-52}$$

Therefore, the length periodicity of the mode phase of equation (2-48) will be reduced three times. N folded self-images of the input field may be obtained at:

$$L = \frac{ML_\pi}{N} \tag{2-53}$$

The modes contributing to the imaging are mode pairs 0-1, 3-4, 6-7..., thus this mechanism is called paired interference. For this case, the number of the input waveguides is limited to two (at x = ±We/6).

Symmetric Interference

If the excitation field is launched at the centre of the multi-mode region, only the even symmetric modes will be excited (c_v = 0 for ν odd). For this case:

$$mod_4\,[v(v+2)] = 0 \quad for\ v\ \ even \tag{2-54}$$

With this condition, the length periodicity of the mode phase of equation 2.50 will be reduced four times. Therefore, N-fold self-images of the input field may be obtained by:

$$L = \frac{3ML_\pi}{4N} \tag{2-55}$$

Directional Coupler Theory

A directional coupler in its most basic configuration, consists of two waveguides formed in close proximity as shown in Figure 2-19, so that light from waveguide A can couple into waveguide B via its evanescent wave, and vice versa. As light propagates in the waveguides, light is continuously transferred from one waveguide to the other and then back again in a spatially periodic fashion. This continuous transfer of light from one waveguide to another is primarily used for power splitting. The following treatment of directional coupler theory is taken from [162]. The coupled mode equations express the change in intensity in one of the waveguides in

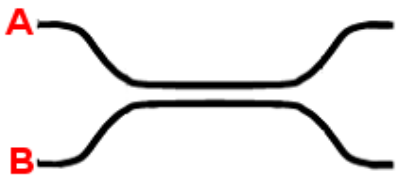

Figure 2-19 : General structure of a directional coupler

terms of the intensity in the other waveguide such that,

$$\frac{dA(z)}{dz} = k_{ab}B(z)exp - (2j\delta z) \tag{2-56}$$

$$\frac{dB(z)}{dz} = k_{ba}A(z)exp - (2j\delta z) \tag{2-57}$$

where k_{ab} and k_{ba} are the coupling coefficients (from waveguide a to b, and b to a respectively), and δ is the normalised phase deviation and is related to the difference in the propagation constants of the two modes and the spatial variation of the perturbation. Considering that light is initially injected only into one of the waveguides such that;

$$A(z = 0) = 0 \qquad B(z = 0) = B_0 \tag{2-58}$$

the solution to the coupled mode equations in equation (2-57) are therefore,

$$A(z) = \frac{k_{ab}B_0}{\sqrt{k^2 + \delta^2}} \exp(-j\delta z) \sin\left(z\sqrt{k^2 + \delta^2}\right) \tag{2-59}$$

$$B(z) = B_0 \exp(j\delta z)\left[cos\left(z\sqrt{k^2 + \delta^2}\right) - \frac{j\delta}{k^2 + \delta^2} sin\left(z\sqrt{k^2 + \delta^2}\right)\right. \tag{2-60}$$

Where, κ = $|k_{ab}|$ = $|k_{ba}|$. Pertaining to the thermo-optic complete coupling of light from one waveguide to the other this condition is expressed only for phase matching (δ = 0), such that

$$A(z) = B_0(k_{ab}/k) \sin(kz) \tag{2-61}$$

$$B(z) = B_0\, cos(kz) \tag{2-62}$$

The complete transfer of light from waveguide A to B in this case, occurs at the coupling length,

$$L = \frac{\pi}{2k} \tag{2-63}$$

where, κ, the coupling coefficient is calculated according to the following equation:

$$k = \frac{\beta_0 - \beta_1}{2} = \frac{\pi\left(n_{eff0} - n_{eff}\right)}{\lambda} \tag{2-64}$$

Equations (2-63) and (2-64) provide a convenient means of specifying the length of a directional coupler for complete power transfer. For equal power splitting, a length of Lc/2 is necessary,

Numerical Methods

Throughout this work, simulation of PLC devices have been carried out using cross-sectional mode solvers, and Beam Propagation Methods (BPM), which are accurate numerical methods which allow simulation of the behaviour of light in a PLC. This section serves to give a brief background to these numerical techniques.

Mode Solvers

The basic function of cross-sectional mode solvers is to provide an accurate means by which the Electromagnetic field distribution in a waveguide cross-sectional structure can be calculated. There are a number of different algorithms available to achieve this aim, some basic e.g. Effective index method, Marcatili method and some more advanced algorithms including, Multi-grid finite difference algorithms, and the "Bend 2D" algorithm which is the most accurate of all [16], and is therefore used in this work.

The mode solver was used for two main purposes. Firstly, they are an indispensable tool for specification of the waveguide parameter necessary for single-mode operation: waveguide cross-sectional dimensions, and refractive index contrast between the waveguide core and the surrounding cladding. Secondly, the mode solver is especially useful as a means to calculate the effective refractive index of a

waveguide structure, which was used in the design of both directional coupler and MMIC-based devices in this work.

The Beam Propagation Method (BPM)

Throughout this work, the Beam Propagation Method (BPM) has been employed for simulation of the propagation of light in the various PLC platforms that have been designed and developed (using Olympios Integrated Optics Software, C2V, Netherlands). The purpose of these simulations has been two-fold. Firstly, to verify the operating principles of the platforms prior to fabrication, and secondly, BPM data was used as means of specifying the device dimensions necessary for the platforms to effectively carry out their functions.

The BPM algorithm is a numerical method of solving the Helmholtz wave equation [16],

$$\left(\frac{\partial^2 E_y}{\partial x^2}\right) + \left(\frac{\partial^2 E_y}{\partial z^2}\right) + (k^2 + \beta^2)E_y = 0 \qquad (2\text{-}65)$$

The 1D version of this equation was derived here for the asymmetric slab waveguide equation (2-14). It does this by means of the slowly varying envelope approximation (SVEA), in which the electric field is divided into a slowly varying envelope function (φ(x, y, z)) and a fast oscillatory phase term (exp(-jβz)), such that [16, 17][163],

$$E(x, y, z) = \emptyset(x, y, z)\exp(-j\beta z) \qquad (2\text{-}66)$$

yields the following expression [17],

$$\left(\frac{\partial^2 \emptyset}{\partial z^2}\right) + 2j\beta\left(\frac{\partial \emptyset}{\partial z}\right) + \nabla_{\perp}^2\emptyset + (k^2 + \beta^2)\emptyset = 0 \qquad (2\text{-}67)$$

Where, ∇2 ⊥ = ∂2/∂x2 + ∂2/∂y2, which is the Laplacian operator in the lateral direction. The first term (∂2φ/∂z2) is disregarded in BPM simulations so as to arrive at an expression that is first-order in z, greatly reducing computation time. A mode solvers is used to establish the starting field distribution and propagation constants, which are typically used as initial conditions for a BPM simulation [164]. This starting condition is then propagated along the z direction in discrete steps (defined

by the z discretisation of the simulation) as shown in Figure 2-20, using equation (2-67) in a finite difference calculation.

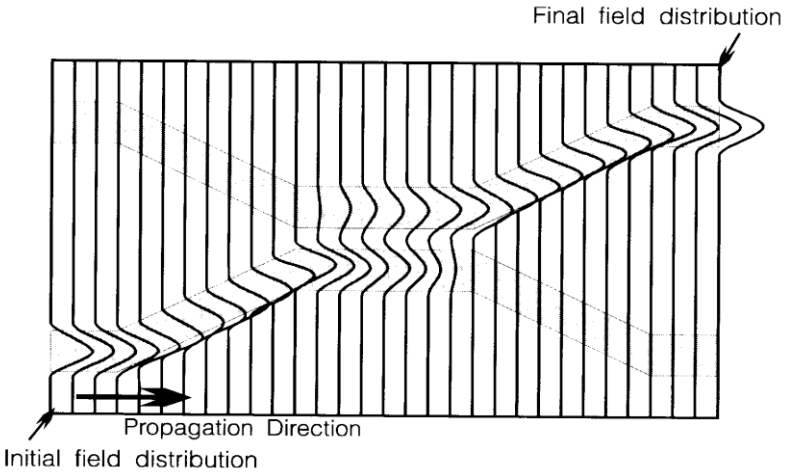

Figure 2-20 : Example of a wave propagating in discrete steps through a structure (di- rectional coupler) [16]

2.4 Hybrid Organic-Inorganic Sol-Gel Materials

2.4.1 Introduction

Optical quality materials called Sol-gel can be chemically synthesized. Basically, the sol-gel process includes the mixture of a chemical precursor, usually a metal alkoxide, with water yielding an inorganic network within the liquid phase [165]. The coating of materials (sols), often by means of dip-, spin- or spray-coating, results in the formation of high optical quality thin films (gels). The gels criteria can be precisely varied by selecting the appropriate precursors and processing conditions. As illustrated in Figure 2-21: Crystal and other types of glassware coated with dye-doped hybrid sol-gel materials, embedding or grafting organic chromophores in a sol-gel gives, the diversity of coloured hybrid coatings.

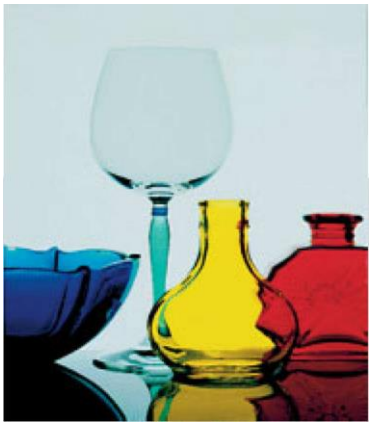

Figure 2-21: Crystal and other types of glassware coated with dye-doped hybrid sol-gel materials[166]

Over the past decade, a new area of sol-gel research has gained increasing attention, where hybrid sol-gel materials share the same basic processing principles with the pure inorganic sols. However, hybrid sol-gel materials are classified as an inorganic and an organic component according to the chemical nature of the precursors used during the synthesis [167, 168]. This advantage gives a wide variety of engineered materials with multiple functionalities incorporated in a single hybrid material, which can be utilized in electrochromic coatings for windows [169, 170], corrosion protection [171], porous sensor membranes for gas phase sensing[172, 173], and entrapment of biomolecular probes for biosensors [174, 175].

PLCs have promising applications in the area of optics, such as using a photosensitive organic moiety to form planar channel waveguides directly from photopattern the thin films, as illustrated by Figure 2-22. The advantages of hybrid sol-gel materials for PLC fabrication in comparison to the more established techniques has been reviewed [176-179], as follows

• Hybrid sol-gels materials allow the most rapid PLC fabrication, only rivalled by polymer processing techniques, in comparison to the prolonged depositional techniques for the waveguide core Layer, such as chemical vapour deposition (CVD).

• Inexpensive materials and equipment used in PLCs, such as UV mask aligner, compared to a CVD system.

• The synthesis can be performed at the ambient room temperature without the need for sophisticated equipment.

• The process can be at moderate temperature (~ 100-150 °C) and ambient pressure.

• PLCs can be utilised to give active properties to the material such as thermo- or electro-activity for switching.

• Due to direct photopatterning, sol-gel PLC devices do not endure waveguide scattering losses of the indirectly patterned PLCs, which are induced by reactive ion etching (RIE) processes that result in rough sidewalls.

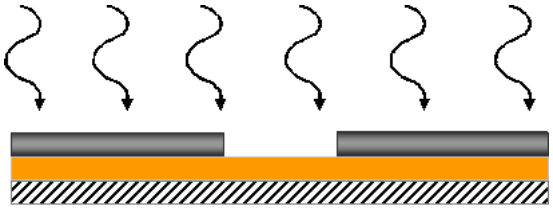

Figure 2-22: Illustration of the selective irradiation of photosensitive film by a photolithographic process

• Combining the advantages of the inorganic network (mechanical strength and thermal resistance) with the organic functional groups, the best properties of both can be obtained in a single material.

The following section will outline the development in the field of sensing and telecommunications platforms.

2.4.2 The Sol-Gel Process

History of the sol-gel process

The sol-gel process is probably one of the most exciting preparation techniques that have emerged in the past decade in the material sciences in general and in the chemistry of materials in particular. Sols and gels are two forms of matter that exist in nature and that are known since the beginning of humanity. They comprise inert materials such as clays and inks or living systems such as milk and serum [180]. The sol is defined as a homogenous dispersion of submicron particles within a liquid and its viscosity is generally comprised between those of water and light oils. The study of sols commenced in 1845 when Selmi prepared silver chloride dispersions. Ebelmen has been the first to report in 1846 the gelation of silicon tetrachloride within an alcohol solvent in the presence of water [J. J. EBBELMEN. Ann., 57, 331, (1846)]. In 1930, Geffcken mentioned for the first time the concept of alkoxide

polycondensation and the formation of three-dimensional networks for silicate-based gels. Hurd described these structure gels as silicic acid polymeric skeleton embedded in continuous liquid phase [181] and Graham was the first to propose in 1961 the initial principle of the colloidal science [182, 183]. The 1960s have been the key years for the sol-gel science as possible alternative to conventional high temperature processes for the preparation of glassy materials. Levene and Thomas proposed in 1967 the first glasses prepared by a mass production sol-gel-based process for sputtering applications [184].

The Deryagin, Landau, Verwey and Overbeck theory, usually called DLVO theory or electrostatic theory, enabled the explanation of physics phenomena responsible for the stability of colloidal sols. In summary, this theory indicates that solid particles (with greater densities than their solvent dispersant) may remain dispersed within their solvent if the forces responsible for the stabilisation (electrostatic forces) are not overtaken by the gravitation forces. For this, the particle size has to remain sufficiently small to avoid any undesired agglomeration and sol destabilisation.

Principle of the sol-gel process

Two distinct ways of synthesis are distinguished in the sol-gel process: 1) the destabilization of a colloidal solution (DCS) and 2) the polymeric route. They give rise to the colloidal gel (or physical gel) and to the polymeric gel (or chemical gel), respectively. The essential difference between these two gels is in the ability to reversibly retrieve their initial form. Under the application of a shearing force, physical gels have the characteristic to retrieve their initial liquid form. They are also called thixotropic gels because of the formation of strong and irreversible chemical bonds, chemical gels remain solid.

The nature and elimination conditions of the solvent phase of the material are also used to define the various gels. When the solvent is water, gels are defined as aquagels or hydrogels. When the solvent is mainly composed of alcohol, gels are called alcogel.

The gel-solid transition requires the elimination of the solvent. When this elimination is performed thermally, gels are called xerogel. However, this technique does not always allow the formation of bulk gels because of the elimination kinetic of the solvents, which can generate physical constraints in the material, thus cracking

and in some cases causes solid powder formation. To avoid this phenomenon, solvents could be eliminated by supercritical drying. In this process, the drying can be performed above the critical point, when both liquid and gas forms become indistinguishable and the interfacial energy (liquid-gas), responsible for the presence of capillary forces, becomes nil. Gels prepared by this process are called aerogel.

The preparation of gels by DCS is performed by bringing together the interacting spheres either by evaporation of the solvents or chemically by the addition of an electrolyte, which decreases the particles charges. The polymeric sol-gel process is extensively described in the literature [168, 185-189]. The basic physico-chemical principles illustrated above are the fundamentals which govern the formation of sols. They also show the different stages leading to the fabrication of thin films from organometallic and organosilicate precursors.

Hydrolytic sol-gel process

In this case, the precursors are metal alkoxides, the general chemical formula of which are RxM(OR')4-x. M represents a metal atom, generally silicon or a metal transition. R and R' are organic chains. The characteristic of the M-O-R bond is to be reactive upon hydrolysis, to form metal hydroxide bonds (M-OH), which can react together via polycondensation reactions to form three-dimensional networks of metal-oxo bridges (M-O-M). The bigger the size of R', the slower the kinetic of hydrolysis is observed, due to steric hindrances. The hydrolysis and condensation reactions are the two essential chemical processes that take place in the formation of the sol and subsequently the gel in the polymeric sol-gel process. The factors influencing the kinetic of reactions are the hydrolysis pH and the water to reactive alkoxide ratio. The final structures of materials depend on these parameters. I propose to study the influence of these various parameters on the reactional mechanisms of the hydrolysis and condensation.

Hydrolysis

Generally, the precursors are initially dispersed in an alcoholic solvent prior to hydrolysis. For a good control of the process, the reactions must be conducted in homogeneous medium. For this, the solvent is used to allow the miscibility of all precursors. However, when highly concentrated systems are used no solvent can be

added. Therefore, the reaction is done in heterogeneous medium and the alcohol resulting from the hydrolysis eventually allows the miscibility of all present precursors. In addition, when the water content against the alkoxide is elevated, the pH of the aqueous solution becomes the principal factor in the control of the hydrolysis kinetics. The pH can be controlled by the addition of either inorganic or organic acids or bases. Acidity and basicity are known to favour hydrolysis and condensation, respectively [190-193]. Solvation also plays a crucial role in the hydrolysis process. A protonic solvent has the ability to bind to nucleophilic groups such as hydroxyl deprotonated

Condensation

The condensation step is the formation of oxo-bridges responsible for the growth of the three-dimensional network. It is performed by condensation reactions between hydroxyl and alkoxide groups (alcoxolation), and between two hydroxyl groups (oxolation) by generating water and alcohol molecules respectively. These are sketched in the following schemes:

Si–OH + RO–Si → Si–O–Si + ROH (alcoxolation)

Si–OH + OH–Si → Si–O–Si + H2O (oxolation)

Like the hydrolysis, the condensation process is also influenced by the pH of the solution. In acid conditions, neutral species are attacked by protonated silanols (alcoxolation and oxolation of reactions). However, in basic conditions, the formation of deprotonated species (Si–O-) is favoured because of the greater nucleophilic character (in comparison with the protonated species). The increase of the nucleophilic character produces an increase of the alcoxolation and oxolation reation kinetics, as sketched in the following schemes:

Si-O- + RO-Si → Si-O-Si + RO-

Si-O- + OH-Si → Si-O-Si + OH-

Such phenomena have been thoroughly described in the literature for the preparation of dual inorganic oxides [190, 191, 194-196] and hybrid organic-inorganic gels [188, 197]

Aging gels

This phenomenon consists of the expulsion of the solvent and is called syneresis. this results in the increase of the connectivity of the network to its mechanical properties. This phenomenon, predominantly occurring in acid media, consists of the distance reduction and in crosslinking of the various species chains formed during the condensation (Figure 2-23).

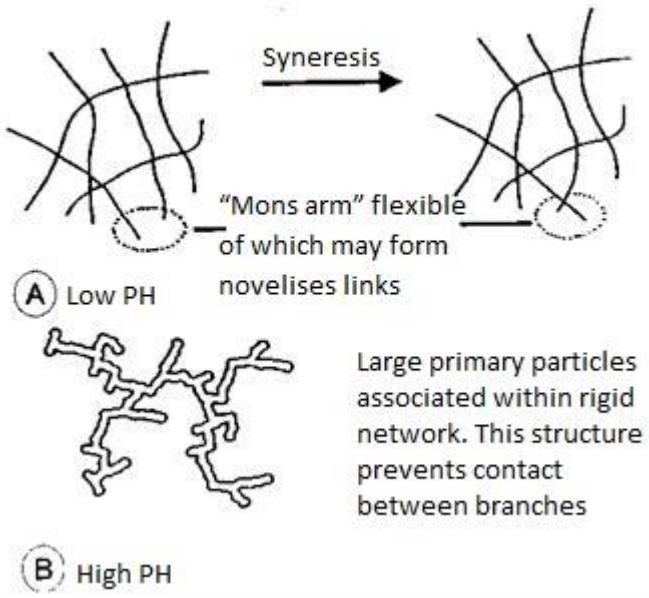

Figure 2-23: Schematic acid gels (A) and base (B).

Gel-solid transition

This step is designed to fully evacuate the liquid phase of the gel in order to obtain a solid material. Unfortunately, drying gels by evaporation or thermal effect is inevitably accompanied by a set of constraints between the liquid and solid, the result of which is the appearance of cracks in the gel. Supercritical drying cancels the interfacial tensions and allows the expulsion of the liquid phase without constraints. Meanwhile, aerogel has different mechanical properties of the gel from which it originated: drying increases the particle cohesion, thus increasing rigidity.

After the drying step, the densification of the gel is performed in order to achieve materials with minimum or no porous volume. This densification is usually done by sintering process.

Non - hydrolytic processes

Non- hydrolytic sol-gel processes are particular methods of the sol- gel technology. They are based on the condensation reactions with metal chlorides that act as oxygen donor groups such as water for metal alkoxides (reaction 1), ethers (reaction 2) or alcohols (reaction 3).

M-Cl + M-OR → M-O-M + R-Cl (reaction 1)

M-Cl + R-O-R→ M-OR + R-Cl (reaction 2)

M-Cl + R-OH → M-OR + HCl (reaction 3)

Reaction 1 can form a covalent bond directly, while reactions 2 and 3 require an intermediate step of the formation of the corresponding alkoxide by etherolysis and alcoholysis reactions, respectively. In the case where M is silicon, the non-hydrolytic condensation path requires a chloro- metal type catalyst ZrCl4 [198].

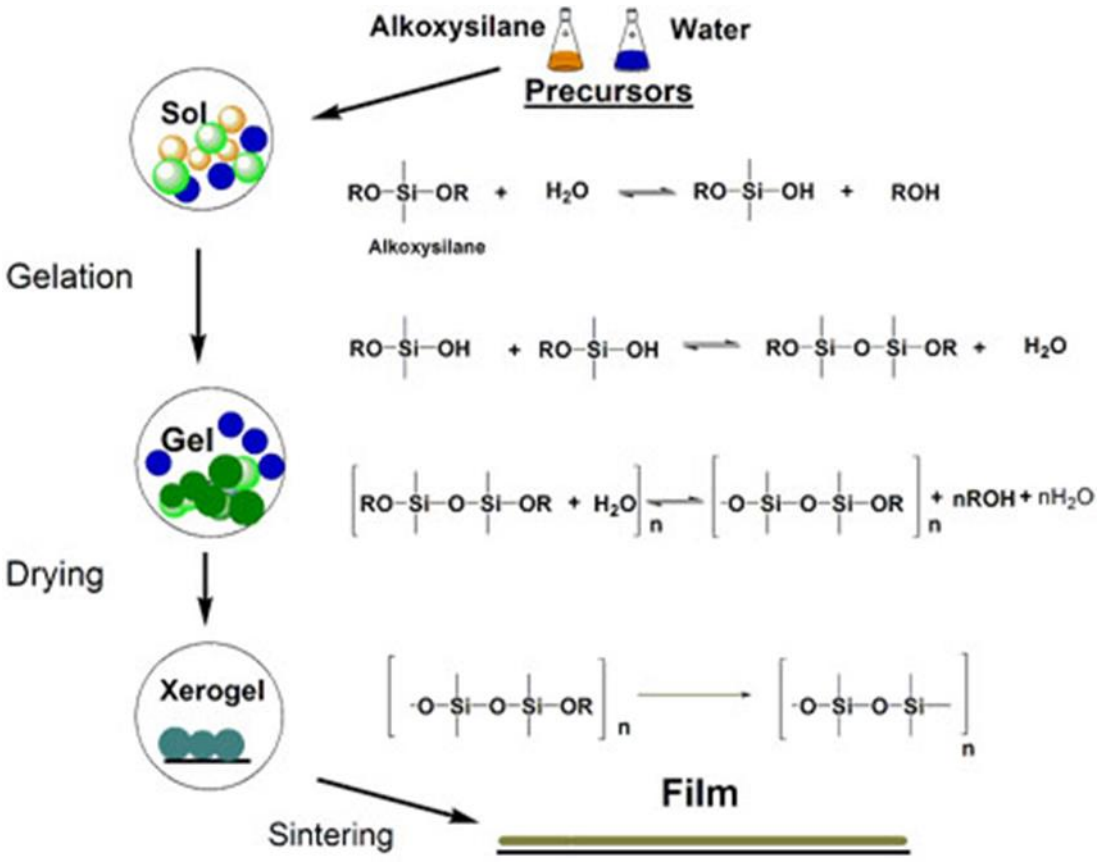

Figure 2-24: General principle of the sol-gel process for the formation of thin films.

2.4.3 Hybrid Sol-Gel Materials

History

Hybrid Organic-Inorganic Materials (HOIM) are generally described at the molecular level as the combination of an inorganic component and an organic one forming as composite materials. Nature over a billion years of evolution has been successfully experienced such mixing of MOIM composites which led to multi-functional and hierarchical multi-scale (from Nanometer to Angstrom) systems [181, 182]. Only recently, relevant to the geologic time scale, that humanity starts making and utilizing HOIM material. Due to their high natural availability and their intrinsic properties (such as high adsorption ability, interesting ion-exchange capacity, and good thermal, mechanical and chemical stabilities), HOIM from organically modified clays have been part of human existence and being used for artistic, societal, environmental, industrial and commercial uses [183, 184]. Probably one of the first uses of clays-based HOIM was in the Mediterranean region, where clay and soil were mixed with decaying urine to enhance laundry processes. Over the course of human history, the use of hybrid clays spread progressively all over the world. For example, in China, hybrid clays permitted the production of very thin ceramics (eggshell porcelain) as a result of intercalating urea inside the interlayer spaces led to further improving their delamination plasticity [185]. On the other hand, pre-Colombian civilization in South America left their frescoes which is a well-known pigment called the Maya blue. This pigment was intertwined with their artistic and religious life resulted from the incorporation of a natural organic dye (blue indigo) within the channels of micro-fibrous clay (palygorskite) [186]. This hybrid is characterised by a strong blue coloring and more resistant material against weathering and bio-degradation than the fragile indigo dye alone. The stabilization of the organic dye by the mineral part allows us to admire vestiges 12 centuries old codices, frescoes, and sculptures, thus, to appreciate these lost civilizations.

These first historical examples summarise core principles of MOIM: coupling at the molecular level organic and inorganic components, synergistic effects of this coupling, (multi)functionality, outstanding processability and applicability, strong links with civil society. Over the 20th century, MOIM had a strong industrial and commercial development [199, 200]. For example, in the 1940s, silicones, hybrid nano-pigments, and shortly later, organically templated zeolites provided a huge set

of functional hybrid materials that have found interest in automotive, aerospace, construction, medical and paint industries and for catalytic transformations of primary resources in gas and oil industries. However, the name "hybrid materials" was not mentioned at that time. Mixed organic–inorganic materials nucleated in the middle of 1980s with the expansion of "soft chemistry" [201-205]. Then the concept of "hybrid organic–inorganic" nanocomposites exploded in 1990s when pluridisciplinar research projects started to be encouraged to tackle multi-faceted problems.

From a scientific and R&D perspective, hybrid materials have been amongst the most popular materials explored in the past 25 years. From a few papers published in the early 1990s, since then the growth of published studies has reached over 16,000 in 2013, as shown in Figure 2-25 .

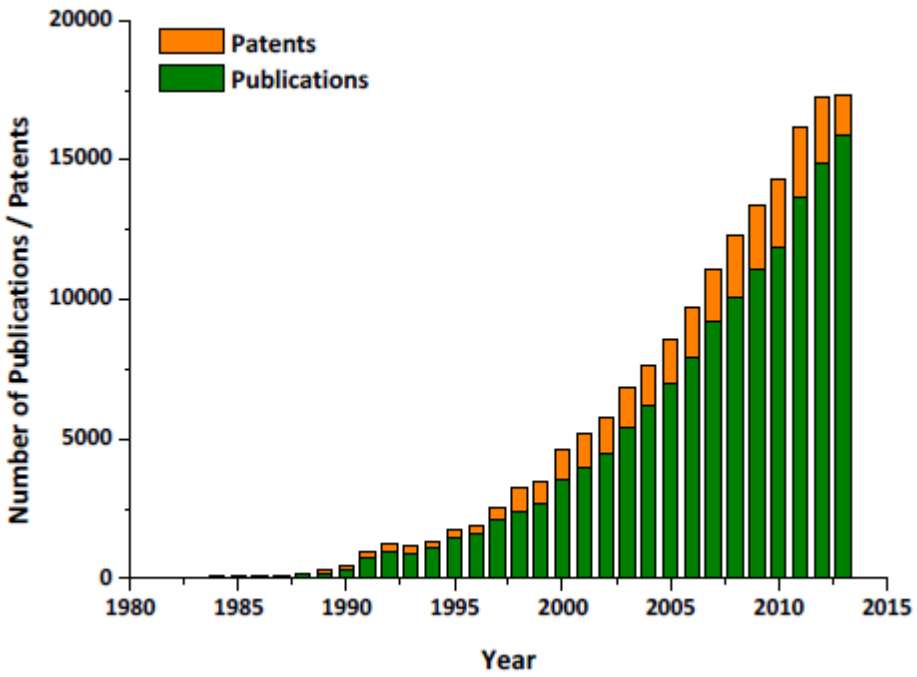

Figure 2-25: Number of papers and patents related to hybrid materials [17].

Structure and classification

A hybrid material is a molecular system that comprises both organic and inorganic moieties. This general definition includes within the same family, materials with very different structures: monomolecular, bimolecular or multimolecular. To avoid any confusion between these various structures, a classification has been proposed

by Clément Sanchez [189]. This classification takes into consideration the level of interaction at the molecular level between the organic (O) and inorganic (I) moieties, as shown in Table 2-1.

Class	**Interactions between O et I**	**Structure**
Class 1	- weak, electrostatic interactions	- embedment, O in I or I in O
Class 2	- Strong, covalent bonds - Strong and weak, covalent and electrostatic interactions	- grafted, O-I - Grafting and embedment, I and/or O in O-I

Table 2-1: Classification of hybrid organic – inorganic O and I materials.

Organic and inoragnic moities can be colloidal particles, plymers or monomers. Organic colloids, the most famous of which being the latex, are generally in forms of spherical particles stabilised in a solvent by the occurrence of electrostatic interactions. Inorganic colloids, the most popular of which are the silicate-based ones, have diameter sizes generally lower than 50 nm and are stabilized in a polar solvent. Polymers are in the form of macromoleclues, the size of which is defined by the polymerization degree and is fixed before mixing with the inorganic moiety.

From a structural point of view, isolated molecules can act as network builders or modifiers. Network modifiers are functional systems with unreactive groups, which mean that their role is limited to prevent further linkage between the other reactive groups and reduce connectivity. These are usually molecules with fully saturated alkane groups (CnH2n+1). Network builders are composed of reactive groups that can create a network upon thermal or radical polymerization, such as epoxy and unsaturated alkyl groups (alkenes and acrylates).

Class 1 hybrid materials correspond to hybrid systems, where organic species are homogeneously dispersed within an inorganic matrix, or inversely. The preparation of such materials is performed in the liquid phase by vigorous mixing of the various chemistries. If a lack of miscibility is apparent, it is essential to overcome it by adding a co-solvent (generally tetrahydrofuran), into which both chemicals are miscible. The role of the co-solvent is to avoid phase separation at the macroscopic

level so that the various molecules can get closer together. The occurrence of bipolar chemical bonds is due to inorganic species, as the presence of a highly electropositive metal, covalently linked to one or several highly electronegative atoms, such as oxygen, involves a strong bipolar bond. Unlike inorganic molecules, organic monomers and polymers can be strongly apolar, this is the case of the pure alkane and alkene based ones. Apart from these exceptions, generally organic monomers and polymers comprise at least one C–X (X = - O, =O, -Cl or -F) chemical group, which creates a polarity in the molecule, which possible interactions and miscibility with polar systems (such as the inorganic species). Though, the interactions between both systems remain relatively weak, this is sufficient to achieve materials within homogenous concentrations. Nevertheless, the materials remain multiphasic at the molecular level and have to be considered as composite systems.

Class 2 hybrid materials correspond to hybrid systems where both organic and inorganic moieties are chemically linked via at least a chemical bond. This class of materials also comprises families of material chemically linked mixed with those issued from Class 1 hybrid materials, which can be called multi-molecular hybrids.
The possibility to incorporate or chemically link systems with different properties results in materials with more diverse and intermediate properties to the conventional inorganic or organic materials. Widely tailored properties can be achieved, including 1) modification of the mechanical properties [206, 207] (elasticity, scratch resistance etc.), 2) improved processing of films, 3) mouldability [208], 4) porosity control, 5) hydrophilicity/ hydrophobicity [209, 210]. The organic component often contributes to a peculiar material functionality such as; 1) optical [203, 211], 2) electrical [212], 3) electrochemical [213], 4) chemical or biochemical functionality [28–30] [214-216]. The condensed inorganic backbone is generally considered to give enhanced mechanical and thermal strength, while also allowing the tuning of refractive index [217, 218], or other interesting electrochemical, electrical or magnetic properties [219, 220].

Radical photopolymerisation of hybrid materials

This work has concentrated on development of hybrid class 2 materials, based on the photoreactive ORMOSIL® precursor 3-methacryloxypropyltrimethoxysilane (MAPTMS, Assay 99% in methanol, Aldrich), the chemical structure of which is shown in Figure 2-26.

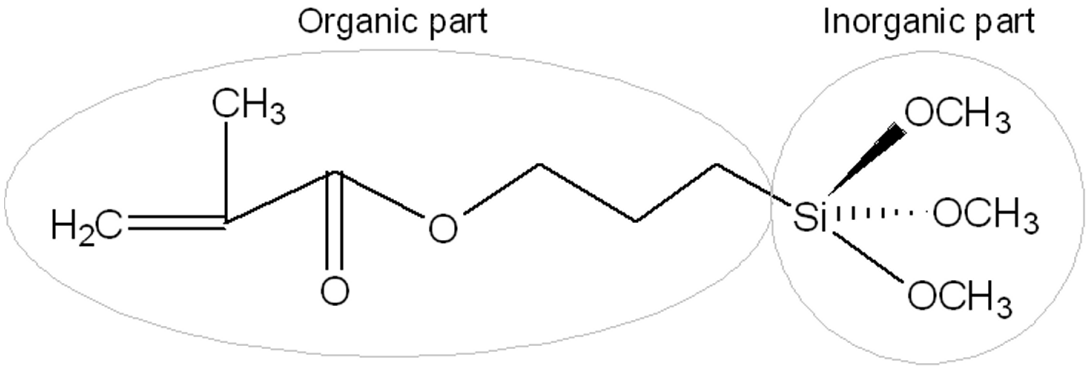

Figure 2-26: Chemical structure of MAPTMS

This precursor has a double capability of reaction. First it can react via sol-gel process to form a 3D network of hybrid nanoparticles via hydrolysis and condensation reactions of the silane based groups. Second via radical photopolymerisation of the methacrylate functionality to from linear chains embedded within the 3D inorganic network, upon UV-irradiation. This property of photoreactivity is essential for the fabrication of optical waveguides by selective UV-irradiation. The photochemical mechanisms, by which the organic groups of MAPTMS are cross-linked upon UV irradiation, are described in the following Section.

As mentioned in previous Sections, the organosilane precursor MAPTMS is used for sol-gel synthesis in this work because, in presence of a photoinitiator, the resulting sol becomes photopolymerisable/photocurable. Photoinitiators can be defined as molecular systems that contain chromophores which through a light absorption process can generate active species able to initiate the polymerisation and cross-linking of mono and multi-functional monomers and oligomers [221]. This photocurability allows the formation of fully reticulated regions by selective UV-irradiation of a thin film of the sol-gel material. The organic part of the MAPTMS molecule is involved in the photoreaction, specifically the methacrylic group (carbon double bond). A typical reaction mechanism is shown in Figure 2-27 (using the

photoinitiator Irgacure-184 for illustration purposes), and involves three main steps: 1) initiation, 2) propagation, and 3) termination.

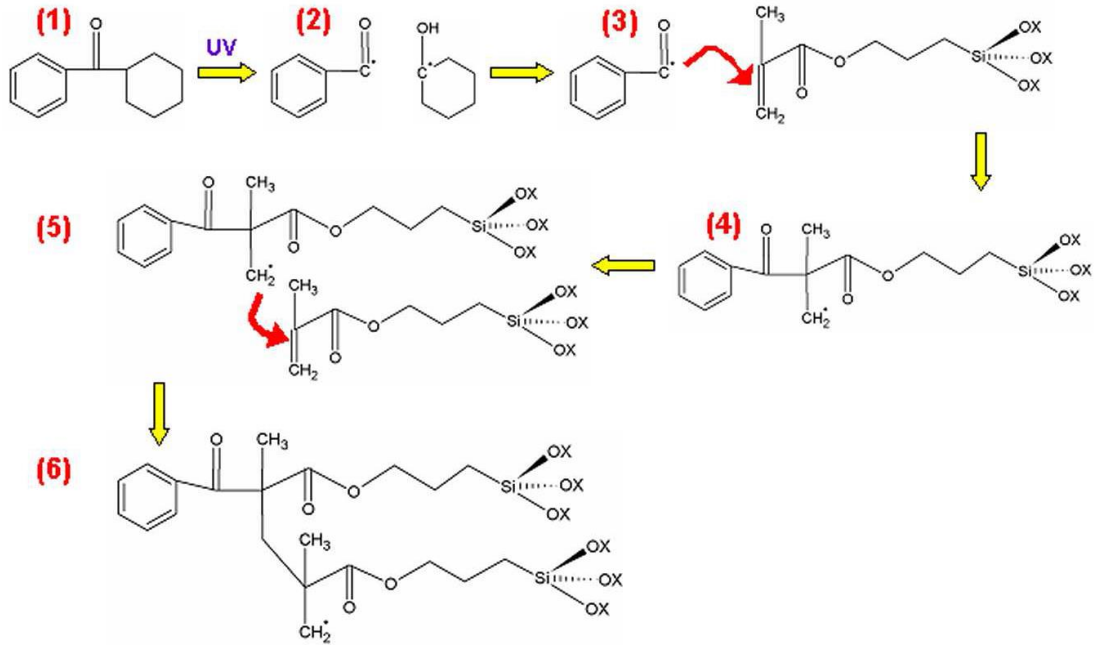

Figure 2-27: Schematic schemes explaining photoinitiator radical formation and reaction with MAPTMS under UV exposure

Initiation starts in Step 1 with the UV irradiation of the photoinitiator, progressing to step 2 which shows the UV-induced splitting of the photoinitiator (photolysis or haemolytic scission) to create two radicals. Radicals are defined as atomic or molecular species with unpaired electrons on an otherwise open shell configuration, and have extremely high reactivity [221]. In step 3, one of the radicals produced is in close proximity with the MAPTMS molecule, with the arrow indicating the methacrylic bond which the radical is able to break. The start of propagation is shown in step 4, where the radical has broken the methacrylic bond of MAPTMS, thus creating a larger radical molecule. In step 5, propagation continues as this larger radical is pictured in proximity to another MAPTMS molecule where it can once again break a methacrylic bond in order to form an even larger radical (shown in step 6). This process will continue until it is terminated by reaction with another radical (either one of the photoinitiator fragments from step 2, or another large radicals like itself) or by cessing the UV – irradiation process. In this way, UV – exposure of the sol-gel thin film causes crosslinking of the organic components of the network, notwithstanding the inorganic network which is already formed to an extent which

depends upon the sol aging time. The cross-linked parts of the film are now quite durable even when immersed in alcohol, while the unexposed parts are readily rinsed away by alcohol. In this way, various structured patterns, such as ridge channel waveguides, can be formed.

2.4.4 Application of Hybrid Sol-gel Materials

Sensing

Sensors are defined as "devices that confer continuous and reversible monitoring of physical parameters, or of the concentration of chemical or biological target analytes" [222] . In many facets of daily life, sensors are becoming rapidly integrated, such as wireless motion sensors for security, force sensing technology in video games and sensors monitoring of chemical and biological environmental pollutants and in indoor air quality. According to the method of transduction, different types of sensors are classified into mechanical, electrochemical or optical. In optical sensing, further classification can be made based on the sensing principle employed.

Direct optical sensors are used when an intrinsic physical property of an analyte, such as absorption at a particular wavelength or refractive index, changes as a result of alteration in the concentration of the analyte [60]. While, reagent-mediated sensor platforms use reagent, such as a fluorescent label, to signal the presence of an analyte e.g.: the detection of molecular biorecognition by means of fluorescently labelled probe molecules [223]. Both direct and reagent-mediated sensor platforms, developed herein, are based on hybrid sol-gel PLCs. The direct sensing platforms are called refractometric, by measuring extremely small changes in refractive index of the medium in the sensing region. On the other hand, the reagent-mediated sensing format focuses on the development of a fluorescence-based sensing platform for multianalyte biosensing.

Telecommunications

As mentioned previously, Planar Lightwave Circuit (PLC) research has been driven by the telecommunications sector throughout its history, only later branching into other applications such as sensing. With the increased demands for bandwidth from

todays consumers, optical fiber links are moving increasingly close to the end-user, with fiber-to-the-home (FTTH) being implemented in some countries such as Japan, South Korea, and the U.S.A. [224, 225].

The bandwidth bottleneck presented by the 'last mile' electrical links to consumers are mainly responsible for current limitations in telecommunications. Therefore, a shift to all-optical networks will eventually become a reality as demand continues to grow exponentially, driven by the internet, gaming, voice over IP (VoIP) and many other applications [225, 226]. Up until recently, signals in the optical network have typically been routed and regenerated by converting from the optical to the electrical domain (using photodetector), and then retransmitting the same signal into the appropriate output fiber for routing, or simply amplifying it for regeneration. These components are known as optical-electrical-optical (OEO) components. However, as the bandwidth increase beyond 10 Gbit/s the (OEO) begin to get more expensive, overly complex and suffer from huge power dissipation and thermal problems.

The solution to this problem is to process information entirely in the optical domain, using "all-optical" components to perform the same functions as the currently employed OEO components. Using the low-cost sol-gel materials and process to fabricate a thermo-optical switch which is activated by means of the high thermo-optic response of the sol-gel materials, may solve this problem.

2.5 Microfabrication Processes of Hybrid Organic-Inorganic Photoreactive Sol-Gel

2.5.1 Introduction

The objective of this work is to fabricate our Planar Lightwave Circuit (PLC) platform by photolithography microstructuration of hybrid organic-inorganic photoreactive sol-gel thin films. In this chapter the problems in relation with the thin film fabrication and the photolithography techniques are discussed from both a general point of view and with a particular emphasis to the materials aimed in this work.

2.5.2 Thin Film Fabrication

Dip-Coating

To develop a sample limited in one dimension with a high homogeneity, dip-coating lend itself well to this process. This is a key process largely used in the coatings industry, especially in the metallurgy industry (e.g hot dip-galvanisation of steel, anodisation of aluminium surfaces). This process involves two steps, as outlined in Figure 2-28

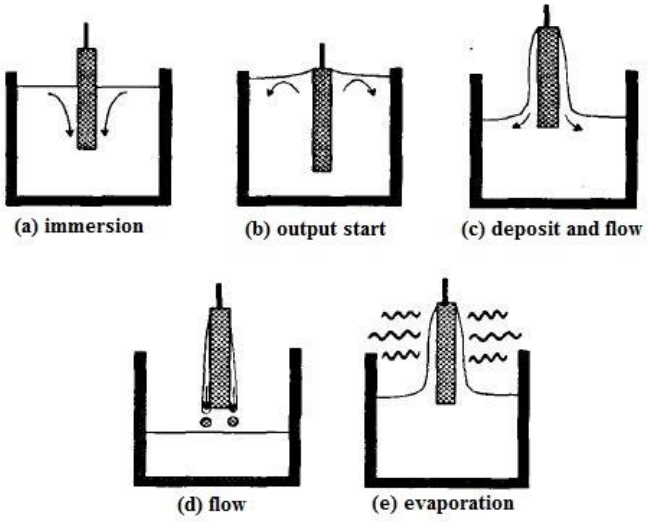

Figure 2-28: Steps of dip-coating process

The first step consists of immersing the substrate in the fluid. The second consists of withdrawing the substrate at a constant speed. Several parameters determine the thickness of the fabricated film (h), including the speed (U), the liquid-vapour surface tension (γ_{LV}), the density (ρ) and the viscosity (η). An equation correlating these different parameters has been empirically established:

$$h = 0.94\frac{(\eta U)^{\frac{2}{3}}}{\gamma_{LV}^{\frac{1}{6}}(\rho g)^{\frac{1}{2}}} \qquad (2\text{-}68)$$

In this equation, g is the acceleration gravity and it can be clearly seen that as most of the other parameters are fixed for a given fluid. The main factor governing the thickness is the withdrawal speed. The faster the withdrawal speed is the thicker will be the coatings on a given substrate.

To simplify this, the forces acting on the film during the process can be divided into two opposing set of forces, as outlined in Figure 2-29.

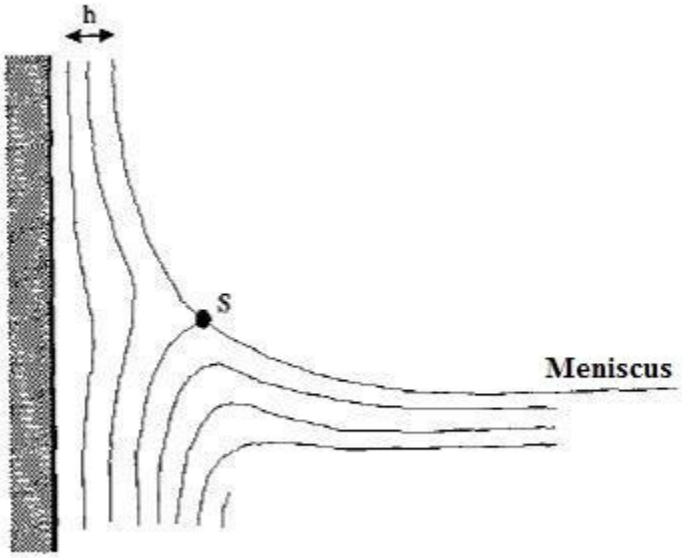

Figure 2-29: Flow of fluid during removal of the substrate

Forces that tend to keep the fluid on the substrate and those that resist movement of fluid from the substrate, which is the fluid viscosity. The other forces are the gravitational force and the viscous drag of the contain these tend to drag the fluid from the substrate.

Sol-gel materials are systems that react with ambient atmosphere to further pursue the hydrolysis and condensation reactions. Obviously, during the deposition process, the first areas to be employed to the ambient atmosphere will react condense while the remaining part of the substrate is still in its unreacted form, as seen in Figure 2-30.

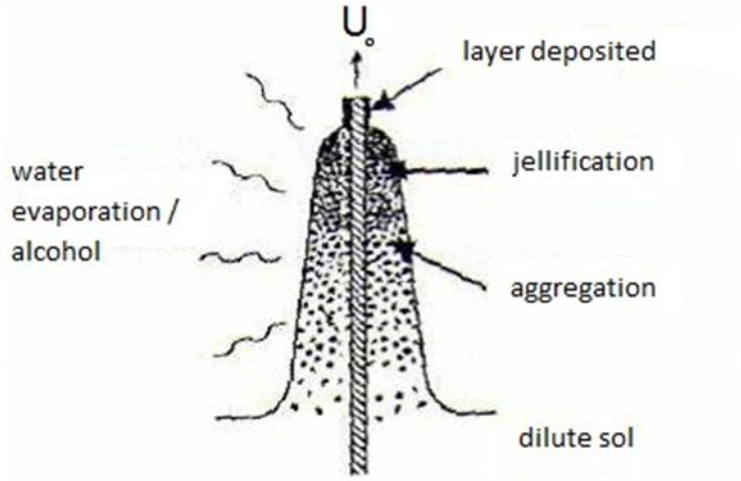

Figure 2-30: Hydrolysis and condensation reactions

This means that in order to form a fully compact and homogeneous coating, the withdrawal speed will need to be sufficiently elevated to minimise the heterogeneity of the coatings. More critically, as the condensation relies on the ambient atmosphere, this means that a reproducible control of the coating thickness will be difficult to achieve for sol-gel materials, as a strict control of the ambient surrounding humidity is required. Thus, the general equation shown above does not strictly apply to sol-gel systems as it does not consider the occurrence of the gelation process.

Spin-Coating

The main advantage of the spin-coating technique is that it is ideally suited to coating of circular substrate such as wafers. This technique is commonly used to produce a uniform deposition of photoresist materials on the wafer in the semiconductor and photonics industries. This process can be divided into four stages: the first stage is deposition which involves dispensing an initial volume of sol in the centre of the substrate. The second stage is spin-up represented, when the liquid is driven radially from the centre covering the whole surface of the substrate. A third stage is where excess sol is driven off the surface by water flowing to the wafer edge and forming droplets. Finally the fourth stage is evaporation which refers to the thinning of the film even after radial outflow of fluid has ceased [227]. Meyerhofer's equation (2-69) shows the parameters that control the final film thickness (h_f) can be achieved by spin-coating, by controlling the flow and evaporation characteristics of the sol.

$$h_f = c_0 \left(\frac{3\nu\epsilon}{2(1-c_0)\omega^2} \right)^{\frac{1}{3}} \qquad (2\text{-}69)$$

Where, C_0 is the initial concentration of solids in the liquid, ν is the viscosity, ϱ is the rate of evaporation, and ω is the angular velocity. The important point to note here is that film thickness decreases for increasing spin speed, as $h_f \propto \omega^{\frac{2}{3}}$.

As mentioned in the case of the dip-coating the complicated behaviour of sol, here also in spin-coating evaporation plays a slightly more complicated role because the evaporation phase strongly overlaps with the spin-off stage [228].

2.5.3 Microstructuration Processes

Standard Photolitography

Photolithography is the process by which surface relief structures are formed in a photosensitive thin film of material by means of exposure to electromagnetic radiation. This is a well-known process largely used in the semiconductor industries. This process involves selective irradiation of the thin film by employment of photolithography mask.

Figure 2-31 illustrates the three main types of photolithography techniques [229];

- **Contact photolithography** – where the mask is in direct physical contact with the surface of the thin film.
- **Proximity photolithography** – where the small gap (z) in the order of micrometers is kept between the mask and the thin film.
- **Projection photolithography** – where an optical projection system is used to demagnify the image produced by the mask to achieve smaller feature sizes on thin film.

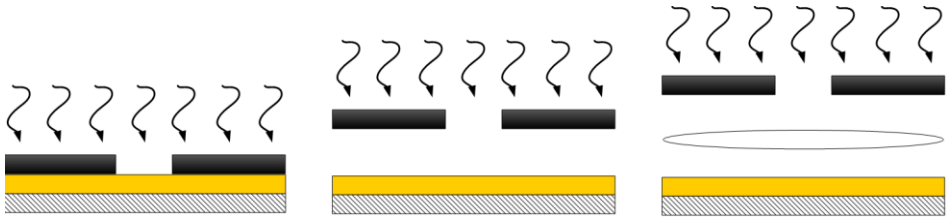

Figure 2-31 : Schematic diagram of a) contact, b) procimity and c) projection photolithography

The photosensitive thin films are either positive-tone, or negative-tone depending upon their behaviour on irradiation [230]. The difference is illustrated in Figure 2-31 where, after irradiation, positive-tone films can be etched away in areas exposed while the unexposed areas remain. The opposite is the case for negative-tone materials, i.e., on irradiation they typically polymerise so that the irradiated areas remain and the unexposed areas are removed when etched. Photolithography is an essential microfabrication tool for many technological industries. In this case, the photosensitive films used to construct microprocessors are called photoresists and commercial photoresists have been used in this work. However, photolithography have been employed in conjunction with a class of photosensitive materials

developed in our laboratory known as hybrid sol-gel materials, for the fabrication of planar lightwave circuits.

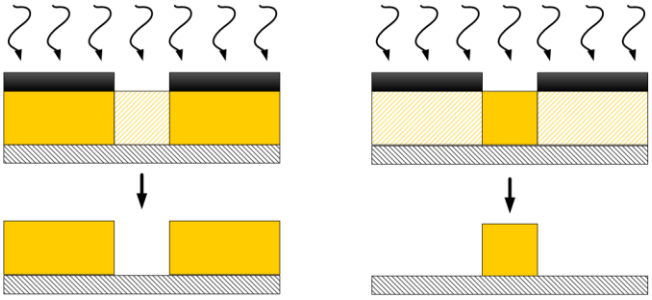

Figure 2-32: Selective UV irradiation of; a) positive-, and b) negative-photoreactive thin films.

Sidewall Verticality

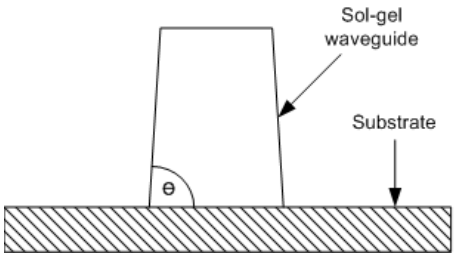

Figure 2-33: Sidewall slope

Photolithography can be used for optical waveguide fabrication. Therefore, the slope of the sidewall of the photolithographic feature is very important, as changes in the waveguide cross-sectional structure will changes the optical properties of the waveguide. Since all waveguides have been modelled assuming a square cross-sectional structure, the aim of the photolithography process is to match this as closely as possible. The sidewall slope of a feature is defined as an equation (2-70) [231]

$$\tan(\theta) = \frac{dT}{dx} \qquad (2\text{-}70)$$

Where, θ is the sidewall angle as illustrated in Figure 2-33 and T is the thickness of the thin film (i.e. the distance from the substrate to the top film). T can vary between zero and the initial thin film thickness, depending upon the level of crosslinking of the material, which is directly related to the UV exposure dose. Equation (2-70) can be expressed as,

$$\frac{dT}{dx} = \frac{dT}{dD}\frac{dD}{dx} \tag{2-71}$$

With D the exposure dose defined as,

$$D(x) = I(x)t \tag{2-72}$$

Where, I(x) is the intensity distribution and t is the exposure time. Equation (2-71) allows convenient separation of the terms dictating the resist profile, where dT/dD is a characteristic only of the sol-gel thin film (encompassing photo-reactivity and processing conditions), and dD/dx is solely determined by the light intensity distribution in the thin film (which is a function of the photomask feature size and the optics of the exposure system). This equation clearly demonstrates how the material properties and the exposure optics interact in the formation of features that have sidewalls with a high degree of verticality.

Material contrast

The first part of equation (2-71) above is related to the contrast of the sol-gel thin film. Figure 2-34 the relationship between the thicknesses of a thin film polymerised in response to different UV exposure doses is shown for a typical negative photoresist (analogous to sol-gel).

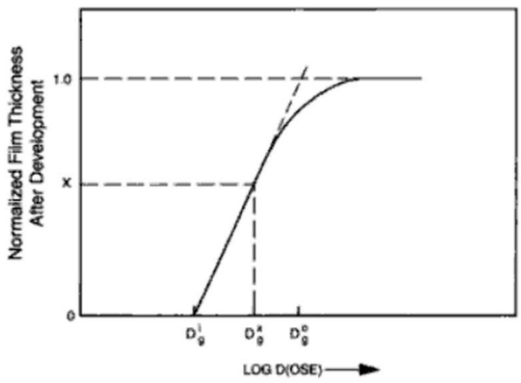

Figure 2-34: Determination of the contrast of a negative-tone photoresist/sol [230].

Using Figure 2-34 the contrast of the film (γ) is defined as the lope of the graph [230] (dT/dD) such that,

$$\frac{dT}{dD} = \gamma = log \frac{D_g^i}{D_g^o} \quad (2\text{-}73)$$

Where D_g^i is the critical exposure dose corresponding to the onset of crosslinking and D_g^o is the exposure dose required to reach 100% of the initial film thickness.

Two-Photon Polymerisation

The principle of 2-Photon-Polymerization (2PP) was demonstrated for the first time in 1997 [232]. Originally developed from multi-photon microscopy, during the last 10 years 2PP became an important microfabrication technology representing interdisciplinary efforts of physicists, engineers and chemists. 2PP with tightly focused femtosecond laser pulses is an easily scalable process allowing the fabrication of structures with a feature resolution, depending on focusing optics, in the range of 100 nm - 100 μm. 2PP is the only true 3-dimensional technique providing unprecedented freedom in the structural design. This is a unique advantage compared to other micro- and nano-structuring technologies. Using femtosecond laser pulses it is also possible to inscribe structures into a solid monomer and to achieve guiding of light by the change of the refractive index induced by polymerization [233, 234]. A recent collaboration between the National Centre for Sensor Research at Dublin City University and the Laser Zentrum Hannover (LZH) have investigated the 3D microstructuration of photocurable hybrid sol-gel materials. They have shown that in comparison with organic monomers non-shrinking 3D microstructures can be achieved with no additional mechanical compensation and have attributed this difference to the presence of inorganic moieties that can rigidify and strengthen the organic backbone fabricated by photopolymerization [235, 236]. Examples of such non-shrinking microstructures are shown in Figure 2-35 and Figure 2-36.

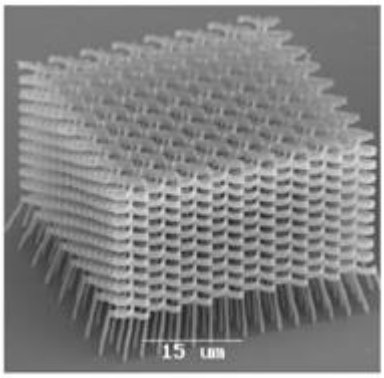

Figure 2-35 : Spiral 3D photonic crystal [6].

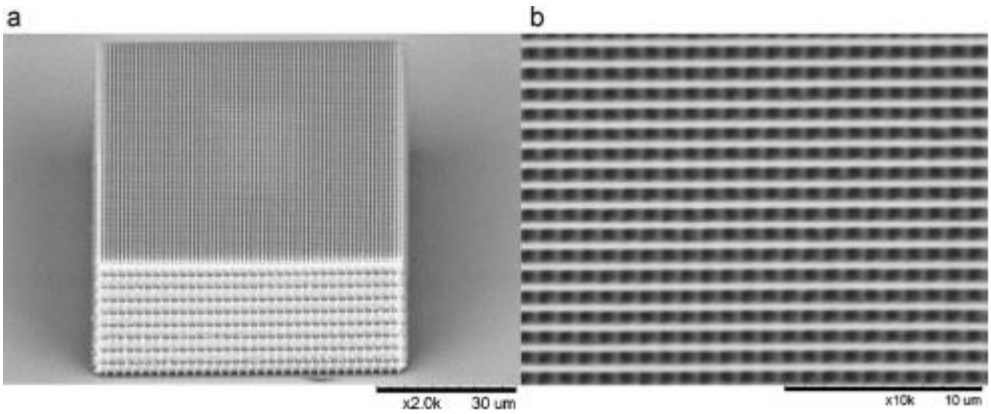

Figure 2-36 : Three-dimensional 70_m×70_m×35_m size woodpile structure fabricated with the 2PP technique. (a) 45° sideview; (b) topview. Average laser power used was 260μWand scanning speed of 200μm/s [237].

The 2PP has been demonstrated in a few labs around the world as a well working scientific tool for the fabrication of micro- and nanostructures. Nevertheless there has been no commercially available system for the fabrication of 2PP structures until 2006. At the end of 2006 the first commercial systems for 2PP has been developed and presented by the LZH [237]. Ti:Saphire-Lasers with a pulse duration of approximately 200 fs working in the near-infrared spectrum range (at 800 - 700 nm) were used for 2PP and 3-D material processing. Up to now several femtosecond laser systems are available. These systems show sufficient energy stability and output power required for research applications of the 2PP technique. For the industrial implementation of 2PP technology, more powerful systems suitable for the industrial production environment are needed. The basic set-up for a 2PP-system is depicted in Figure 2-37.

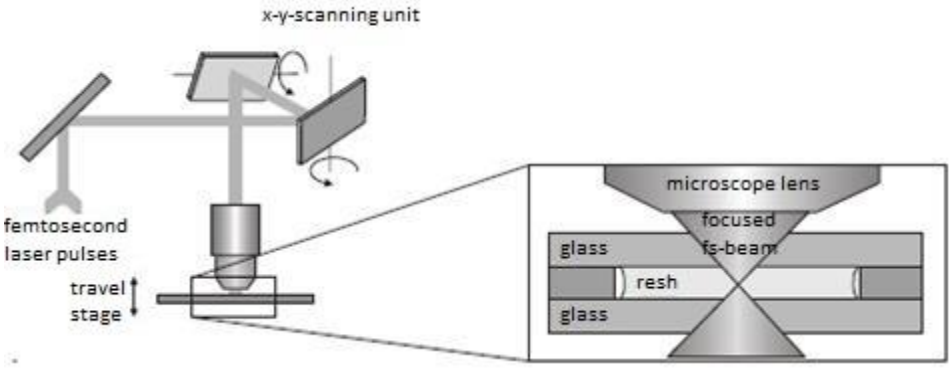

Figure 2-37 : Basic set-up for a 2PP system.

Chapter 3

Materials and Methods

3.1 Biosensor Fabrication Technology

3.1.1 Thin Film Photolithography Processing

Two techniques were employed for planar lightwave circuits and sensor windows fabrication: (1) the deposition of photoreactive sol-gel thin films by spin-coating deposition and (2) the UV-patterning of the optical waveguides and sensor windows. Intermediate steps including curing of the coatings are also described as shown in Figure 3-1. The general procedure for the waveguide fabrication consists of the following steps:

1. **Deposition and stabilisation of a buffer layer**.

   The role of the buffer layer is to act as a lower cladding layer, thus providing both mechanical and optical isolation to the subsequent optical waveguide core. As explained in section 4.2.1, the buffer layer is selected so that the refractive index contrast with the waveguide core can be thoroughly controlled to allow singlemode propagation of the light. For this reason, Material O has been selected for the fabrication of the buffer layer. The full stabilisation of this material was investigated in section 4.1.2 and found to necessitate UV irradiation for 600 s. However, the thickness of this layer has to be further optimised to minimise any attraction of the propagating light towards the substrate, thus avoiding any loss that would dramatically alter the sensing performances of our platform.

2. **Deposition of the guiding layer.**

   Optimisation of the deposition and fabrication condition of this layer is central to the success of this research as it is from this layer that the core of the waveguide was developed.

3. **Thickness optimisation and UV – patterning of the guiding layer**.

In addition to the refractive indexes of this layer (characterised in section 4.2.1), the critical parameters to identify here are the thickness and the dimension of the patterned waveguides.

4. **Etching of the guiding layer.**

   Following the selective UV-irradiation of the guiding layer, the etching of the guiding layer can be performed by employing an alcoholic solvent (ethanol, propanol or butanol).

5. **Deposition of the protective layer.**

   Having fabricated both the upper cladding and the core of the optical waveguide, the next step consists of providing a symmetrical refractive index contrast all around the core of the waveguide. For this purpose, the deposition of a protective layer is performed employing the exact same material as used for the fabrication of the buffer layer. Unlike the buffer layer, the deposition conditions for the protective layer have to be optimised so that a thickness of at least 3 microns can be deposition on top of the core of the waveguides to ensure full covering and optical isolation from the upper environment. However, as the upper environment is expected to be water-based, with a refractive index less than 1.4, the thickness is not required to be as high as that of the buffer layer.

6. **Etching of the sensor spots and full stabilisation of the protective layer.**

   The sensor spot fabrication and the stabilisation of the protective layer are performed simultaneously by selective irradiation using a photomask. A chromium photomask has been designed to cover areas of the protective layer to render accessible the surface of the waveguide core. This selective irradiation is performed using the same conditions as used for the stabilisation of the buffer layer. Importantly, as it has been shown that the refractive index is stable above 600s of irradiation, this further UV – exposure will not alter the optical properties of the lower cladding and the core of the optical waveguide. Following this stabilisation, the sensor spots were etched employing isopropyl alcohol.

7. **Deposition and stabilisation of the high refractive index layer.**

The final step consists of spin-coating the HRIL at a given speed to achieve the desired thickness. A thermal curing at 110 ºC for one hour finalise the fabrication of the biosensor platform.

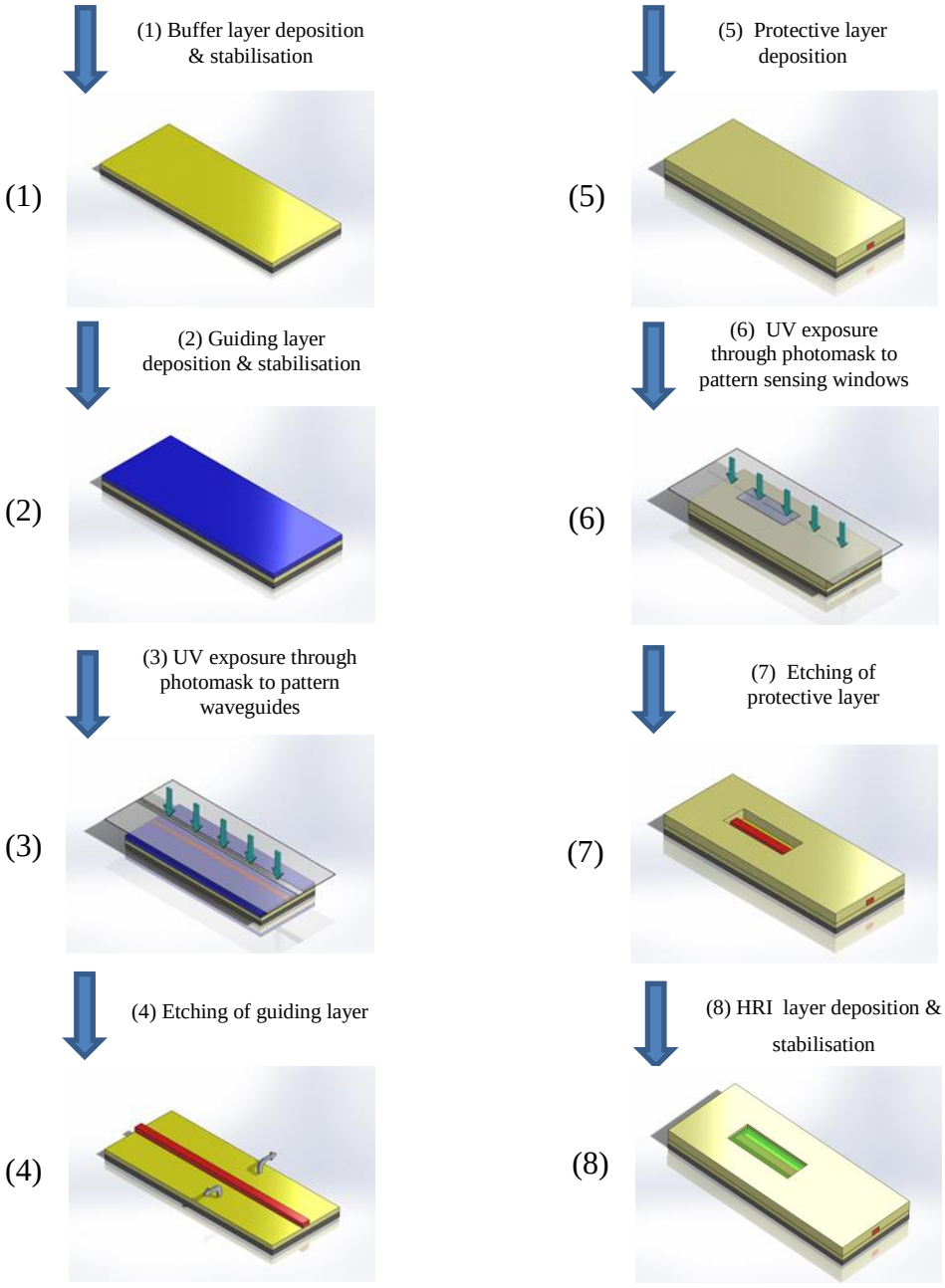

Figure 3-1: Fabrication process for biosensor chip including, optical waveguide processing and patterning of sensing windows.

3.1.2 Effect of the UV – irradiation time

Having established the deposition conditions to achieve the desired thicknesses for the lower cladding layer and the guiding layer, the next step consisted of defining the

UV-irradiation parameters to fabricate waveguides with widths as close as 6 microns, as per the simulation studies. To do this, the PLC patterns have been microstructured employing a mask aligner and photomasks designed accordingly, as represented in Figure 3-2.

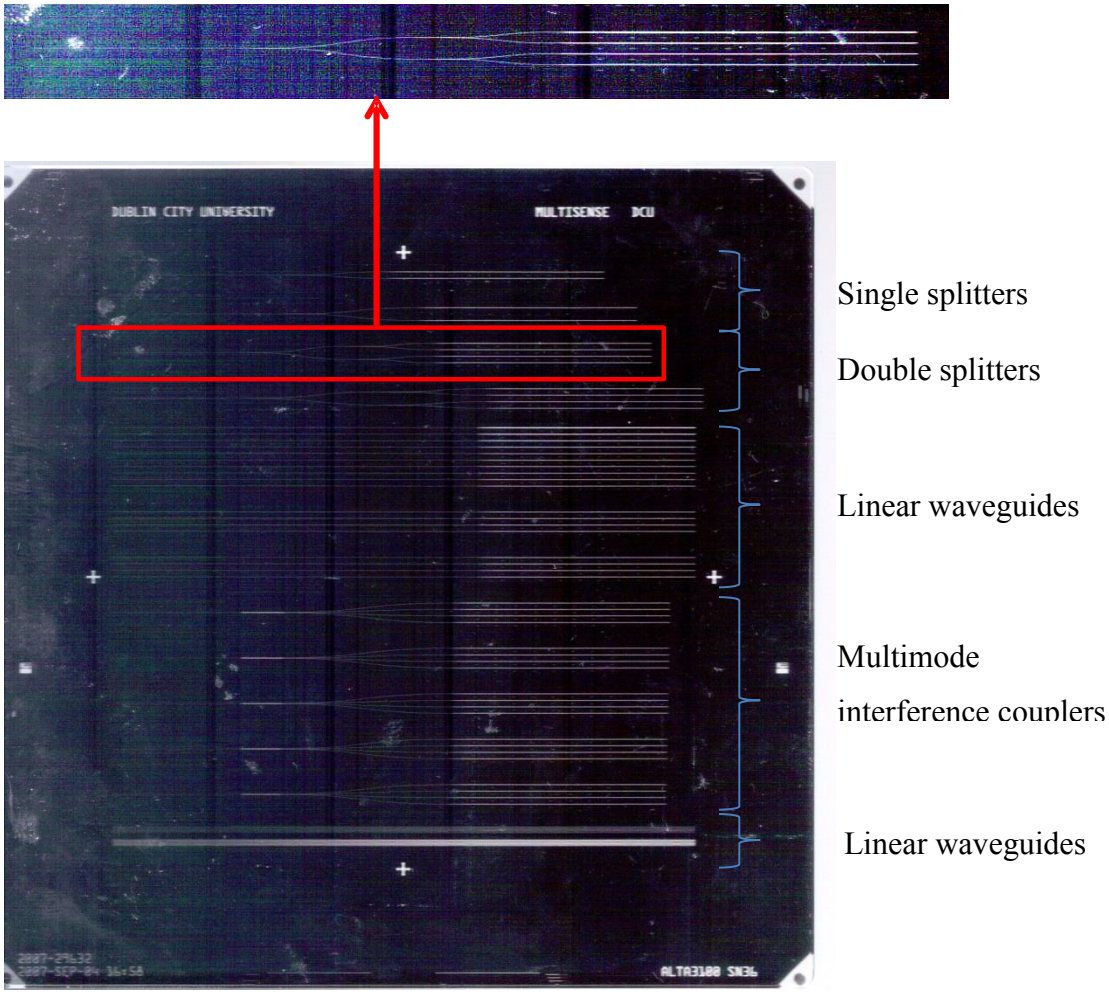

Figure 3-2: Photomask employed in the photolithography processing of PLC platform.

3.1.3 Optical Bench Set-up

The biosensor platform was characterised using the experimental set-up shown in Figure 3-3. Light was emitted into the single-mode input waveguide by an end-fire coupling from a pigtailed laser diode with maintained TE polarization (Thorlabs, λ = 639 nm), with a relative alignment of waveguide and fibre assisted by a microscope positioned above. Light was collected from the out-put waveguide of the platform by

a microscope objective lens and focused onto a photodiode detector (Thorlabs DET210) for quantification. The read out from the photodiode was handled by a Device Automatic Alignment System (DALi, Elliott Scientific) which was interfaced with a PC for real-time signal acquisition via a National Instruments DAQ card.

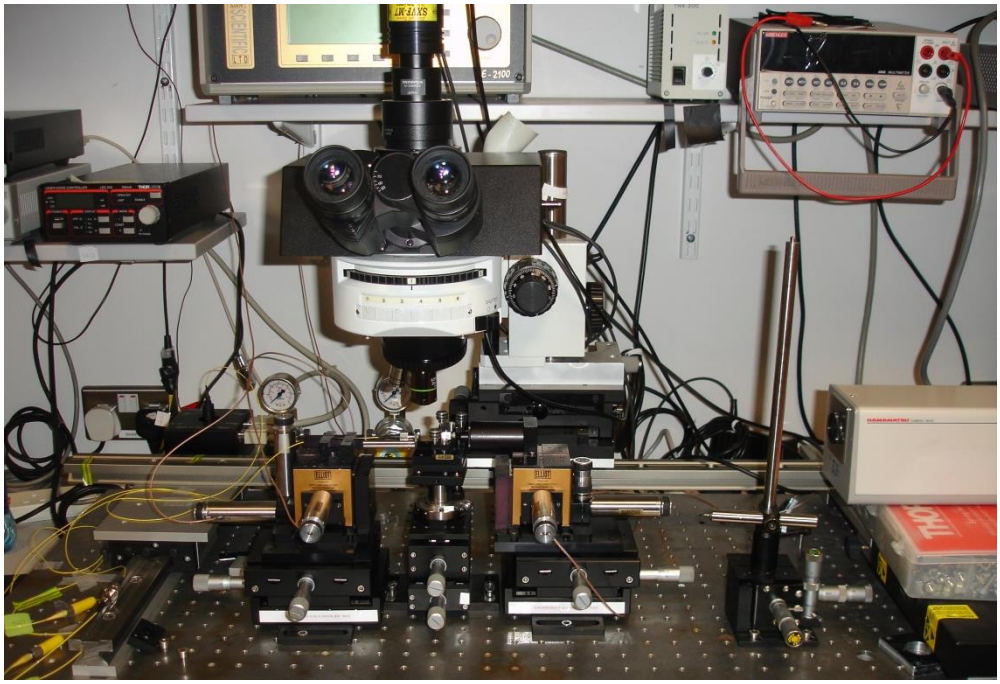

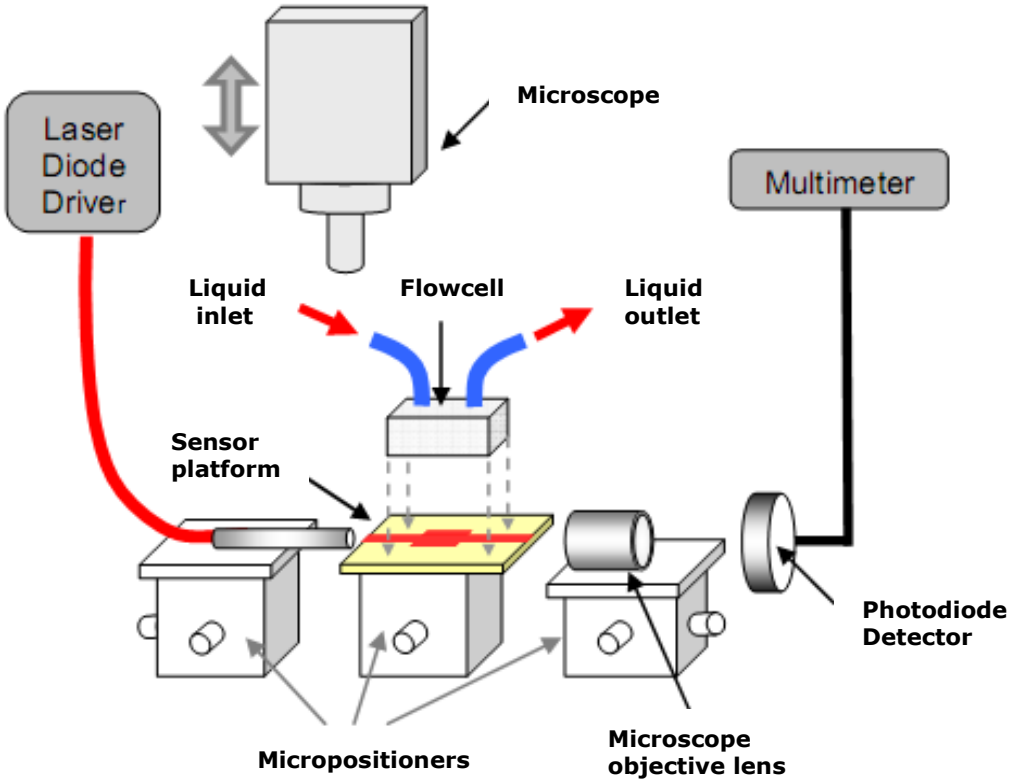

Figure 3-3: Experimental set-up for the characterisation of the biosensor platform.

3.1.4 PLC Fabrication Instruments

Spin Coater

Spin-coating of all thin films were prepared on glass and silicon substrates using a Laurell WS-650S® spin-coater

Figure 3-4). The sol-gel materials were spun at 1000 rpm under an alcohol saturated environment. The purpose of spin-coating in this environment was to control the kinetics of evaporation of the solvents during the deposition process, thus obtaining high optical quality and homogeneous thin films. For this purpose, the spin-coater was adapted to receive alcohol saturated N_2 which was produced by flowing N_2 through sealed flasks containing isopropanol.

Figure 3-4: Laurell WS-650S® spin-coater

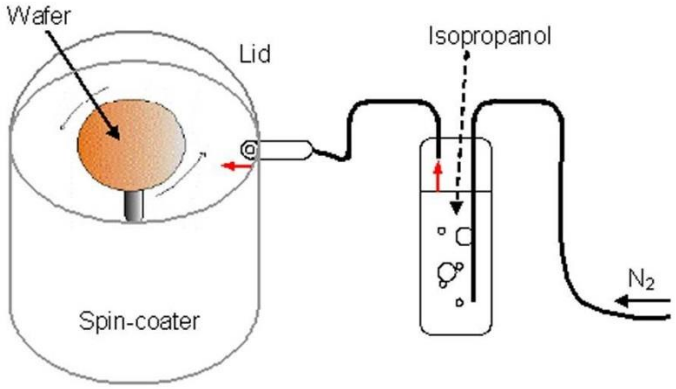

Figure 3-5: spin-coater set-up with isopropanol vapor generation in the chamber.

The introduction of N_2 into the spin-coater significantly reduce the levels of atmospheric humidity present during spin-coating (relative humidity is typically reduced to <10%), thus inhibiting the formation of a surface gel layer during spinning by rapid hydrolysis and condensation reactions on the surface, which is another cause of coating defects.

All deposition and fabrication conditions were performed in a clean room environment (10000 class clean room). The general procedure for the deposition of the sol-gel materials involved the filtering of the above solutions through a 0.2µm Teflon filter prior to spin-coating. This was essential to avoid the presence of undesired large particles that could have contaminated the sol-gels during the materials preparation, which may affect the propagation of the light within the final optical waveguides and therefore its optical characteristics.

In order to minimise surface roughness due to inhomogeneous drying of the coating during the spinning process, the spin-coater was adapted to receive vapour alcohol saturated nitrogen which was produced by flowing nitrogen through sealed flasks containing isopropanol, as illustrated in Figure 3-4 and Figure 3-5.

This technique, previously described, allows the elimination of the residual humidity in the spin coater, responsible for the fast gelation and formation surface skin and can dramatically increase the surface quality and homogeneity of sol-gel coatings [238].

Mask Aligner

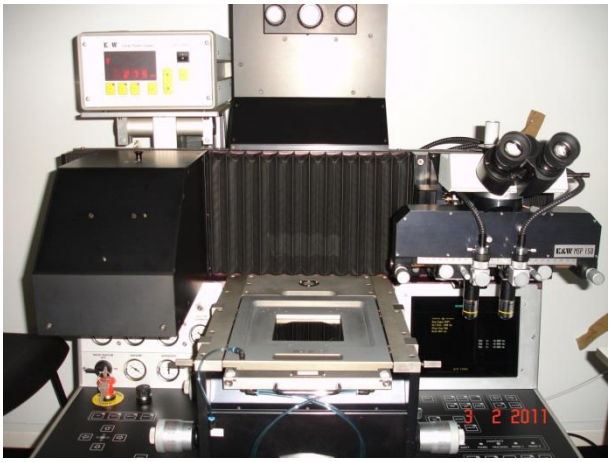

Figure 3-6: KARL SUSS MA 1006 mask aligner

Throughout this work, the UV Mask-Alignment system (KARL SUSS MA 1006) shown in Figure 3-6 was employed. This can operate in both contact and proximity mode. The mask aligner was used in contact mode in order to maximise the resolution and fidelity of the transferred pattern. The UV light source is a mercury lamp the spectrum of which was shown in Figure 3-7. The effect of a i-line filter is evident, which is fitted so that exposure was confined to a UV band centering on 365 nm.

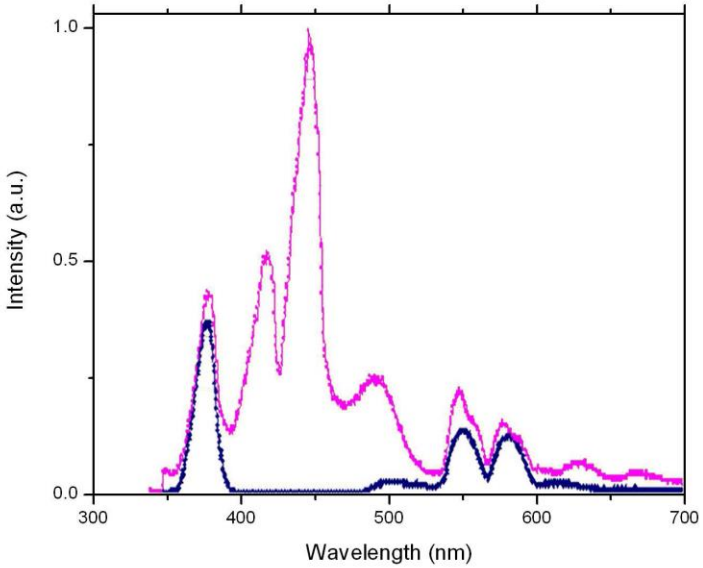

Figure 3-7: Emission spectrum of the mercury lamp of the mask aligner with (blue) and without an i-line filter (red)

Hot Plate

Hot plates were used to thermally stabilise the fabricated coatings. Typical stabilisation was performed in the range 100 – 120 ºC. For this purpose hotplates fitting 10cm diameter silicon wafers were used, as shown in Figure 3-8. Such hotplates are specially designed for a full contact between the back surface of the wafers to ensure homogeneous and full thermal distribution all over the hybrid materials.

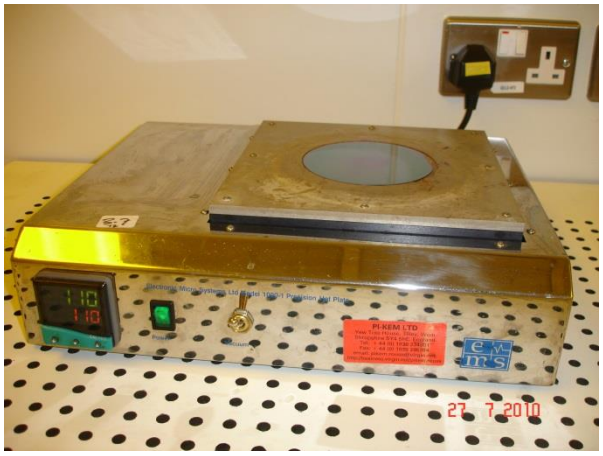

Figure 3-8: Hotplates used for the thermal coating stabilisation.

3.1.5 Tools for Sol-Gels and Thin Film Characterisation

Dynamic Light Scattering

Sol–gel particle sizes were determined using a Malvern Nano-ZS instrument (Figure 3-9), using the dynamic light scattering (DLS) technique. The technique is a well-established optical method used to study dynamic processes of liquids and solids. Prior to analysis, the sol-gels were filtered using a 0.2micron teflon filters and diluted in a 1/10 ratio in absolute isopropanol. Experiments were conducted at ambient temperature.

Figure 3-9: Malvern Nano-ZS instrument used for the particle size analysis of the sol-gels.

Thermogravimetric analysis and differential scanning calorimetry

Thermogravimetric Analysis and Differential Scanning Calorimetry were performed using a DTG – 60 SHIMADZU set-up (Figure 3-10). Samples were prepared by dropping 10 µl of the liquid sol-gel into aluminium sample pans and curing at 100 °C for 1 h in an oven. All calorimetric measurements were carried out between 50 °C and 500 °C in open pans under ambient atmosphere at a heating rate of 10 °C per minute.

Figure 3-10: DTG – 60 SHIMADZU used for the thermal characterisation of the sol-gels.

Prism Coupling Method

Refractive index values for the photocurable sol-gel materials were determined on spin-coated thin films using the prism-coupling method (also known as m-lines technique) at 632.8nm. Using this technique, a refractive index measurement accuracy of ± 0.0005 was achievable, the operating principle of which is sketched in Figure 3-11. Refractive index values were measured for TE modes. For all measurements, the modes were comprised within the measurement accuracy and the values reported in this work are averages of the TE and TM results. The prism coupling instrument used in this work is the Metricon 2010 and is shown in Figure 3-12.

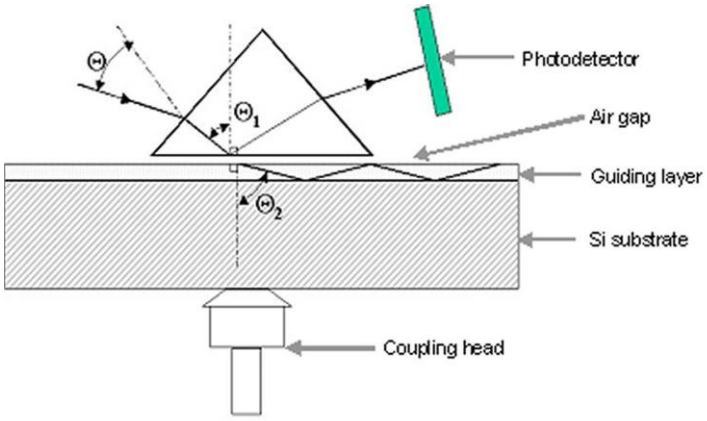

Figure 3-11: Principle of the refractive index measurement by prism-coupling method.

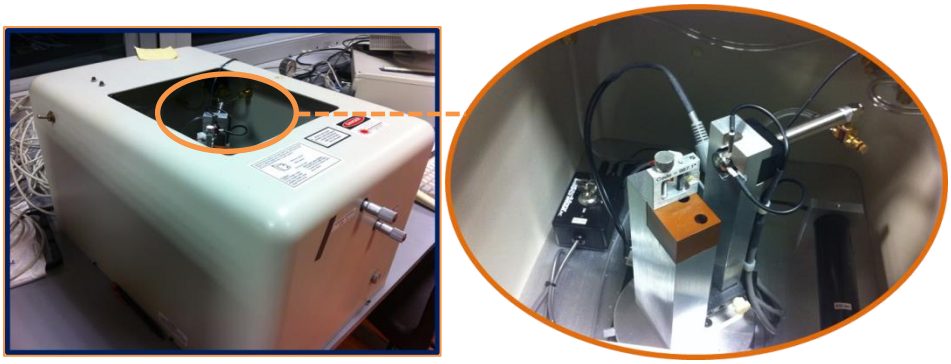

Figure 3-12: Metricon 2010 instrument used for the prism-coupling method.

Ellipsometry

Optical measurements including refractive index and optical transmission of the high refractive index (HRI) materials were performed using ellipsometry (Figure 3-13) in order to determine the performance of the developed materials. Ellipsometry measurements were conducted over the 400-900 nm spectral range. Thickness and refractive index of the films were calculated using the Tauc-Lorentz model fitted to the ellipsometry data [239]. The interest of using the ellipsometry is to allow measurement of optical properties of thin films with sub-micron thicknesses, which the prism-coupling method is unable to achieve. The expected thicknesses for our HRI are located in the range 10 – 100 nm, as per the modelling studies described in section 3.3.4.

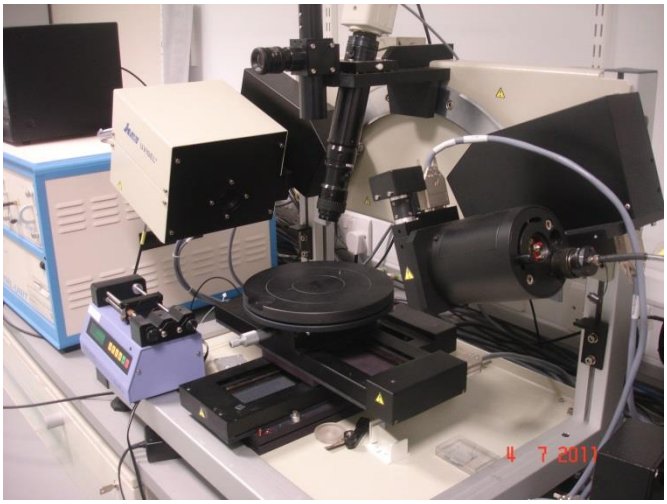

Figure 3-13: Ellipsometer

UV-Visible Spectroscopy

The UV-Visible (UV-Vis) spectroscopy technique was used primarily in order to characterise the evolution of the sol depending upon alterations to the synthesis. Chemical changes in response to these alterations were highlighted by shifts in the absorption spectra in the UV wavelength range in which these sol-gel formulations have been designed to react. The UV-Vis absorption spectra (200-800 nm) were obtained using a Cary Varian 50 scan spectrophotometer with a resolution of 4 cm^{-1}. The scan speed used was 600 nm per minute. In all cases, samples were prepared by sandwiching the liquid sol between two quartz films in order to obtain a film of 100 μm thickness.

3.2 Materials and Experimental Set-up

3.2.1 Sol-Gel Preparation

The initial synthesis of sol-gel was performed utilising molecular ratios of MAPTMS/ ZPO/MAAH of 10/4/4 in order to prepare a stable and homogeneous solution. The degree of hydrolysis of the overall alkoxide groups were investigated in the range 25 – 100%. The general procedure is presented in Figure 3-14.

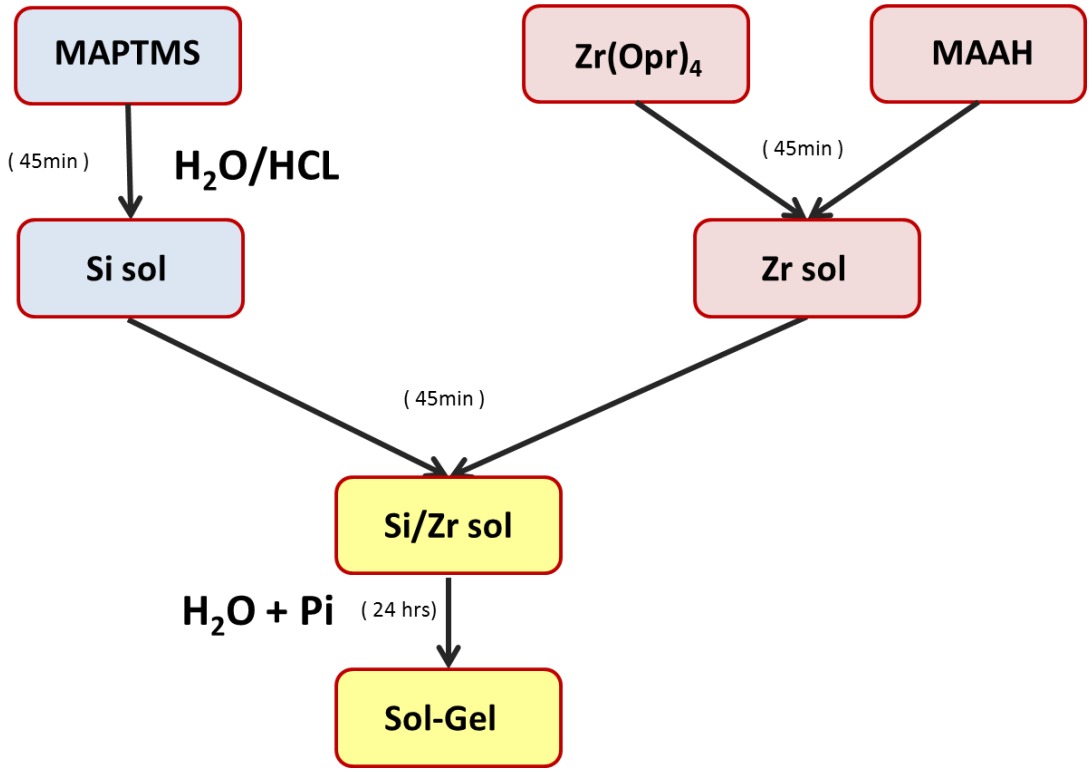

Figure 3-14: Sol-gel synthesis of the photocurable sol-gel material

MAPTMS was pre-hydrolysed with an aqueous solution (HCl 0.005 N), employing a 1.00 : 0.75 water to alkoxide molar ratio. Initially the solution shows two phases: the water in suspension within the MAPTMS. However, after 20 min of stirring, the solution became fully transparent. This was due to the occurrence of hydrolysis and condensation reactions that lead to the production of methanol that allows the miscibility of all species present in solution. Actually, here the methanol is both miscible in water and the MAPTMS, and as such can be defined as a co-solvent formed in-situ by the sol-gel reactions.

In parallel with this pre-hydrolysis, a second pot was used to chelate the ZPO by MAAH. These initial trials used a 1/1 stoichiometric ratio against both precursors as indicated in a previous study [240]. This was done to control the subsequent hydrolysis–condensation of ZPO and avoid the formation of any undesired zirconium oxide precipitate that would dramatically alter the initial ratio of organosilane and metal transition species. MAAH was used in ZPO as a chelating agent to bind with the zirconium atom through two oxygen atoms (Figure 3-15).

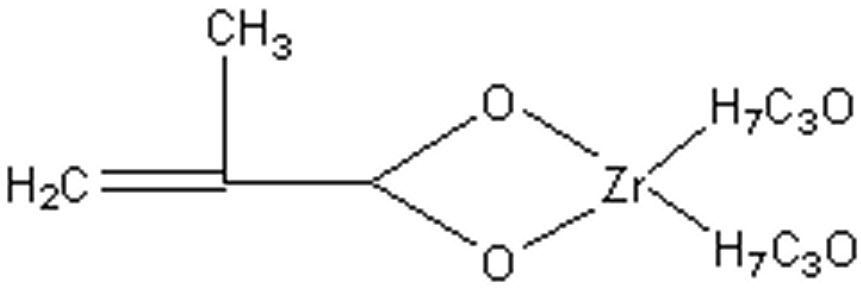

Figure 3-15: Structure of the ZPO/MAAH chelate.

After 20 minutes of reaction, the pre-hydrolysed MAPTMS solution was added drop-wise to the zirconium complex. Following 45 minutes of reaction, in order to improve the homogeneity of both molecular systems, a second hydrolysis employing water (pH 7) was performed leading to a hydrolysis of 50% of the total alkoxide groups. 5mol % of Irgacure 184 against the MAPTMS content was added to the sol to make the materials photoreactive under UV-irradiation. The final sol was left stirring for 24 hours before use. At the end of the synthesis development, the solution was found to be highly homogenous and transparent, suggesting that all the employed precursors are fully miscible and that the sol-synthesis has been performed successfully. The optimisation of this photocurable sol-gel material has to be

undertaken in parallel with the platform fabrication, in particular the coatings properties after deposition and UV-irradiation. Nevertheless, a clear increase in the viscosity of the solutions was observed with the increase of the degree of hydrolysis. More importantly, the sols prepared with hydrolysis degrees greater than 60% were found to be highly viscous and inadequate for the deposition of thin films, with thicknesses close to 5 microns. Therefore, these investigations focused on the solution prepared with a hydrolysis degree of 50%, as this was the one that provided the most promising results in terms of coatings homogeneity.

The deposition of this material by spin-coating led to a homogeneous coating. After deposition the coating was found to be slightly wet. Following a UV-irradiation of 600 seconds (details of the irradiation conditions are presented in section 4.1.2) this led to a touch-dry coating, suggesting that the photopolymerisation processes had taken place and resulted in a fully stable coating. The spin coated second layer did not show any inhomogeneity or cracking. However, the UV-irradiation of this second layer resulted in cracking. This result demonstrated that the multilayer integration poses a critical question on the interfacial tensions taking place in the hybrid sol-gel systems. Following these results, the strategy consisted of investigating routes in order to increase the flexibility of these sol-gel materials. The first hypothesis made considered that the observed cracks could be due to the high vitreous character of the material. One possibility to alter this property consists of reviewing the organosilane / zirconium complex ratio.

3.2.2 Development and Characterisation of Sol-Gel Materials

All materials utilised in this sensor fabrication were prepared employing the sol-gel synthesis method employing alkoxide and photoreactive precursors. As such they are spin-on processable and structurable via standard photolithography microfabrication. The following sections describe the synthesis of all required materials, including the photocurable hybrid organic-inorganic sol-gel material and the high refractive index sol-gel layer.

3.2.3 Photocurable Hybrid Sol-Gel Materials

Chemicals and materials

The precursors have been chosen so that the final material could be processed as thin films and fulfil simultaneously the following required microfabrication and sensor operating conditions:

- Viscosity – between those of water and light oils
- Photoreactivity – to enable photopolymerisation reactions in the UV-domain.
- Transparency in the visible and near infrared domain – to minimise the light absorption in this spectral range and avoid any misinterpretation of the biological systems influence on the measured output values.

For this, a material recently developed by researchers at the National Centre for Sensor Research at Dublin City University was identified that possibly could fulfil all essential conditions [241].

This material is based on the formation of a homogenous solution composed of a mixture of a photoreactive organosilane and a zirconium complex. The photoreactive silane is the 3-methacryloxypropyltrimethoxysilane (MAPTMS, assay 99% in methanol) and the zirconium complex was prepared by the chelation of zirconium(IV) n-propoxide (ZPO, assay ~70% in propanol) employing methacrylic acid (MAAH, $C_4H_6O_2$, assay ~98%, Sigma-Aldrich® Ireland) as chelating agent.

These precursors were all used as received without any further purification. The chemical formula of these precursors is presented in Figure 3-16.

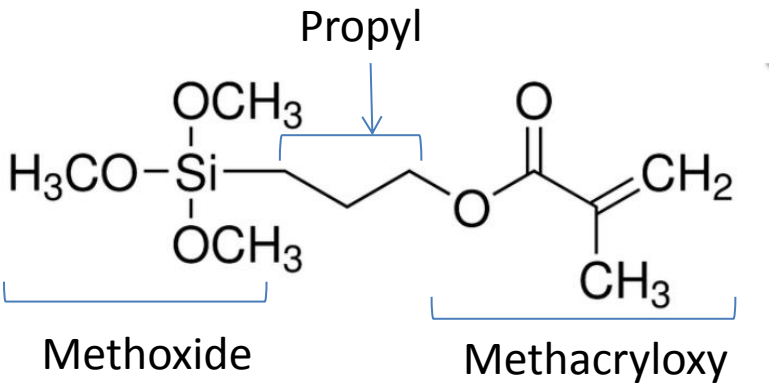

Figure 3-16: Reactive groups of MAPTMS

The MAPTMS is composed of two reactive groups at each extremity of the molecule (methoxide and metahacryloxy functionalities) separated by a chemically inert group

(propyl alkyl chain). The two reactive groups provide to this molecule (and to the subsequent final system) a double capability of polymerisation:

- Inorganically through the sol-gel polymerisation of the methoxide groups. The hydrolysis reactions will produce the formation of silanols groups (Si-OH), which will polymerise to from a 3D siloxane network involved by the polymerisation of silanol bonds. Sol-gel reactions that take place in this system are described below:

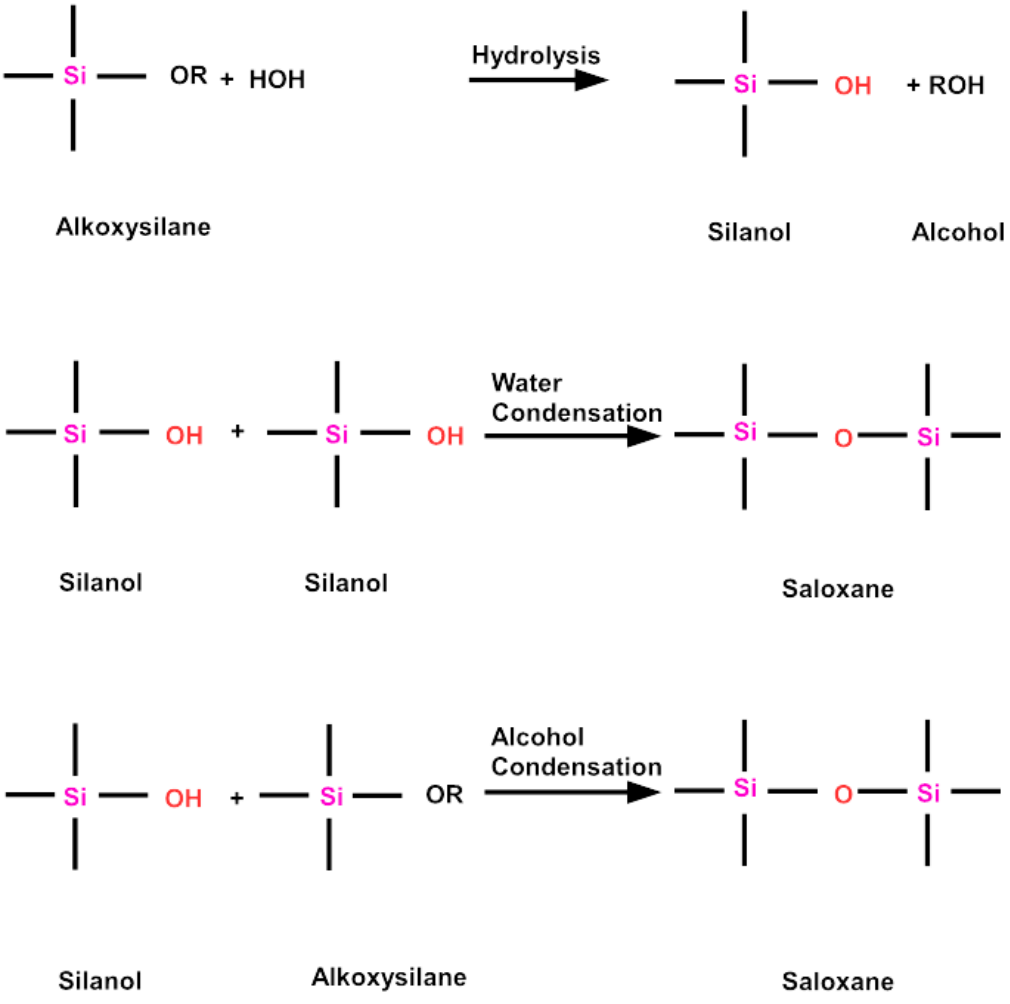

- Organically through the radical polymerisation of the methacryloxy group. The addition of a photoinitiating molecule (photoinitiator, PI) to the MATPMS will be able to initiate radical polymerisation of the vinyl groups through UV-irradiation. The final network will be a 3D organic network of interconnected oligomers.

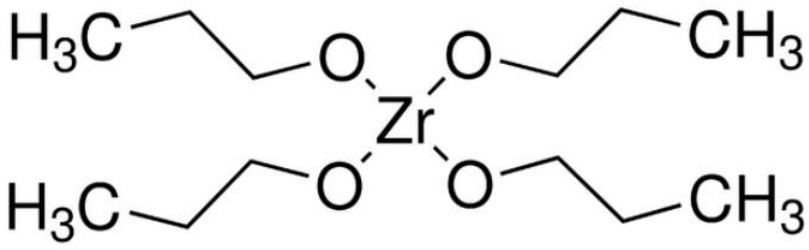

Figure 3-17: Zirconium propoxide

The zirconium propoxide is composed of four propoxide groups covalently linked to the zirconium atom Figure 3-17. Similarly to the methoxide groups contained in the MATMS, these groups can react via hydrolysis and condensation reactions to form a 3D network of zirconium oxide bonds. However, like most metal transition alkoxides, ZPO reacts violently with water forming irreversible zirconium oxide powders. To decrease the kinetics of reactivity, the use of a chelating agents, such as methacrylic acid, is required (Figure 3-18).

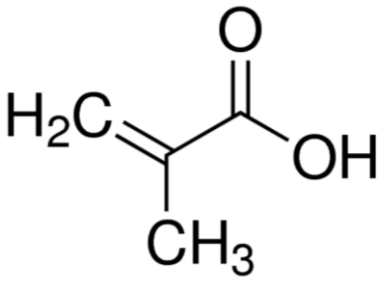

Figure 3-18: Methacrylic acid

The methacrylic acid is composed of a carboxylic acid group covalently linked to an unsaturated vinyl group. These two groups provide a double capability of reaction to this molecule:

- Inorganically, it can form a hybrid complex with alkoxide molecule through the formation of a chelate system.
- Organically, in presence of a PI and under UV-irradiation, it can polymerise via radical organic polymerisation to form a 3D network of organic molecules. Thus, MAAH is an ideal ligand to be combined with ZPO and MAAH as it can react with both sol-gel reactive precursors and probably leading to dense and homogenous systems, required for the fabrication of PLC platforms.

Having described the background on the role of each precursor and the expected molecular structures, the following subsection described the TGA / DSC analyses performed.

3.2.4 TGA/DSC Analyses

The employed procedure is described as follow. The TGA was initially zeroed by ensuring that the reading was 0.000g. Once this was complete the apparatus was opened and the aluminium pan removed and one drop of the sol-gel material was placed on the pan. The pan was then placed back in the instrument and it was closed once again. Before starting acquisition, it was important that the weight of the sample was read correctly. To ensure this the weight was read both on the computer and the TGA apparatus. The heating rate was set at 10 $^{\circ}$C per minute, with a start temperature of 25 $^{\circ}$C and a maximum temperature of 500 $^{\circ}$C. The sample was allowed to rest at the maximum temperature for 10 minutes.

3.3 Refractive Index Experimental Set-up and Modelling

3.3.1 High Refractive Index Sol-Gel Material

Introduction

This section highlights the development of materials with high refractive indices theses can be deposited at the surface of the sensor windows and cured at temperatures not greater than 100 ºC to avoid any modification of the materials properties and naturally their optical properties. For his purpose, the first step consisted of carrying out a literature review on the state-of-the-art in the development of such materials.

It was found that many technologies in photonics use high refractive index thin film materials (typically >1.65) to improve the performance of optical devices. In photovoltaic applications, anti-reflection coatings comprising high refractive index thin films are used in solar cells to trap the incident light and increase the amount of light coupled into the solar cell [242, 243]. In waveguide-based optical sensors, it has been demonstrated that a high refractive index superstrate layer on the waveguide surface results in lower limits of detection [244, 245]. In integrated optical devices, multilayer thin films with high refractive index contrast are extensively used for the fabrication of optical interference filters and mirrors [246, 247]. In addition to high refractive index, important requirements for high refractive index materials include high optical quality and transparency over the visible spectral range. Film thickness

control is also critical and the optimum thickness depends on the refractive index value and is usually between 30 and 150 nm [245-248]. Furthermore, a low temperature deposition process is frequently desirable to facilitate the integration of different optical components on substrates such as glass or plastic.

High refractive index layers are usually obtained with metal oxide materials. Metal oxide materials such as TiO_2 or Ta_2O_5 exhibit refractive index values above 1.8 and are transparent in the visible range. These materials are often deposited through evaporation or sputtering. Unfortunately, these methods are not only expensive, but post-deposition high temperature treatments are often necessary to obtain good adhesion and good optical properties [245]. In addition to these pure inorganic materials, hybrid organic-inorganic materials are found to be promising candidates for the low cost fabrication of high refractive index materials with good optical quality because they offer the possibility to combine the high refractive index of bulk metal oxides with the low temperature processing conditions typical of sol-gel derived materials. Recent work on the development of hybrid organic-inorganic coatings of metal oxides such as TiO_2 [249, 250] and ZrO_2 [251, 252] have reported an increase in the refractive index of hybrid sol-gel materials. Metal oxides are particularly interesting because of the high refractive index of the bulk material (in the range of 2.13 and 2.2 for zirconium oxide). These metal oxides are often transparent in the visible range which makes them advantageous for optical devices requiring high refractive index and high transparency. Most hybrid materials reported in the literature are based on ZrO_2 and TiO_2 metal oxides [249-252]. However, though these metal oxides give rise to hybrid materials with excellent optical properties, they are generally obtained after annealing at high temperature (> 400°C) [186, 249] . This makes them incompatible with many device fabrication processes and in particular our fabrication process.

The next section will investigate the development of hybrid sol-gel materials with a high concentration of inorganic precursors to minimise the contribution of organic molecules that are well-known to decrease the RI. However, in order to keep the curing process at temperature as low as possible, a minimum concentration of organic species is required.

HRI coatings based on niobium, tantalum and vanadium hybrid sol-gels

In this section, the development of a low temperature route for the deposition of high refractive index thin films based on niobium, tantalum and vanadium alkoxides will be investigated. These materials will offer a wider choice in the final definition of the HRI coating to be used in the sensor platform.

HRI Sol-gel preparation

The objective was to prepare transparent and homogeneous transition metal oxide-based thin film materials from the following niobium, tantalum and vanadium alkoxide precursors: niobium ethoxide (99.95%), Sigma-Aldrich; tantalum ethoxide (99.98%), Sigma-Aldrich; and vanadium tri-isopropoxide, (>98%) Strem. The synthesis employed here is the hydrolytic sol-gel route, which involves hydrolysis and condensation reactions resulting in the formation of a metal oxide three-dimensional network. The syntheses were performed in a 3 step process: (1) formation of hybrid complexes by chelation of the metal alkoxide precursors, (2) dilution of the hybrid complexes; (3) hydrolysis and condensation of the hybrid complexes. To avoid the formation of undesired agglomerates during the hydrolysis reaction, a chelating agent was utilized to decrease the reactivity of the employed metal alkoxide precursors. This was achieved by addition of a strong complexing ligand to the alkoxide [186]. In this study, methacrylic acid (MAA, Sigma-Aldrich, 99%) was employed as the complexing ligand. This caused the formation of hybrid complexes in which the number of reactive alkoxide groups is decreased, thereby making this precursor less reactive to hydrolysis. In order to obtain the highest possible refractive index without the performance of a high temperature post-bake heat treatment, the chelating agent concentration must be minimal. Such a compromise was found with 1mol. % of MAA with respect to the transition metal alkoxide concentration for all materials. In order to further slow-down the condensation kinetics of the hybrid complex and allow precise control of the film thickness, a dilution step was performed after 1 hour of reaction employing isopropanol (IPA, Sigma-Aldrich, 99%) with a volume ratio of 1:200 / hybrid complex: IPA. Following another hour of reaction, the hydrolysis step was performed utilizing pH 7 deionized water with a molar ratio of 1:10 with respect to the metal transition alkoxide precursor. Prior to hydrolysis, the deionized water was

diluted 500 times with IPA to prevent any formation of agglomerates. All sols were synthesised under the same conditions and then left stirring for 24 hours before use.

3.3.2 Optical and Coatings Characterisations

Zirconium based hybrid sol-gel was deposited by spin-coating on silicon substrate to form transparent thin films, and heat treated at 100 °C for the final stabilisation of the layer. Optical measurements and physical characterisations were made in order to determine the performance of this material with ellipsometry, profilometry and absorption measurements. Thickness and refractive index of the films were calculated using the Tauc-Lorentz model from the ellipsometry measurements. For both series of materials, the thickness of the thin films was measured to be between 80 and 150 nm. The roughness measurements were performed with a non-destructive optical profilometer (Veeco Wyko NT1100). The Veeco Wyko NT1100 is an optical profiler providing three-dimensional surface profile measurements without contact. The measurements were carried out in PSI (Phase Shift Interference) mode.

3.3.3 Simulations of the evanescent field and strategies to increase the biosensor platform sensitivity.

The evanescent field model was used within the Olympios software beacause it was found by other researchers [253] to be excelant at determining a single mode and the overact thickness of the high refractive index to achieve this according to analysis from the utilised Olympios software, the intensity of the evanescent field (EF) in the first 50 nm at the surface of the waveguide was found to be 0.001% of the light propagating in the core of the waveguide. This is characteristic of pure singlemode waveguides, where the fundamental mode is essentially confined within the core of the waveguide.

It is however possible, as reported previously in the literature [244], to increase the intensity of the EF by depositing at the surface of the optical waveguide a top layer with a High Refractive Index Layer (HRIL). For this purpose, the refractive index value and the thickness of this layer should be chosen carefully, as the distribution of the optical power among the waveguide is highly dependent on these parameters, as demonstrated in section 3.3.4.

Figure 3-19 shows the typical design for this configuration. The main difference between this configuration and the standard buried channel waveguide is:

- The top surface of the waveguide is covered by a coating of a high refractive index value.
- The surrounding environment at the top surface of this high refractive index layer is defined as water. This was chosen as our biosensor is aimed to characterise the presence of biological systems dispersed in aqueous media composed essentially of water.

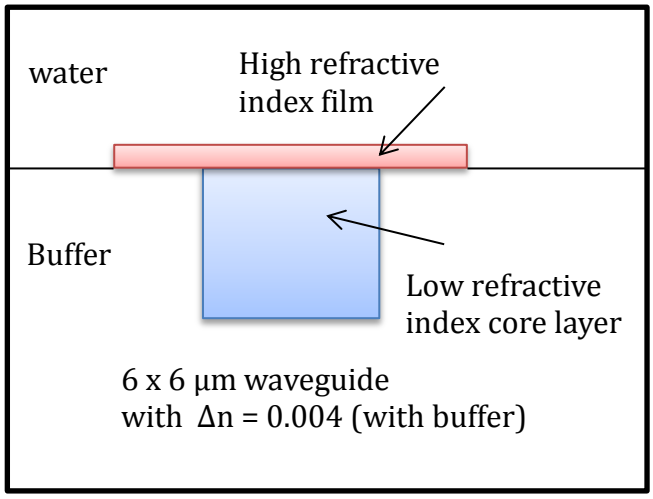

Figure 3-19: Configuration of the waveguide with high refractive layer on top of the sensing windows.

Having defined the structure of this new platform, in order to fully assess the effect of the HRIL coating, simulations were performed by varying the value of the refractive index and the thickness of the coating. Each variable was investigated independently of the other one as both can affect the EF intensity. For this purpose, initial simulations were done by fixing the refractive index at 2.1 and varying the coating thickness. This refractive index is amongst the highest that are reported for oxide materials, such as Ta_2O_5 [254]. For this RI, thicknesses investigated below 31 nm showed no improvement of the EF. However, as shown in Figure 3-20, the variation of the thickness in a domain comprised between 31–33 nm has a dramatic effect on the waveguide definition and the subsequent EF intensity. For thicknesses below 32 nm, the propagation of the light occurs within the core of the waveguide.

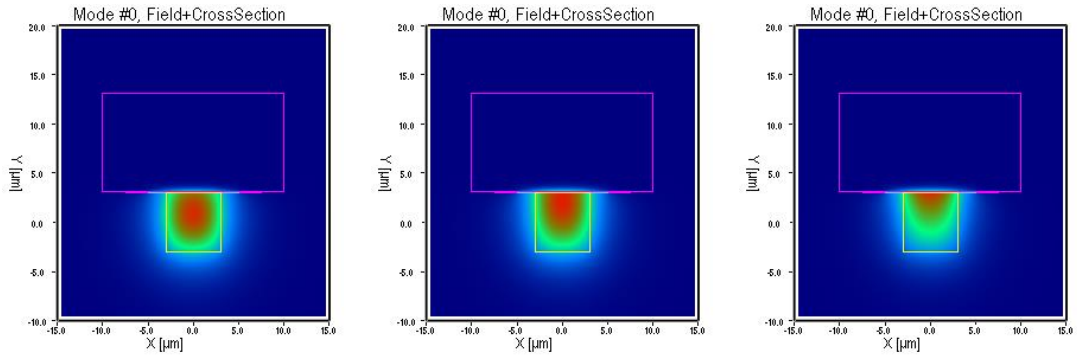

Figure 3-20: Simulation of the waveguide definition as a function of the HRIL thickness.

An increase of 1 nm to 33 nm forces the light to propagate into the upper layer, namely the HRIL. This is an undesired phenomenon, the consequence of which would be the impossibility to quantify the output intensity and monitor the sensing capability of the biosensor platform. The effect of the thickness on the light propagation is sketched in Figure 3-21. For a specific refractive index of 2.1, the cut-off thickness, where the light still remains propagating within the core of the waveguide, is found to be 32 nm. Based on this result, the next step consisted of evaluating the EF intensity at the cut-off.

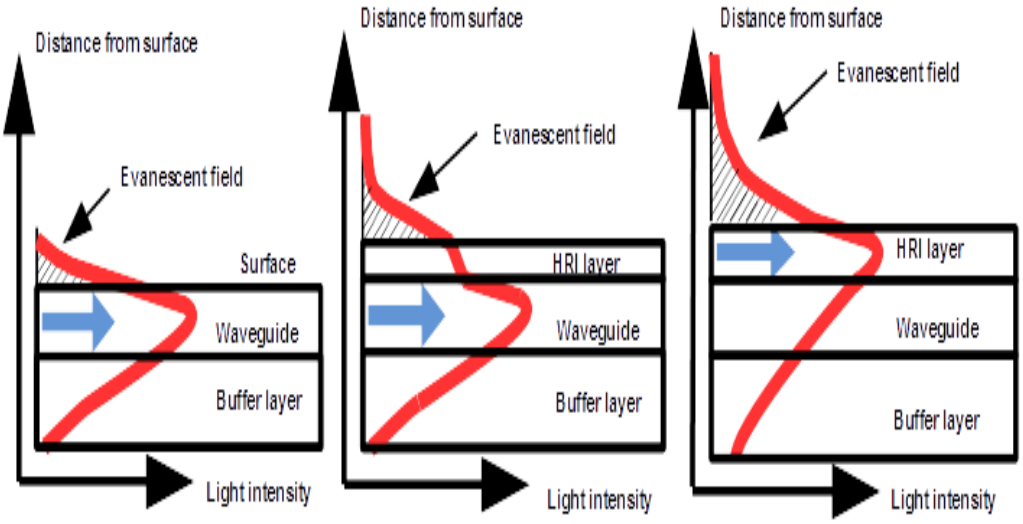

Figure 3-21: Modelling of the propagation of the light within the sensing region (optical waveguide with an upper HRIL).

To evaluate these calculations, the thickness of the HRIL was fixed at 31nm. Furthermore, in order to evaluate the tolerance on EF intensity and the thickness of

the HRIL, the study was extended to refractive indices in the range 1.65 – 2.1 and an additional simulation was performed for a coating of thinner thickness of 5 nm.

Figure 3-22 represents the % of the EF intensity within the first 50 nm on top of the waveguide core. It can be seen that this intensity varies from 0.32 to 0.63 depending on the thickness. This result shows that the EF can be increased by 320 to 630 times in comparison with the configuration without HRIL.

These simulations also show that a decrease of the optimum HRIL thickness before cut-off by 5 nm produces a decrease of the EF in the range of 55 – 85%. Minimum and maximum decrease is observed for refractive index of 1.7 and 2.1, respectively.

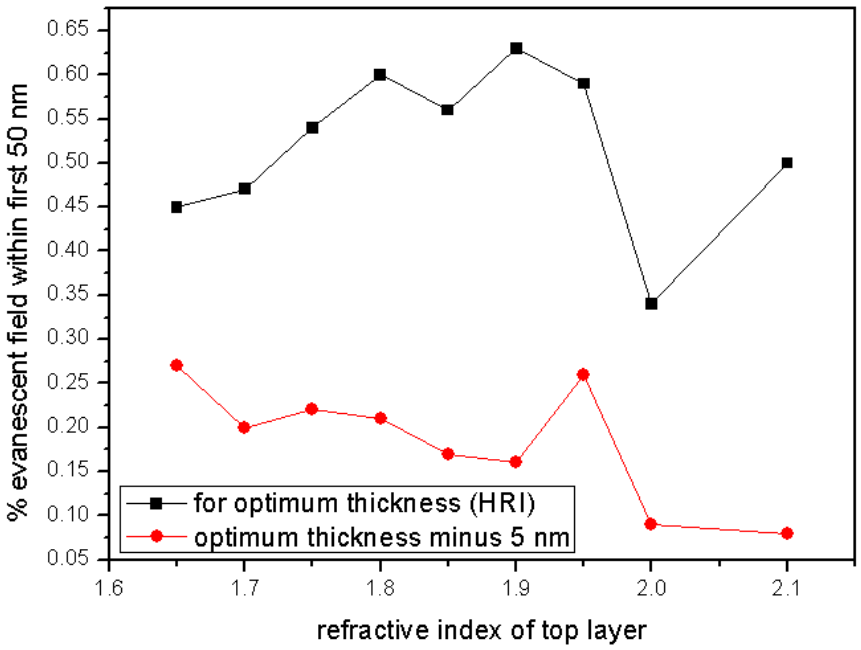

Figure 3-22: The correlation between the cut-off thickness and the refractive index of the HRIL.

The correlation between the cut-off thickness and the refractive index of the HRIL is represented in Figure 3-22, as provided by the simulations. It can be seen that the thickness is strongly dependent on the refractive index of the HRIL, and that the greater the refractive index is, the thinner the required cut-off thickness. This can be primarily explained by the capability of the coating to attract the propagating light at the waveguide surface. The strength of a coating (or more generally of a material) relies on its refractive index. To balance this effect, the coating thickness has to be adequately adjusted to avoid any propagation in the HRIL, modelled in Figure 3-23.

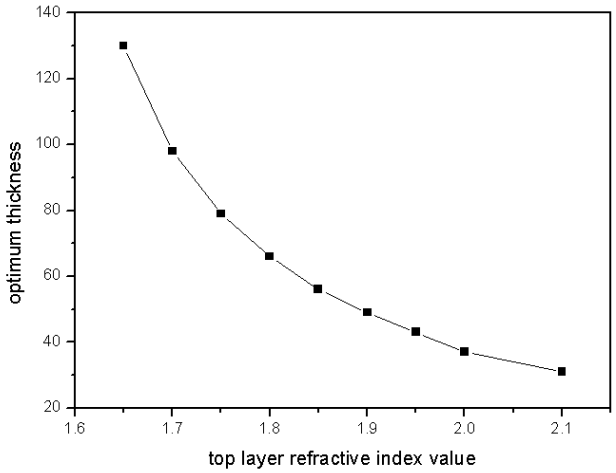

Figure 3-23: Correlation between the optimum thickness and to layer refractive index to maximise the EF intensity.

Figure 3-24 materialises the profile of the optical definition of the light propagating in both the waveguide and the sensors window in presence of a HRIL. In this figure, both the cut-off thickness and cut-off thickness less than 5 nm have been taken into account for the HRIL in the sensor window. It can be seen that in the core of the waveguide, the light uniformly propagates in a single mode manner, due to the uniform refractive index distribution around the waveguide core. However, in the sensor window, the profile of the light becomes clearly multi-modal. This is due to the fact that the surrounding environment of the core is not uniform in refractive indexes Moreover, as expected the value of the HRIL thickness clearly has an effect on the span length of the optical profile in the top layer.

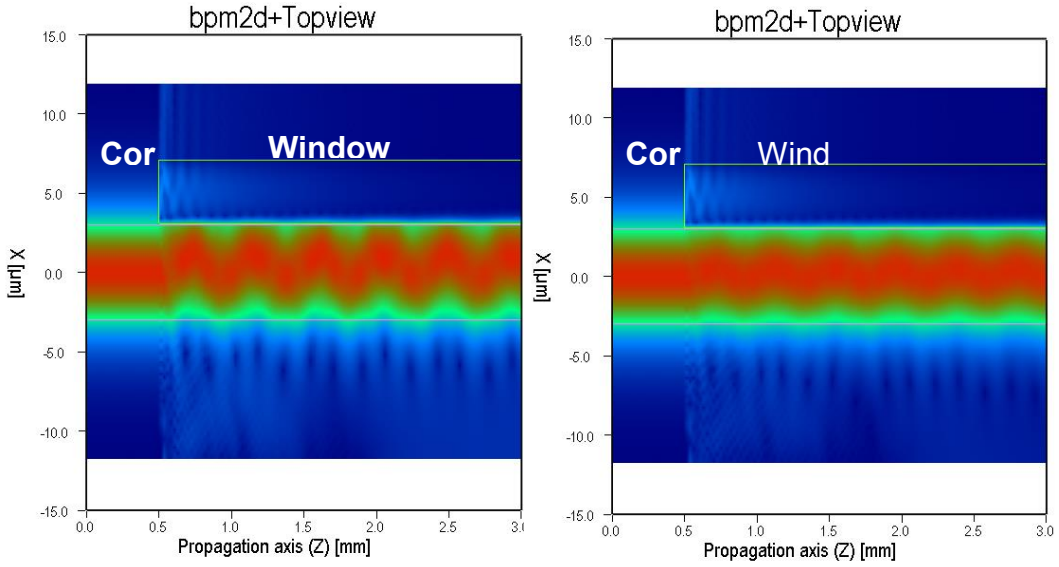

Figure 3-24: BPM Simulation of the light propagation in Z direction through a 6x6µm^2 in the channel waveguide and sensor window for the cut-off (left) and cut-off minus 5 nm (right).

These results suggest that a precise control of the HRIL thickness is required to significantly enhance the EF intensity. However, the proposed sol-gel process that is going to be employed in the development of the HRIL material is a liquid-phase process that allows the deposition of coatings via dip- or spin-coating, which may not provide reproducible thicknesses at the nanometre scale. Thus, the development of materials with refractive indices that would allow the highest tolerance possible on the thickness without dramatically affecting the EF intensity is desirable. This was taken into account during the material development phase and characterisation phase of this work.

3.3.4 PLC Modelling and Operating Principle

Biosensor design and operating principle

In this study, the sensing principle required was to detect the biofilm formation using highly sensitive optical waveguide. This can be achieved by the local modification of either refractive index or absorption, which can result in a significant variation of the collected output light intensities. To exploit these intrinsic waveguide properties, the

biosensor platform was based on a doubly split waveguide platform: two 3dB coupler stages were cascaded to divide the incoming optical light into four optical signals using Y branching, as sketched in
Figure 3-25. Sensing windows were patterned at the surface of three of the output waveguides while the remaining one waveguide was kept as a reference. This allowed the normalisation of the intensities measured from the sensing arms, and so was fully protected from the surrounding environment by a protective layer.

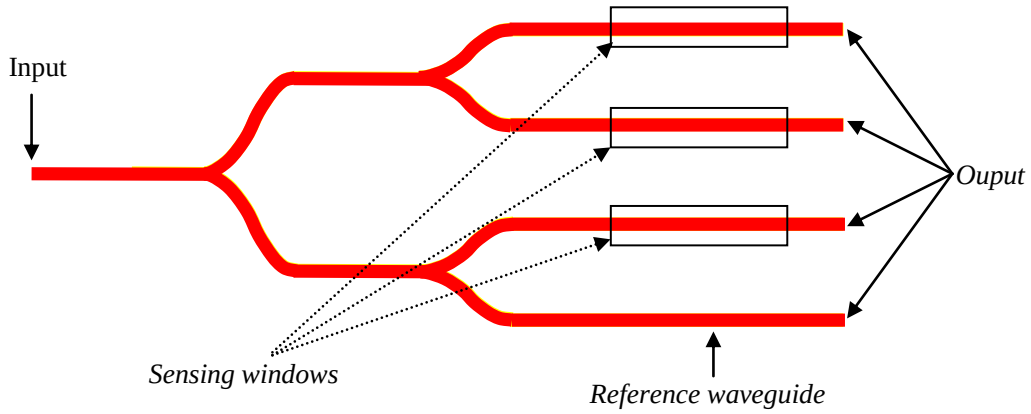

Figure 3-25: Design of the waveguide-based double splitter platform.

This configuration allows an equal share of the light to be distributed between the four output waveguides issued from the single-mode input and equal interaction levels between the evanescent field of the optical waveguides and their surrounding environment. The evanescent fields of optical waveguides are known to be sensitive to variations in refractive index and the absorption of the surrounding medium [255]. Therefore, any interaction change in the local environment will lead to a change in the optical waveguide's output intensity. The deposition of the biofilm on the surface of the optical waveguide should produce two simultaneous phenomena. Both in theory must strongly affect the out-coupled optical mode intensity through absorption sensing mode and transverse intensity distribution.
In order to define both the materials and geometry requirements of the biosensor platform, simulations were undertaken using the software of choice for optical circuits designs, namely the Olympios software. With this study the materials critical parameters to allow the fabrication of singlemode operating waveguides, such as the

refractive indices and transparency as well as dimensions were defined. In order to optimise the sensitivity of the biosensor, the interaction between the evanescent field of the propagating light (within the core of the waveguides) and its surrounding environment has to be defined. Strategies to increase this interaction were based on simulation results. These were the objectives of the next section.

3.3.5 Effectiveness of Biofilm Formation

Biofilms were grown under laboratory conditions by using nutrient solutions prepared by adding either 1% yeast extract or 1% glucose nutrients to tap water. These solutions were then left for a few days under light exposure to enable microorganism formation. The sensing mechanism as detailed in Chapter 3 (section 3.3.4.1) involves the interaction of the evanescent field with the biofilm at the surface of the optical waveguide in the sensor window. Considering that the formation of the biofilm is effective, the overall absorption in the visible range should be increased as the biofilm is expected to be essentially composed of microorganisms and living cells which are mainly constituted of organic and inorganic species.

Prior to the characterisation of the biosensor platform, it was essential to verify the effectiveness of the biofilm growth on the HRIL coating. The characterisation technique of choice for this objective was found to be UV-Visible spectrometry for two reasons. First, any adhesion of microorganisms and/or living cells at the surface of the HRIL coating would be identified by an increase of the overall absorption in the UV-Visible spectral range. Second, the required characterisation wavelength for the biofilm characterisation (539nm), situated within the UV-Visible spectral range and as such it could be used to corroborate the possible output change in the biosensor platform to the biofilm absorption. Furthermore, the employment of the tantalum oxide sol-gel material as HRIL is ideal as this coating is fully transparent (as characterised by ellipsometry in Figure 4-22) and as such would not interfere with identified absorption. In addition to the HRIL coating, blank glass slides were also utilized for comparison.

3.3.6 Data and Statistics Analysis Method

To graph the error bars which represent the variability of data for all the experimental results throughout this work, the error values were calculated according to 95% confidence interval using the formula:

$$e = 1.96 \times \frac{S}{\sqrt{n}}$$

Where S is the standard deviation and n is the number of experiments
At least three runs for each experiment were carried out.

However for the quasi-static flow experiment highlighted in section 4.3.3, this experiment was run five times to ensure an accurate set of results. This gave a value of 5 for 'n' in this range of experiments.

All other experiments related to the biosensor performance were run at least three times and a value of $n = 3$ was therefore used in the statistical analysis method outlined above.

Chapter 4

Results and Discussion

Chapter four will highlight the key results of a range of experiments carried out to develop a noval bio-sensor using waveguide technology and optical sensing.
This chapter will include the results related to:

(a) Material characterisation
(b) Simulations
(c) Biosensor characterisation

4.1 Materials characterisation

4.1.1 Sol-gel characterisation

Sol-gel characterisation formulations were carried out using the range of experiment highlighted in chapter 3. The composition of these formulations is shown in Table 4-1

Table 4-1: The composition of sol-gel formulations

Chemicals - Degree of hydrolysis	MATPMS	ZPO	MAAH	H2O/HCl	H2O (pH 7)
25	15	11.31	2.1	0.8	0.32
35	15	11.31	2.1	0.8	0.77
45	15	11.31	2.1	0.8	1.22
50	15	11.31	2.1	0.8	1.45
55	15	11.31	2.1	0.8	1.67
60	15	11.31	2.1	0.8	1.90
75	15	11.31	2.1	0.8	2.57
100	15	11.31	2.1	0.8	3.70

Table 4-2: Investigated formulations and the associated chemical compositions

Chemicals - Molar ratio	MATPMS	ZPO	MAAH
Material A	10	3.5	3.5
Material B	10	3	3
Material C	10	2.5	2.5
Material D	10	2	2
Material E	10	1.5	1.5
Material F	10	1	1
Material G	10	0.5	0.5

Table 4-3: Investigated formulations and the associated chemical compositions

Chemicals - Weights (grams)	MATPMS	ZPO	MAAH	H2O/HCl	H2O (pH 7)
Material A	15	9.89	1.83	0.8	1.37
Material B	15	8.48	1.57	0.8	1.29
Material C	15	7.06	1.31	0.8	1.21
Material D	15	5.65	1.05	0.8	1.14
Material E	15	4.24	0.78	0.8	1.06
Material F	15	2.82	0.52	0.8	0.98
Material G	15	1.41	0.26	0.8	0.90

The ZPO formulation was found to be the most reactive sol-gel precursor and as such decreasing its concentration was found to have significant effect on the flexibility of the fabricated coatings and thus lead to crack-free coatings. The new investigated formulations and the associated chemical compositions are summarized in Table 4-2 and Table 4-3, respectively.

The coatings properties depending on the applied treatment, either heat treatment or UV curing are summarised in the Table 4-4.

Table 4-4: Touch-dry properties A, B, C, D, E, F and G materials

Sample / Treatment	**Material A**	**Material B**	**Material C**	**Material D**	**Material E**	**Material F**	**Material G**
Heat-treatment at 100 ºC for 1 hour	Touch-dry	Touch-dry	Touch-dry	Sticky	Wet	Wet	Wet
Post UV-curing for 600seconds	Touch-dry	Touch-dry	Touch-dry	Touch-dry	Touch-dry	Sticky	Sticky/Wet

These results show that a direct correlation between the materials composition and the coatings properties is evident. The progressive decrease of the ZPO concentration (material A held the highest concentration and material G the lowest) leads to the fabrication of coatings with weaker condensation capabilities. Materials A to C were fully dryed after heat treatment at 100 ºC for one hour, whereas materials D to G remain sticky or wet. Furthermore, a similar trend was observed with the photocurability (UV curing) of the materials containing decreased concentration of ZPO. Materials F and G still remain sticky, whereas materials A to E are fully cured. This suggest that the cut-off ZPO concentration to fabricate fully stable cotaings is between materials D and E. In order to further optimise the photocurable hybrid sol-gel material, the focus shifted to determining the exact ZPO concentration to achieve the desired coatings qualities that will minimise or avoid the formation any undesirable cracks after the final multilayer integration. To achieve this objective, a new set of materials with concentrations of ZPO in the range 2 – 2.5 had to be developed. The molar ratios and formulations of these concentrations are depicted in Table 4-5 and Table 4-6. The coatings properties associated to these materials are reported in Table 4-7.

Table 4-5: The molar ratios and formulations of H, I, J, and K materials

Chemicals - Molar ratio	MATPMS	ZPO	MAAH
Material H	10	2.1	2.1
Material I	10	2.2	2.2
Material J	10	2.3	2.3
Material K	10	2.4	2.4

Table 4-6: The chemical weights of H, I, J, and K materials

Chemicals - Weights (grams)	MATPMS	ZPO	MAAH	H2O/HCl	H2O (pH 7)
Material H	15	5.93	1.10	0.8	1.15
Material I	15	6.22	1.15	0.8	1.17
Material J	15	6.50	1.20	0.8	1.18
Material K	15	6.78	1.26	0.8	1.20

Table 4-7: Coating properties of H, I, J and K materials

Sample / Treatment	Material H	Material I	Material J	Material K
Heat-treatment at 100 °C for 1 hour	Sticky	Touch-dry	Touch-dry	Touch-dry
Post UV-curing for 600 seconds	Touch-dry	Touch-dry	Touch-dry	Touch-dry

This study shows that coatings prepared with materials H still remain sticky after undergoing the heating curing step. This reveals that the cut-off ZPO concentration is more precisely located between materials H and I. Another possibility to increase the drying process would consist of providing a higher degree of condensation to the zirconium atom within the coating. This can be achieved by reducing the concentration of chelating agent. In this order, a new set of materials were developed with a progressive reduction of the MAAH. The associated molar ratios and

formulations are depicted in Table 4-8 and Table 4-9, respectively. Their coating properties are described in Table 4-10.

Table 4-8: The molar ratios and formulations of L, M, N, and O materials

Chemicals - Molar ratio	**MATPMS**	**ZPO**	**MAAH**
Material L	10	2.1	1.0
Material M	10	2.1	0.5
Material N	10	2.1	0.25
Material O	10	2.1	0.125

Table 4-9: The chemical weights of L, M, N, and O materials

Chemicals - Weights (grams)	**MATPMS**	**ZPO**	**MAAH**	**H2O/HCl**	**H2O (pH 7)**
Material L	15	5.93	0.55	0.8	1.15
Material M	15	5.93	0.27	0.8	1.17
Material N	15	5.93	0.13	0.8	1.18
Material O	15	5.93	0.06	0.8	1.20

Table 4-10: Touch-dry properties L, M, N, and O materials

Sample / Treatment	**Material L**	**Material M**	**Material N**	**Material O**
Heat-treatment at 100 ºC for 1 hour	Sticky	Touch-dry	Touch-dry	Touch-dry
Post UV-curing for 600seconds	Touch-dry	Touch-dry	Touch-dry	Touch-dry

The decrease of the concentration of the chelating agent produces an effect on the coatings mechanical property. It is clear that after the heat curing step, materials M

to O were all touch-dry. Material L still shows some minor tackiness. Following this study, with the objective to select the most promising material to be used for the multilayer integration, material M fulfilled the required conditions of coatings homogeneity.

Material M was applied as a buffer layer (first layer deposited) on both glass and silicon wafer substrates, fully stabilised by post-heat curing and UV-irradiation. All materials prepared here, including the reference material (10/4/4) were applied as a second coating and subsequently underwent the UV-curing step. None of the integrated coatings showed any cracks. This fully confirms the strategy consisting of decreasing the vitreous character of the coatings by reduction of the ZPO amount was successful. Further mechanical characterisations to better quantify and understand the fundamental aspects of the role of ZPO in the elasticity of hybrid sol-gel materials could be undertaken. Though this would be an exciting study to perform, this is not part of the scope of this work.

4.1.2 Optical Characterisation of the Photocurable Hybrid Sol-Gel Materials

As outlined in the simulation studies (section 4.2.1), in order to fabricate singlemode channel waveguides a refractive index contrast between the core and the cladding comprised in the 0.001-0.004 window is required for a 6x6 μm^2 waveguide operating at 635nm. To optimize the fabrication process of such devices, it was essential to characterise the refractive index as a function of the material compositions and processing parameters. The materials was characterised after the heat curing treatment and after the final UV-irradiation. However, before this stage determination of the optimum UV-exposure time was required so that all coatings were assessed on the hypothesis that they have reached their maximum condensation degree. This is defined by the maximum irradiation time. For this study, five test samples were taken from the 3 materials, namely the reference material, material C, material H and material M.

The refractive index values were determined on thin films spin-coated on silicon wafers using the prism coupling method at 632.8 nm (using a Metricon 2010).

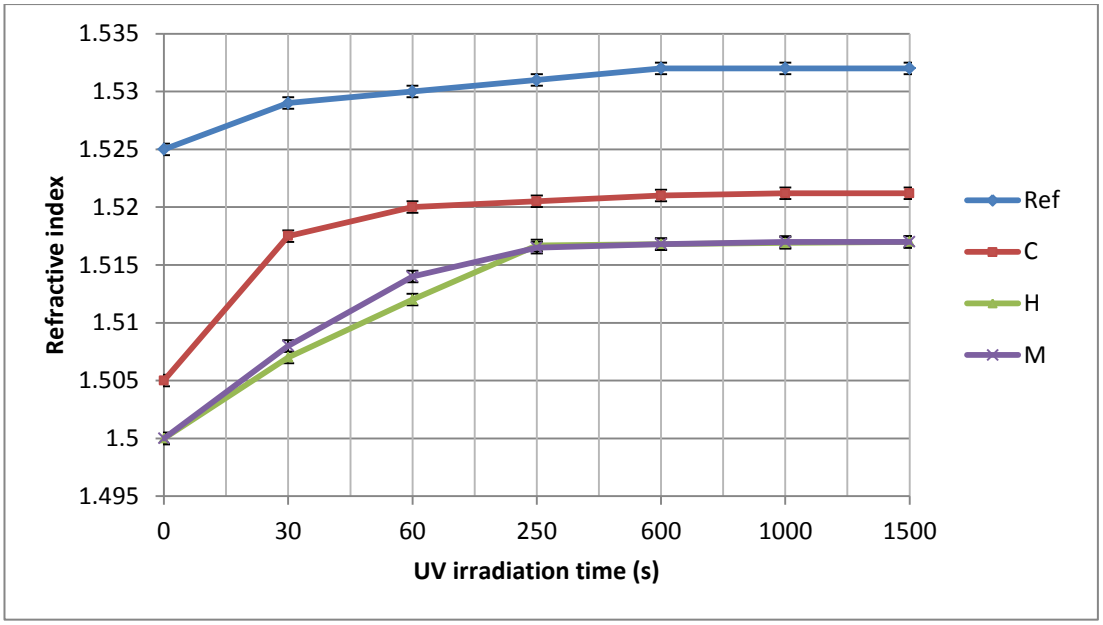

Figure 4-1: Evolution of Refractive index of the reference material and materials C, H and M as function of UV-irradiation time.

As plotted in Figure 4-1, the refractive index of the developed photocurable sol-gel materials clearly relies on the UV-irradiation dose. This shows that for all materials, the refractive index increases progressively up to 600 s and then stabilizes within the measurement uncertainty for exposure times up to 1500 s. this demonstrates that the main physico-chemical phenomena responsible for the materials stabilization, including organic photopolymerisation and inorganic condensation, occur predominantly during the first 600 s. Furthermore, it is worthy to note that a more rapid increase of the refractive index is noted with the increase of ZPO. This proves that the inorganic groups have an active role in the polymerization process, as previously described for similar tests [256]. Also, it can be noted that materials H and O having the same content of ZPO but a different concentration of chelating agent exhibit the same refractive index from 600 s up to 1500 s. However, it can be seen that the kinetic increase of the refractive index is faster for material H. this suggests that providing a higher degree of liberty to the zirconium atom enhances the radical polymerisation reactions. Interestingly, from this figure, material C with a refractive index of 1.52 exhibits a refractive index contrast of 0.003 with material M. This refractive index contrast is in the range of those indicated by the simulation studies to achieve singlemode waveguides at 538nm. Thus, the couple of materials M and C could be used for the fabrication of the cladding and core of the waveguide,

respectively. From this study it can be concluded that the stabilisation UV-irradiation time is 600 s. This time will was used to determine the refractive index of the other series of materials and in the fabrication of the PLC platform.

The refractive index values of materials A to G have been measured in thin films post-cured at 100°C and exposed to UV-irradiation for 600seconds. It was observed that the refractive index increases with the increase of the ZPO content and a wide range of values from 1.497 to1.532 can be achieved with a simple adjustment in the ZPO quantity. These results are in agreement with the trend obtained in Figure 4-2 and confirm that the main component acting on the refractive index is the concentration of metal transition complex in the hybrid sol-gel coating. This behaviour may be attributed to either the effect of the polarisability created by the complex or to the formation of larger particles. The consequence of this would be a decrease of the light propagation, during the refractive index measurement. In section 4.1.3.1.14.1.3, this was addressed by measuring the nanoparticle size of the sol-gel system in liquid phase using DLS and correlating the measured optical values to the structure of the materials.

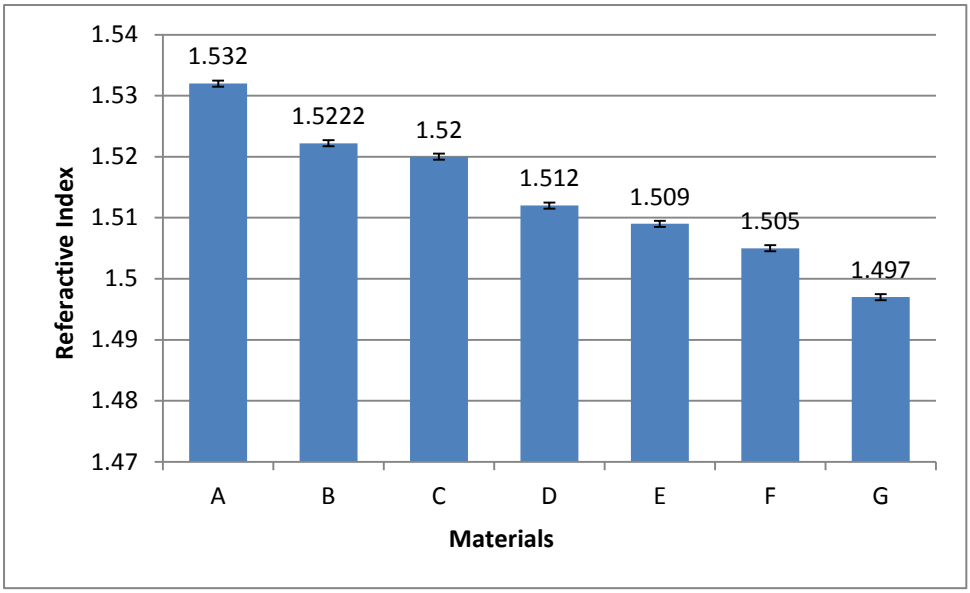

Figure 4-2: Refractive index values recorded for materials A to G, in addition to the reference material (10/4/4) after post-curing treatment at 100 ºC for one hour and UV-irradiation for 600seconds.

Similar studies were also performed for materials H to K. Refractive index values for these series as function of UV irradiation time are presented in Figure 4-3.

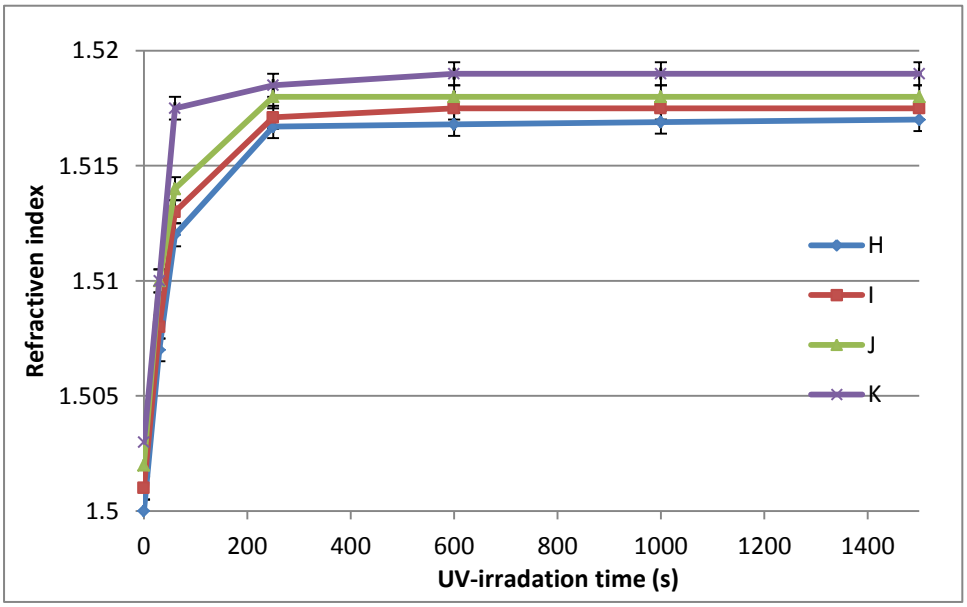

Figure 4-3: Evolution of the refractive index of coatings prepared form materials H, I, J and K as a function of UV-irradiation time.

It can be seen from Figure 4-3 that a small alteration of the ZPO quantity can have a significant effect on the overall refractive index of the coatings.

These materials were developed in order to identify the formulations that could match the required refractive index contrast with the chosen cladding (material O). Therefore, the refractive index difference between the cladding and the materials was calculated, and the results are plotted in Figure 4-4. Materials L, M and N have not been plotted as they were found to exhibit the exact same refractive index as material O, as indicated previously.

The refractive index after 600 s exhibits a linear increase with a growth coefficient of 0.0065 per ZPO concentration unit, as shown in Figure 4-4.

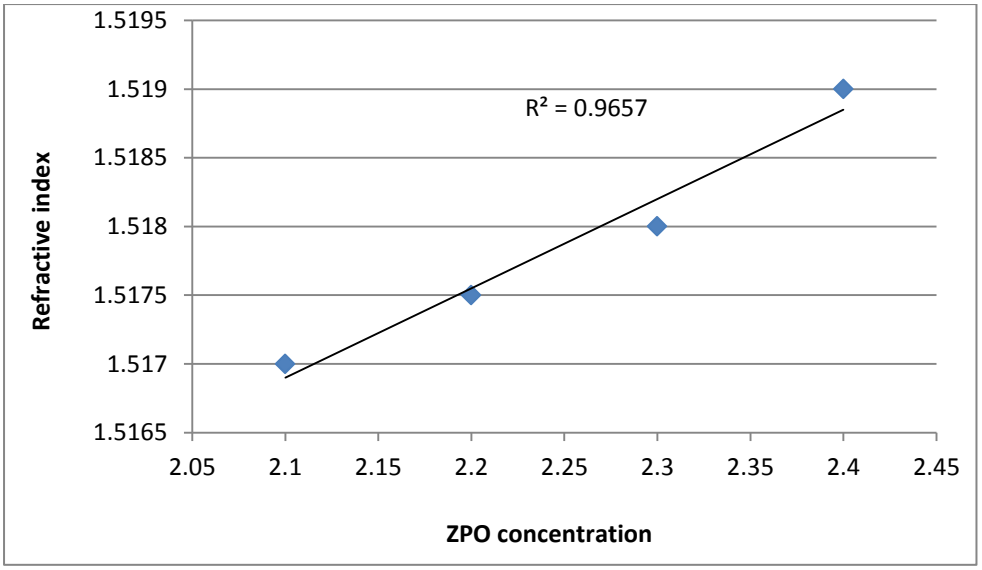

Figure 4-4: Evolution of the refractive index as function of ZPO concentration as calculated from Figure 2-12.

Figure 4-5 presents the refractive index contrast (RIC) between A to K materials

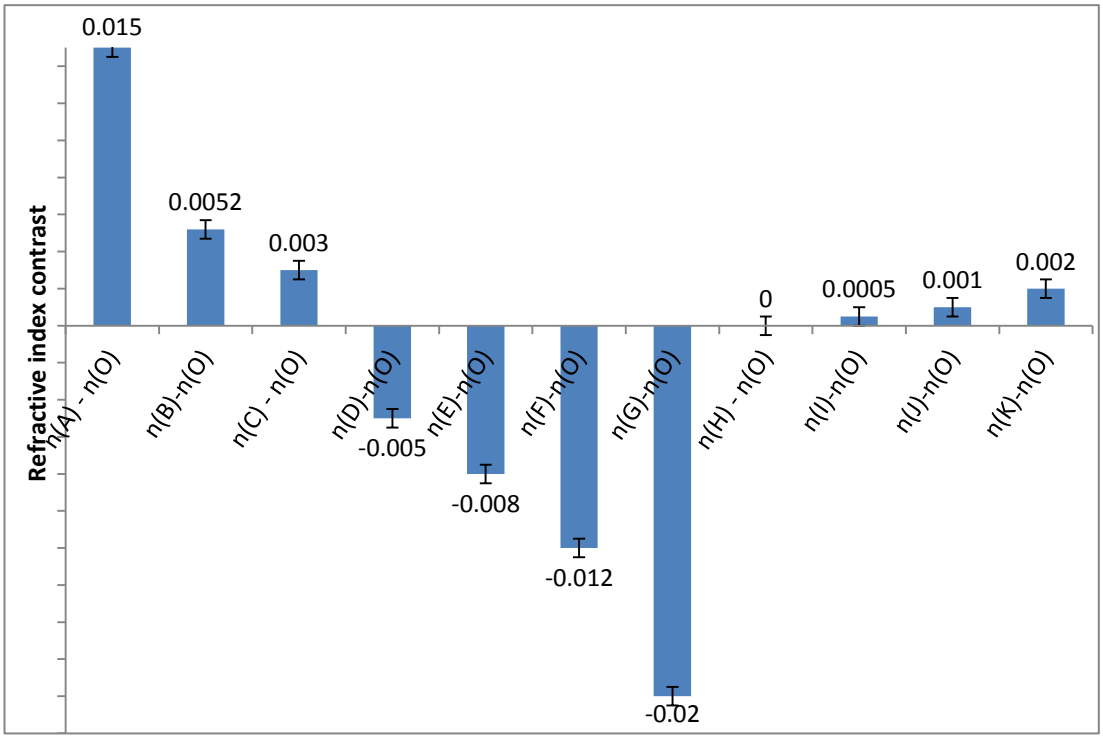

Figure 4-5: Refractive index contrast between a given material and material O.

Based on the simulation studies, shown in section 4.2.1 in Chapter 4, it is easy to select from Figure 4-5, the materials that can match the required refractive index contrast of 0.001 – 0.004 to be used for the fabrication of the waveguide core of the PLC platform. Materials D, E, F and G were discarded as they show a negative

refractive index contrast. This means that the light would not be able to propagated in these materials and would be, in the majority of applications lost in the cladding (material O). The same applies for materials H and O as the Refractive Index Contrast (RIC) is below the range defined by the simulations. Materials A and B exhibit a RIC greater than the one required, therefore they also have to be eliminated, as their employment would create a multimode waveguide that would induce losses during the propagation of the light before reaching the sensor windows. Finally, the only materials that can be considered for future PLC fabrication are materials C, J and K, which exhibit a refractive index contrast within the required range of 0.001 - 0.004.

4.1.3 Structural and Thermal Characterisation of the Hybrid Sol-Gel Material

Dynamic light scattering

DLS was performed on all sol-gels over a period of time ranging from 2h to 48h to determine the particle size of the family of photocurable sol-gel materials developed here. The particle size evolution were time is an important property to assess so that the sol-gel lifetime and deposition time can be determined. For this assessment, three materials representative of the series developed have been selected, namely, the reference material, materials C and M.

Prior to analysis, the sol-gels were filtered using a syringe and a Whatman syringe filter (0.45 μm pore size) to avoid the appearance of particles of a size greater than 450 nm. The solutions were transferred into a plastic cuvette using a pipette. The cuvette was then placed in the DLS and recorded.

The DLS spectra of the reference material, materials C and M are shown in Figure 4-6, respectively. These spectra reveal that 2 hours after the synthesis, the reference material and material C exhibit particles of sizes comprised between 6 – 8 nm, whereas the particle sizes of material M are centred at 3nm. It is important to note that for all materials full width at half maximum (FWHM) of the bands is close to 7 – 8 nm. This indicates that these materials are polydisperse but the main particle populations exhibit sizes of the maximum band. After 24 and 48 hours of ageing, no significant evolution of the particle size is observed for the reference material and

material C. However, material M shows a band maximum close to those observed for the two other materials.

These results demonstrate that the particles sizes of the sol-gel materials are typically comprised between 10 and 20 nm within 24 and 48 hours of ageing after the synthesis. To avoid any aging effect and possible development of larger particles that would modify the optical properties of these materials, the PLC platform should be developed within this time-frame.

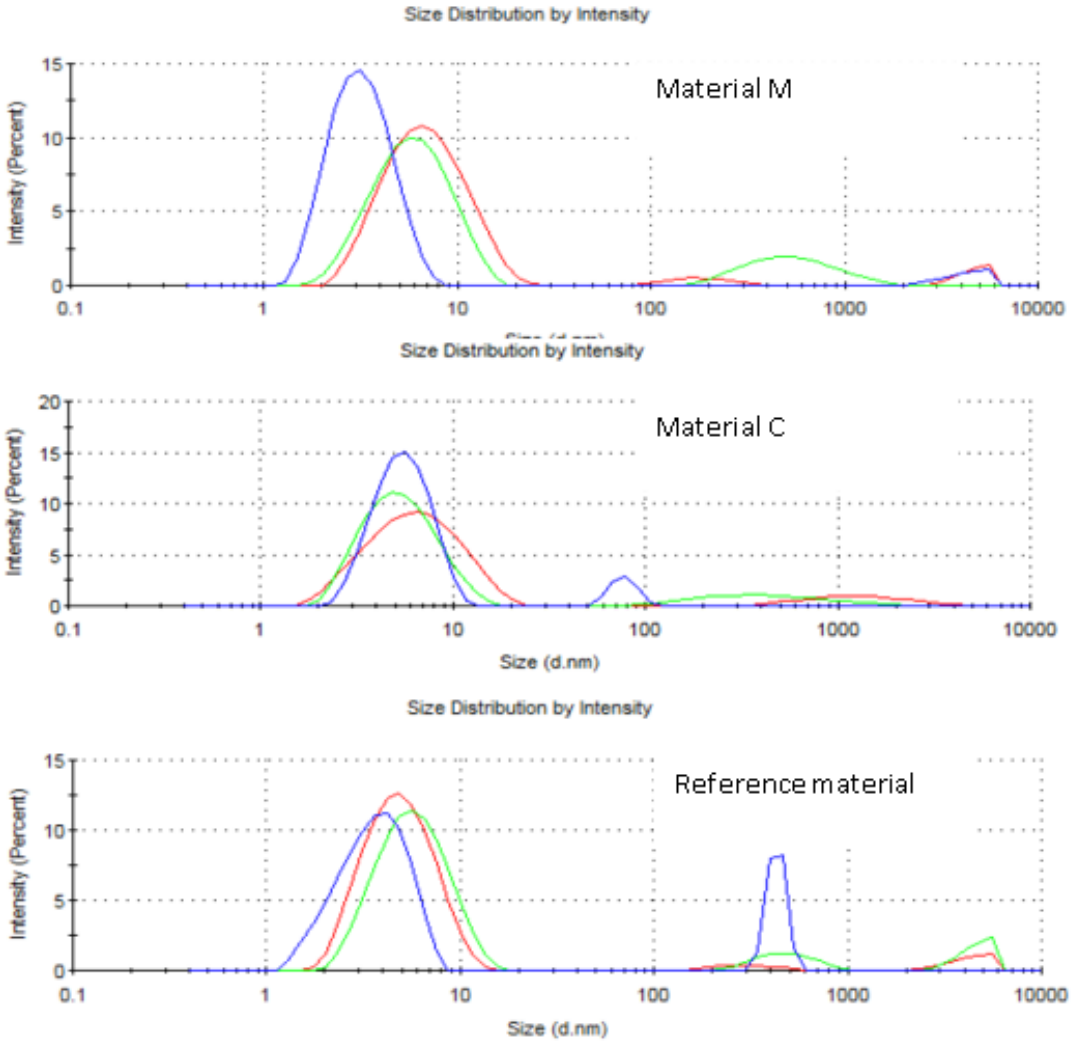

Figure 4-6: DLS spectra of the reference material, material C and M at 2, 24 and 48 hours after the synthesis.

Thermo gravimetric analysis

In order to identify the thermal behaviour of the family of photocurable sol-gel materials developed here, TGA/DSC analyses were performed on the reference material and materials C and M.

TGA/DSC spectra for the reference material, materials C and M are shown in Figure 4-7, Figure 4-8 and Figure 4-9. Three-step behaviour can be identified for all recorded materials. A) Strong weight loss below 100 °C, B) moderate weight loss from 100 to 300 °C and C) an acceleration of the weight loss from 300 to 500 °C. The weight loss as a function of temperature was also calculated and plotted in Figure 4-7 to Figure 4-9.

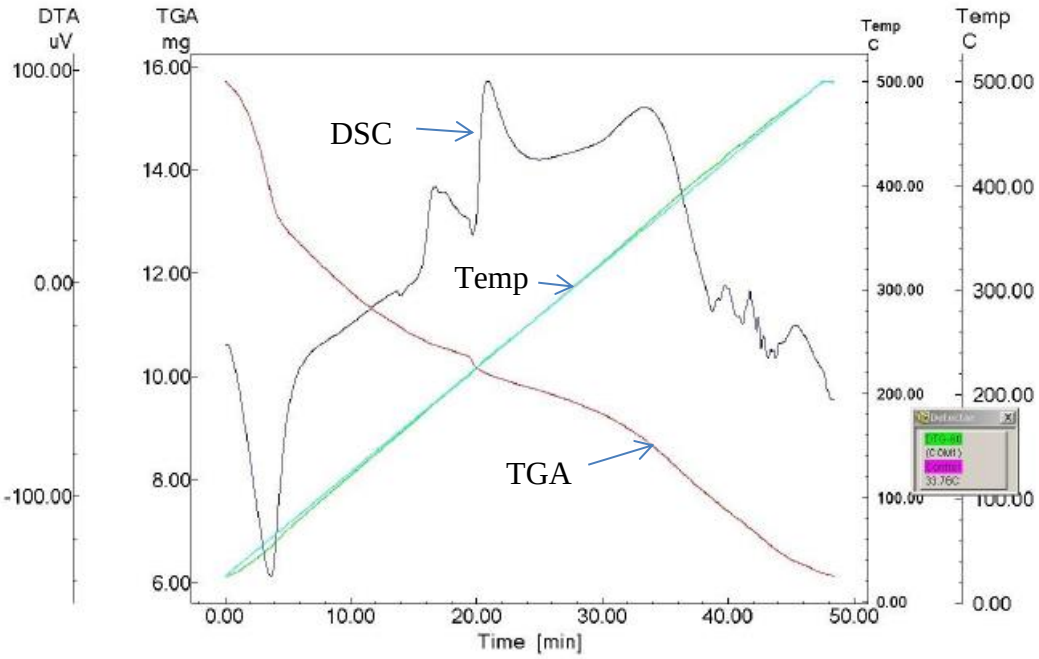

Figure 4-7: TGA/DSC spectra of the reference material

The first weight loss is typical of the elimination of the solvents, both inherent to the precursors and due to the formation of alcohols during the hydrolysis and condensation reactions involved by the sol-gel process. This assumption is confirmed by the strong endothermic band observed in the DSC curve. The second weight loss can be explained by the production of water due to the condensation of the inorganic species, including the silanols (Si-OH) and zirconium hydroxide (Zr-

OH) bonds into the formation of siloxane (Si-O-Si), zirconium oxide (Zr-O-Zr) and silicon/zirconium oxide bonds (Si-O-Zr).

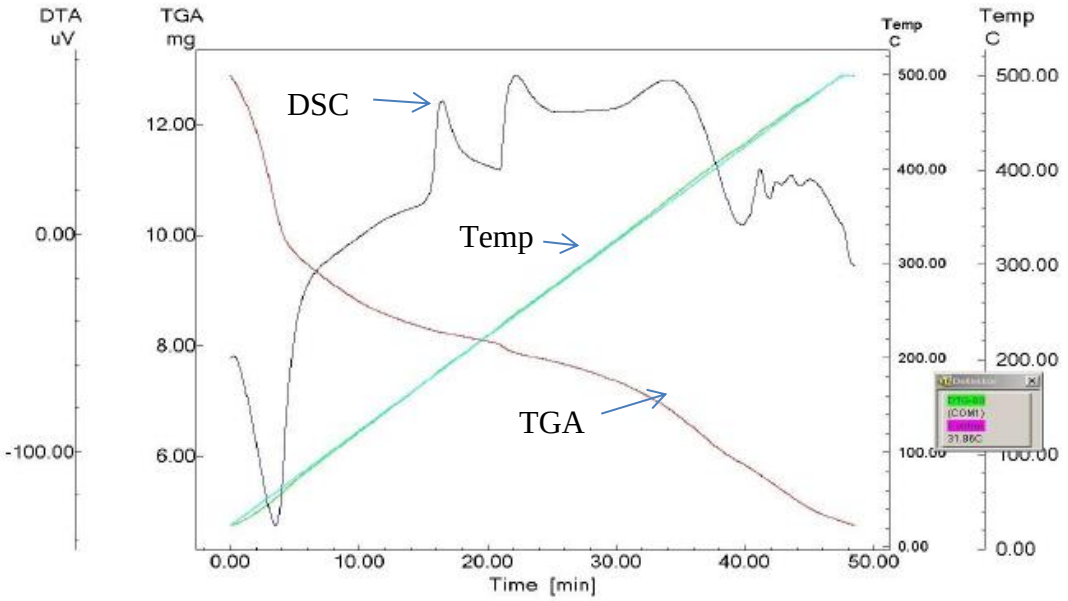

Figure 4-8: TGA/DSC spectra of materiel C.

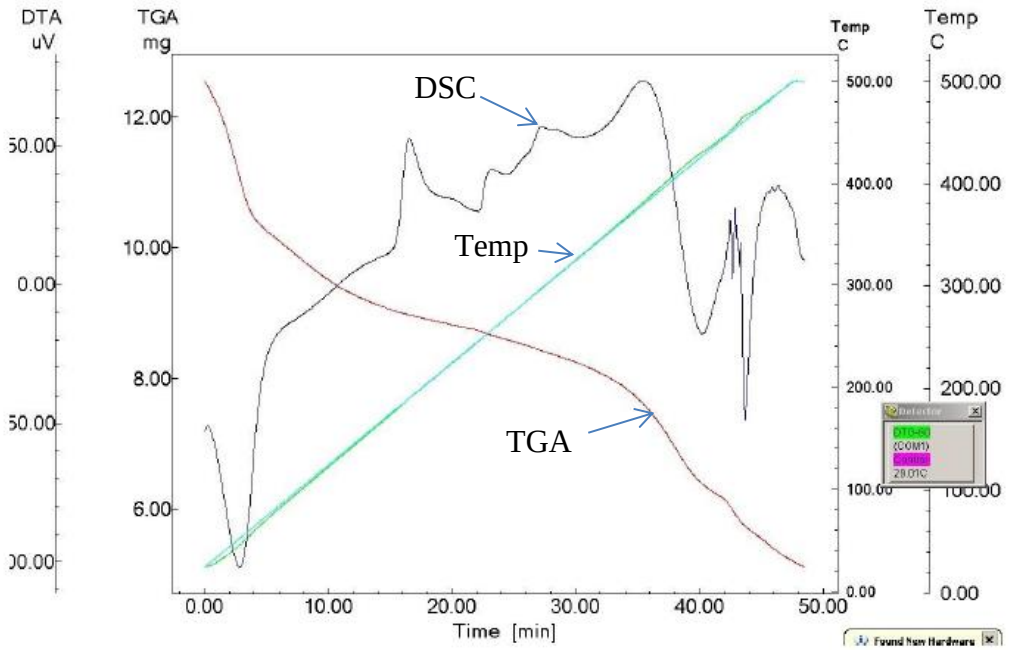

Figure 4-9: TGA/DSC spectra of materiel M

The 3-4 exothermic bands confirm the formation of irreversible chemical bonds and are in agreement with the formation of the three types of chemical groups. The third step is due to the oxidation of the elimination of the organic compounds contained both in the MAPTMS and in the MAAH. Interestingly, it can be seen that these

oxidation phenomena are accompanied by the appearance of an exothermic band in the DSC curve. This can only be attributed to the formation and crystallisation of inorganic structures only implying silicon, zirconium and oxygen. These results show that the characterised materials exhibit a good stability at 100 ºC, as most of the volatile compounds have been released.

4.1.4 Optimisation of the Coatings Thicknesses and Surface Characterisations

Experiments were calculated to optimise the thickness of the coatings for materials C and M. Materials C and M were deposited at speeds in the range 500 – 1700 rpm. The corresponding thicknesses are represented in Figure 4-10.

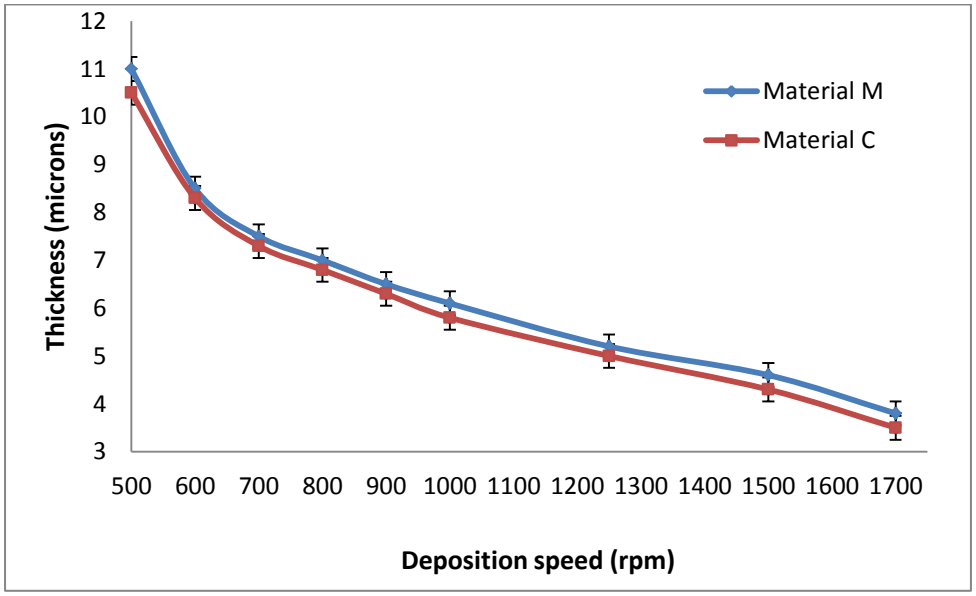

Figure 4-10: Evolution of the coating thickness for materials C and M (of 24 hours age) as function of the deposition speed.

From this figure it can be seen that the trend for both materials is very similar and that coating thickness relies on the deposition speed. Interestingly, material M exhibits an average coating with thicknesses of around 0.25microns greater than those measured for material C. This can be attributed to the different concentration of ZPO in these materials, which affect the overall viscosity of the materials. However, knowing that the error bar on the prism-coupling method is close to 0.5micron, it can be confirmed that both materials exhibited a quasi-identical

coatings thickness whatever the deposition speed used in this study. Consequently, according to Figure 4-10, it is possible to fabricate coatings with 6 microns at 1000rpm for both materials within 24 hours aging process. Based on this result and knowing that polycondensation reactions in sol-gel systems keep going until gelation takes place, it is noteworthy to identify the effect of ageing on the thickness of the coatings deposited at 1000rpm. This is essential to identify the time usability of the sols after synthesis. These characterisations have been performed for up to 21 days for sols kept in a freezer at -4 ºC to slowdown the ageing of the sols. Coatings were fabricated and associated thicknesses measured every day for the first 3 days and subsequently every week for materials C and M, as represented in Figure 4-11.

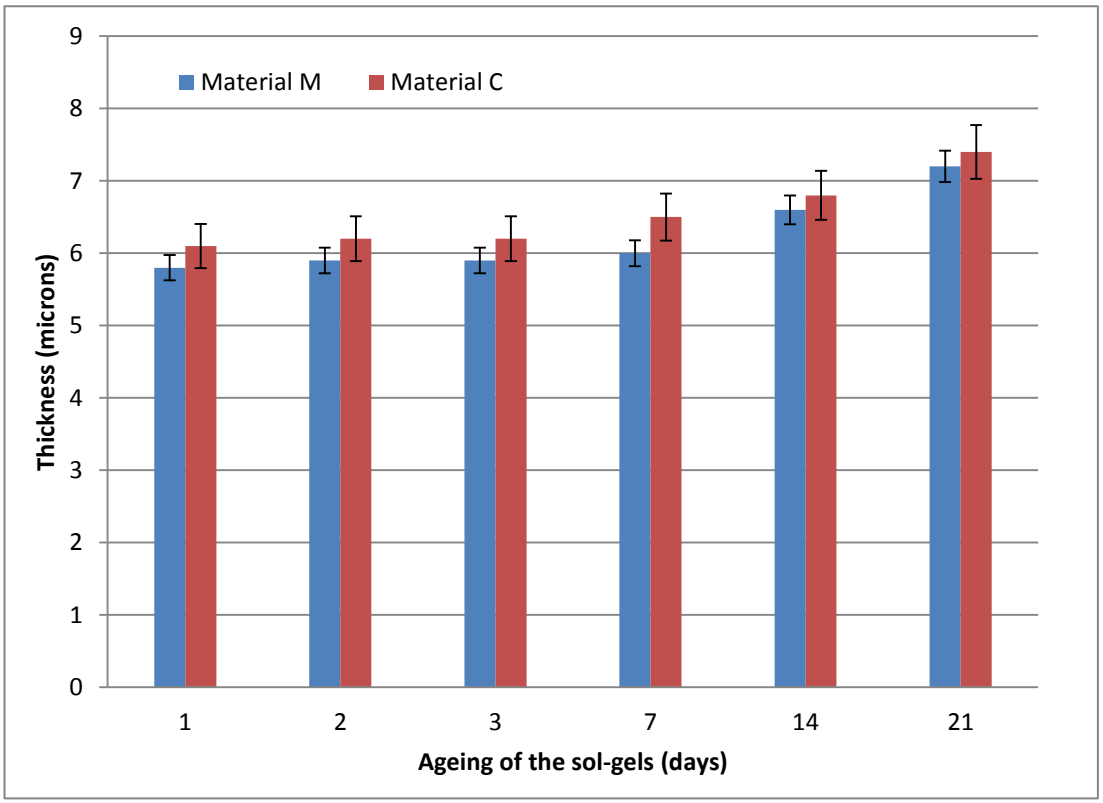

Figure 4-11: Evolution of coatings thicknesses for materials C and M deposited at 1000rpm as function of sol-gel ageing.

It can be observe that during the first 14 days no thickness change above the uncertainty measurement (0.5micron) is recorded. However, after 21 days of ageing, coating thicknesses were recorded at 7.2 and 7.4 microns for material M and C, respectively. This increase is clearly outside the uncertainty measurement and demonstrates that these sol-gels would not be useful to achieve the desired thicknesses. It is however important to outline that the most critical thickness for the

waveguiding properties is that of material C as this is the one that defines the waveguide core thickness. Nevertheless, to avoid any further discussions on the thickness parameter it was decided not to use the sol-gels after a maximum age of 3 days.

4.1.5 Zirconium-HRI Based Sol-Gel Materials

Here, the strategy consists of synthesizing different materials employing a chelating agent and organosilane precursors with the addition of zirconium propoxide to increase the refractive index. The optical properties of zirconium based hybrid material are compared according to the concentration and type of precursors. The process temperature never exceeded 100 °C.

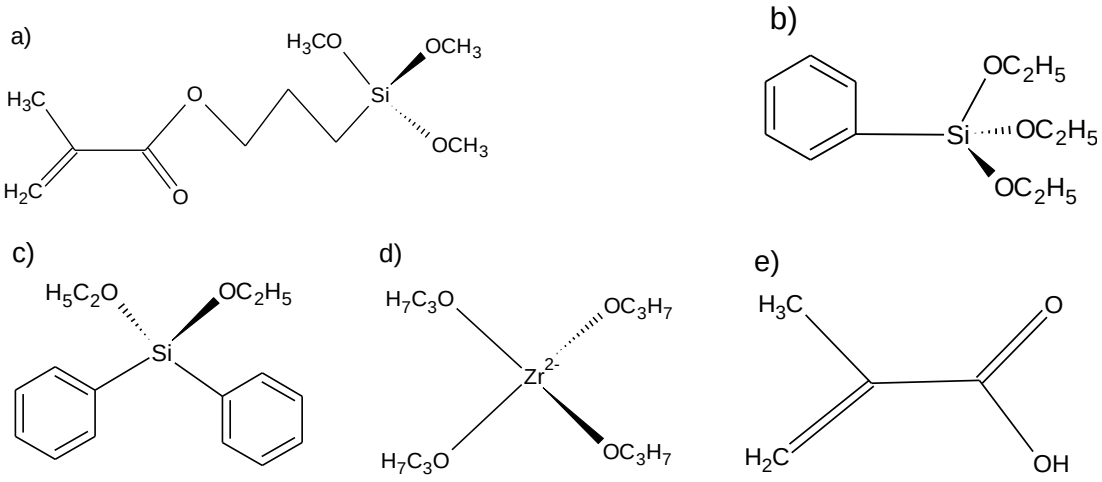

Figure 4-12: Chemical structure of the precursors employed in the sol-gel synthesis, a) zirconium propoxide (ZPO), b) methacryloxypropyltrimethoxysilane (MAPTMS), c) phenyltriethoxysilane (PHTES), d) diphenyldiethoxysilane (DPHDES) and e) methacrylic acid (MAAH).

As sketched in Figure 4-13(a), two strategies have been employed to synthesise transparent and homogeneous hybrid zirconium solutions. The first involved a two-step process, employing a pre-hydrolysed Ormosil precursor, MAPTMS, PHTES or DHPDES (Figure 4-12). Firstly, the organosilane precursor was pre-hydrolysed under a vigorous stirring for 45 minutes using an HCl 5.10-3 N aqueous solution with degree of hydrolysis of 25% against the reactive methoxide groups. This allowed the formation of silanol groups (Si-OH) and initiates the formation of the

siloxane (Si-O-Si) backbone. The solution was then diluted 20 times using 2-propanol (IPA) and left stirring for another 45 minutes prior to the second hydrolysis. As demonstrated before [15], the introduction of zirconium propoxide (ZPO) within a pre-hydrolysed organosilane system involves catalysis of the formation of the siloxanes bonds by attraction of the OH groups located on the silane network. This results in an indirect and slow hydrolysis of the ZPO precursor, leading to stable and transparent solutions. The second step involved a dropwise hydrolysis of the whole system employing a pH 7 aqueous solution, leading to 50 mol.% hydrolysis compared to the total number of reactive alkoxide groups.

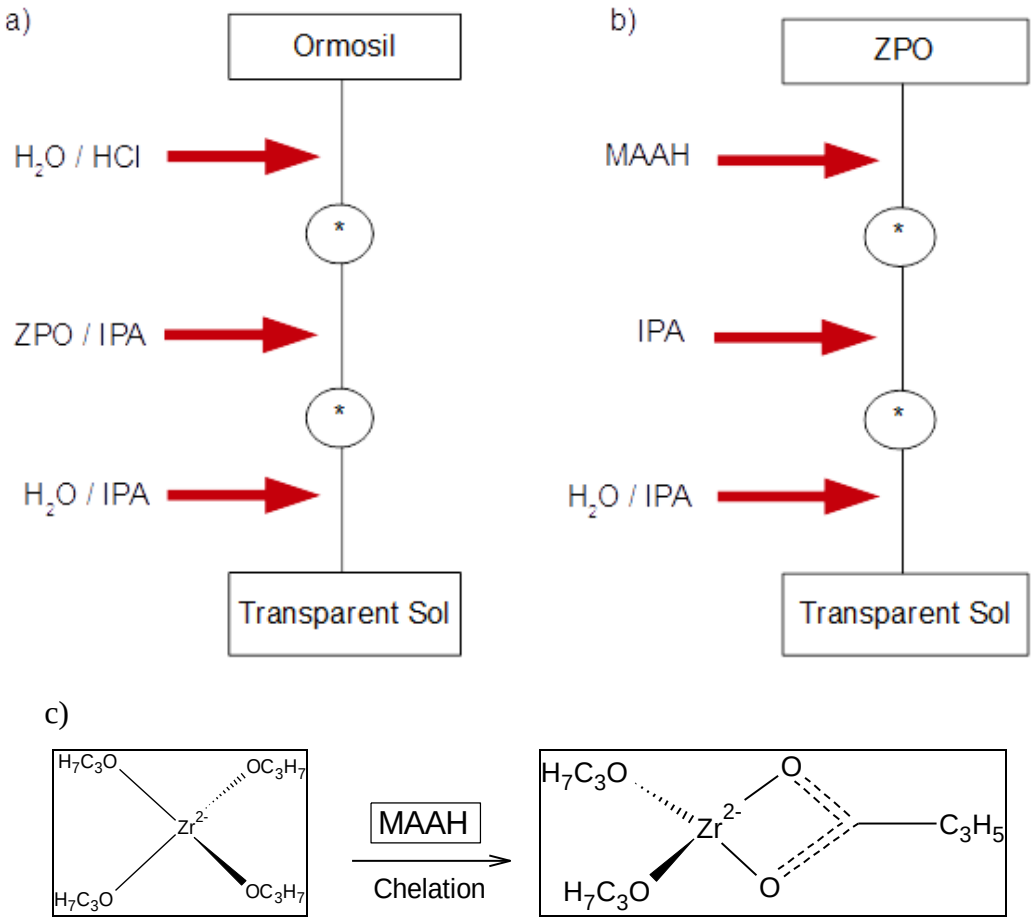

Figure 4-13: Schematic diagram of the a) ormosil and b) chelation routes employed in the sol-gel synthesis of Z_rO_2 thin films and c) the chemical scheme of the zirconium chelation by the methacrylic acid

The second route utilised a chelating agent to decrease the reactivity of the ZPO precursor in the presence of a strong nucleophilic groups, such as water

(Figure 4-13b and Figure 4-13c). The addition of methacrylic acid (MAAH) to ZPO caused the formation of a zirconate complex, in which the number of reactive alkoxide groups is decreased, thereby making this precursor less reactive to hydrolysis. Furthermore, the dilution with IPA (400 times) contributed to further inhibit the condensation kinetics during the hydrolysis step, allowing the development of fully stable solutions.

4.1.6 Optical and Coatings Characterisations

Effect of the nature of the organosilane precursor on the refractive index value

The materials prepared using the three different type of organosilane precursors (MAPTMS, PHTES and DPHDES) were optically characterised. To compare and discuss the influence of the nature of the organosilane precursor on the final refractive index value, the concentration of each precursors was kept at 10 mol.% against the ZPO precursor. The refractive index values were measured to be 1.692, 1.710 and 1.711 at 635 nm for the films containing MAPTMS, PHTES and DPHDES, respectively. The progressive increase of the refractive index can be primarily explained by the molecular structure of the employed precursor. PHTES and DPHDES contain one and two phenyl groups, respectively (Figure 4-13) compared to MAPTMS which does not contain phenyl groups. Such aromatic groups exhibit higher polarisabilities than linear aliphatic groups, the result of which was a significant increase of the refractive index. The electron cloud in the π aromatic bonds was easily distorted, inducing a high electric field. In fact, this property results from the mesomeric effect generated by the permanent circulation of the π electrons contained in the conjugated bonds of the cyclic groups. Furthermore, the high sterical hindrance of the aromatic group can also contribute to the increase in the average size of oligomers, then leading to higher refractive index values. Following these results, the focus of the work was placed on employing the DPHDES as the main organosilane network modifier in order to investigate the effect of its concentration on the optical properties of the ZPO precursor.

Effect of the DPHDES molar concentration on the refractive index value

Figure 4-14 shows the variation of the refractive index of the material as a function of DPHDES concentration at three different wavelengths (475, 635 and 830 nm). One can observe that for any selected wavelength, the refractive index exhibits the same tendency, within two distinct domains from 0 to 1 mol.% and from 1 to 10 mol.% of DPHDES. At 635 nm, the progressive decrease of the DPHDES concentration from 10 to 1 mol.% results in a regular increase of the refractive index from 1.71 to 1.746. However, for concentration of DPHDES below 1 mol.%, the refractive index decreases down to 1.739. In general, the refractive index of thin film materials is intimately related to the morphological and structural characteristics. The morphology is mainly associated with the porosity and the roughness of the films; although the structure relates more to the composition of the employed materials. From these considerations it can be proposed that for concentration of DPHDES above 1 mol.%., the refractive index follows the law of composition of mixtures where the refractive index value is mainly determined by the overall molar refraction. This suggests that in this range of concentrations, the developed materials exhibit almost identical densities. However, below 1 mol.%. of DHPDES, the morphological aspect seems to predominate over the structural considerations, as a decrease of the refractive index is observed, which is attributed to formation of pores in the inorganic network thus decreasing its density.

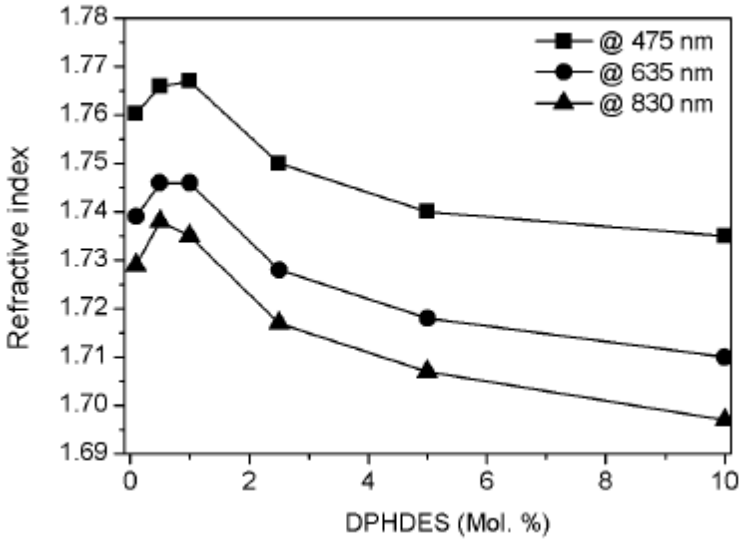

Figure 4-14: Refractive index as a function of DPHDES molar concentration at selected wavelengths (475 nm, 635 nm and 830 nm)

Effect of the chelating agent on the refractive index value

Figure 4-15 shows the wavelength dependant refractive index of hybrid zirconium materials as a function of the chelation degree employing MAAH. It can be observed that a progressive decrease of the MAAH content in the range 0.01-1 mol.% (while keeping the ZPO concentration constant) causes a quasi-linear increase of the refractive index values from 1.587 to 1.716, which is proof of the high homogeneity of the developed materials. Unlike the DPHDES, for any selected wavelength, no decrease of the refractive index can be observed for the lowest concentration of MAAH, which demonstrates that the optical properties are strictly dependant on the molar refraction of the materials. However, the exact explanation of the morphological differences could be explained by the structures of the inorganic network created by both organic modifiers, which is at this stage still not fully identified and is not the main scope of this study.

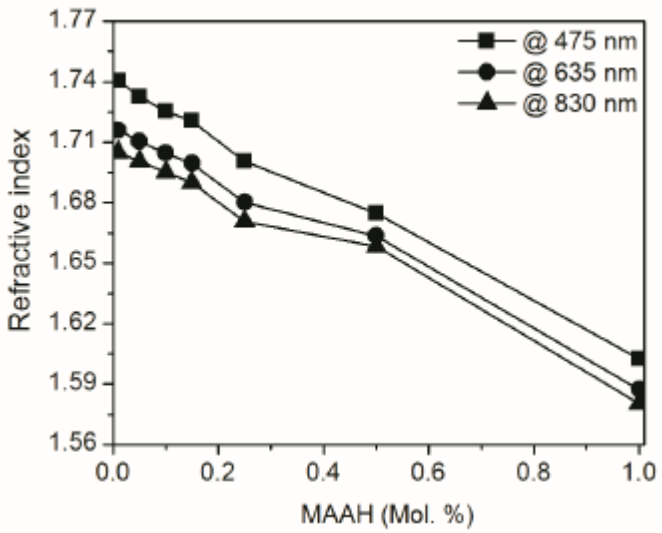

Figure 4-15: Refractive index as a function of MAAH molar concentration at selected wavelengths (475 nm, 635 nm and 830 nm)

Optical quality

The optical performance of the material that gave the highest refractive index for both strategies was determined through visible absorption spectroscopy and roughness measurements. Figure 4-16 shows the absorbance spectra of the two optimised sol-gels: a) 1 mol.% of DPHDES and b) 0.01 mol.% of MAAH. The absorption for the sol-gel containing 1 mol.% of DPHDES was higher than for the one containing 0.01 mol.% of MAAH. This can be explained by the presence of aromatic compounds in the DPHDES which are known to present stronger absorption in the UV range [257].

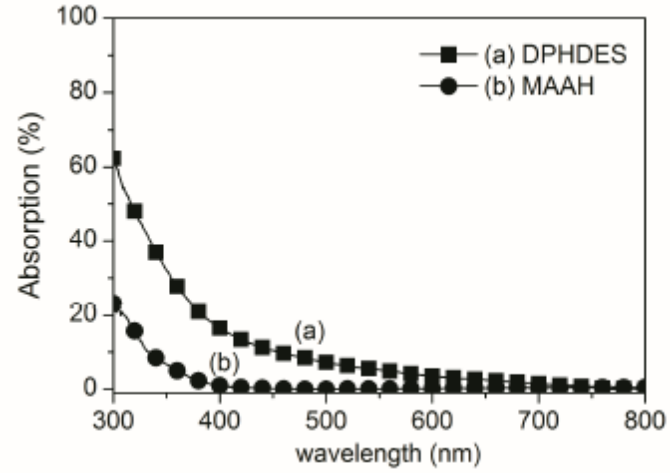

Figure 4-16: Absorbance spectra of hybrid zirconia sol-gel thin films containing 1mol% DPHDES and 0.01mol% MAAH.

The roughness of the thin films, as measured by an optical profilometer, revealed that on average the materials composed of DPHDES exhibit surface inhomogeneities approximately two times higher than those composed of MAAH based materials, as shown in Figure 4-17 and Figure 4-18. It was observed that DPHDES based materials tend to form regular inhomogeneities with an average roughness of 3.14 nm. Inhomogeneities seem to be more dispersed in the MAAH based thin films, resulting in a decrease of the average roughness.

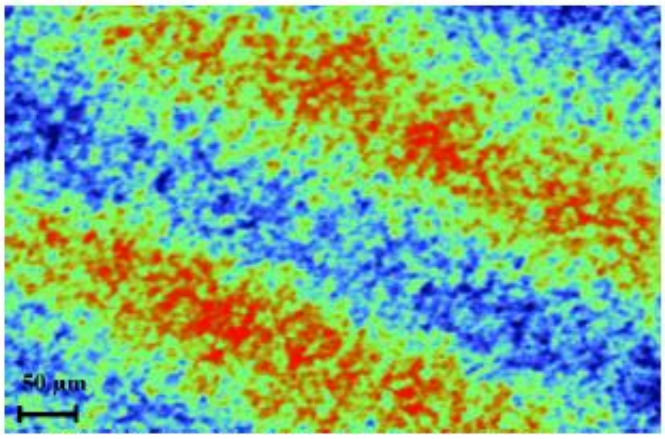

Figure 4-17: Roughness of 1.73 nm measured of sample containing 0.01 mol.% of MAAH.

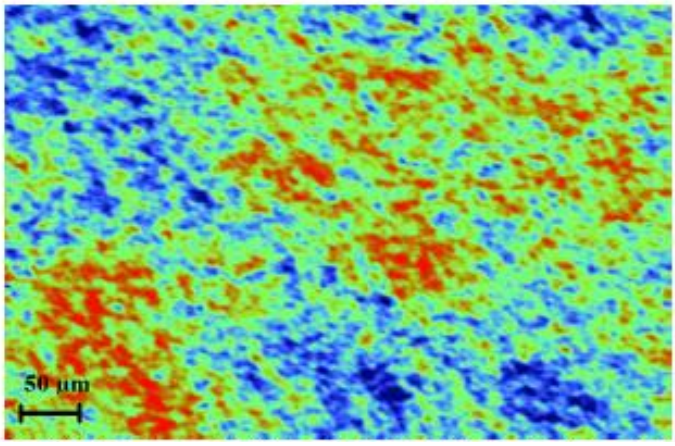

Figure 4-18: Roughness of 3.14 nm measured of sample containing 1 mol.% of DPHDES.

From these results it can be concluded that the material composed of 0.01 mol.% of MAAH is the most suitable and promising material for optical sensor applications requiring high refractive index and excellent optical performances.

In summary, high refractive index materials have been prepared using two original syntheses strategies at ambient temperature. The first strategy employed organosilane precursor while the second one employed chelating agent. The correlation between the refractive index and the material composition is discussed and it is proposed that the effect of the molar refraction and the morphology of the thin film materials are the main factors influencing the refractive index values. The maximum refractive indexes obtained were 1.746 for the material containing 1 mol.% of DPHDES and 1.716 for the material containing 0.01 mol.% of MAAH. However the material containing 0.01 mol.% of MAAH showed lower roughness and better optical absorption compared to the material containing 1 mol.% of DPHDES, hence making it as an excellent candidate for the development of optical sensors requiring high refractive index and low propagation loss in the visible range.

Optical and structural characterisation

Similar to the Zr based HRI material, the hybrid materials based on the three different transition metal alkoxides (niobium, tantalum and vanadium) were deposited by spin-coating on glass and silicon substrates to form transparent thin films, and heat treated at 100°C for 1 hour for the final stabilization of the layer.

Optical measurements were performed using ellipsometry and transmission measurements in order to determine the performance of the materials. Transmittance spectra and ellipsometry measurements were conducted over the 400-900 nm spectral range. Thickness and refractive index of the films were calculated using the Tauc-Lorentz model fitted to the ellipsometry data [258]. In order to characterise the propagation losses, thin films were deposited on silicon substrates with a thick optical isolation layer. A ZrO_2 based hybrid material with a refractive index around 1.5 and a thickness of 6 µm was chosen as the optical isolation layer due to its low absorption in the visible range and its well-known optical properties [259]. The thickness of the obtained hybrid thin films was specified at 100 nm for single-mode waveguiding, in accordance with beam propagation method calculations (OlympiOs, C2V Netherlands). The thickness of the films was controlled primarily by the rotating speed of the spin-coater during deposition.

Optical propagation loss measurements in the planar waveguides were conducted using a polarization maintaining fibre (TE mode) coupled laser diode at 638 nm.

Light was coupled into the waveguides using a high refractive index TiO_2 prism. Propagation losses were estimated from the exponential profile of the scattering losses from the surface of the waveguides as a function of propagation distance, using a high resolution CCD camera [239].

Figure 4-19 shows the variation of the refractive index as a function of the wavelength for the three different metal oxide compositions investigated here. Normal dispersion curves were obtained, with higher refractive index values for lower wavelength as expected. Refractive indices of 1.870, 2.039 and 2.308 were measured at 635 nm for tantalum, niobium and vanadium hybrid thin films, respectively.

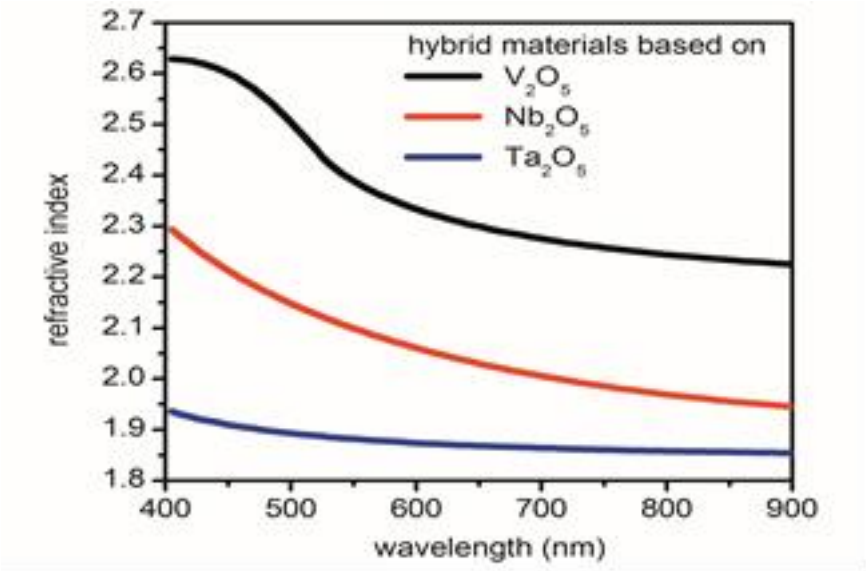

Figure 4-19: Refractive index of the V2O5, Nb2O5 and Ta2O5 hybrid based materials versus the wavelength in the visible range.

The difference in the refractive index value of these materials can be explained by the ability of the metal transition to condense and form large clusters or possibly agglomerates during the sol-gel synthesis, the deposition and the final thermal stabilization. As the three transition metals employed here exhibit similar physico-chemical properties (electron configuration, oxidation states, atomic radius, electronegativity), the main parameter governing the condensation process was the atomic size, which can be correlated with the measured refractive indices. The smaller the atomic size, the higher the refractive index suggesting that the condensation process of the oligomeric species into larger clusters is facilitated by smaller molecules. This hypothesis was supported by the fact that polycondensation reactions in sol-gel chemistry require accessibility to the active hydroxide sites. This

access is dependent on steric hindrance which can be caused by the presence of large atoms such as transition metals, thereby limiting the polycondensation reaction propagation. To my knowledge, this essential physico-chemical sol-gel phenomenon has not been highlighted before and complementary investigations are ongoing in our research group to confirm the fundamental chemistry of this phenomenon.

The transmission spectra in the visible range of the developed materials deposited on glass are plotted in Figure 4-20. For comparison purposes, the thickness of the three samples was adjusted to 100nm.

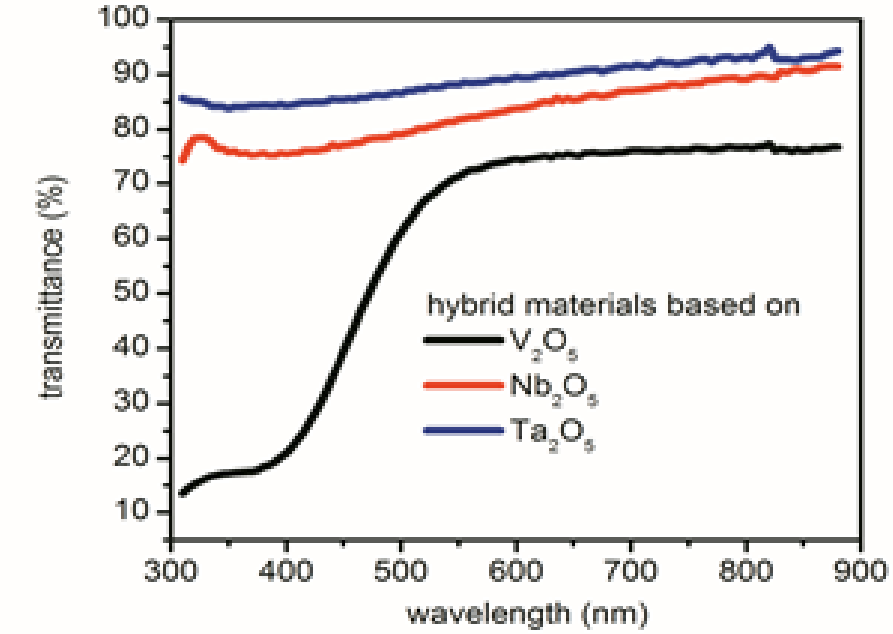

Figure 4-20: Transmission spectra of hybrid materials for the three metal oxides.

It was followed that the transmission spectra was strongly dependant on the nature of metal oxide that has been incorporated into the hybrid material. The highest transmission was obtained with the tantalum based material, followed by niobium and vanadium, with transmission values at 635 nm of around 90, 85 and 75%, respectively. It is important to note that after deposition and thermal stabilization of all films, the V_2O_5 based hybrid thin film was yellowish in comparison with the two other samples which were colorless. It is well known that color changes of transition metal-based materials are due to a modification of the number of electrons in the d orbitals of the transition metal [16]. Here, the most plausible explanation of yellowing found was that the molecule of water released during the sol-gel condensation reactions (V-OH+V-OH → V-O-V + H_2O) was re-utilized in the hydrolysis of the vanadium precursor, leading to larger oligomers in which the

number of electrons in the ‘d’ orbitals of the vanadium atom is significantly increased explaining both the color change of the vanadium based thin film and reinforcing the hypothesis proposed earlier regarding the reactivity of the vanadium precursor.

Loss measurements based on measurement of the scattered light profile in planar waveguides (638 nm - TE polarized light) containing tantalum and niobium are shown in Figure 4-21. It was impossible to measure the losses in the hybrid material containing V_2O_5 since no light could be propagated into the waveguide. This was due to the strong visible absorption that has been observed in the transmission measurement. The propagation losses of Nb_2O_5-based waveguides were measured to be 2.45 dB/cm, while the tantalum-based waveguides exhibited slightly lower losses of 1.98 dB/cm.

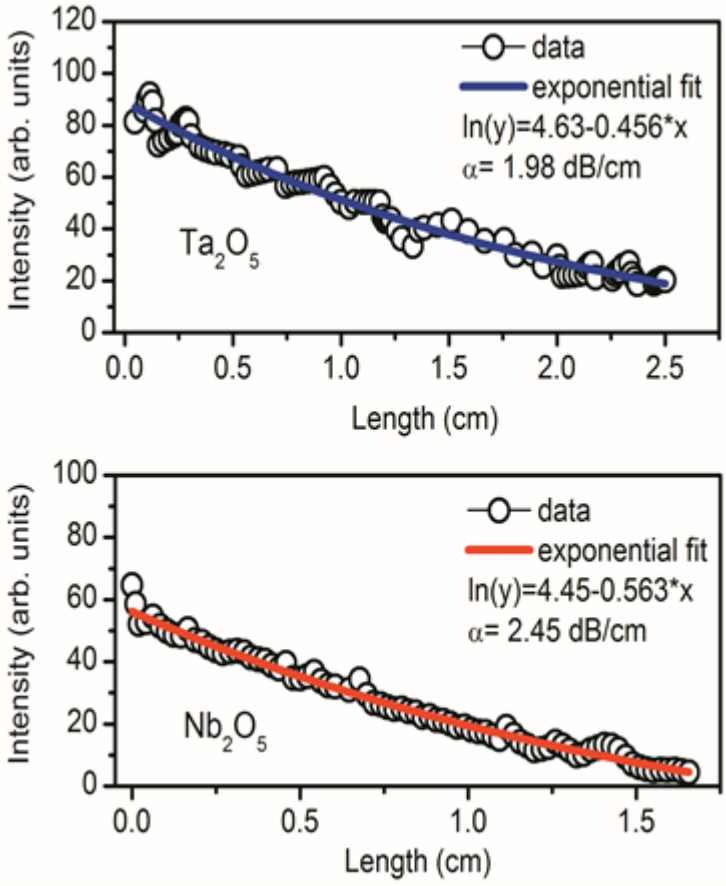

Figure 4-21: Results of top-side surface measurements of scattered light intensity along propagation axis of the planar waveguides fabricated with hybrid materials based on Ta2O5 and Nb2O5.

These results suggest that the propagation losses are mainly related to the material absorption. Therefore, these propagation losses are comparable to those reported in the literature for hybrid materials containing ZrO_2 or TiO_2 [250, 252].

In summary, the optical properties of hybrid thin films synthesized from three different transition metal alkoxides were compared. It was found that the hybrid material containing tantalum had lower optical propagation losses than the one containing niobium. No light could be propagated into the waveguide containing vanadium, probably due to the strong absorption of the vanadium in the visible range. Based on these results the tantalum based material is the most promising HRIL solution to be used to enhance the sensitivity of the biosensor platform. This will be used in future platform fabrication. To achieve this objective, further characterisation of the refractive index and optimisation of the deposition conditions, including the correlation between the spin-speed and thickness were essential.

Properties of the Tantalum based HRI based thin film

Figure 4-22 shows the variation of the refractive index and transmission as a function of the wavelength for the tantalum sol-gel material investigated here. A typical dispersion curve was obtained with higher refractive index values for lower wavelength. A refractive index value of 1.870 was measured at 638 nm for tantalum. At this wavelength the transmission of the material was 89.8% for a film thickness adjusted to 100nm.

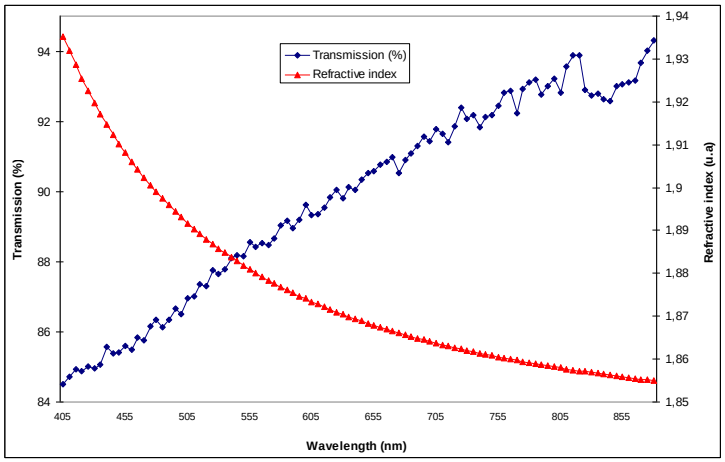

Figure 4-22: Evolution of the refractive index and transmission of the HRI material as a function of the wavelength.

It is important to note that after deposition and thermal stabilization the films were transparent to slightly whitish, which can explain the observed absorption in the whole visible range. The whitish colour is the proof of the formation of oxide groups (Ta-O-Ta), probably as oligomeric clusters resulting from the sol-gel condensation reactions of reactive Ta-OH groups during the synthesis, deposition process and thermal drying of the coatings. These results suggest that the optimum thickness for a refractive index of 1.870 needs to be 57 nm in order to provide an optimum EF enhancement, without guiding the light in the HRI layer.

The thickness of the HRI deposited by spin-coating on a silicon substrate at speeds comprised between 300-500 rpm was found to range between 55 and 80nm, as shown in Figure 4-23.

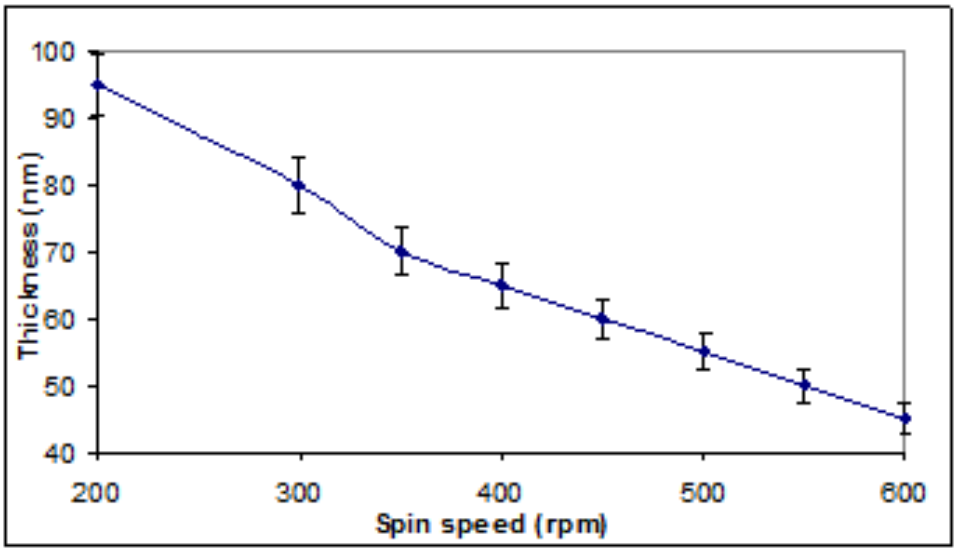

Figure 4-23: Thickness of the HRI tantalum based sol-gel material as a function of the deposition speed on a silicon substrate.

However, as the film thicknesses is generally dependant on the nature of the substrate (due to adhesion effects) and as the measurement of the HRI layer thickness could not be performed after deposition on the photoreactive sol-gel layer (because of difficulties in defining a valid ellipsometry model simulating two layers of significant refractive index difference), it was necessary to perform tests with deposition speeds varied throughout the range of speeds utilized in the thickness characterisation on the silicon substrate. This was the only way to ensure that the desired thickness will be obtained.

4.1.7 Optimisation of the Waveguide Fabrication

Effect of the UV – irradiation time

The mask aligner used in this study exhibits fixed wavelength and power (365 nm and 20 mW/cm^2, respectively), the only variable that can be employed to adjust the waveguide widths was the irradiation time. Initial broad exposure times investigations showed that the waveguides with width close to 6 microns can be achieved with exposure times ranging between 20 – 45 seconds, as represented in Figure 4-24.

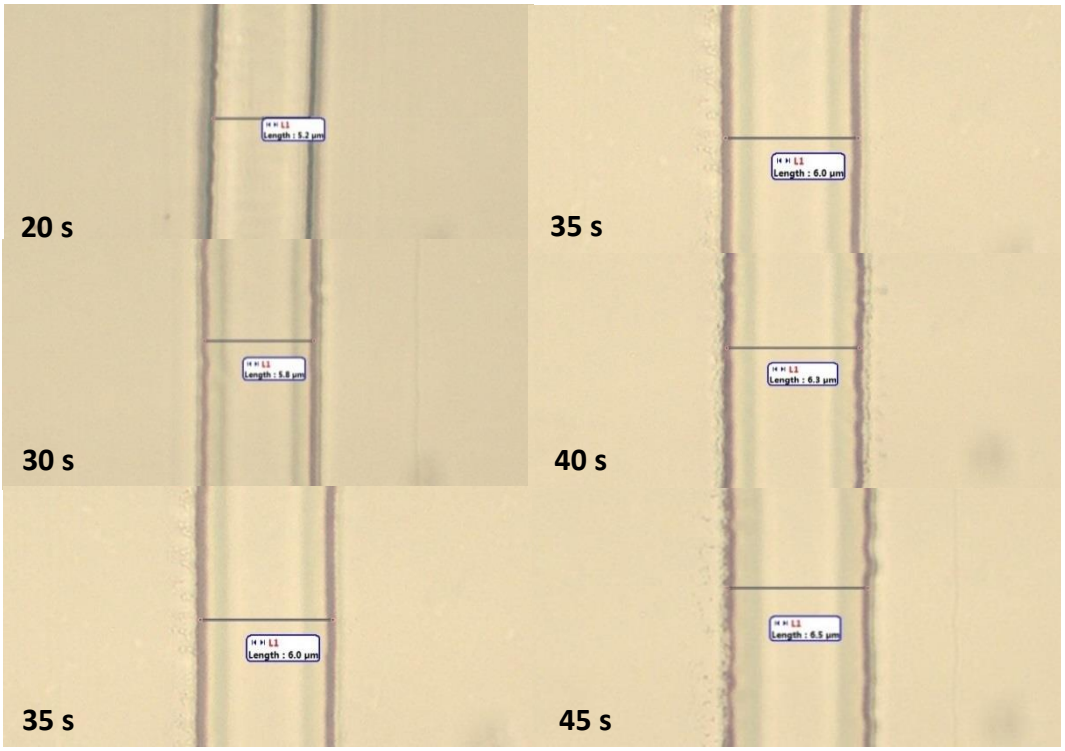

Figure 4-24: Top view optical images of waveguides photopatterned employing different UV-irradiation times.

From Figure 4-24, it can be seen that the progressive increase of the irradiation time produces a slight increase of the waveguide width. Values for the measured width including error bar measurement (±0.1micron) are plotted in Figure 4-25.

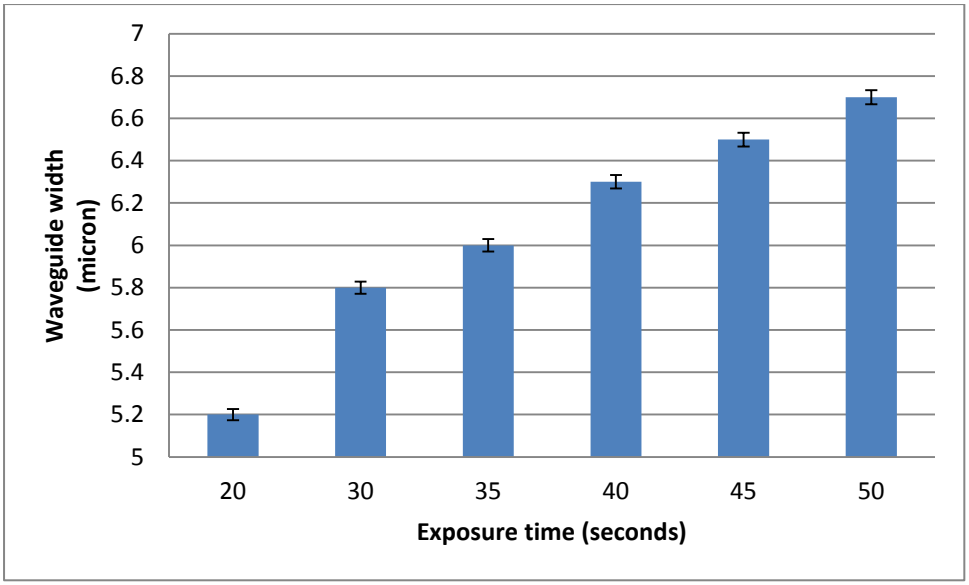

Figure 4-25: Waveguides width as function of the irradiation time.

Figure 4-25 shows that the most adequate exposure time to fabricate 6microns width waveguides is 35seconds. Optical and SEM images of the waveguides cross-sections fabricated employing this irradiation time are represented in Figure 4-26 and Figure 4-27.

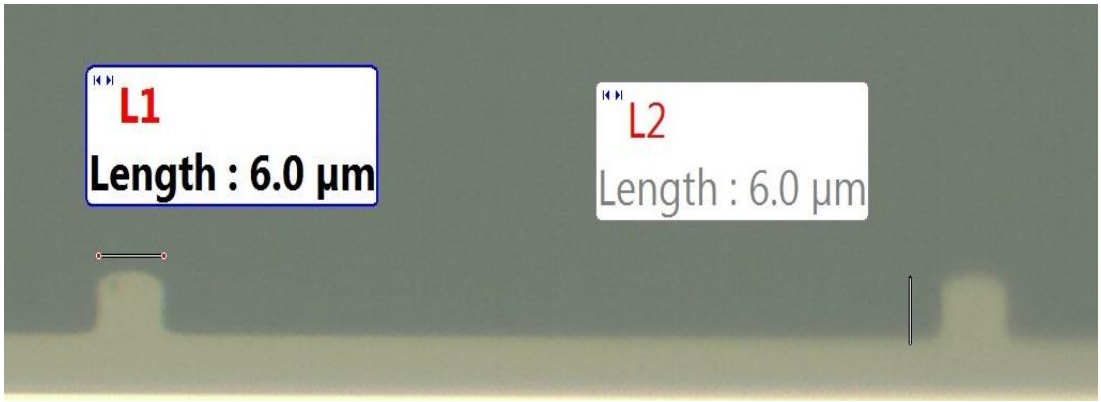

Figure 4-26: Cross-section optical image of waveguide fabricated with 35seconds UV – exposure time.

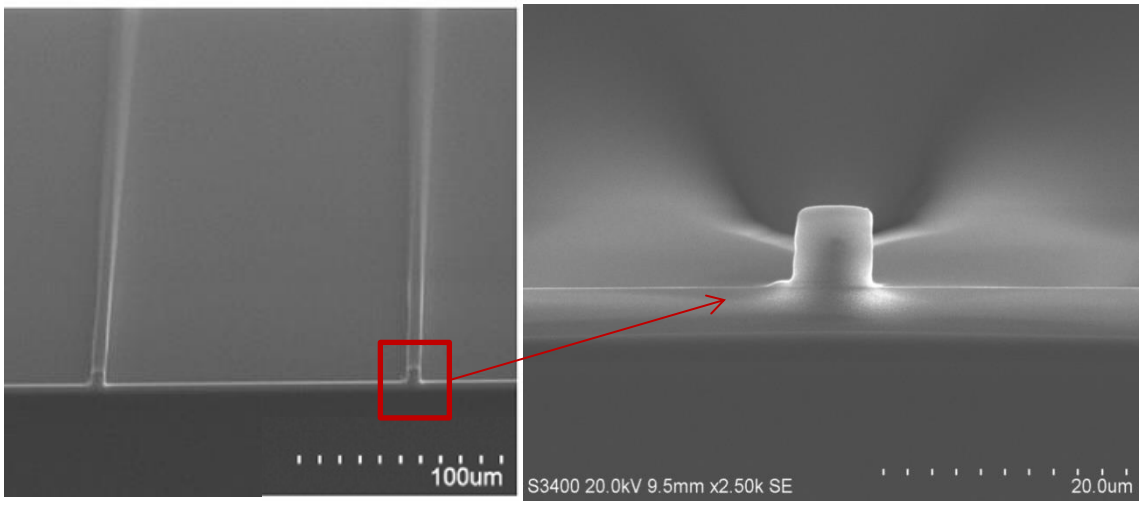

Figure 4-27: Cross-section SEM image of waveguides fabricated with 35seconds UV – exposure time.

These images (Figure 4-27) confirm that the geometry of the waveguide is quasi-square (slightly rounded at the top) with a 6 micron cross section. Furthermore, the buffer layer, fabricated by spin-coating material M at 1000 rpm, is also found to exhibit a thickness close to 6 microns. These images confirm the thickness values measured previously by the m-lines technique.

In order to further confirm the dimensions of the waveguides, optical profilometry was performed, as shown in Figure 4-28.

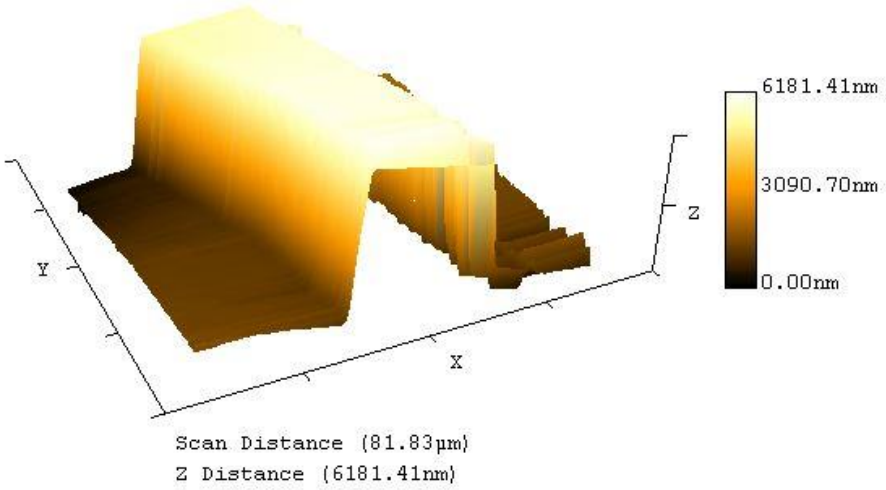

Figure 4-28: Optical profilometry of waveguides fabricated with 35seconds UV – exposure time.

Optical profilometry reveals that waveguides exhibit a height of approximately 6.18 microns and a width of 6 microns. Based on this final characterisation, there is no doubt that the fabricated waveguides are quasi-square with a cross section close to 6microns.

It is of great importance to remember that if the core of the optical waveguides can be fabricated with a 35 second irradiation time, the required refractive index to allow singlemode operation necessitates a further UV-irradiation of 600 seconds (as described in section 4.1.2). This can be achieved after deposition and stabilisation of the protective layer as described earlier in this chapter.
Having identified both the deposition and UV-exposure conditions to achieve squared waveguides with a section of 6 microns, the double splitter biosensor platform was fully fabricated and is presented in Figure 4-29.

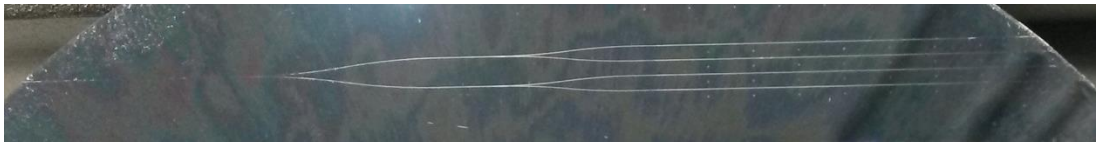

Figure 4-29: Photograph image of the double splitter based biosensor platform.

4.2 Simulations

4.2.1 Simulation of the singlemode waveguides

In order to identify the effect of each of the structural parameters on the subsequent optical properties of the singlemode waveguides, the simulation studies have been divided into two sub-sections: the effect of the dimensions and the effect of the refractive index contrast between the core and the cladding of the waveguide. These studies have been performed at three different wavelengths of interest: 635, 1310 and 1550nm.

4.2.2 Effect of the waveguide cross-section

The waveguides cross-section sizes were varied in the range 4 – 10 microns. The objective was to define the required refractive index contrast to obtain singlemode waveguides with any of the dimensions. As shown in Figure 4-30, for any of the studied wavelengths, one can see the progressive increase of the cross-section waveguide necessitates the increase of the refractive index contrast in the singlemode waveguides.

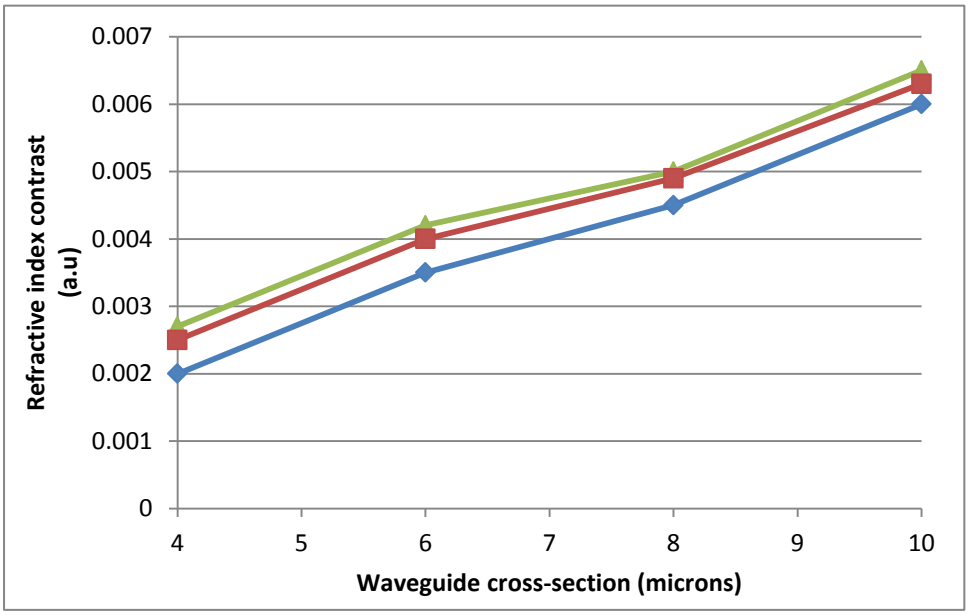

Figure 4-30: Relationship between the waveguide cross-section and the refractive index contrast to achieve singlemode waveguides as obtained by simulations with Olympios software.

4.2.3 Effect of the refractive index contrast on the optical definition of a 6×6µm² waveguide.

Figure 4-31 shows the numerical simulation in TE modes of a single-mode waveguide of 6×6µm^2 cross-section with two different refractive index contrasts (RIC) 0.001 and 0.002 at 635, 1310 and 1550nm. The white square is drawn to represent the waveguide cross-section.

It can be seen that for a RIC of 0.001, the propagating light is well confined in the waveguide at 635nm, whereas it is clearly dispersed outside it at 1310 and 1550nm. Also, the dispersion seems greater at 1550 nm than 1310nm, which tends to confirm

that the dispersion increases with the increase of the wavelength for a given RIC. By increasing the RIC, one can clearly observe the decrease of the light dispersion outside the core of the waveguide at 1310 and 1550nm. It can be concluded that singlemode waveguides are obtained whatever the RIC at 635nm, whereas an RIC of 0.002 is required for the infrared wavelengths.

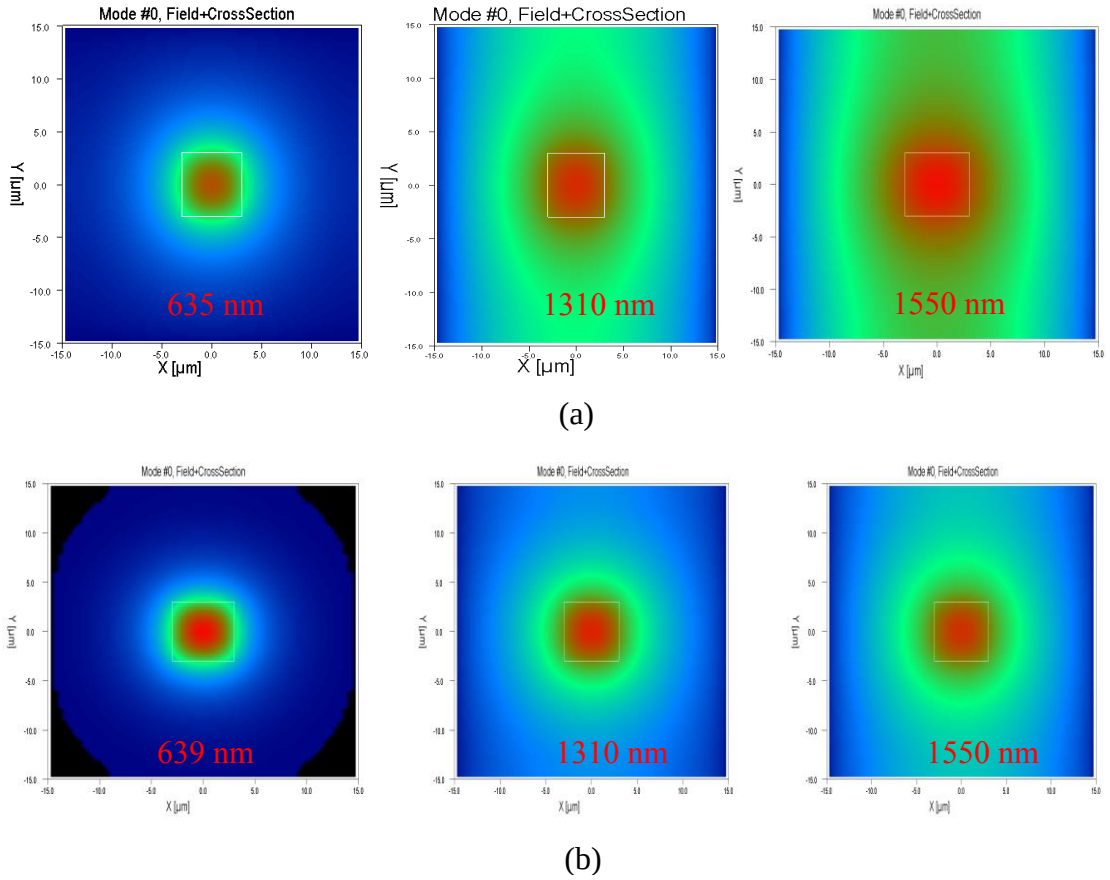

Figure 4-31: Near-field simulations of 6×6 µm^2 waveguides at 639, 1310 and 1550 nm with RIC of 0.001 (a) and 0.002 (b).

In order to further investigate the effect of the RIC onto the optical definition of waveguides at 635 nm and identify the RIC tolerance window for our future materials development phase, simulations involving increase of the RIC up to 0.004 were performed, and represented in Figure 4-32.

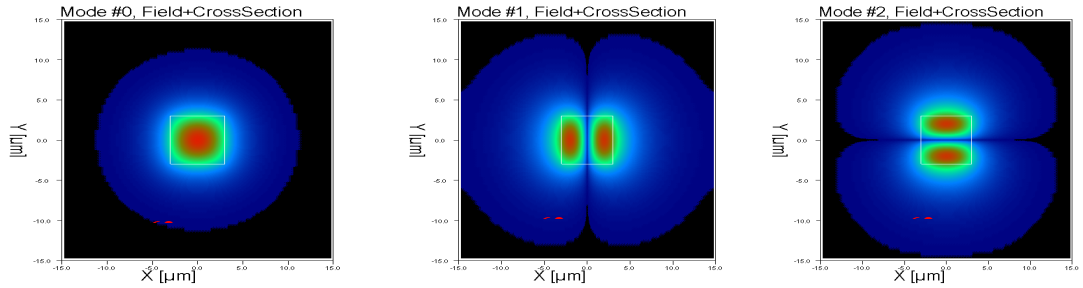

(a) 1st mode (b) 2nd mode (c) 3rd mode

Figure 4-32: Near-field simulations of 6×6 µm² waveguides at 635 with RIC of 0.004. First, second and third modes are shown in a, b, and c.

This figure demonstrates that for a 0.004 RIC three modes are observed. However, one can see that the second and third modes are mostly centred within the waveguide core and limited intensity is dispersed within the waveguide cladding. A calculation of the intensity of the dispersed light outside the core was found to be greater than 5%. It can be concluded that the waveguides can be still considered purely singlemode with a RIC of 0.004 at 635nm. This result is critical in the perspective of the material development as it offers a large window of RIC (from 0.001 to 0.004) without significantly affecting the optical definition of the waveguides.

Further simulations of the waveguide in the near infrared were performed at RIC up to 0.008 RIC, as shown in Figure 4-33. These simulations showed the appearance of the second and third modes in horizontal and vertical positions, respectively. These are clearly positioned outside the white square (core of the optical waveguide), the intensities of which have been estimated to 38% and 35% of the input laser intensity.

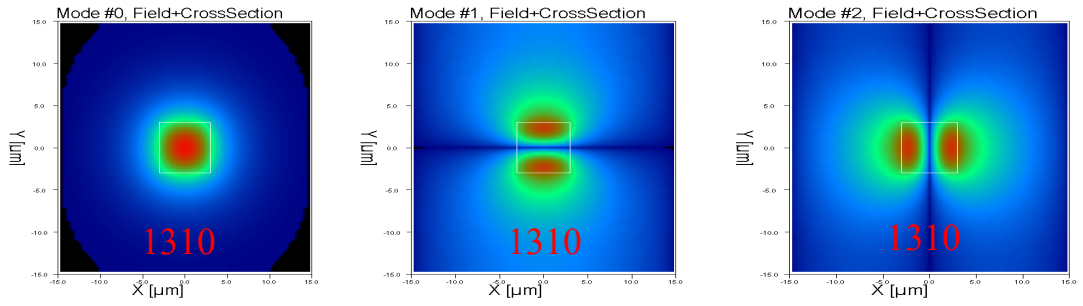

1rst 2nd 3rd

Figure 4-33: Near-field simulations of 6×6 µm² waveguides at 1310 nm with RIC of 0.008.

Having in this section defined the conditions to achieve singlemode optical waveguides; the future objective of the simulations studies is to quantify the intensity of the evanescent field and the possible strategies to increase it, therefore increasing the sensitivity of the biosensor. This is the subject of the following section.

4.3 Biosensor Characterisation

4.3.1 Characterisation Set-up

An experiment was conducted by fully immersing the substrates in the analyte solution for a given period of time, withdrawing the samples and leaving to dry before recording the UV-Visible spectra. These were recorded every 10 minutes up to 120 minutes of immersion. Recorded spectra are presented in Figure 4-34. It can be clearly seen that a progressive increase of the absorption in the whole UV-Visible spectral range occurred within a standard time frame. Two essential conclusions can be drawn from this result. First, the formation and adhesion of the biofilm on the HRIL is demonstrated. Second, the fact that absorption was observed after 10 minutes of immersion suggests that the biofilm formation starts soon after the sample is immersed in the analyte solution. Furthermore, this also indicates that to be detected by the UV-spectrometer, the biofilm thickness must be greater than 5 nm.

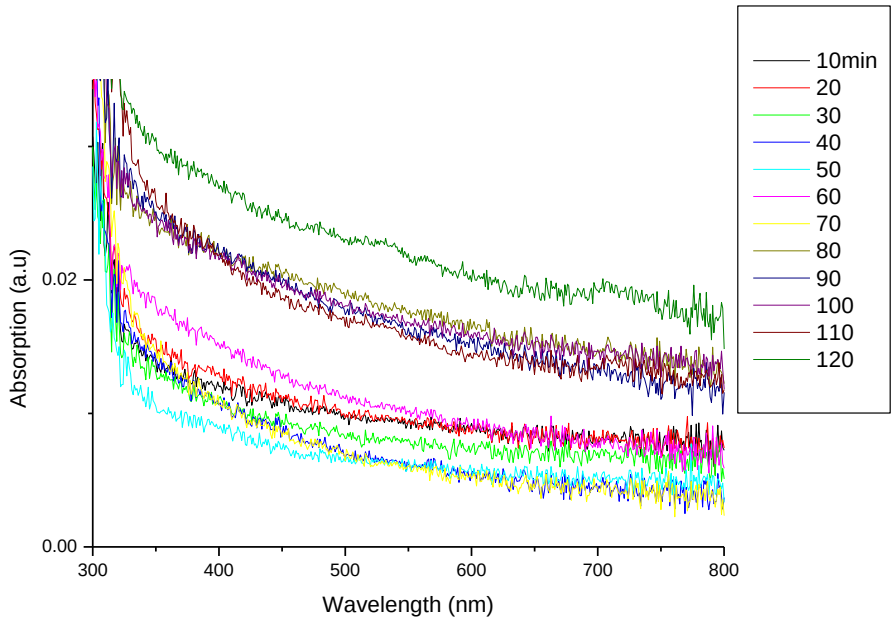

Figure 4-34: UV-Visible absorption of the biofilm as function of time.

Though the results shown in this section highlight the biofilm formation by the identification of its absorption, they are unable to provide information on other physical phenomena that can also contribute to the alteration of the EF intensity. These include scattering due to the change in the surface refractive index and possible formation of large particles/agglomerates. Such clarifications are of great interest for this study in order to quantify the effect of each physical phenomenon. However, the biofilm was found to be relatively rough when measured by the Metricon 2010. Therefore, the prism-coupling method and the ellipsometry were found unreliable to provide refractive index values. On the other hand, as the agglomeration of the various components of the biofilm takes place during the growth of the biofilm, measurement of the particle sizes, usually performed using DLS in liquid samples was impossible on solid surfaces with the standard techniques used in material science and chemistry labs. This may be possible to perform with neutron scattering technique, as shown in a recent publication [260]. Unfortunately access to such instruments was limited.

4.3.2 Characterisation of the Channel Optical Waveguides

In order to identify the suitability of the fabricated optical waveguides for the biosensor sensing application it was essential to initially characterise their optical properties including the optical modes and propagation performances at the operating optical wavelength (639nm).

For this purpose, individual waveguides of the double splitter PLC platform were characterised by propagating light into the input waveguide by an end-fire coupling from a pigtailed laser diode with maintained TE polarization (Thorlabs, $\lambda = 639$ nm). The relative alignment of waveguide and fibre was assisted by a microscope positioned above. In addition to the sensing wavelength (639nm), two other laser diodes at 1310 and 1550 nm were also employed to further identify the nature of the optical modes and help in correlating the structure of the waveguides (dimension and refractive indices contrast between the core and the cladding) to their optical properties and propagation performances.

Figure 4-35 shows the propagation of the light within the four optical waveguides of the fabricated double splitter. From this figure it can be observed that the fabricated double splitter is effectively operating as the splitting of the light at both Y junctions resulted in four output signals issued from one single source. Furthermore, it can be seen that the light is clearly confined in the core of the optical waveguides, suggesting limited loss of light in the waveguide core. This demonstrates the success of the whole process developed in this thesis including the effectiveness of the simulation studies, the choice of the materials and the means to develop them as well as the optimisation of the fabrication process.

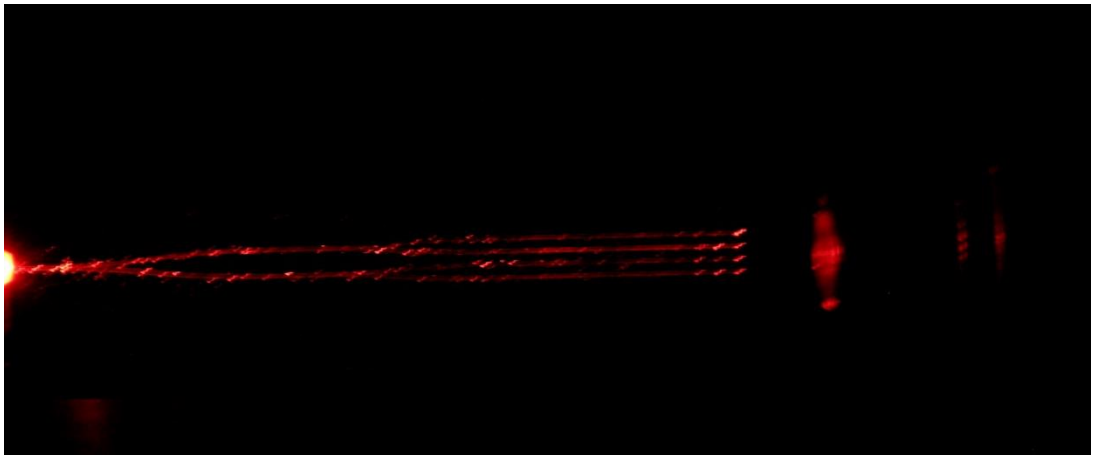

Figure 4-35: Photograph image of the propagation of the light within the four waveguide issued from a 639 nm laser diode source

However, although the operation of the double splitter is demonstrated, the nature of the light propagation needed to be further investigated. An initial screenshot of the near field light rays of the four waveguide outputs were recorded, as shown in Figure 4-36.

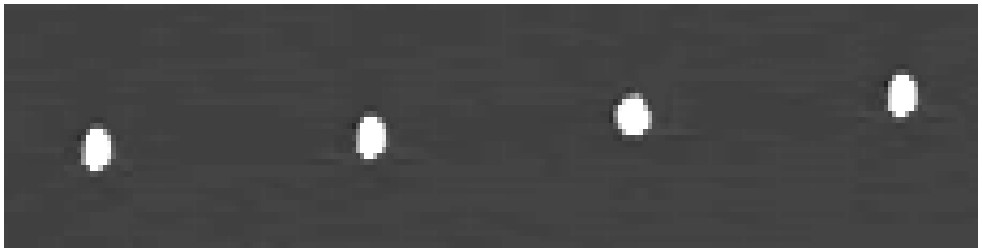

Figure 4-36: Near field image of the four waveguide outputs at 639 nm.

It can be observed that the four waveguides exhibit a similar output signal, with a spherical definition, suggesting that the light is propagating similarly within each of the four waveguides. However, to identify more clearly the nature of each waveguide, it is necessary to characterise them individually to identify differences due to either the presence of the sensing windows or due to the wavelength of the input laser. For this purpose and to avoid any confusion with the analyses of the waveguide properties it was necessary to remember the structure of the PLC platform, in particular the position of the sensing windows and the reference waveguide (Figure 4-37).

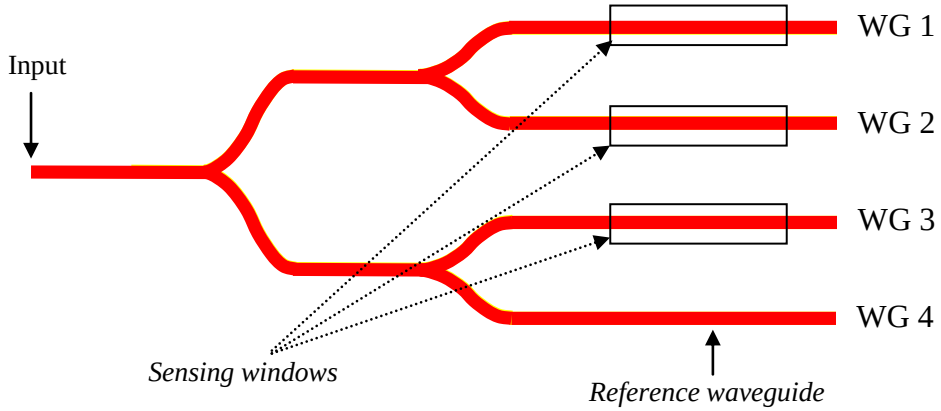

Figure 4-37: Design of the biosensor platform.

Figure 4-38 presents images of the near field spectra of the four waveguide. It can be seen that all waveguides located in the first row (images a to d) recorded with the 639 nm laser diode exhibit a spherical signal. Waveguide 4 seems however to exhibit a slightly larger spot than the three others, the size of which fits into the red square. The regular sphericity in the optical definition of these near field images demonstrates that all four waveguides are singlemode. However, the fact that the optical spot for waveguide 4 exceeds the dimensions of the other three indicate that the presence of the protective layer in the sensor window would result in a better confinement of the optical signal in the waveguide core and as such optical losses are minimised.

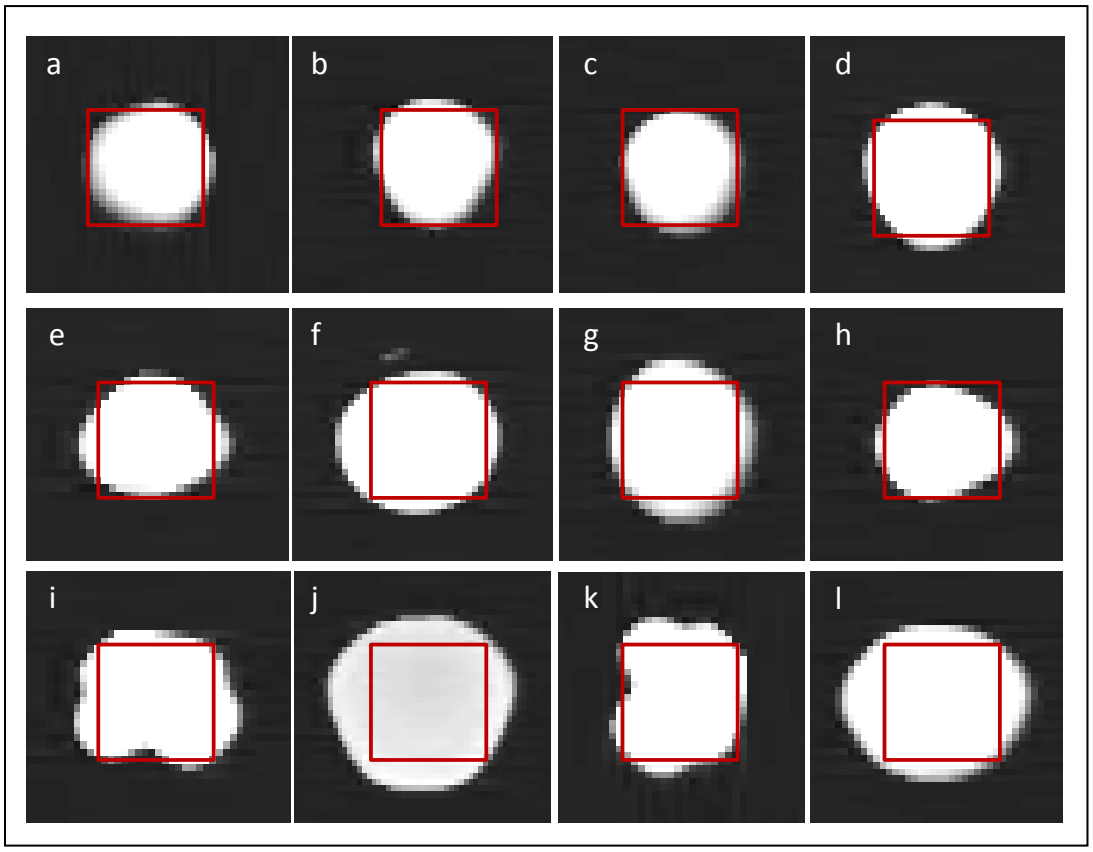

Figure 4-38: Near field images of the four output waveguides recorded employing three different laser diodes tuned at 639, 1510 and 1550nm. The red square represents the theoretical signal of 6 microns singlemode squared waveguide and is a guide for the eye to help in comparing the different signal spots.

The second row of near field images (images e to h) characterised using a laser diode tuned at 1310 nm show in general a distortion of the optical signal, especially for waveguides 1 and 4, which tend toward an elliptic horizontal shape. These optical waveguides are definitely multimode at this wavelength. Furthermore, the fact that no significant difference in the optical definition between waveguide 1 and 4 is observed indicates that the confinement due to the presence of the protective layer in the reference waveguide does not produce any effect on the nature of the optical definition of the output signal. In addition to this, near field imaged for all waveguides exceeds the red square further confirming the multimode character of these waveguides. The multimode character is even more accentuated when employing the laser diode tuned at 1550nm. Waveguide I and k clearly highlights the appearance of four lobs at each of their extremities, symbolising the presence of four modes (at least). Furthermore, the near-field spots are significantly larger than the

red square. Importantly, these results are in very good agreement with the simulation studies summarised in Figure 4-31, where it was found that for both 1310 and 1550 nm the near-field images exceeds the dimensions of the waveguides, while they remain within it for a laser diode tuned at 639nm.

In summary, these optical characterisations have highlighted that singlemode waveguides can be achieved at 639 nm with quasi-squared waveguides having a refractive index contrast of 0.003 between the core and the cladding.

4.3.3 Sensing Performance

In previous section, the effectiveness of the developed biosensor platform in static systems (where no flow rate is applied to the analyte solution) was discussed. The objective of this section is to evaluate the performance of the developed biosensor platform under quasi-static flow rate (by progressively increasing the flow rate). Consequently, the sensing performance was correlated to the physico-chemical phenomenon taking place at the waveguide/solution interface.

Quasi-static flow rate

The sensing performance of the platform was characterised by monitoring the output intensity while the analyte of interest was circulating across the sensing windows to allow the formation of the biofilm on the sensing windows, employing the experimental set-up described in

Figure 3-3. As shown in Figure 4-23, the thickness of the HRIL material can be controlled by the deposition speed. Also as detailed in Figure 3-23, the optimum thickness for HRIL is 57 nm so that the intensity of the EF is maximised at 639nm, as shown in Figure 3-22. In order to maximise the opportunity to get a thickness as close to 57 nm, as required to maximise the EF, it was decided to perform a range of trials with HRIL coatings deposited at different speeds. Typically, the speeds used for the HRIL thickness characterisation (300 – 500 rpm) were employed as at these speeds the HRIL thickness was found to range between 55 and 80 nm.

As shown in Figure 4-39, the intensity of the light collected at the output of the waveguides as function of the reaction time (biofilm growth) is clearly relying on the

HRIL deposition speed. One can observe two different behaviours depending on the HRIL deposition speeds. For any speed in the range 300-450 rpm, the output intensity does not appear to significantly vary above the measurement uncertainty. However, the output intensity measured with the HRIL deposited at 500rpm shows a clear dependency over the reaction time. In this curve three trends can be noticed as function of the reaction time: 1) a strong decrease in slope of 7.6.10-3 IU/min (R^2>90%) from 0 to 50min of reaction; 2) linear decrease with slope of 1.9.10-3 IU/min (R^2>96%) for reaction times comprised between 50 and 90min; 3) stagnation of the intensity within the error bar measurement for reaction times from 90 to 140min.

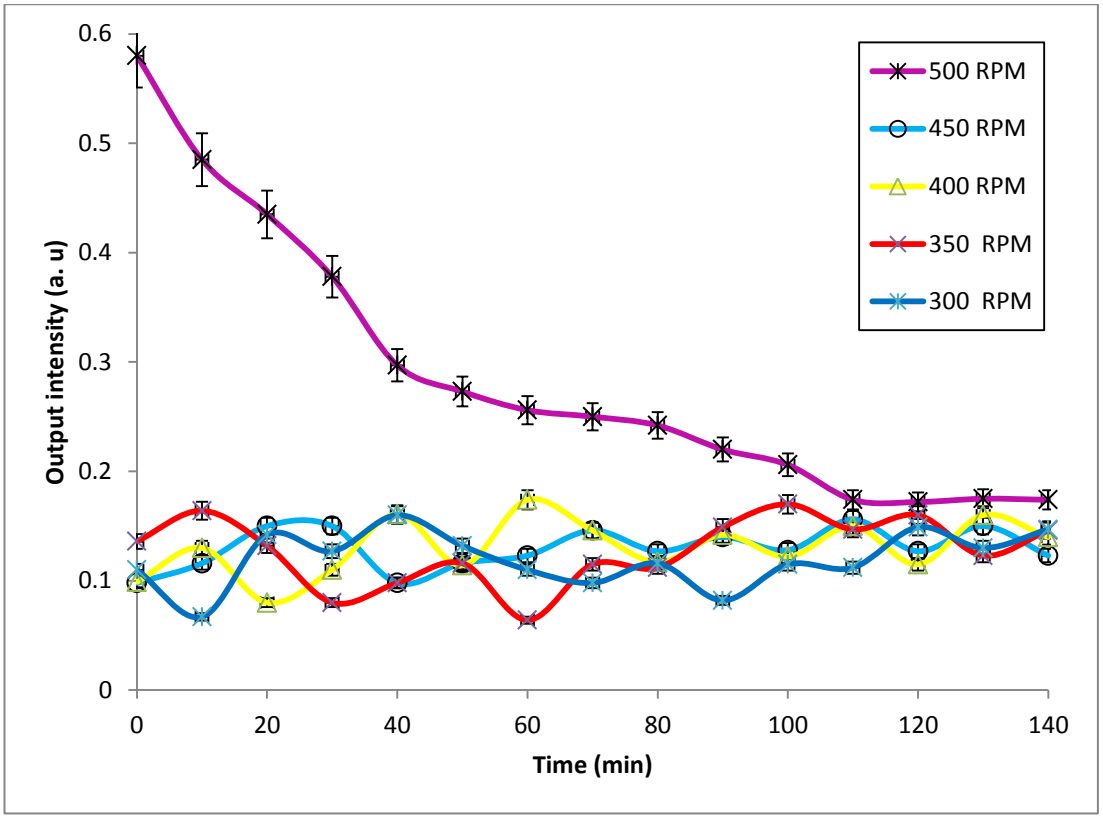

Figure 4-39: Normalized output intensity of the waveguides as function of reaction time for the quasi-static flow-rate regime.

As expected by the simulation study, the sensing response of our waveguide-based biosensor platform relies on the interaction between the evanescent field and its surrounding environment. The stability of the output intensity observed for the samples prepared with HRILs deposited with speeds ranging from 300-450rpm, suggest that the sensor platform is insensitive to the biofilm formation at the surface of the waveguide. The thicknesses measured on the silicon wafer substrate comprises

between 62 and 90nm, which according to the simulations of the HRI layer, should act as guiding layer and not as an evanescent field enhancement layer. By correlating the simulations studies with the experimental sensing responses of the biosensor platform, one can conclude that the main phenomenon explaining the insensitivity to biofilm formation is associated with the transfer of the whole optical signal in the HRIL. This is confirmed by the relatively low output intensity compared to the sample prepared with a deposition speed of 500rpm. In addition, when the light is guided within the HRIL, scattering of the light at the interface with the interface windows surface, is a further source of optical losses explaining the drastic decrease of the output intensity. Therefore, the fact that no significant change in the output intensity is observed suggest that the transfer of the optical signal to the HRIL occurs similarly and is not affected by the HRI layer, as long as it exceeds the thickness threshold, thereby confirming the simulation studies.

The decrease in output intensity observed with the HRIL deposited at 500rpm can be explained by the progressive attenuation of the evanescent field due to the biofilm growth. In general, attenuation of optical waveguides is well-known to be intimately associated with absorption and/or scattering phenomena. In our case, one can believe that both phenomena may be simultaneously taking place. The absorption can be confirmed by the UV-Visible characterisation performed on both glass slides and HRIL coatings, as detailed in section 3.3.5. The absorption of the biofilm is clearly observed in the whole UV-Visible spectral range with a progressive increase in the reaction time, undoubtedly demonstrating the absorption of the evanescent field at 638nm. This result clearly supports the decrease of the output intensity versus reaction time in the waveguide-based biosensor. Therefore, the three-step behaviour observed with the HRIL deposited at 500rpm can be explained by the evolution of the thickness of the biofilm at the surface of the waveguide with time and its interaction with the EF. As the EF intensity decreases at the surface of the waveguide (maximum intensity at the surface and intensity nil at distance of 50nm), the interaction between the EF and the biofilm is maximised at the waveguide/biofilm interface, thus explaining the strong decrease (7.6.10-3 IU/min) of the output intensity until 50min of reactions. At 90min of reaction and as the EF intensity decreases, the output intensity undergoes a more moderated decrease (1.9.10-3 IU/min). Finally, above 90min of reactions the output intensity remains constant, while the biofilm is still growing, no additional interaction with the EF is

taking place, and that the thickness of the biofilm is exceeding the evanescent depth penetration.

In summary, these trials have highlighted the following essential points:

1. The closest HRIL thickness to the optimum thickness has been achieved by spin-coating the HRIL solution at 500rpm. Therefore, this deposition speed was used for all further investigations.
2. The output intensity was found to be sensitive for timeframe as short as 10 minutes. This highlights the formation of an initial biofilm layer at the HRIL surface. It is likely that the biofilm growth commences from the initial contact between the analyte solution and the waveguide surface.
3. The three-step behaviour of the output intensity over time can be directly correlated with the growth in biofilm thickness and in these quasi-static conditions; a 50 nm thickness was observed after 90 minutes of reactions.
4. These results have been summarized in a paper published in Sensor and Actuators B: Chemical [260].

Dynamic flow rate

Having demonstrated the concept of this biosensor in section 4.3.3.1 in a quasi-static flow-rate, the next step was to investigate the effect of the flow rate on the biofilm formation. The main objective being the determination of the kinetics of biofilm formation and the correlation of the sensing properties of the platform to the dynamic conditions imposed on the analyte solution. For this purpose, the same characterisation set-up was used with the only alteration being the flow rate imposed during circulation of the analyte solution across the sensor windows. Three different flow rates were applied: 1, 5 and 10 ml/s. Because of the size of the biosensor platform, a 10ml/s flow rate was found to be the highest that could be applied in order to get a real-time record of the output value.

The recorded normalised output intensities of the waveguides as function of the flow rate are represented in Figure 4-40. For comparison purposes, the values for the quasi-static flow conditions are added.

It was observed that, depending on the imposed flow rate, the variation of the output intensity as function of time shows different behaviour. For the majority of flow

rates a three-step behaviour similar to the quasi-static mode can be noted. A strong decrease of the transmission after 20min of reaction (attenuation of 19.2%) was found. This was followed by a quasi-linear decrease up to 110 minutes (where the attenuation is 52%) and then a stabilization of the transmission from 130 minutes of reactions (attenuation of ~32%).

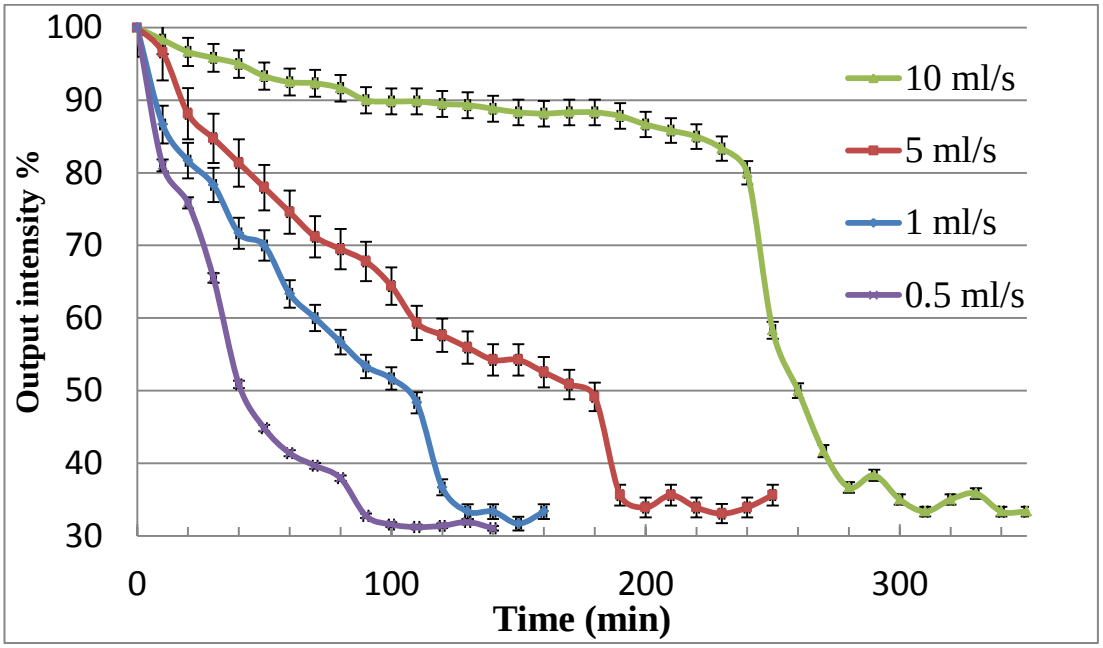

Figure 4-40: Normalised output intensity of the waveguides as function of reaction time with flow-rates at 0.5(purple), 1(blue), 5(red) and 10ml/s (green).

Each of the graphs maybe analysed as follows

Phase A: slow conditioning of the surface to attract deposits. This is a time-dependant process during which biofilm is slowly deposited as an induction layer onto the surface of the waveguide.

Phase B: once the induction layer is attached to the conditioned surface rapid deposition occurs during phase B. This is highlighted by a rapid drop in output intensity which is evident at all flowrates.

Phase C: fully formed, thick, bio layer. Some further deposition and also some removal, steady growth in thickness. Also outside EF range.

At low flowrates 0.5 ml/s the output intensity fell rapidly. This can be attributed to a rapid deposition of the biofilm on the sensor window. However at high flow rates (10 ml/s) a prolonged induction period was noted. This can be attributed to a slow

deposit of biofilm during which the surface is conditioned to accept deposits. Each flowrate will now be examined in detail.

0.5 ml/s flow-rate

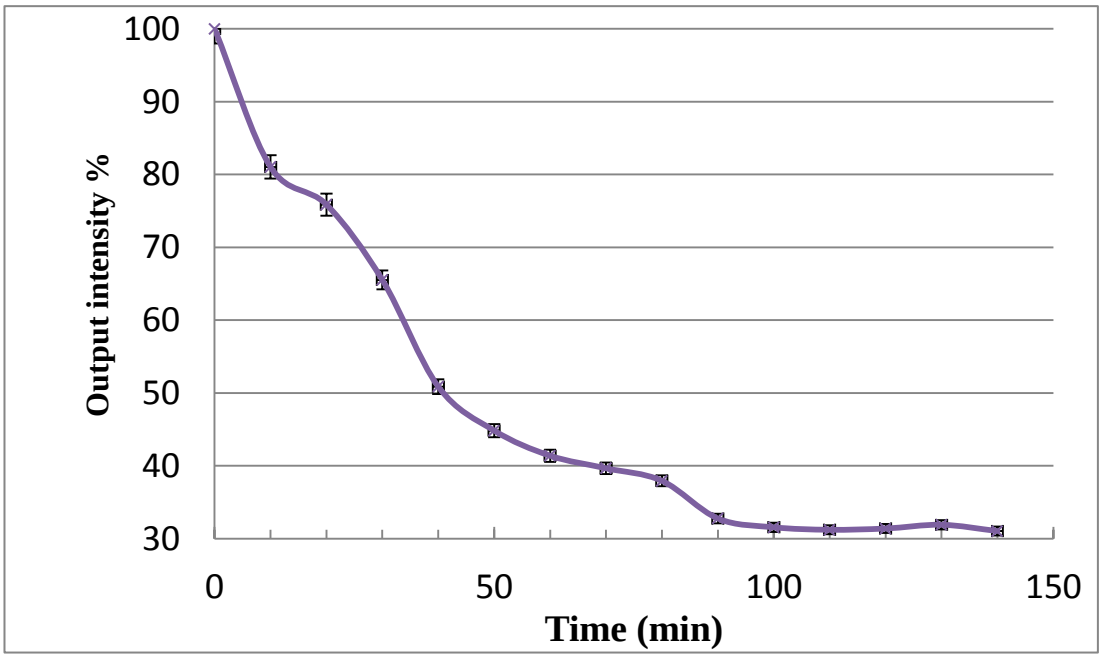

Figure 4-41: Normalised output intensity of the waveguides as function of reaction time for a 0.5ml/s flow rate.

It is clear from the results presented for a flowrate of 0.5 ml/s that a rapid deposition of biofilm formed on the waveguide windows. This resulted in a rapid drop in output intensity. In relation to the three phases outlined for each of the higher flowrates, phase A and B are merged at this low-flowrate of 0.5 ml/s. This can be attributed to a steady deposition of bio-material onto the sensor. At this flowrate limited removal rate coefficient occur. Therefore limited shear occurs at the surface of the sensor and the result is a steady deposition of the material. This indicates that the waveguide biosensor is highly sensitive at low flowrates, a key requirement of a new novel sensing method to detect early stage bio-sensing. The sensor was found to be exhausted/in-effective after 100 min of deposition.

1 ml/s flow-rate

The results of biofilm deposition at 1 ml/s are presented below

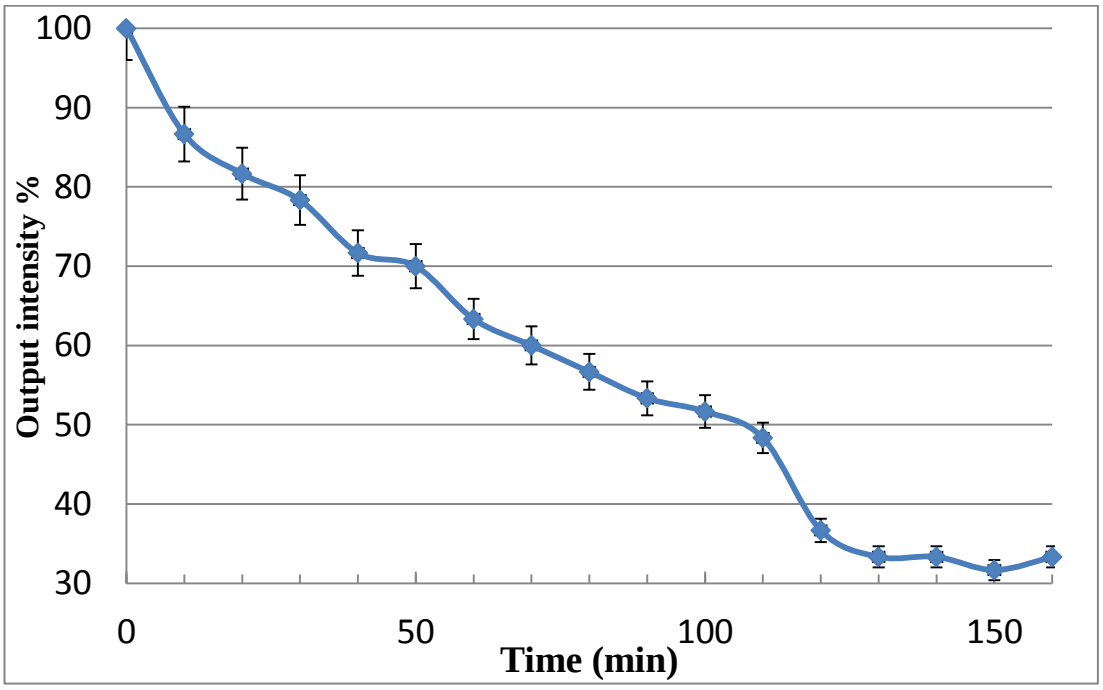

Figure 4-42: Normalised output intensity of the waveguides as function of reaction time with 1ml/s flow-rate.

Three phases are clear within this range of data corresponding to conditioning, initial deposition of biofilm, rapid deposition and then a stabilisation of the film thickness outside the EF range of the sensor. The steady deposition stage was present for 110 min and the intensity of the output of the sensor fell from 100 % to 50 % during this phase. The final output was similar to that at the 0.5 ml/s flowrate. However a rapid decrease in intensity from 50 % to approximately 30 % occurred over a 10 min period following the steady deposition stage. This rapid decrease in the intensity can be attributed to a rapid deposition of biofilm with limited removal of materials throughout this phase. A stabilisation of output intensity of the waveguide sensor was noted from 120 min to the end of the test. This would indicate that the thickness of the biofilm layer was now beyond the sensitivity of the sensor.

5 ml/s flow-rate

The 5 ml/s flowrate graph is presented below for a range of experiments that tested for 250 min each.

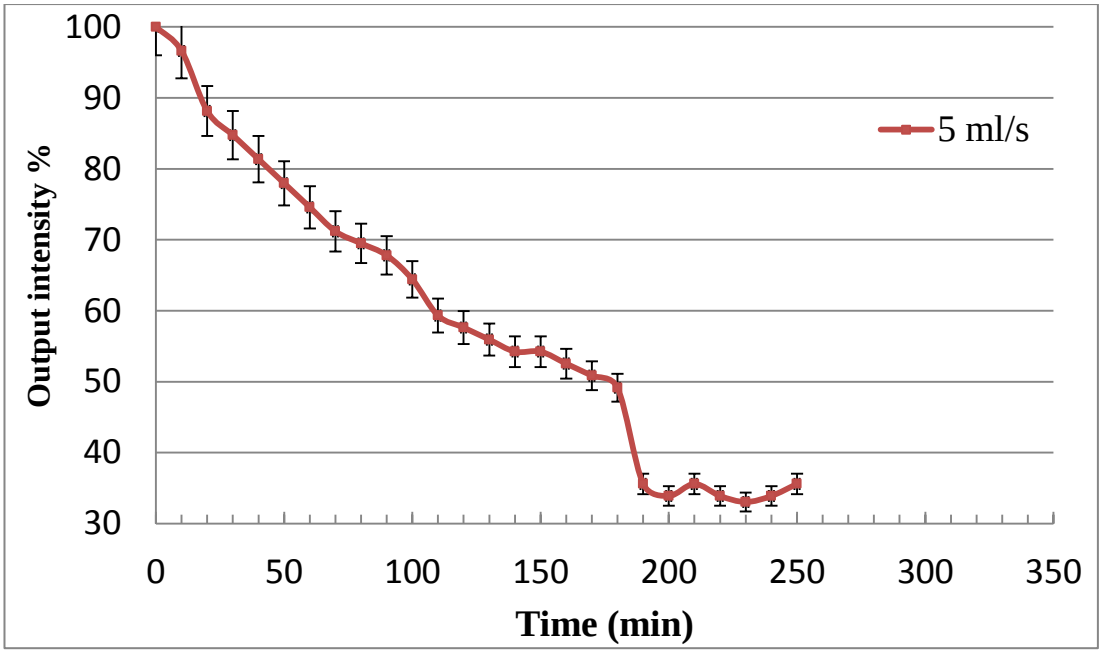

Figure 4-43: Normalised output intensity of the waveguides as function of reaction time for a 5ml/s flow rate from 0 to 250min

Again three phases of biofilm formulation are evident within this plot. The induction phase at this flowrate is longer than the previous lower flowrates. The induction phase ran for a period of 190 min with an intensity loss over this timeframe of 50 %. Once again this induction period was followed by a rapid deposition period lasting less than 10 min. Once again this can be attributed to rapid deposition of bio-material. However the higher flowrate resulted in this phase occurring at a much later time within the overall cycle. The sensor was found to be exhausted after 200 mins of operation at this flowrate. At this flowrate a steady deposition of material occurs for the first 180 mins of operation followed by a 5-10 min rapid deposition with the surface of the sensor could no longer detect further increases in biofilm thickness.

10ml/s flow-rate

The effect of doubling the flowrate from 5 to 10 ml/s is presented below.

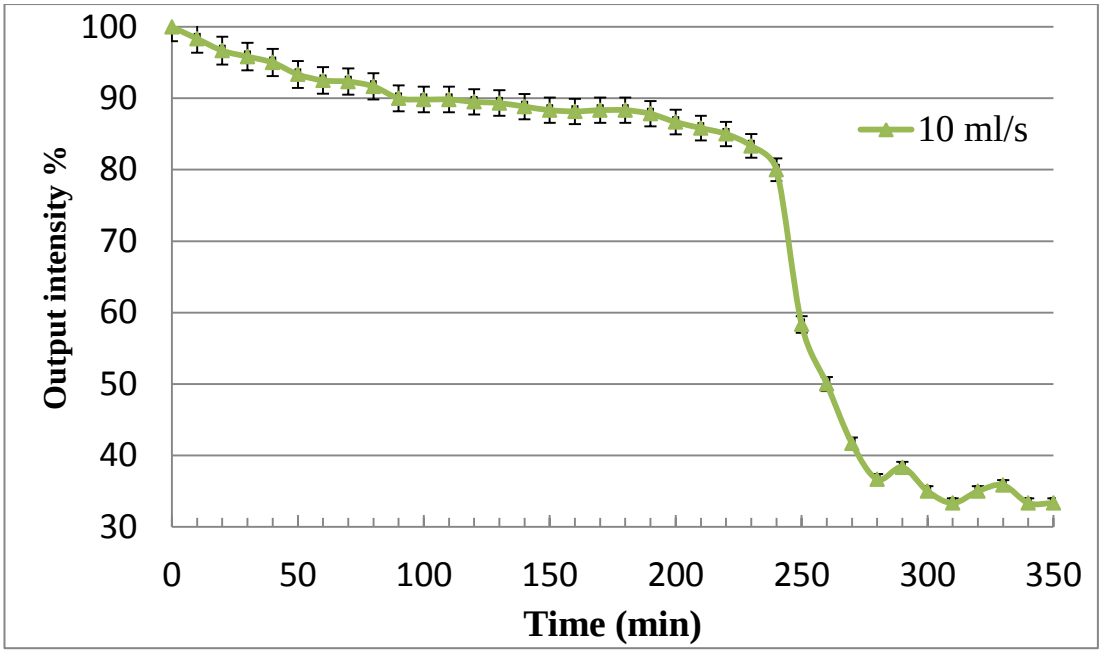

Figure 4-44: Normalised output intensity of the waveguides as function of reaction time for a 10 ml/s flowrate.

This increase in flowrate to 10 ml/s presents a completely different behaviour of output intensity as a function of time. Three phases of behaviour can still be observed offering an induction phase, rapid deposition phase and an unduallating final phase. A steady deposition and resulting decrease in intensity occurs from the startof the experiments to 100 min. At this flowrate this 7 % slow decrease in output intensity can be attributed to a steady deposition and removal of material. This results from increased shear at the waveguide sensor window due to the higher velocities resulting from the high flowrates.

It should be noted that at 0.5 ml/s the sensor was exhausted, the biofilm fully formed. However at 10 ml/s the induction phase continued for a further 140 min. At 240 min the surface was fully conditioned to accept rapid deposition of bio-material and to therefore rapidly increase the biofilm thickness. This highlights the end of a long induction phase consisting of a steady deposition from 0 – 90 min and a slower almost linear deposition phase from 90 – 240 min. At this end point and before the transition into the rapid deposition phase the output intensity of the sensor only fell by approximately 15 %. It should be noted that between 200 and 240 min the rate of

deposition increase and output intensity of the device fell a further 5% over this 40 mins.

Once the sensor output intensity reached 80 % a sudden dramatic drop occurred from 80 % to 60 % over a short period of 5 mins. The drop in output intensity slowed again from 60 % to 55 % over a timeframe of 15 mins before undulating for the remainder of the test. This high flowrate phase, apart from the three phases noted in the previous flowrates, is distinctly different from those seen at lower flowrates.

This can be attributed to the high flowrates resulting in high velocities and turbulent flow across the sensor window. During the induction phase this will prolong the deposition of material, sweeping bio-material from the surface of the sensor, making deposition more difficult. However once sufficient material/thickness has formed this makes it easier for farther deposits to develop (For example from 200 – 230 min). A critical point was reached at 230 mins where the conditions for rapid deposition was reached and a sudden drop in intensity was noted, a 45 % drop over 10 min period.

The undulating final phase can be attributed to additional deposition of bio-material onto the sensor window. This will increase the thickness of the biofilm however a point is reached where the high flowrate of the fluid can remove some of the material deposited. This will reduce the thickness of the biofilm previously deposited and result in an increase in output intensity of the sensor. This is evident at 295 min in Figure 4-44. Once this removal phase is complete additional material can now deposit again until the thickness is reached where the high flowrate can once again remove material. This undulating process of deposition and removal rates is evident at the end stage of the graph from 290 – 330 mins.

These patterns of induction, rapid deposition and finally undulating deposition and removal rates are typical of biofilm formation with the boundary layers of the surfaces of pipe previously described in the literature review.

Based on the individual analysis of each flow-rate, a correlation between the reaction time and the applied flow rate to allow the growth of biofilm thickness to the critical cut-off point defined to be 50 nm (as per simulations) was established.

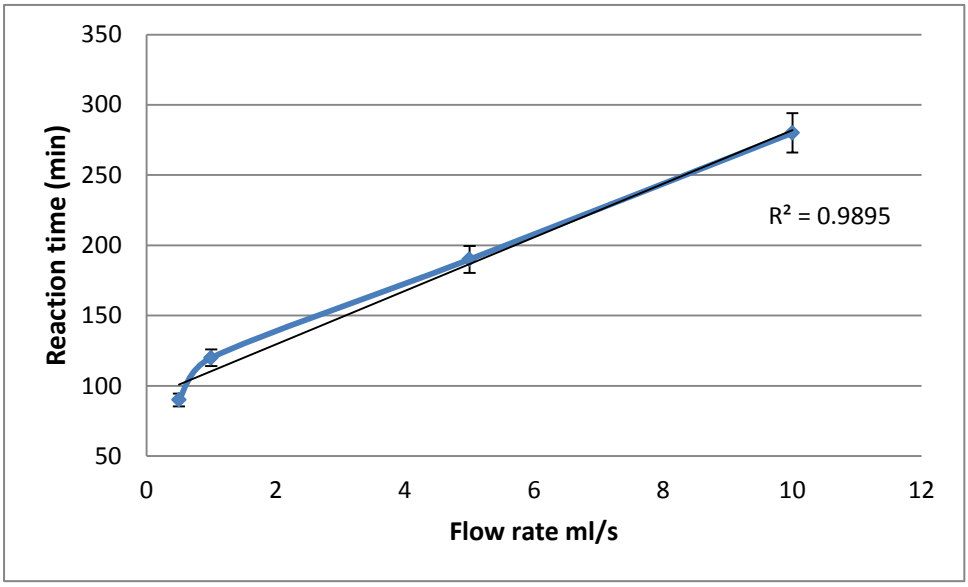

Figure 4-45: Reaction time to cut-off thickness as function of the applied flow-rate.

Figure 4-45 shows that the correlation between the reaction time to reach the cut-off thickness as function of the applied flow rate and this can be confidently modelled by a linear equation, as the R^2 was found to be close to 99%. Moreover, the slight deviation to the linearity was found to be due to the quasi-static regime, as if this condition is not considered in the simulation, the R^2 is equal to 99.99%, which is a perfect fit with a linearity behaviour.

Finally, it was possible to make a hypothesis that the biofilm growth at the waveguide surface can be predicted from flowrate based on an inverse relationship between growth and flowrate as presented in Figure 4-46.

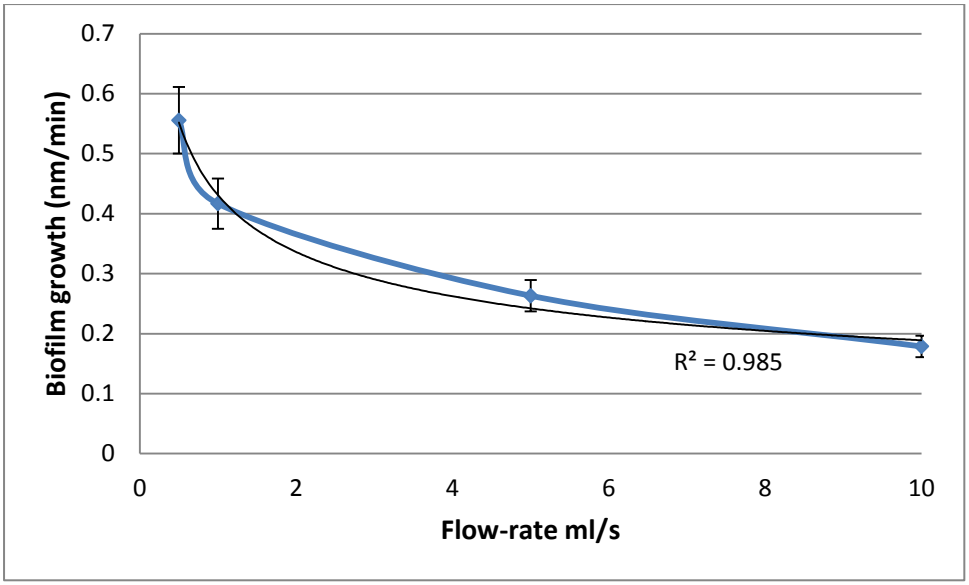

Figure 4-46: Biofilm growth as function of applied flow-rate

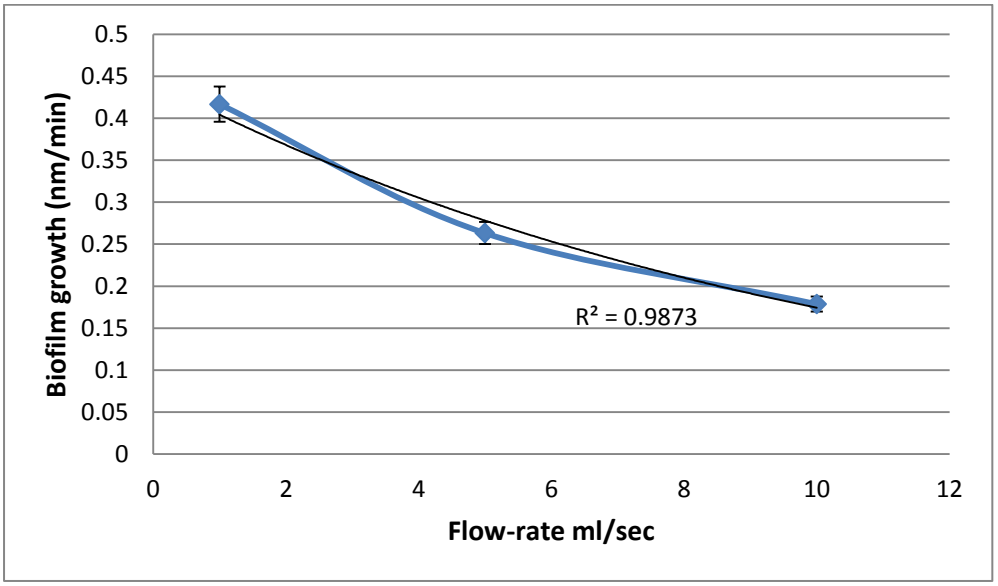

Figure 4-47: Biofilm growth at 1, 5 and 10 ml/s applied flowrates.

Figure 4-47 confirms that the biofilm growth is dependent on the applied flow-rate but also highlights that no linearity exists between these two factors. However, if the quasi-static flow rate is neglected, an exponential behaviour was found to be the best fit to that behaviour (R^2>98.7%), as sketched in figure A. This means that it is very likely that a critical biofilm growth kinetic can be attained but at flow-rates greater than those investigated here.

In summary a novel biosensor was been successfully developed using a waveguide platform. The device was found to be highly sensitive at low flowrates. Low flowrates were found to result in rapid deposition onto the waveguide sensor window. The sensor was highly responsive to this deposition. At high flowrates the sensor was capable of capturing the entire deposition and removal rate conditions over the complete timeframe of the experiments.

Three distinct phases of deposition were noted for all flowrates examined. These included a slow deposition /conditioning phase, followed by a rapid deposition phase and finally a steady final phase. This steady phase was replaced by an undulating final phase at high flowrates. These phases are typical of biofilm formation previously presented in literature. However previous research has commented on the difficulty of early stage detection of bio-fouling and this waveguide sensor is clearly capable of detecting this early phase deposition/conditioning at low flowrates. Such sensitivity is of interest of researchers interested in

- Reducing early stage biofilm formation
- Conditioning of surfaces to prevent early stage bio-fouling
- Accurate measurement of early stage biofilm thicknesses

4.3.4 Conclusion

The sensing performance of a waveguide-based photonic sensor platform exploiting the interaction between the optical modes of channel waveguides and the surrounding environment has been developed and fully characterised.

This integrated optical platform was fabricated from photocurable hybrid sol-gel materials, which were patterned using a direct UV-photolithography process.
It was shown that the sensitivity of the platform can be controlled by the deposition of a high refractive index layer at the surface of the optical waveguides. This enabled a stronger interaction between the evanescent field of the waveguides and the biofilm formed on its surface.

The thickness of the high refractive index layer was estimated using an Olympios software package (an optical mode solver). This optimised thickness value of the

tantalum oxide nanoparticles sol-gel solution was achieved experimentally by changing the deposition speed from 350 RPM to 600 RPM in steps of 50 RPM, as shown in Figure 4-23. The sensing performances of the biosensor platform were investigated in both quasi-static and dynamic conditions with flow-rates ranging from 0.5 to 10 ml/s. It was clearly shown that the kinetics of biofilm formation relies on the applied flow-rate. Moreover, the sensing platform was able to detect biofilm formation in a quite short timeframe (under 10 minutes) under experimental conditions. The difference in the measured output intensities as a function of applied flow-rate was attributed to the kinetics of biofilm growth at the waveguide surface. It was demonstrated that the biofilm growth as function of applied flow rate follows an exponential trend. This suggests that a critical biofilm growth may be attained but at flow-rates greater than those investigated here. Finally, the platform developed here was found to exhibit high sensitivity in the detection of biofilm at very low flowrates and interestingly can be employed to determine the evolution of the biofilm thickness as function of both reaction time and applied flow rate.

Chapter 5

Conclusion and Future Work

The objective of this thesis was to develop a biosensor platform for the detection of early stage biofilm formation. The initial phase of this work concentrated on establishing the state-of-the-art in the bio formation & detection field and has highlighted that the optical techniques deployed here are amongst the most sensitive techniques in this sensor area. Based on this, a concept based on optical waveguiding was established in order to fabricate a photonic biosensor platform for the detection of biofilm formation. Using this concept, the objective was to define a work plan to achieve this novel biosensor platform. Five steps were required to achieve this outcome, including:

- The biosensor design to allow the real-time detection of the biofilm formation
- The definition of the optical and photonic characteristics of the platform to enable as high a sensitivity as possible
- The definition of the materials for the fabrication of the biosensor platform
- The optimisation of the fabrication process and characterisation of the optical performances of the photonic platform
- The determination of the sensing performances of the platform in both quasi-static and dynamic conditions.

This integrated optical platform was fabricated from photocurable hybrid sol-gel materials, which were patterned using a direct UV-photolithography process. It was shown that the sensitivity of the platform can be controlled by the deposition of a high refractive index layer at the surface of the optical waveguides, enabling a stronger interaction between the evanescent field of the waveguides and the biofilm formed on its surface. Formation of the biofilm in a quasi-static flow-monitoring process was shown to occur within the first ten minutes of the sensing test, highlighting the high sensitivity of the platform in comparison to other optical platforms proposed in the literature.

Furthermore, this platform can be employed to determine the evolution of the biofilm thickness during the sensing test. Owing to its generic nature, the platform can be viewed as an ideal device for bioenvironmental applications, where the real-time read-out can be leveraged for monitoring of affinity reactions in environmental sensing. However, the work performed in this thesis would deserve to be further developed including materials and fabrication process as well as detection methods to enable the development of a robust, compact and cost-effective biosensor platform with greater sensitivity and specificity to the detection of microorganism living systems.

The functionalization of the surface of the sensing windows of this platform in order to specifically immobilize biomolecules of interest could bring novel high impact applications to the device developed in this study. The hybrid nature of the materials developed in this study permits integration of a large range of functional groups, including organic molecules, for the immobilization of organic pollutants via the occurrence of organic reactions, and inorganic groups that can target inorganic or mineral species via complexation and/or co-condensation reactions. Another possible functionalization could consist of integrating functional nanoparticles, similar to those employed in the biomedical diagnostic area, designed for the specific immobilization of a molecule of interest.

In addition to the functionalization issues highlighted above, which are essential to provide increased performance of the biosensor platform, future work would be required to precisely and reproducibly control the thickness of the high refractive index layer responsible for the enhancement of the sensitivity of the sensor. Employment of techniques such as the ALD (Atomic Layer Deposition) would be ideal for this as control of the thickness is possible at the sub-nanometre scale, thus completely fulfilling the requirement of the platform.

From an engineering standpoint, it would be of a great value to develop strategies for the integration of a microfluidic device on top of the sensor windows that would deliver the analyte of solutions without any leaking issues and would certainly allow the circulation of the solutions of interests at higher flow-rates and therefore further correlating the sensitivity of the photonic biosensor platform at high flow-rates. Determining light coupling methods into the waveguides was also found to be an important aspect to the current platform. Determining methodologies to integrate

both the input and output optical fibres to this platform would be a significant practical advantage to increase detection efficiency (increased input light intensity), higher misalignment tolerated margin, and enhance reproducibility in the detection values.

Such investigations will certainly have an important impact on the development of a robust and cost-effective platform and possibly a biosensor of commercial interest as well as contributing to advance basic research in bioenvironmental science. Success in these objectives would have a significant impact on the current societal and industrial problems in this key bio-sensor field.

References

[1] Elmaghrum, S. , (2006), "CFD analysis of pharmaceutical water distribution systems: T-junctions", Master of Engineering, Dublin City University,.

[2] Costerton, J.W., Stewart, P.S.and Greenberg, E.P., (1999), "Bacterial Biofilms: A Common Cause of Persistent Infections", *Science,* Vol.284 (5418), pp. 1318-1322.

[3] Donlan, R.M. (2002), "Biofilms: Microbial Life on Surfaces", *Emerging Infectious Diseases,* Vol.8 (9), pp. 881-890.

[4] H. Heukelekianand A. Heller., (1940), "Relation between food concentration and surface for bacterial growth1", *J Bacteriol,* Vol.40 (4), pp. 547-558.

[5] Claude E. Zobell. (1943), "The effect of solid surfaces upon bacterial activity'", *J Bacteriol,* Vol.46 (1), pp. 39-56.

[6] H. C. Jones, et al. (1969), "Electron Microscopic Study of a Slime Layer", *J Bacteriol,* Vol.99 (1), pp. 316-325.

[7] Characklis WG. (1973), "Attached microbial growths-II. Frictional resistance due to microbial slimes.", *Water Res,* Vol.7 pp. 1249-1258.

[8] Costerton, J.W. (1978), "How Bacteria Stick", *Sci Am,* Vol.238 (1), pp. 86-95.

[9] Manuel Simões, Lúcia C. Simões, Maria J. Vieira. (May 2010), "A review of current and emergent biofilm control strategies", *LWT - Food Science and Technology,* Vol.43 (4), pp. 573-583.

[10] T.J. Battin, et al. (2003), "Contributions of microbial biofilms to ecosystem processes in stream mesocosms", *Nature,* Vol.426 pp. 439-442.

[11] T. Harder., (2009), "Springer Series on Biofilms", *in H.-. Flemming, P.S. Murthy, R. Venkatesan, et al, eds., Marine and Industrial Biofouling,* 4, Berlin Heidelberg, pp. 219-231.

[12] Stickler, D.J.and Feneley, R.C.L., (2010), "The encrustation and blockage of long-term indwelling bladder catheters: a way forward in prevention and control", *Spinal Cord,* Vol.48 (11), pp. 784-790.

[13] Vinten, A.J.A., et al. (2011), "Comparison of microbial community assays for the assessment of stream biofilm ecology", *J.Microbiol.Methods,* Vol.85 (3), pp. 190-198.

[14] O'Toole, G.A.and Kolter, R., (1998), "Initiation of biofilm formation in Pseudomonas fluorescens WCS365 proceeds via multiple, convergent signalling pathways: a genetic analysis", *Mol.Microbiol.,* Vol.28 (3), pp. 449-461.

[15] Nguyen, C.T., et al. (2012), "Noninvasive in vivo optical detection of biofilm in the human middle ear", *Proceedings of the National Academy of Sciences*, Vol.109 (24), pp. 9529-9534.

[16] Waszczuk, K., et al. (2010), "Evaluation of Pseudomonas aeruginosa biofilm formation using piezoelectric tuning forks mass sensors", *Procedia Engineering*, Vol.5 (0), pp. 820-823.

[17] Ward, A.J., et al. (2011), "Evaluation of near infrared spectroscopy and software sensor methods for determination of total alkalinity in anaerobic digesters", *Bioresour.Technol.*, Vol.102 (5), pp. 4083-4090.

[18] Lewin, R. (1984), "Microbial adhesion is a sticky problem", *Science*, Vol.224 pp. 375-377.

[19] Characklis, W. (1983), "Process analysis in microbial systems: biofilms as a case study", *Mathematics in Microbiology*, pp. 171-234.

[20] Eggins, B.R., (2008), *Chemical sensors and biosensors*, , John Wiley & Sons,.

[21] Janata, J., (2009), "Thermal Sensors", *Principles of Chemical Sensors*, Springer, pp. 51-62.

[22] O'Sullivan, D.and Millero, F., (1998), "Continual measurement of the total inorganic carbon in surface seawater", *Mar.Chem.*, Vol.60 (1), pp. 75-83.

[23] Kimoto, H., et al. (2002), "Achieving high time-resolution with a new flow-through type analyzer for total inorganic carbon in seawater", *Analytical sciences*, Vol.18 (3), pp. 247-254.

[24] Kaltin, S., Haraldsson, C.and Anderson, L.G., (2005), "A rapid method for determination of total dissolved inorganic carbon in seawater with high accuracy and precision", *Mar.Chem.*, Vol.96 (1), pp. 53-60.

[25] Bandstra, L., Hales, B.and Takahashi, T., (2006), "High-frequency measurements of total CO< sub> 2</sub>: Method development and first oceanographic observations", *Mar.Chem.*, Vol.100 (1), pp. 24-38.

[26] Eidelman, N., et al. (2004), "Combinatorial approach to characterizing epoxy curing", *Macromolecular rapid communications*, Vol.25 (1), pp. 259-263.

[27] Werle, P. (1998), "A review of recent advances in semiconductor laser based gas monitors", *Spectrochimica Acta Part A: Molecular and Biomolecular Spectroscopy*, Vol.54 (2), pp. 197-236.

[28] Allen, M.G. (1998), "Diode laser absorption sensors for gas-dynamic and combustion flows", *Measurement Science and Technology*, Vol.9 (4), pp. 545.

[29] Linnerud, I., Kaspersen, P.and Jaeger, T., (1998), "Gas monitoring in the process industry using diode laser spectroscopy", *Appl.Phy. B,* Vol.67 (3), pp. 297-305.

[30] Kosterev, A.A. (2002), "Chemical sensors based on quantum cascade lasers", *Quantum Electronics, IEEE Journal of,* Vol.38 (6), pp. 582-591.

[31] Hvozdara, L., et al. (2002), "Quantum cascade lasers for mid-infrared spectroscopy", *Vibrational Spectroscopy,* Vol.30 (1), pp. 53-58.

[32] Capasso, F., et al. (2000), "New frontiers in quantum cascade lasers and applications", *Selected Topics in Quantum Electronics, IEEE Journal of,* Vol.6 (6), pp. 931-947.

[33] Hvozdara, L., et al. (2000), "Spectroscopy in the gas phase with GaAs/AlGaAs quantum-cascade lasers", *Appl.Opt.,* Vol.39 (36), pp. 6926-6930.

[34] Sharpe, S., et al. (1998), "High-resolution (Doppler-limited) spectroscopy using quantum-cascade distributed-feedback lasers", *Opt.Lett.,* Vol.23 (17), pp. 1396-1398.

[35] Schaden, S., et al. (2004), "Direct determination of carbon dioxide in aqueous solution using mid-infrared quantum cascade lasers", *Appl.Spectrosc.,* Vol.58 (6), pp. 667-670.

[36] Kosterev, A.A., et al. (2000), "Effective utilization of quantum-cascade distributed-feedback lasers in absorption spectroscopy", *Appl.Opt.,* Vol.39 (24), pp. 4425-4430.

[37] Weber, W., et al. (2002), "Using a wavelength-modulated quantum cascade laser to measure NO concentrations in the parts-per-billion range for vehicle emissions certification", *Appl.Spectrosc.,* Vol.56 (6), pp. 706-714.

[38] Nelson, D.D., et al. (2004), "High precision measurements of atmospheric nitrous oxide and methane using thermoelectrically cooled mid-infrared quantum cascade lasers and detectors", *Spectrochimica Acta Part A: Molecular and Biomolecular Spectroscopy,* Vol.60 (14), pp. 3325-3335.

[39] Wu, B., et al. (2006), "Measurement of non-methane hydrocarbons in Taipei city and their impact on ozone formation in relation to air quality", *Anal.Chim.Acta,* Vol.576 (1), pp. 91-99.

[40] Patra, D.and Mishra, A., (2002), "Total synchronous fluorescence scan spectra of petroleum products", *Analytical and bioanalytical chemistry,* Vol.373 (4-5), pp. 304-309.

[41] Ryder, A.G. (2004), "Assessing the maturity of crude petroleum oils using total synchronous fluorescence scan spectra", *J.Fluoresc.,* Vol.14 (1), pp. 99-104.

[42] Poulli, K.I., Mousdis, G.A.and Georgiou, C.A., (2006), "Synchronous fluorescence spectroscopy for quantitative determination of virgin olive oil

adulteration with sunflower oil", *Analytical and bioanalytical chemistry*, Vol.386 (5), pp. 1571-1575.

[43] Scott, S.M., et al. (2003), "Total luminescence spectroscopy with pattern recognition for classification of edible oils", *Analyst*, Vol.128 (7), pp. 966-973.

[44] Wu, B., et al. (2006), "Measurement of non-methane hydrocarbons in Taipei city and their impact on ozone formation in relation to air quality", *Anal.Chim.Acta*, Vol.576 (1), pp. 91-99.

[45] Drezek, R., et al. (2001), "Autofluorescence Microscopy of Fresh Cervical-Tissue Sections Reveals Alterations in Tissue Biochemistry with Dysplasia¶", *Photochem.Photobiol.*, Vol.73 (6), pp. 636-641.

[46] Brookner, C.K., et al. (2000), "Autofluorescence Patterns in Short- Term Cultures of Normal Cervical Tissue", *Photochem.Photobiol.*, Vol.71 (6), pp. 730-736.

[47] Vivian, J.T.and Callis, P.R., (2001), "Mechanisms of tryptophan fluorescence shifts in proteins", *Biophys.J.*, Vol.80 (5), pp. 2093-2109.

[48] Monsellier, E.and Bedouelle, H., (2005), "Quantitative measurement of protein stability from unfolding equilibria monitored with the fluorescence maximum wavelength", *Protein Eng.Des.Sel.*, Vol.18 (9), pp. 445-456.

[49] Laserna, J. (2001), "An Introduction to Raman Spectroscopy: Introduction and Basic Principles", *Raman Resource including Vibrational Spectroscopy*, *http://www.spectroscopynow.com/Spy/basehtml/SpyH/1.1181*, pp. 6-1.

[50] Owen, C.A., et al. (2006), "Progress in Raman spectroscopy in the fields of tissue engineering, diagnostics and toxicological testing", *J.Mater.Sci.Mater.Med.*, Vol.17 (11), pp. 1019-1023.

[51] Uzunbajakava, N., et al. (2003), "Nonresonant confocal Raman imaging of DNA and protein distribution in apoptotic cells", *Biophys.J.*, Vol.84 (6), pp. 3968-3981.

[52] Shafer- Peltier, K.E., et al. (2002), "Model- based biological Raman spectral imaging", *J.Cell.Biochem.*, Vol.87 (S39), pp. 125-137.

[53] Puppels, G.J. (2002), "Preface to the special issue on medical applications of Raman spectroscopy", *J.Raman Spectrosc.*, Vol.33 (7), pp. 496-497.

[54] Kneipp, J., et al. (2003), "Characterization of breast duct epithelia: a Raman spectroscopic study", *Vibrational spectroscopy*, Vol.32 (1), pp. 67-74.

[55] Notingher, I., et al. (2004), "Discrimination between ricin and sulphur mustard toxicity in vitro using Raman spectroscopy", *J.R.Soc.Interface*, Vol.1 (1), pp. 79-90.

[56] Stuart, D.A., et al. (2006), "In vivo glucose measurement by surface-enhanced Raman spectroscopy", *Anal.Chem.,* Vol.78 (20), pp. 7211-7215.

[57] Deckert, V., et al. (1998), "Near-field surface-enhanced Raman imaging of dye-labeled DNA with 100-nm resolution", *Anal.Chem.,* Vol.70 (13), pp. 2646-2650.

[58] Chen, K., et al. (2006), "Application of surface-enhanced Raman scattering (SERS) for the identification of anthraquinone dyes used in works of art", *J.Raman Spectrosc.,* Vol.37 (4), pp. 520-527.

[59] Chen, K., et al. (2006), "Direct identification of alizarin and lac dye on painting fragments using surface-enhanced Raman scattering", *Anal.Chim.Acta,* Vol.569 (1), pp. 234-237.

[60] McDonagh, C., Burke, C.S.and MacCraith, B.D., (2008), "Optical chemical sensors", *ChemInform,* Vol.39 (18), pp. no-no.

[61] Oter, O., et al. (2006), "Emission-based optical carbon dioxide sensing with HPTS in green chemistry reagents: room-temperature ionic liquids", *Analytical and bioanalytical chemistry,* Vol.386 (5), pp. 1225-1234.

[62] Baldini, F., et al. (2003), "Continuous monitoring of gastric carbon dioxide with optical fibres", *Sensors Actuators B: Chem.,* Vol.90 (1), pp. 132-138.

[63] Segawa, H., et al. (2003), "Sensitivity of fiber-optic carbon dioxide sensors utilizing indicator dye", *Sensors Actuators B: Chem.,* Vol.94 (3), pp. 276-281.

[64] Wetzl, B.K., et al. (2004), "Ein Chamäleon- Marker zur Anfärbung und quantitativen Bestimmung von Proteinen", *Angewandte Chemie,* Vol.116 (40), pp. 5515-5517.

[65] Suzuki, Y., Nakano, N.and Suzuki, K., (2003), "Portable sick house syndrome gas monitoring system based on novel colorimetric reagents for the highly selective and sensitive detection of formaldehyde", *Environ.Sci.Technol.,* Vol.37 (24), pp. 5695-5700.

[66] Kawamura, K., et al. (2005), "Development of a novel hand-held formaldehyde gas sensor for the rapid detection of sick building syndrome", *Sensors Actuators B: Chem.,* Vol.105 (2), pp. 495-501.

[67] Badr, I.H.and Meyerhoff, M.E., (2005), "Fluoride-selective optical sensor based on aluminum (III)-octaethylporphyrin in thin polymeric film: Further characterization and practical application", *Anal.Chem.,* Vol.77 (20), pp. 6719-6728.

[68] Teshima, N., et al. (2005), "Determination of acetone in breath", *Anal.Chim.Acta,* Vol.535 (1), pp. 189-199.

[69] Lobnik, A., (2006), *Absorption-based sensors,* , Springer,.

[70] Lin, J.and Liu, D., (2000), "An optical pH sensor with a linear response over a broad range", *Anal.Chim.Acta,* Vol.408 (1), pp. 49-55.

[71] Makedonski, P., et al. (2004), "Synthesis of new kinds of reactive azo dyes and their application for fibre-optical pH-measurements", *Dyes and Pigments,* Vol.61 (2), pp. 109-119.

[72] Kermis, H.R., Kostov, Y.and Rao, G., (2003), "Rapid method for the preparation of a robust optical pH sensor", *Analyst,* Vol.128 (9), pp. 1181-1186.

[73] Sanchez-Barragan, I., et al. (2006), "A ratiometric approach for pH optosensing with a single fluorophore indicator", *Anal.Chim.Acta,* Vol.562 (2), pp. 197-203.

[74] Le, T.P., Rogers, J.E.and Kelly, L.A., (2000), "Photoinduced electron transfer in covalently linked 1, 8-naphthalimide/viologen systems", *The Journal of Physical Chemistry A,* Vol.104 (29), pp. 6778-6785.

[75] áPrasanna de Silva, A.and Rice, T., (1999), "A small supramolecular system which emulates the unidirectional, path-selective photoinduced electron transfer (PET) of the bacterial photosynthetic reaction centre (PRC)", *Chemical Communications,* (2), pp. 163-164.

[76] Li, Z., et al. (2006), "A novel fluorescence ratiometric pH sensor based on covalently immobilized piperazinyl-1, 8-napthalimide and benzothioxanthene", *Sensors Actuators B: Chem.,* Vol.114 (1), pp. 308-315.

[77] Chen, X., et al. (2004), "Fluorescent response of sol–gel derived ormosils for optical ammonia sensing film", *Anal.Chim.Acta,* Vol.506 (1), pp. 9-15.

[78] Carter, J.C., et al. (2006), "Fabricating optical fiber imaging sensors using inkjet printing technology: A pH sensor proof-of-concept", *Biosensors and Bioelectronics,* Vol.21 (7), pp. 1359-1364.

[79] Duong, H.D., et al. (2006), "An optical pH sensor with extended detection range based on fluoresceinamine covalently bound to sol–gel support", *Microchemical journal,* Vol.84 (1), pp. 50-55.

[80] Choi, S., Choi, B.and Park, S., (2002), "Electrochemical sensor for electrochemically inactive β-D ( )-glucose using α-cyclodextrin template molecules", *Anal.Chem.,* Vol.74 (9), pp. 1998-2002.

[81] Fuller, Z., et al. (2003), "Photostability of luminescent ruthenium (II) complexes in polymers and in solution", *Anal.Chem.,* Vol.75 (11), pp. 2670-2677.

[82] McDonagh, C., et al. (2002), "Characterisation of porosity and sensor response times of sol–gel-derived thin films for oxygen sensor applications", *J.Non Cryst.Solids,* Vol.306 (2), pp. 138-148.

[83] Kerry, J.and Papkovsky, D., (2002), "Research AdVances in Food Science", .

[84] O'Mahony, F.C., et al. (2006), "Non-destructive assessment of oxygen levels in industrial modified atmosphere packaged cheddar cheese", *Food Control,* Vol.17 (4), pp. 286-292.

[85] O'Riordan, T.C., et al. (2005), "Study of migration of active components of phosphorescent oxygen sensors for food packaging applications", *Anal.Chim.Acta,* Vol.530 (1), pp. 135-141.

[86] Lee, S.and Okura, I., (1997), "Photostable Optical Oxygen Sensing Material: PlatinumTetrakis (pentafluorophenyl) porphyrin Immobilized in Polystyrene", *Anal.Commun.,* Vol.34 (6), pp. 185-188.

[87] Glenn, S.J., et al. (2001), "Lifetime-based fiber-optic water sensor using a luminescent complex in a lithium-treated Nafion™ membrane", *Anal.Chim.Acta,* Vol.448 (1–2), pp. 1-8.

[88] Bedoya, M., et al. (2006), "Humidity sensing with a luminescent Ru (II) complex and phase-sensitive detection", *Sensors Actuators B: Chem.,* Vol.113 (2), pp. 573-581.

[89] McGaughey, O., et al. (2006), "Development of a fluorescence lifetime-based sol–gel humidity sensor", *Anal.Chim.Acta,* Vol.570 (1), pp. 15-20.

[90] Wright, J.D. and Sommerdijk, N.A., (2000), *Sol-gel materials: chemistry and applications,* , CRC press,.

[91] Tao, Z., et al. (2006), "Stable sensors with tunable sensitivities based on class II xerogels", *Anal.Chem.,* Vol.78 (6), pp. 1939-1945.

[92] Bukowski, R.M., et al. (2005), "High-performance quenchometric oxygen sensors based on fluorinated xerogels doped with [Ru (dpp) 3] 2", *Anal.Chem.,* Vol.77 (8), pp. 2670-2672.

[93] Bukowski, R.M., et al. (2006), "O< sub> 2</sub>-Responsive Chemical Sensors Based on Hybrid Xerogels that Contain Fluorinated Precursors", *Appl.Spectrosc.,* Vol.60 (9), pp. 951-957.

[94] Klimant, I., et al. (1999), "Fast response oxygen micro-optodes based on novel soluble ormosil glasses", *Microchimica Acta,* Vol.131 (1-2), pp. 35-46.

[95] Grosso, D., et al. (2004), "Fundamentals of Mesostructuring Through Evaporation- Induced Self- Assembly", *Advanced Functional Materials,* Vol.14 (4), pp. 309-322.

[96] Nicole, L., et al. (2004), "Advanced selective optical sensors based on periodically organized mesoporous hybrid silica thin films", *Chemical communications,* (20), pp. 2312-2313.

[97] Tao, S., et al. (2004), "Optical-fiber sensor using tailored porous sol-gel fiber core", *Sensors Journal, IEEE,* Vol.4 (3), pp. 322-328.

[98] McDonagh, C., Burke, C.S.and MacCraith, B.D., (2008), "Optical chemical sensors", *Chem.Rev.,* Vol.108 (2), pp. 400-422.

[99] O'Neal, D.P., et al. (2004), "Oxygen sensor based on the fluorescence quenching of a ruthenium complex immobilized in a biocompatible poly (ethylene glycol) hydrogel", *Sensors Journal, IEEE,* Vol.4 (6), pp. 728-734.

[100] Valledor, M., et al. (2006), "Luminescent ratiometric method in the frequency domain with dual phase-shift measurements: Application to oxygen sensing", *Sensors Actuators B: Chem.,* Vol.117 (1), pp. 266-273.

[101] Chen, L., et al. (2006), "Fiber-optic sensor for iodine based on a covalently immobilized aminobenzanthrone Schiff base", *Analytical sciences,* Vol.22 (7), pp. 977.

[102] Vasylevska, G.S., et al. (2006), "Indicator-loaded permeation-selective microbeads for use in fiber optic simultaneous sensing of pH and dissolved oxygen", *Chemistry of materials,* Vol.18 (19), pp. 4609-4616.

[103] Huber, C., et al. (2001), "Dual lifetime referencing as applied to a chloride optical sensor", *Anal.Chem.,* Vol.73 (9), pp. 2097-2103.

[104] Ahmad, M., et al. (2005), "A compact fibre-based fluorescence sensor", *Sensors and Actuators A: Physical,* Vol.119 (1), pp. 84-89.

[105] Park, E.J., et al. (2005), "Ratiometric fiber optic sensors for the detection of inter-and intra-cellular dissolved oxygen", *Journal of Materials Chemistry,* Vol.15 (27-28), pp. 2913-2919.

[106] Preejith, P., Lim, C.and Chia, T., (2006), "Serum protein measurement using a tapered fluorescent fibre-optic evanescent wave-based biosensor", *Measurement Science and Technology,* Vol.17 (12), pp. 3255.

[107] Moreno, J., Arregui, F.J.and Matias, I.R., (2005), "Fiber optic ammonia sensing employing novel thermoplastic polyurethane membranes", *Sensors Actuators B: Chem.,* Vol.105 (2), pp. 419-424.

[108] Gupta, B.and Sharma, N.K., (2002), "Fabrication and characterization of U-shaped fiber-optic pH probes", *Sensors Actuators B: Chem.,* Vol.82 (1), pp. 89-93.

[109] James, S.W.and Tatam, R.P., (2006), "Fibre Optic Sensors with Nano-Structured Coatings.", .

[110] Sang, X., et al. "May teevarunyoo T and Lu NG 2006 Chin", *Phys.Lett,* Vol.23 pp. 3202.

[111] Falciai, R., Mignani, A.and Vannini, A., (2001), "Long period gratings as solution concentration sensors", *Sensors Actuators B: Chem.,* Vol.74 (1), pp. 74-77.

[112] DeLisa, M.P., et al. (2000), "Evanescent wave long-period fiber bragg grating as an immobilized antibody biosensor", *Anal.Chem.,* Vol.72 (13), pp. 2895-2900.

[113] Liu, N., et al. (2006), "Nanoporous zeolite thin film-based fiber intrinsic Fabry-Perot interferometric sensor for detection of dissolved organics in water", *Sensors,* Vol.6 (8), pp. 835-847.

[114] Benounis, M., et al. (2005), "Study of a new evanescent wave optical fibre sensor for methane detection based on cryptophane molecules", *Sensors Actuators B: Chem.,* Vol.107 (1), pp. 32-39.

[115] Jung, Y., et al. (2006), "Compact three segmented multimode fibre modal interferometer for high sensitivity refractive-index measurement", *Measurement Science and Technology,* Vol.17 (5), pp. 1129.

[116] Burke, C.S., et al. (2005), "Development of an integrated optic oxygen sensor using a novel, generic platform", *Analyst,* Vol.130 (1), pp. 41-45.

[117] Malins, C., Niggemann, M.and MacCraith, B., (2000), "Multi-analyte optical chemical sensor employing a plastic substrate", *Measurement Science and Technology,* Vol.11 (8), pp. 1105.

[118] Chang-Yen, D.A.and Gale, B.K., (2003), "An integrated optical oxygen sensor fabricated using rapid-prototyping techniques", *Lab Chip,* Vol.3 (4), pp. 297-301.

[119] Burke, C.S., et al. (2006), "Development of an optical sensor probe for the detection of dissolved carbon dioxide", *Sensors Actuators B: Chem.,* Vol.119 (1), pp. 288-294.

[120] Huang, S.and Tseng, F., (2005), "Development of a monolithic total internal reflection-based biochip utilizing a microprism array for fluorescence sensing", *J Micromech Microengineering,* Vol.15 (12), pp. 2235.

[121] Rowe-Taitt, C.A., et al. (2000), "Array biosensor for detection of biohazards", *Biosensors and Bioelectronics,* Vol.14 (10), pp. 785-794.

[122] Duveneck, G.L., et al. (2002), "Planar waveguides for ultra-high sensitivity of the analysis of nucleic acids", *Anal.Chim.Acta,* Vol.469 (1), pp. 49-61.

[123] Malins, C., et al. (1999), "Personal ammonia sensor for industrial environments", *Journal of Environmental Monitoring,* Vol.1 (5), pp. 417-422.

[124] Lavers, C., et al. (2000), "Planar optical waveguides for sensing applications", *Sensors Actuators B: Chem.,* Vol.69 (1), pp. 85-95.

[125] Yang, L.and Saavedra, S.S., (1995), "Chemical sensing using sol-gel derived planar waveguides and indicator phases", *Anal.Chem.,* Vol.67 (8), pp. 1307-1314.

[126] Yang, L., Saavedra, S.S.and Armstrong, N.R., (1996), "Sol-gel-based, planar waveguide sensor for gaseous iodine", *Anal.Chem.,* Vol.68 (11), pp. 1834-1841.

[127] Skrdla, P.J., Armstrong, N.R.and Saavedra, S.S., (2002), "Starch-iodine films respond to water vapor", *Anal.Chim.Acta,* Vol.455 (1), pp. 49-52.

[128] Puyol, M., et al. (1999), "Integrated waveguide absorbance optode for chemical sensing", *Anal.Chem.,* Vol.71 (22), pp. 5037-5044.

[129] Puyol, M., et al. (2002), "Improved integrated waveguide absorbance optodes for ion-selective sensing", *Anal.Chem.,* Vol.74 (14), pp. 3354-3361.

[130] Hisamoto, H., et al. (1997), "Ion-sensitive and selective active waveguide optodes", *Anal.Chim.Acta,* Vol.342 (1), pp. 31-39.

[131] Lambeck, P.V. (2006), "Integrated optical sensors for the chemical domain", *Measurement science and technology,* Vol.17 (8), pp. R93.

[132] Gauglitz, G. (2005), "Direct optical sensors: principles and selected applications", *Analytical and bioanalytical chemistry,* Vol.381 (1), pp. 141-155.

[133] Lambeck, P.V. (2006), "Integrated optical sensors for the chemical domain", *Measurement science and technology,* Vol.17 (8), pp. R93.

[134] Ymeti, A., et al. (2007), "Fast, ultrasensitive virus detection using a Young interferometer sensor", *Nano letters,* Vol.7 (2), pp. 394-397.

[135] Hradetzky, D., Mueller, C.and Reinecke, H., (2006), "Interferometric label-free biomolecular detection system", *Journal of Optics A: Pure and Applied Optics,* Vol.8 (7), pp. S360.

[136] Hoffmann, C., et al. (2007), "Rapid protein expression analysis with an interferometric biosensor for monitoring protein production", *Analytical and bioanalytical chemistry,* Vol.387 (5), pp. 1921-1932.

[137] Yuan, W., et al. (2007), "Surface Plasmon Resonance Biosensor Incorporated in a Michelson Interferometer With< newline/> Enhanced Sensitivity", *Sensors Journal, IEEE,* Vol.7 (1), pp. 70-73.

[138] Koster, T.and Lambeck, P., (2002), "Fully integrated optical polarimeter", *Sensors Actuators B: Chem.,* Vol.82 (2), pp. 213-226.

[139] Stamm, C., Dangel, R.and Lukosz, W., (1998), "Biosensing with the integrated-optical difference interferometer: dual-wavelength operation", *Opt.Commun.,* Vol.153 (4), pp. 347-359.

[140] Äyräs, P., et al. (1998), "Thin-film chemical sensors with waveguide Zeeman interferometry", *Pure and Applied Optics: Journal of the European Optical Society Part A,* Vol.7 (6), pp. 1261.

[141] Kribich, K., et al. (2005), "Novel chemical sensor/biosensor platform based on optical multimode interference (MMI) couplers", *Sensors Actuators B: Chem.,* Vol.107 (1), pp. 188-192.

[142] Hecht, J., (2004), *City of light: the story of fiber optics*, , Oxford University Press on Demand,.

[143] Crisp, J. and Elliott, B., (2005), *Introduction to fiber optics*, , Newnes,.

[144] DeCusatis, C., (2011), *Handbook of fiber optic data communication: a practical guide to optical networking*, , Academic Press,.

[145] Goff, D.R. and Hansen, K.S., (2002), *Fiber optic reference guide: a practical guide to communications technology*, , Focal Pr,.

[146] Marcuse, D. (1974), "Theory of dielectric optical waveguides", *New York, Academic Press, Inc., 1974.267 p.*, Vol.1 .

[147] Briley, B.E., (1988), *An introduction to fiber optics system design*, , North-Holland Amsterdam etc.,.

[148] Kapron, F., Keck, D.B.and Maurer, R.D., (1970), "Radiation losses in glass optical waveguides", *Appl.Phys.Lett.*, Vol.17 (10), pp. 423-425.

[149] Tamir, T. and Alferness, R., (1990), *Guided-wave optoelectronics*, , Springer-Verlag Berlin,.

[150] Marcuse, D., (1974), *Theory of dielectric optical waveguides*, , Access Online via Elsevier,.

[151] Lee, D.L. and Lee, D., (1986), *Electromagnetic principles of integrated optics*, , Wiley New York (NY) et al.,.

[152] Ulrich, R. (1975), "Light-propagation and imaging in planar optical waveguides", *Nouvelle Revue d'Optique*, Vol.6 (5), pp. 253.

[153] Ulrich, R.and Ankele, G., (1975), "Self- imaging in homogeneous planar optical waveguides", *Appl.Phys.Lett.*, Vol.27 (6), pp. 337-339.

[154] Ulrich, R.and Kamiya, T., (1978), "Resolution of self-images in planar optical waveguides", *JOSA*, Vol.68 (5), pp. 583-592.

[155] Soldano, L.B., et al. (1992), "Planar monomode optical couplers based on multimode interference effects", *Lightwave Technology, Journal of*, Vol.10 (12), pp. 1843-1850.

[156] Roijen, R.v., et al. (1994), "Compact InP- based ring lasers employing multimode interference couplers and combiners", *Appl.Phys.Lett.*, Vol.64 (14), pp. 1753-1755.

[157] Kribich, K. R., et al., 2004, "Thermo-optic switches using sol-gel processed hybrid materials", "Thermo-optic switches using sol-gel processed hybrid materials", *Proc. of SPIE Vol*,Vol.5451, 519.

[158] Lagali, N.S., et al. (1999), "Analysis of generalized Mach-Zehnder interferometers for variable-ratio power splitting and optimized switching", *J.Lightwave Technol.,* Vol.17 (12), pp. 2542.

[159] Paiam, M.and MacDonald, R., (1998), "A 12-channel phased-array wavelength multiplexer with multimode interference couplers", *Photonics Technology Letters, IEEE,* Vol.10 (2), pp. 241-243.

[160] Hibino, Y. (2002), "Recent advances in high-density and large-scale AWG multi/demultiplexers with higher index-contrast silica-based PLCs", *Selected Topics in Quantum Electronics, IEEE Journal of,* Vol.8 (6), pp. 1090-1101.

[161] Soldano, L.B.and Pennings, E.C., (1995), "Optical multi-mode interference devices based on self-imaging: principles and applications", *Lightwave Technology, Journal of,* Vol.13 (4), pp. 615-627.

[162] Ebeling, K.J., (1993), *Integrated optoelectronics: waveguide optics, photonics, semiconductors,* , Springer-Verlag,.

[163] Kawano, K.and Kitoh, T., (2001), "Introduction to Optical Waveguide Analysis: Solving Maxwell's Equations and Schrödinger Equation, 233–248", .

[164] Dakin, J.P. and Brown, R.G., (2006), *Handbook of optoelectronics,* , CRC Press,.

[165] Brinker, C.J. and Scherer, G.W., (1990), *Sol-gel science: the physics and chemistry of sol-gel processing,* , Academic Pr,.

[166] Sanchez, C., et al. (2003), "Optical properties of functional hybrid organic–inorganic nanocomposites", *Adv Mater,* Vol.15 (23), pp. 1969-1994.

[167] Sanchez, C., et al. (2003), "Optical properties of functional hybrid organic–inorganic nanocomposites", *Adv Mater,* Vol.15 (23), pp. 1969-1994.

[168] Sanchez, C., Ribot, F.and Lebeau, B., (1999), "Molecular design of hybrid organic-inorganic nanocomposites synthesized via sol-gel chemistry", *J.Mater.Chem.,* Vol.9 (1), pp. 35-44.

[169] Avellaneda, C., Dahmouche, K.and Bulhoes, L., (2002), "All Sol-Gel Electrochromic Smart Windows: CeO 2-TiO 2/Ormolyte/WO 3", *Molecular Crystals and Liquid Crystals,* Vol.374 (1), pp. 113-118.

[170] Avendano, E., et al. (2006), "Electrochromic materials and devices: Brief survey and new data on optical absorption in tungsten oxide and nickel oxide films", *Thin Solid Films,* Vol.496 (1), pp. 30-36.

[171] Hamdy, A.S. (2006), "Advanced nano-particles anti-corrosion ceria based sol gel coatings for aluminum alloys", *Mater Lett,* Vol.60 (21), pp. 2633-2637.

[172] Higgins, C., et al. (2007), "Novel hybrid optical sensor materials for in-breath O2 analysis", *Analyst,* Vol.133 (2), pp. 241-247.

[173] Lei, B., et al. (2006), "Mesostructured silica chemically doped with RuII as a superior optical oxygen sensor", *Advanced Functional Materials,* Vol.16 (14), pp. 1883-1891.

[174] Besanger, T.R.and Brennan, J.D., (2006), "Entrapment of membrane proteins in sol-gel derived silica", *J.Sol Gel Sci.Technol.,* Vol.40 (2), pp. 209-225.

[175] Gupta, R.and Chaudhury, N., (2007), "Entrapment of biomolecules in sol–gel matrix for applications in biosensors: problems and future prospects", *Biosensors and Bioelectronics,* Vol.22 (11), pp. 2387-2399.

[176] Eldada, L. (2004), "Optical communication components", *Rev.Sci.Instrum.,* Vol.75 (3), pp. 575-593.

[177] Eldada, L. (2001), "Advances in telecom and datacom optical components", *Optical Engineering,* Vol.40 (7), pp. 1165-1178.

[178] Coudray, P., et al., 1998, "Integrated optical devices achieved by sol gel process", "Integrated optical devices achieved by sol gel process", *Society of Photo-Optical Instrumentation Engineers (SPIE) Conference Series,*Vol.3278, 252-258.

[179] Najafi, S.I., et al. (1998), "Sol-gel glass waveguide and grating on silicon", *J.Lightwave Technol.,* Vol.16 (9), pp. 1640.

[180] Pierre, A.C. (1992), "Introduction aux procédés sol-gel", *Project forceram, .*

[181] Charles B. Hurd. (1938), "Theories for the Mechanism of the Setting of Silicic Acid Gels.", *Chem. Rev.,* Vol.22 (3), pp. 403-422.

[182] Hamilton, D.and MacKenzie, W., (1960), "Nepheline Solid Solution in the System NaAISiO4–KAISiO4–SiO2", *J.Petrol.,* Vol.1 (1), pp. 56-72.

[183] Luth, W.and INGAMELL. CO., (1965), "Gel preparation of starting materials for hydrothermal experimentation", *Am.Mineral.,* Vol.50 (1-2), pp. 255-&.

[184] Levene, L.and Thomas, I.M., (1972), *Process of converting metalorganic compounds and high purity products obtained therefrom, .*

[185] Voronkov, M.G., Mileshkevich, V.P.and Yuzhelevskii, Y.A., (1978), "The siloxane bond", *Consultants Bureau, New York,* Vol.196 .

[186] Livage, J.and Sanchez, C., (1992), "Sol-gel chemistry", *J.Non Cryst.Solids,* Vol.145 (0), pp. 11-19.

[187] Babonneau, F.and Maquet, J., (2000), "Nuclear magnetic resonance techniques for the structural characterization of siloxane–oxide hybrid materials", *Polyhedron,* Vol.19 (3), pp. 315-322.

[188] Yuh, S., et al., 1994, "Rare-earth doped, low hydroxyl organically modified silicates", "Rare-earth doped, low hydroxyl organically modified silicates", *MRS Proceedings,*Vol.346,: Cambridge Univ Press 803.

[189] Sanchez, C.and Ribot, F., (1994), "Design of hybrid organic-inorganic materials synthesized via sol-gel chemistry", *New Journal of Chemistry,* Vol.18 (10), pp. 1007-1047.

[190] Corriu, R.J., et al. (1992), "Preparation of monolithic gels from silicon halides by a non-hydrolytic sol-gel process", *J.Non Cryst.Solids,* Vol.146 pp. 301-303.

[191] Acosta, S., et al. (1994), "Novel non-hydrolytic sol-gel route to metal oxides", *J.Sol Gel Sci.Technol.,* Vol.2 (1-3), pp. 25-28.

[192] Arnal, P., et al. (1997), "A solution chemistry study of nonhydrolytic sol-gel routes to titania", *Chemistry of materials,* Vol.9 (3), pp. 694-698.

[193] Bourget, L., Leclercq, D.and Vioux, A., (1999), "Catalyzed nonhydrolytic sol-gel route to organosilsesquioxane gels", *J.Sol Gel Sci.Technol.,* Vol.14 (2), pp. 137-147.

[194] Acosta, S., et al. (1994), "Preparation of alumina gels by a non-hydrolytic sol-gel processing method", *J.Non Cryst.Solids,* Vol.170 (3), pp. 234-242.

[195] Robert, J.and HubertáMutin, P., (1996), "Preparation of anatase, brookite and rutile at low temperature by non-hydrolytic sol–gel methods", *Journal of Materials Chemistry,* Vol.6 (12), pp. 1925-1932.

[196] Bourget, L., Leclercq, D.and Vioux, A., (1999), "Catalyzed nonhydrolytic sol-gel route to organosilsesquioxane gels", *J.Sol Gel Sci.Technol.,* Vol.14 (2), pp. 137-147.

[197] Mennig, M., Michael Zahnhausen and Helmut K. Schmidt 1998, "Novel nonhydrolytic sol-gel route to low-OH-and CH-containing organic-inorganic composites", "Novel nonhydrolytic sol-gel route to low-OH-and CH-containing organic-inorganic composites", *SPIE's International Symposium on Optical Science, Engineering, and Instrumentation,*: International Society for Optics and Photonics 68-78.

[198] Bourget, L., et al. (1998), "Non-hydrolytic sol–gel routes to silica", *J.Non Cryst.Solids,* Vol.242 (2), pp. 81-91.

[199] Sanchez, C., et al. (2005), "Applications of hybrid organic–inorganic nanocomposites", *Journal of Materials Chemistry,* Vol.15 (35-36), pp. 3559-3592.

[200] Sanchez, C., et al. (2011), "Applications of advanced hybrid organic–inorganic nanomaterials: from laboratory to market", *Chem.Soc.Rev.,* Vol.40 (2), pp. 696-753.

[201] Livage, J. (1977), "Vers une chimie écologique in", *Le Monde,* Vol.26 .

[202] Gharbi, N., et al. (1982), "Mixed-valence poly (vanadic acid) gels", *Inorg.Chem.,* Vol.21 (7), pp. 2758-2765.

[203] Avnir, D., Levy, D.and Reisfeld, R., (1984), "The nature of the silica cage as reflected by spectral changes and enhanced photostability of trapped rhodamine 6G", *J.Phys.Chem.,* Vol.88 (24), pp. 5956-5959.

[204] Schmidt, H., Scholze, H.and Kaiser, A., (1984), "Principles of hydrolysis and condensation reaction of alkoxysilanes", *J.Non Cryst.Solids,* Vol.63 (1), pp. 1-11.

[205] Sanchez, C., et al. (1988), "Chemical modification of alkoxide precursors", *J.Non Cryst.Solids,* Vol.100 (1), pp. 65-76.

[206] Sur, G.and Mark, J., (1985), "Elastomeric networks cross-linked by silica or titania fillers", *European polymer journal,* Vol.21 (12), pp. 1051-1052.

[207] Morikawa, A., et al. (1992), "Preparation of new polyimide–silica hybrid materials via the sol–gel process", *Journal of Materials Chemistry,* Vol.2 (7), pp. 679-689.

[208] Schmidt, H.K.and Popall, M., (1990), "Inorganic-organic composites (ORMOCERs) for optical", *Sol-gel optics: 11-13 July 1990, San Diego, California,* .

[209] Izumi, K., et al. (1990), "Coating of fluorine-doped ZrO< sub> 2</sub> films on steel sheets by sol-gel method", *J.Non Cryst.Solids,* Vol.121 (1), pp. 344-347.

[210] Chujo, Y.and Saegusa, T., (1992), "Organic polymer hybrids with silica gel formed by means of the sol-gel method", *Macromolecules: Synthesis, Order and Advanced Properties,* pp. 11-29.

[211] Dunn, B.and Zink, J.I., (1991), "Optical properties of sol–gel glasses doped with organic molecules", *Journal of Materials Chemistry,* Vol.1 (6), pp. 903-913.

[212] Schottner, G. (2001), "Hybrid sol-gel-derived polymers: applications of multifunctional materials", *Chemistry of Materials,* Vol.13 (10), pp. 3422-3435.

[213] Audebert, P., Griesmar, P.and Sanchez, C., (1991), "Electrochemical probing of the sol–gel–xerogel evolution", *J.Mater.Chem.,* Vol.1 (4), pp. 699-700.

[214] Ellerby, L.M., et al. (1992), "Encapsulation of proteins in transparent porous silicate glasses prepared by the sol-gel method", *Science,* Vol.255 (5048), pp. 1113-1115.

[215] Yamanaka, S.A., et al. (1992), "Enzymatic activity of glucose oxidase encapsulated in transparent glass by the sol-gel method", *Chemistry of materials,* Vol.4 (3), pp. 495-497.

[216] Audebert, P., Demaille, C.and Sanchez, C., (1993), "Electrochemical probing of the activity of glucose oxidase embedded sol-gel matrixes", *Chemistry of materials,* Vol.5 (7), pp. 911-913.

[217] Wang, B., et al. (1991), "High refractive index hybrid ceramer materials prepared from titanium tetraisopropoxide and poly (arylene ether phosphine oxide) through sol-gel processing", *Polymer communications,* Vol.32 (13), pp. 400-402.

[218] Oubaha, M., et al. (2005), "New organic inorganic sol–gel material with high transparency at 1.55 μm", *Opt.Commun.,* Vol.253 (4–6), pp. 346-351.

[219] Sorek, Y., et al. (1997), "Zirconia and zirconia-ORMOSIL planar waveguides prepared at room temperature", *Chemistry of materials,* Vol.9 (3), pp. 670-676.

[220] Decker, C. (1998), "The use of UV irradiation in polymerization", *Polym.Int.,* Vol.45 (2), pp. 133-141.

[221] Decker, C. (1998), "The use of UV irradiation in polymerization", *Polym.Int.,* Vol.45 (2), pp. 133-141.

[222] H. K. Tnshoff and I. Inasakia., (2002), *Sensors in Manufacturing,* , Wiley-VCH Verlag,.

[223] Borisov, S.M.and Wolfbeis, O.S., (2008), "Optical biosensors", *Chem.Rev.,* Vol.108 (2), pp. 423.

[224] Abrams, M., et al. (2005), "FTTP deployments in the United States and Japan-equipment choices and service provider imperatives", *Lightwave Technology, Journal of,* Vol.23 (1), pp. 236-246.

[225] O'Mahony, M.J., et al. (2006), "Future optical networks", *J.Lightwave Technol.,* Vol.24 (12), pp. 4684-4696.

[226] Karim, S.and Hovell, P., (2007), "Everything over IP—an overview of the strategic change in voice and data networks", *BT Technology Journal,* Vol.25 (3), pp. 198-204.

[227] Bornside, D., Macosko, C.and SCRIVEN, L., (1987), "On the modeling of spin coating", *Journal of imaging technology,* Vol.13 (4), pp. 122-130.

[228] Bornside, D., Macosko, C.and Scriven, L., (1989), "Spin coating: One-dimensional model", *J.Appl.Phys.,* Vol.66 (11), pp. 5185-5193.

[229] Brodie, I.and Muray, J., "The physics of microfabrication. 1982", .

[230] Madou, M. "Fundamentals of microfabrication. 1997", *CRC Press LLC.Capítulo,* Vol.1 pp. 1-50.

[231] Rai-Choudhury, P., (1997), *Handbook of microlithography, micromachining, and microfabrication,* , Inspec/Iee,.

[232] Maruo, S., Nakamura, O.and Kawata, S., (1997), "Three-dimensional microfabrication with two-photon-absorbed photopolymerization", *Opt.Lett.,* Vol.22 (2), pp. 132-134.

[233] Schmidt, V., et al., 2007, "Application of two-photon 3D lithography for the fabrication of embedded ORMOCER waveguides", "Application of two-photon 3D lithography for the fabrication of embedded ORMOCER waveguides", *Proc. SPIE,*Vol.6476, 64760P.

[234] Langer, G. and Markus Riester 2007, "Two-photon absorption for the realization of optical waveguides on printed circuit boards", "Two-photon absorption for the realization of optical waveguides on printed circuit boards", *Integrated Optoelectronic Devices 2007,*: International Society for Optics and Photonics 64750X-64750X-9.

[235] Ovsianikov, A., et al. (2008), "Ultra-low shrinkage hybrid photosensitive material for two-photon polymerization microfabrication", *Acs Nano,* Vol.2 (11), pp. 2257-2262.

[236] Ovsianikov, A., et al. (2008), "Two-photon polymerization of hybrid sol-gel materials for photonics applications", *Laser Chemistry,* Vol.2008 .

[237] Oubaha, M., et al. (2011), "Novel tantalum based photocurable hybrid sol–gel material employed in the fabrication of channel optical waveguides and three-dimensional structures", *Appl.Surf.Sci.,* Vol.257 (7), pp. 2995-2999.

[238] Birnie Iii, D.P. (2004), "Surface skin development and rupture during sol-gel spin-coating", *J.Sol Gel Sci.Technol.,* Vol.31 (1-3), pp. 225-228.

[239] Gorin, A., et al. (2008), "Fabrication of silicon nitride waveguides for visible-light using PECVD: A study of the effect of plasma frequency on optical properties", *Optics Express,* Vol.16 (18), pp. 13509-13516.

[240] Oubaha, M., et al. (2003), "Spectroscopic characterization of intrinsic losses in an organic–inorganic hybrid waveguide synthesized by the sol–gel process", *J.Non Cryst.Solids,* Vol.318 (3), pp. 305-313.

[241] Ovsianikov, A., et al. (2008), "Ultra-low shrinkage hybrid photosensitive material for two-photon polymerization microfabrication", *Acs Nano,* Vol.2 (11), pp. 2257-2262.

[242] Hu, J.and Gordon, R.G., (1991), "Textured fluorine-doped ZnO films by atmospheric pressure chemical vapor deposition and their use in amorphous silicon solar cells", *Solar Cells,* Vol.30 (1), pp. 437-450.

[243] Leguijt, C., et al. (1996), "Low temperature surface passivation for silicon solar cells", *Solar Energy Mater.Solar Cells,* Vol.40 (4), pp. 297-345.

[244] R. Bernini, et al. (2006), "Development and characterization of an integrated silicon micro flow cytometer", *Analytical and Bioanalytical Chemistry,* Vol.368 (5), pp. 1267-1272.

[245] Stewart, G., Muhammad, F.A.and Culshaw, B., (1993), "Sensitivity improvement for evanescent-wave gas sensors", *Sensors Actuators B: Chem.,* Vol.11 (1–3), pp. 521-524.

[246] Richard, C., et al. (2009), "An integrated hybrid interference and absorption filter for fluorescence detection in lab-on-a-chip devices", *Lab on a Chip - Miniaturisation for Chemistry and Biology,* Vol.9 (10), pp. 1371-1376.

[247] Kim, N.and Stebbins, J.F., (2011), "Structure of amorphous tantalum oxide and titania-doped tantala: 17O NMR results for sol-gel and ion-beam-sputtered materials", *Chemistry of Materials,* Vol.23 (15), pp. 3460-3465.

[248] Bernini, R., et al. (2006), "Planar waveguides for fluorescence-based biosensing: Optimization and analysis", *IEEE Sensors Journal,* Vol.6 (5), pp. 1218-1225.

[249] Chang, C., et al. (2010), "Preparation and characterization of TiO2 hybrid sol for UV-curable high-refractive-index organic–inorganic hybrid thin films", *J.Sol Gel Sci.Technol.,* Vol.55 (2), pp. 199-206.

[250] Lü, C.and Yang, B., (2009), "High refractive index organic–inorganic nanocomposites: design, synthesis and application", *Journal of Materials Chemistry,* Vol.19 (19), pp. 2884-2901.

[251] Luo, K., Zhou, S.and Wu, L., (2009), "High refractive index and good mechanical property UV-cured hybrid films containing zirconia nanoparticles", *Thin Solid Films,* Vol.517 (21), pp. 5974-5980.

[252] Popovici, M., et al. (2010), "Zirconia thin film preparation by wet chemical methods at low temperature", *Thin Solid Films,* Vol.519 (2), pp. 630-634.

[253] Copperwhite, R., et al. (2011), "Sensing performance of a refractometric optical sensor platform based on multimode interference couplers", *IEEE Sensors Journal,* Vol.11 (12), pp. 3269-3275.

[254] Ahluwalia, B.S., et al. (2009), "Fabrication of submicrometer high refractive index Tantalum Pentoxide waveguides for optical propulsion of microparticles", *Photonics Technology Letters, IEEE,* Vol.21 (19), pp. 1408-1410.

[255] Lee, D.L. and Lee, D., (1986), *Electromagnetic principles of integrated optics,* , Wiley New York (NY) et al.,.

[256] Oubaha, M., et al. (January 2011), "Influence of hybrid organic-inorganic sol-gel matrices on the photophysics of amino-functionalized UV-sensitizers", *Journal of Materials Science,* Vol.46 (2), pp. 400.

[257] Oubaha, M., et al. (2011), "Influence of hybrid organic–inorganic sol–gel matrices on the photophysics of amino-functionalized UV-sensitizers", *J.Mater.Sci.,* Vol.46 (2), pp. 400-408.

[258] Oubaha, M., et al. (2006), "Development of photo-patternable organo-mineral hybrid films from the sol–gel condensation of alkoxysilanes", *Thin Solid Films,* Vol.510 (1), pp. 334-338.

[259] Oubaha, M., et al. (2003), "Spectroscopic characterization of intrinsic losses in an organic–inorganic hybrid waveguide synthesized by the sol–gel process", *J.Non Cryst.Solids,* Vol.318 (3), pp. 305-313.

[260] Elmaghrum, S., et al. (2013), "Development of a sol–gel photonic sensor platform for the detection of biofilm formation", *Sensors Actuators B: Chem.,* Vol.177 (0), pp. 357-363.